Active Aerodynamic Modification of Wind Turbine Blades to Reduce Load Fluctuation

by

Farid Samara

A thesis
presented to the University of Waterloo
in fulfillment of the
thesis requirement for the degree of
Doctor of Philosophy
in
Mechanical and Mechatronics Engineering

Waterloo, Ontario, Canada, 2020

© Farid Samara 2020

Examining Committee Membership

The following served on the Examining Committee for this thesis. The decision of the Examining Committee is by majority vote.

External Examiner:	David Wood Professor, Dept. of Mechanical and Manufacturing Engineering, University of Calgary
Supervisor:	David A. Johnson Professor, Dept. of Mechanical and Mechatronics Engineering, University of Waterloo
Internal Member:	Fue-Sang Lien Professor, Dept. of Mechanical and Mechatronics Engineering, University of Waterloo
Internal Member:	Sean Peterson Associate Professor, Dept. of Mechanical and Mechatronics Engineering, University of Waterloo
Internal-External Member:	Andrea Scott Assistant Professor, Dept. of Systems Design Engineering, University of Waterloo

I hereby declare that I am the sole author of this thesis. This is a true copy of the thesis, including any required final revisions, as accepted by my examiners.

I understand that my thesis may be made electronically available to the public.

Abstract

Wind turbines operate predominantly in relatively unsteady flow conditions and are typically misaligned with the incoming wind. Moreover, as wind turbines increase in size, the loading on the blades becomes more problematic and obstructs the development of larger and more efficient wind turbines. In this project, a trailing edge flap (TEF) is used to develop an active control strategy to attenuate load fluctuation on the blades in normal environmental conditions. Wind turbine load fluctuation reduction techniques could increase the power produced by the turbine, reduce the capital and maintenance cost while prolonging the life span of not just the blades but the drivetrain and tower.

An experimental 3.5 m diameter wind turbine rig was designed and tested in a large scale wind generation facility operating at different tip speed ratios, blade pitch angles and yaw angles. The instrumentation of the compact blade was capable of measuring rotor torque, flapwise/edgewise blade root bending moment, and normal force coefficient at r/R=0.66 and 0.82. Two custom-built actuation systems were capable of oscillating the pitch and flap independently to create an active control strategy. The blade is of constant pitch and chord of 178 mm while the TEF covers 20% of the chord and 22% of the 1.47 m aerodynamic blade span.

First, a 2D experimental campaign showed how the TEF is fully capable of controlling the airfoil aerodynamics statically and during dynamic stall. It is concluded that even though the TEF was not capable of controlling the formation of the leading edge vortex (LEV), it was however capable of reducing its magnitude and more importantly, a reduction in cyclic loading. Second, a comprehensive and a detailed set of results showed how the rotor torque, flapwise/edgewise blade root bending moment, and normal force coefficient at multiple r/R locations change under different yaw angles, pitch angles, tip speed ratio and TEF angles. When possible the results were compared to numerical models such as the NREL OpenFast code to increase confidence in the results and provide essential conclusions to improve the models. It was found that in non-yawed conditions, OpenFast predictions were accurate but discrepancies start to emerge when the turbine is yawed and operating in dynamic stall conditions. Finally, the pitch and TEF were continuously actuated in separate tests to determine the effectiveness of each system at reducing load fluctuation on a yawed wind turbine. The reduction in load fluctuation due to the TEF and the pitch systems were found to be between 45%-65% and 65%-80% respectively. The data presented throughout this thesis provides a methodical and comprehensive argument to support the use of TEF on a utility-scale turbines to reduce load fluctuation and fatigue levels at the blade root. It also provides insight on the effects of dynamic stall, stall delay and 3D flow induced by the blade rotation on an operating wind turbine.

Acknowledgments

First and foremost, thanks be to God for his many blessings and never-ending Grace during what ended up being the most transformative years of my life.

I would like to give special thanks to my supervisor, Prof. David A. Johnson, for providing invaluable guidance when needed but also the chance to venture on my own to find my own research style. I have been extremely lucky to have a supervisor who listened to my half-baked theories and provided encouragements when it seemed that all hope is lost. He also played an important role in building my passion for cycling, aka an exercise in sustained suffering, because he knew that one day I would have to use that exercise to finish writing this thesis.

A massive thanks to my fellow graduate students and friends at the Wind Energy group for putting up with me for the past five years and for the positive attitude that made this research fun. A special thanks goes to Faegheh Ghorbanishohrat, Michael McKinnon, Alison Zilstra, Tyler Gallant and Nicholas Tam. It would not be fair to call them colleagues, as they became my closest friends who in times of crises showed their true colors of kindness and support.

The support of the technical staff at the University of Waterloo was invaluable in building the experimental rig at the core of this research. Many thanks to Jason Benninger, Neil Griffet and Andy Barber for their expertise, willingness to help and kindness to teach.

I would like to thank my external examiner, Professor David Wood, for his comments and constructive criticism. Many thanks also goes to Professor David Mathews who read the entirety of this thesis for spelling and grammatical error.

This research would not have been possible if it weren't for the unconditional love and support of my family. They have rescued me in times of trouble and shared my joy in times of celebration. To my Mom, Wadiaa Samara, for her kindness and generosity that instills a calmness in my heart. To my Dad, George Samara, for never giving up on me and giving me the most precious thing of all, wisdom. To my brothers, Mofid and Rayan Samara, for keeping me humble and never failing to remind me that a monkey can get his PhD with that many years of schooling.

Finally to all my friends along the way, without you I would have graduated two years earlier with no sense of adventure nor exploration.

Dedication

This thesis is dedicated to my parents.

For their endless love, support and encouragement

Table of Contents

List of Tables xiii

List of Figures xiv

Nomenclature xix

1 Introduction 1

1.1 Wind Energy . . . 1
1.2 Project Motivation . . . 3
1.3 Project Objectives . . . 5
1.4 Thesis Outline . . . 5

2 Background and Theory 7

2.1 2D Airfoil Aerodynamics . . . 7
2.1.1 Airfoil Aerodynamic Forces . . . 8
2.1.2 2D Dynamic Stall . . . 10
2.1.3 Airfoil with Trailing Edge Flap (TEF) . . . 13
2.2 Wind Turbine Aerodynamics . . . 14
2.2.1 Wind Turbine Terminology . . . 14
2.2.2 Actuator Disc and Blade Element Model . . . 15
2.2.3 Blade Loading During Operation . . . 18

2.2.4 Blade Aerodynamics in Steady Yaw . . . 20
2.3 Aerodynamic Modeling Tools . . . 22
2.3.1 XFoil Code . . . 22
2.3.2 PROPID Code . . . 22
2.3.3 AirfoilPrep Code . . . 23
2.3.4 OpenFast Code . . . 23
2.4 Previous Studies . . . 24
2.4.1 Dynamic Stall on 2D Airfoil Equipped with TEF . . . 24
2.4.2 3D Flow Effects . . . 26
2.4.3 Wind Turbine Measurements in a Wind Tunnel . . . 27
2.4.4 Wind Turbine with Individual Pitch Control . . . 30
2.4.5 Wind Turbine with TEF . . . 31

3 Experimental Setup **37**
3.1 TEF Airfoil Design . . . 37
3.1.1 Airfoil Geometry and Selection . . . 37
3.1.2 3D Printed Airfoil . . . 38
3.1.3 Surface Pressure Measurements . . . 41
3.1.4 Flap Actuation . . . 46
3.1.5 Internal Organization . . . 47
3.2 2D TEF Experimental Campaign . . . 49
3.2.1 Closed-Loop Wind Tunnel Specifications . . . 49
3.2.2 Small-Scale Wind Tunnel Setup . . . 49
3.2.3 AOA Actuation . . . 49
3.2.4 Strain Measurements . . . 50
3.2.5 Data Acquisition System . . . 51
3.3 Wind Turbine Experiment . . . 52
3.3.1 UWaterloo Wind Generation Research Facility . . . 52
3.3.2 Wind Energy Group Test Turbine . . . 57
3.3.3 Wind Turbine Rotor Setup . . . 58

4 Experimental Procedure and Verification **66**

4.1 2D TEF Experimental Campaign . . . 66

4.1.1 Static Airfoil Characterization . . . 67

4.1.2 Dynamic Airfoil Oscillation . . . 67

4.2 Wind Turbine TEF Experimental Campaign . . . 70

4.2.1 Wind Turbine Base Loading . . . 70

4.2.2 Dynamic Flap Cases . . . 71

4.2.3 Dynamic Pitch Cases . . . 72

4.3 Convergence Study . . . 72

4.3.1 2D TEF Convergence Study . . . 73

4.3.2 Wind Turbine Convergence Study . . . 73

4.4 Experimental Validation . . . 74

4.4.1 Differential Pressure Measurement Validation . . . 74

4.4.2 Azimuth Angle Validation . . . 77

4.4.3 Step Response . . . 78

4.5 OpenFast Setup . . . 80

4.5.1 Airfoil Parameters . . . 80

4.5.2 Blade Properties . . . 81

4.5.3 Running Conditions . . . 82

4.6 Wind Turbine Performance Measurements . . . 83

4.6.1 Torque Measurements . . . 83

4.6.2 Blade Moment Measurements . . . 83

4.6.3 C_n Measurements . . . 84

4.6.4 Power Spectral Density (PSD) . . . 86

5 2D TEF Experimental Campaign **87**
5.1 Static Results . . . 88
5.1.1 Static Airfoil Characterization . . . 88
5.1.2 High Flap Angle Characterization . . . 90
5.2 Dynamic Pitching . . . 93
5.2.1 Case 1 $\alpha_{mean} = 0°$ . . . 94
5.2.2 Case 2 $\alpha_{mean} = 10°$ . . . 100
5.2.3 Case 3 $\alpha_{mean} = 20°$ . . . 108
5.2.4 Case 4 $\alpha_{mean} = 25°$ . . . 116
5.3 Model Versus Experimental Dynamic Stall . . . 119
5.4 Conclusions . . . 123

6 Full-Scale Testing on a Wind Turbine **125**
6.1 Pitch and Flap System Overview . . . 126
6.1.1 Pitch Outline . . . 126
6.1.2 TEF influence on turbine loading . . . 129
6.1.3 Pitch and Flap Comparison . . . 130
6.2 Steady Pitch and Tip Speed Ratio Cases . . . 132
6.2.1 Outline . . . 132
6.2.2 Tip Speed Ratio Influence . . . 133
6.2.3 Pitch Angle Influence . . . 139
6.2.4 OpenFast Model Conclusion . . . 152
6.2.5 Pitch and Tip Speed Influence Summary . . . 153
6.3 Steady Flap Cases . . . 154
6.3.1 Outline . . . 155
6.3.2 Yaw=0° Flap at r/R=0.82 . . . 156
6.3.3 Yaw=0° Flap at r/R=0.66 . . . 162
6.3.4 Yaw=30° Flap at r/R=0.82 . . . 167
6.3.5 TEF Influence Summary . . . 170

7 Wind Turbine Load Alleviation **172**
7.1 Dynamic Flap Cases . . . 173
7.1.1 Outline . . . 173
7.1.2 $\beta = 3°$ Flap at r/R=0.82 . . . 173
7.1.3 $\beta = 6°$ Flap at r/R=0.82 . . . 177
7.1.4 $\beta = 3°$ Flap at r/R=0.66 . . . 180
7.2 Dynamic Pitch Cases . . . 182
7.2.1 Outline . . . 182
7.2.2 $\beta_{mean} = 3°$ . . . 183
7.2.3 $\beta_{mean} = 6°$ . . . 186
7.3 Dynamic Flap and Pitch Comparison . . . 189
7.3.1 ΔC_p Contour Comparison . . . 190
7.3.2 PSD Reduction Comparison . . . 191
7.3.3 Comparison Matrix . . . 195
7.4 Load Alleviation Summary . . . 198

8 Concluding Remarks **200**
8.1 Summary . . . 200
8.2 Project Objectives Achieved and Contribution . . . 203
8.3 Recommendations . . . 204

References **207**

APPENDICES **219**

A Publications and Conferences **220**

B Technical Experimental Setup **223**

B.1 Detailed Drawing 224

B.2 S833 Surface Pressure Tap Location 224

B.3 Maxon Servo Motor and Controller 225

B.4 Stepper Motor Controller 225

B.5 OpenFast Input Files 226

B.5.1 Airfoil Input Files 226

C Data Calibration **229**

C.1 Pressure Transducer Calibration 229

C.2 Strain Gage Calibration 229

C.3 Torque Sensor Calibration 230

D Uncertainty Analysis **233**

D.1 Review of Experimental Uncertainty 233

D.2 Torque Sensor Uncertainty Calculations 234

D.3 Strain Gage Uncertainty Calculations 235

D.4 C_n Uncertainty Calculations 235

D.5 Angular Momentum Calculations 236

List of Tables

3.1 UWaterloo Wind Facility fan specifications 53
3.2 UWaterloo Wind Facility geometry specifications 53
3.3 Slip ring channel layout 64

4.1 Wind tunnel dynamic airfoil oscillation test cases 69
4.2 Wind turbine base loading test cases 71
4.3 Test matrix for dynamic motion for flap cases 72
4.4 Test matrix for dynamic motion for pitch cases 72

6.1 Test matrix for pitch cases in steady conditions 133
6.2 Test matrix for flap cases in steady condition 156

7.1 Test matrix for dynamic motion for pitch cases 173
7.2 Test matrix for dynamic motion the two pitch cases investigated 183
7.3 A comparison matrix between the flap and pitch system 197

B.1 Tap locations for the S833 airfoil 224
B.2 Motor/gearbox/encoder specifications 225
B.3 Maxon EPOS 24/2 controller 225

C.1 Pressure transducer calibration properties 232

D.1 Uncertainty sources for the Futek Torque Sensor 234

List of Figures

1.1 Wind turbine diameter size growth over time in terms of rotor diameter. . 2

2.1 Airfoil nomenclature typically used in literature 8
2.2 Aerodynamic forces and moments acting on an airfoil 9
2.3 C_L versus α plot illustrating attached and separated flow 11
2.4 Influence of the dynamic stall cycle on the airfoil C_L 12
2.5 Influence of the flap deflection on the lift curve in an ideal case 13
2.6 Terminology of an upwind horizontal-axis wind turbine 16
2.7 2D airfoil showing the velocity triangle and the forces 18
2.8 The coordinate system used to identify the idealized load distribution on the turbine blades 19
2.9 The different types of loading on HAWT blades 20
2.10 A horizontal-axis turbine with a schematic of the velocity triangle for a yawed turbine 21
2.11 Experimental and OpenFast models showing the normal force obtained from the MEXICO project 30
2.12 The location of the newly developed vortex at the TEF 33

3.1 A sketch illustrating the airfoil and flap degrees of freedom 39
3.2 3D model of the airfoil with the three different sections 40
3.3 Different features of the 3D printed model 41
3.4 S833 section with the pressure taps along the suction and pressure side . . 42

3.5 The layout of the pressure transducers on the PCB 45
3.6 Maxon motor and controller assembly inside the airfoil 48
3.7 Internal organization of the airfoil section with cover removed 48
3.8 Wind tunnel experimental setup with the airfoil and actuation 50
3.9 Strain gage setup and position along the shaft 51
3.10 Data acquisition system setup for the wind tunnel 52
3.11 Photographs of UWaterloo Wind Generation Research Facility 54
3.12 Non-dimensional velocity profile at 0.3 D upstream of the turbine 55
3.13 Placement of additional screens in the wind tunnel 56
3.14 Additional screen impact on M_{FW} and C_L 57
3.15 Wind Energy Group test rig drive-train with labels 58
3.16 A 3D model of the connection between the motor and the blade shaft . . . 59
3.17 Layout of the hub, aerodynamic blade and the TEF flap 61
3.18 Pictures of the wind turbine hub and wind tunnel layout 62
3.19 3D model of the wind turbine assembly showing with the main components 63
3.20 Data acquisition system setup for the wind turbine 65

4.1 Kinematics of the airfoil and TEF motion 69
4.2 Coefficient of lift (C_L) and uncertainty for different cycle counts for case 1b 73
4.3 Wind Turbine convergence study on (a) C_n and (b) M_{FW} 74
4.4 Comparison between single-ended pressure measurements and differential pressure measurements 76
4.5 Contours of ΔC_p for the single-ended pressure measurement technique . . . 77
4.6 Azimuth angle validation and calibration based on an air jet 78
4.7 Pitch step response for C_n and M_{FW} 79
4.8 Flap step response for C_n and M_{FW} 80
4.9 Blade velocity variation for a yawed turbine 85

5.1 Measured C_L and C_M versus α for several α_F 89

5.2 Contours of $-\Delta C_p$ versus x/c versus static α . . . 90
5.3 Measured C_L and C_M versus α_F for several α values . . . 92
5.4 Static contours of $-\Delta C_p$ versus x/c versus α_F for various α . . . 93
5.5 C_L and C_M versus α for different flap phases for case 1a . . . 96
5.6 C_L, and C_M versus α for different flap phases for case 1b . . . 97
5.7 Contours of $-\Delta C_p$ versus x/c versus α for case 1b . . . 99
5.8 Contours of STD(ΔC_p) versus x/c versus t/τ for case 1b . . . 100
5.9 C_L, and C_M versus α for different flap phases for case 2a . . . 103
5.10 C_L and C_M versus α for different flap phases for case 2b . . . 105
5.11 Contours of $-\Delta C_p$ versus x/c versus α for case 2b . . . 106
5.12 Contours of log(STD(ΔC_p)) versus x/c versus α for case 2b . . . 107
5.13 C_L and C_M versus α for different flap phases for case 3a . . . 110
5.14 C_L and C_M versus α for different flap phases for case 3b . . . 112
5.15 Contours of $-\Delta C_p$ versus x/c versus α for case 3b . . . 113
5.16 Contour plots showing the STD(ΔC_p) versus x/c versus α for case 3b . . . 115
5.17 Normalized power spectral density distribution for C_L, and moment for different flap phases (ϕ) for case 3a . . . 116
5.18 C_L and C_M versus α for different flap phases for case 4 . . . 118
5.19 Contour plots showing the $-\Delta C_p$ versus x/c versus α for case 4a . . . 119
5.20 C_L and C_M versus α comparing the FixedFlap case to the unsteady aerodynamic model for case 2 . . . 121
5.21 C_L and C_M versus α comparing the FixedFlap case to the unsteady aerodynamic model for case 3 . . . 122

6.1 C_{power}, M_{FW}, and C_n for different β angles and λ . . . 128
6.2 α and C_n distribution along the spanwise of the blade for $\beta = 6°$ from PROPID 129
6.3 C_{power}, M_{FW} and C_n for different α_F angles at $\beta = 6°$ . . . 130
6.4 C_{power}, M_{FW} and C_n for different α_F and β angles for $\lambda = 4.2$ . . . 131
6.5 Turbine performance for various λ values for case 1a . . . 135

6.6 Turbine performance for various λ values for case 1b 139
6.7 Turbine performance for various β for case 1c 142
6.8 Contours of $-\Delta C_p$ versus x/c versus ψ for $\beta = 0°$ and $\beta = 6°$ for case 1c . 143
6.9 Turbine performance for various β for case 1d 147
6.10 C_n versus α for case 1d 148
6.11 Contours of $-\Delta C_p$ versus x/c versus ψ for case 1d 150
6.12 Contours of $STD(\Delta C_p)$ versus x/c versus ψ for case 1d 151
6.13 Turbine performance for various α_F for case 2a 158
6.14 Turbine performance for various α_F for case 2b.R1 159
6.15 Percentage change in M_{FW} and C_n relative to $\alpha_F = 0°$ for case 2a and 2b.R1 161
6.16 Contours of $-\Delta C_p$ for $\alpha_F = -20°$ and $\alpha_F = 20°$ for case 2b.R1 162
6.17 Cycle-averaged turbine performance versus α_F for case 2b.R1 and 2b.R2 . 165
6.18 Contours of $-\Delta C_p$ versus x/c versus ψ at r/R=0.66 for case 2b.R2 166
6.19 Turbine performance for various α_F for case 2c 168
6.20 Contours of $-\Delta C_p$ versus x/c versus ψ for case 2c 169

7.1 Turbine performance with an oscillating flap for different flap phases for case 3a 175
7.2 Normalized power spectral density distribution for M_{FW} and C_n for different flap phases for case 3a 177
7.3 Turbine performance with an oscillating flap for different flap phases for case 3b 178
7.4 Contours of $-\Delta C_p$ versus x/c versus ψ for case 3b 180
7.5 Turbine performance with an oscillating flap for different flap phases for case 3c 181
7.6 Contours of $-\Delta C_p$ versus x/c versus ψ for case 3c 182
7.7 Turbine performance with an oscillating pitch for different pitch phases for case 4a 185
7.8 Normalized power spectral density distribution for M_{FW} and C_n at r/R=0.82 for different pitch phases for case 4a 186

7.9 Turbine performance with an oscillating pitch for different pitch phases for case 4b 188

7.10 Contours of $-\Delta C_p$ versus x/c versus ψ at r/R=0.82 and r/R=0.66 for case 4b 189

7.11 Contours of $-\Delta C_p$ for Fixed case, $\phi_{Pitch} = 0\pi$ and $\phi_{Flap} = 0\pi$ where $\gamma = 30°$, λ=3.5 191

7.12 A bar chart summarizing the % PSD change in C_n and M_{FW} 194

B.3 Enclosure that houses the Galil controller and power supply 226

C.1 Strain gage calibration group 2 for different weights 231

Nomenclature

a	Induction Factor.
C_D	Drag Coefficient.
c	Chord Length [m].
C_L	Lift Coefficient.
C_M	Moment Coefficient.
C_n	Normal Force Coefficient.
C_p	Pressure Coefficient.
C_{power}	Wind Turbine Power Coefficient.
C_T	Thrust coefficient.
C_w	Torsional Damping.
F_D	Drag Force [N].
F_L	Lift Force [N].
f_β	Blade Pitching Frequency [Hz].
f_F	Flap Pitching Frequency [Hz].
f_p	Airfoil Pitching Frequency [Hz].
F_R	Resultant Force [N].
f	Frequency [Hz].
h_t	Hub height [m].
M_{EW}	Edgewise Root Bending Moment [N.m].
M_{FW}	Flapwise Root Bending Moment [N.m].
r	Local Rotor Radius [m].
R	Rotor Radius [m].
k	Reduced Frequency.
Re	Reynolds Number.
U_∞	Upstream Wind Speed [m/s].
U_{rot}	Rotational Velocity Component [m/s].
U_{wind}	Incoming Velocity Component [m/s].

W	Total Relative Wind Velocity [m/s].
α	Angle of Attack [°].
α_F	Flap Deflection Angle [°].
$\alpha_{amp,F}$	Semi-Amplitude of the Flap [°].
α_{mean}	Mean Angle of Attack [°].
α_{amp}	Semi-Amplitude of the Pitch[°].
β	Blade pitch [°].
β_{amp}	Semi-Amplitude of the Blade Pitch[°].
β_{mean}	Mean Blade Pitch [°].
μ	Dynamic Viscosity [kg/m s].
γ	Yaw-offset Angle [°].
ν	Kinematic Viscosity [m^2/s].
λ	Tip Speed Ratio.
Ω	Rotational Speed of Rotor [rad/s].
ϕ	Phase Offset.
ϕ_{Flap}	Flap Phase Offset.
ϕ_{Pitch}	Pitch Phase Offset.
ψ	Azimuthal Position [°].
ρ	Density [kg/m^3].
$2D$	Two Dimensional.
$3D$	Three Dimensional.
ADC	Analog to Digital Converter.
AOA	Angle of Attack.
CFD	Computational Fluid Dynamics.
DAQ	Data Acquisition.
DOF	Degree of Freedom.
$HAWT$	Horizontal Axis Wind Turbine.
ID	Internal Diameter.
PSD	Levelized Cost of Energy.
LE	Leading Edge.
NI	National Instruments.
$NREL$	National Renewable Energy Laboratory.

PCB	Printed Circuit Board.
PSD	Power Spectral Density.
rpm	Revolutions per Minute.
RSS	Root Sum Square.
SG	Strain Gage.
STD	Standard Deviation.
TEF	Trailing Edge Flap.
TI	Turbulent Intensity.
TE	Trailing Edge.
UW	University of Waterloo.
VFD	Variable Frequency Drive.
WEG	Wind Energy Group.
WT	Wind Turbine.

Chapter 1

Introduction

1.1 Wind Energy

Wind energy, an established renewable source of energy, has realized substantial growth over the last several decades reaching over 591 GW of installed capacity globally in 2018 (a growth of 9% compared to 2017) according to the Global Wind Energy Council [1]. In Canada alone there was a 0.6 GW of wind energy capacity increase bringing the country's total capacity to 12.8 GW or about 6% of the electricity demand according to the Canadian Wind Energy Association [2]. The wind energy levelized cost of energy (LCOE), an important parameter widely used in the energy industry, has decreased due to substantial innovation across all levels from turbine design, to wind farm operation, to energy distribution. Innovation has been able to increase energy production while simultaneously reduce wind farm costs [3]. As the LCOE decreases, it enables wind farms to competitively compete with and in some cases outperform the conventional sources of energy such as oil, gas or nuclear. Recent trends, as illustrated in Figure 1.1, show that the size and diameter of wind turbines have been steadily increasing over the years, partly driven to decrease LCOE and capture more energy [4, 5]. Recently, the largest wind turbine built by GE with a diameter of 220 m and a height of 260 m was installed at the port of Rotterdam in The Netherlands [6].

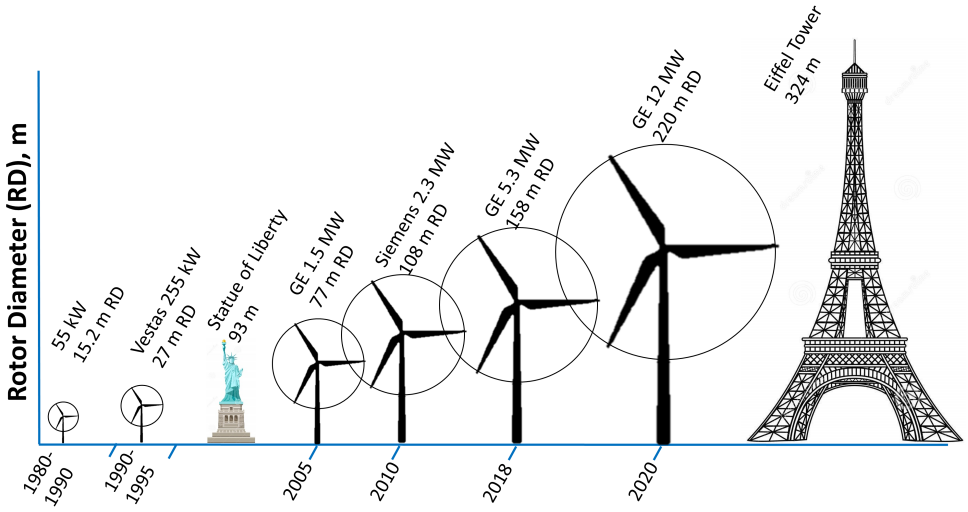


Figure 1.1: Wind turbine diameter size growth over time in terms of rotor diameter. Adapted from [3].

Increasing the wind turbine diameter is not an easy task as it comes with new challenges and requires new technological advancement in wind turbine aerodynamics, material science and controls. The "square cube law", a well known term in the wind energy community, states that as the size of the rotor increases, the power increases by a power of 2 but the mass of the blades would increase by a factor of 3 [7]. So far, with innovation through intensive blade design, the industry has been able to overcome the "square cube law" by increasing the rotor size without significantly increasing the blade mass [3]. However, as the rotor diameter keeps increasing, the current innovations used cannot always overcome the "square cube law" and that hinders the development of larger more efficient turbines that are capable of further decreasing LCOE. It is thus crucially important to find new innovative techniques that allow the industry to keep building larger turbines while keeping the blade mass constant.

As the rotor diameter increases, a major obstacle starts to assert itself and that is associated with the environmental conditions wind turbines typically operate in. It is understood that most wind turbines spend most of the time in a relatively unsteady flow environment caused by many factors including wind shear and turbulence of the wind resource to name a couple [8, 9]. In real environmental conditions wind turbines also experience yaw-misalignment on a regular basis because the rotor is not always capable of following the continuously changing wind direction. Therefore turbines spend most of

their time in yawed conditions. Also, in recent years, wind farm operators have been considering to intentionally yaw turbines to redirect the wake away from downstream turbines to increase the efficiency of the entire wind farm [3, 10]. A yawed turbine causes a significant increase in fatigue loads and that hinders operators from actively pursuing wake redirection. Yaw missalignment also causes flow unsteadiness and that in turn leads to load fluctuation on the blades causing material fatigue while decreasing the lifespan of the blades. In general, even though static loads could be higher than these load fluctuations, the latter tends to be more problematic due to mentioned material fatigue and fatigue life governs the design factors for larger wind turbines [5]. As the blades get longer the load fluctuation at the root increases substantially causing higher material fatigue levels. Thus more research should be aimed at finding new techniques to reduce the mentioned load fluctuation to decrease LCOE.

1.2 Project Motivation

From the previous section, it was concluded that unsteady flow conditions and load fluctuation causes excessive material fatigue on the wind turbine blades. This hinders the development of more efficient turbines and limits LCOE from becoming lower. For these reasons it is imperative to understand, predict with accuracy and reduce the load fluctuation on the blades. Alleviation in blade load fluctuation would also decrease the loads on the drive train, generator and tower further reducing the cost of manufacturing and maintenance. Renewed interest in yaw control for wake redirection and load mitigation in a wind farm setting demands a clear understanding of the effects of running with a yaw offset [11].

Developing a comprehensive and complete understanding of wind turbine aerodynamics in unsteady conditions would help in finding the appropriate technology to reduce blade load alleviation. Many active research groups have been focusing on developing active aerodynamic modification techniques to reduce load fluctuation, material fatigue and unsteady flow conditions. Active modification of the blade shape, also known as 'Smart Rotor', could lead to cost reduction of the blades, towers, drive train and most importantly overcome the "square cube law" [5]. This would enable the industry to build larger wind turbines using lighter and less material in the blade design and increasing the operational-life expectancy of the rotor thus reducing LCOE [12]. Active blade modification would be based on information obtained from different sensors embedded in the wind turbine that measure blade loading. In summary, developing wind turbine load reduction techniques could increase the power produced by the turbine, reduce the capital and maintenance cost while prolonging

the lifespan of the system. The research developed in this thesis incorporates an active aerodynamic modification strategy that is fully capable of reducing load fluctuation and that is a novel contribution to the academic community.

Despite having very limited and older experimental studies on a full-scale wind turbine such as the UAE Phase VI project by Hand *et al.* [13] or the MEXICO project by Schepers *et al.* [14], blade load dynamics in yawed conditions have not been addressed completely. This need for more experimental studies should include a more detailed and high resolution load distribution along with blade rotation to investigate dynamic stall, stall delay and 3D flow effects induced by the blade rotation. More experimental data is needed on a turbine operating in a controlled environment while operating under different conditions. One of the main recommendations from the MEXICO project is that aerodynamic validation is far too limited and that much more detailed aerodynamic measurements are needed in both full-scale and wind tunnel tests. They also highlighted the need for pressure distribution and loads on a turbine operating in yawed conditions to capture the unsteady dynamic behavior. This thesis addresses some of these recommendations, makes an important contribution to the research community and provides detailed experimental data on yawed turbines in a wind tunnel.

In the "Grand Vision for Wind Energy" report published in April 2019 by Dykes *et al.* [3], a group of experts from all around the world identified key challenges that must be addressed to realize the future of wind power. One of the many opportunities they discussed is advances in active aerodynamic control and remote sensing that could help wind turbine designs overcome the "square cubed law" and achieve a longer lifespan. This will enable future blades to be even longer, lighter and most importantly reliable while still adhering to the safety standards required. Another important opportunity that came out of that report is improving the accuracy and reducing the uncertainty in current design tools, models and simulations. By doing so, it allows turbine manufacturers to design blades and other components without using greater-than-optimal safety factors to account for the large inaccuracies in the current design tools. To improve these tools, it is imperative to fully validate and verify the models used to simulate wind turbines and to understand the limitations and uncertainty associated with each model [3]. These models and simulations are reliable for a wind turbine operating in steady conditions but the accuracy starts to degrade once the operating conditions become unsteady and dynamic. 3D flow effects have been identified as a key source of error that limits the simulations from achieving higher accuracy. Thus it is necessary to understand this behavior based on experimental data to improve model predictions. The data presented throughout this thesis makes a major contribution towards this goal and will play an important role in better understanding wind turbine aerodynamics equipped with active aerodynamic control. This thesis will

also identify a few important benefits and lay out a road map for improvements. The experimental data obtained from the wind turbine operating in unsteady conditions is also compared to widely used modeling tools to study their limitations and strengths.

1.3 Project Objectives

Based on the project motivation discussed in the previous section, the high level objectives of this research are summarized as follows: (Note: for this research the trailing edge flap (TEF) is used as the active aerodynamic control)

1. Develop a wind turbine rig capable of active aerodynamic control and measurement of the phase averaged load fluctuation of rotor torque, blade moment and surface pressure on a small blade segment.
2. Characterize the impact of a trailing edge flap (TEF) on a static 2D airfoil coefficients and on a 2D pitching airfoil undergoing dynamic stall.
3. Compare wind tunnel experimental results from a wind turbine operating in steady and unsteady conditions to the OpenFast simulation model [15] to highlight its strengths and limitations.
4. Produce a comprehensive set of experimental data to study the impact of a TEF installed at different blade spanwise locations on wind turbine aerodynamics operating under different conditions.
5. Determine quantitatively and qualitatively how actively pitching the TEF or the entire blade reduces the load fluctuation on a wind turbine blade operating under different conditions.

1.4 Thesis Outline

This section provides an outline for the thesis and a summary of the different chapters. Each of the chapters addresses the different issues discussed previously in Section 1.2.

- **Chapter 2: Background and Theory** provides the background, outline of the concepts, terminology and theories needed to better understand the various topics discussed in later chapters. A brief summary of the various studies found in the literature is compiled showing the most recent development on load fluctuation reduction techniques.

- **Chapter 3: Experimental Setup** briefly describes the facilities used to conduct the different experimental campaigns. The designed and constructed experimental rig utilized to study the influence of TEF on wind turbines along with the various sensors and actuators used is also presented.
- **Chapter 4: Experimental Procedure and Verification** lays out the test matrix used to conduct the various experiments in a 2D environment and on a full-scale wind turbine. A convergence study along with verification of key important experimental parameters is presented.
- **Chapter 5: 2D TEF Experimental Campaign** illustrates how the TEF is capable of influencing the airfoil coefficients in static steady conditions. This chapter also shows and quantifies how the pitching TEF can reduce the impact of dynamic stall on a pitching airfoil in a 2D setting. Finally, the experimental dynamic stall cycle is compared to OpenFast predictions.
- **Chapter 6: Full-Scale Testing on a Wind Turbine** provides a detailed and a comprehensive set of experiments showing how changing the pitch and TEF angles influences loading at three distinct locations on a wind turbine operating in steady and unsteady conditions. Where possible the experimental data is compared to numerical models to highlight their strengths and weaknesses.
- **Chapter 7: Load Alleviation on a Wind Turbine** presents a quantitative and qualitative set of data that describes how the TEF and pitch systems are capable of reducing load fluctuation on a wind turbine operating in unsteady conditions. A comparison between both systems is also provided highlighting the strengths and weaknesses of each system.
- **Chapter 8: Concluding Remarks** provides overall conclusions from the experimental test cases conducted and recommendations for future work. This chapter also highlights the objectives achieved and novelty in the work conducted.

Chapter 2

Background and Theory

This chapter covers the background and theory of wind turbine aerodynamics required to better understand the experimental setup and the results discussed in this research. A brief review of 2D airfoil aerodynamics with emphasis on flow separation and dynamic stall is presented first. This is followed by a summary of wind turbine terminology and blade loading in steady and unsteady conditions. The aerodynamic modeling tools used throughout this research are introduced next. Finally a literature review is presented to discuss the previous work that is relevant to this research.

2.1 2D Airfoil Aerodynamics

To understand how wind turbines extract energy from the atmosphere, it is relevant to present the foundation starting with 2D airfoil aerodynamics before introducing the more complex 3D aerodynamics on a rotating blade. Wind turbine blades are made from a blend of different airfoil geometries. Airfoil design has been extensively studied in the aviation industry but wind turbine airfoil design is distinct and unique because turbines operate under different conditions. This section begins by introducing the terminology and the forces acting on airfoils. The dynamic stall cycle on a 2D airfoil is then presented next showing how it influences airfoil coefficients. Finally, the trailing edge flap (TEF) concept and its characteristics are discussed.

2.1.1 Airfoil Aerodynamic Forces

To begin with, it is relevant to define the nomenclature used to characterize and describe airfoils. The *leading edge* (LE) is the part of the airfoil which usually contacts the fluid first while the *trailing edge* (TE) is the rear edge of the airfoil. The *chord line* is a straight line that connects the leading and trailing edge. The *camber* is the sum of mid-points between the upper and lower surface as measured perpendicular to the chord line. For symmetric airfoils the camber coincides with the chord line. The *chord, c,* is the unit of length between the leading and trailing edge. The *angle of attack* (AOA), α, is the angle between the chord line and the upstream wind speed U_∞. The aerodynamic forces on the airfoil are highly sensitive to α [16]. Figure 2.1 shows the nomenclature described.

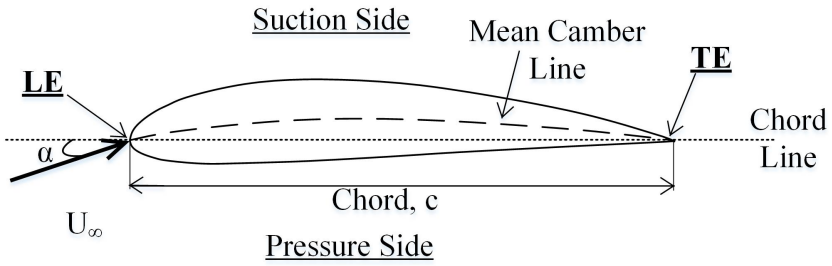


Figure 2.1: Airfoil nomenclature typically used in literature. LE: Leading Edge; TE: Trailing Edge

Lift generation theory such as "circulation", the role of viscosity and the Kutta condition are not discussed in thesis for brevity but are discussed in more detail by Anderson [17]. When an airfoil body is immersed in a moving fluid with a positive α or a positive mean camber, the gauge pressure becomes negative on the upper surface, which is also known as the "suction side". The lower side on the other hand experiences positive gauge pressure and is called the "pressure side" as labeled in Figure 2.1 [17, 18]. Integrating the pressure and shear stress distribution along the entire airfoil surface produces a resultant force F_R and a moment M_p as illustrated in Figure 2.2. The moment on an airfoil, also characterized as the "center of pressure" [18], is often referenced with respect to the quarter chord. There are two frames of reference used to split F_R: perpendicular and parallel to the chord, or perpendicular and parallel to the free stream velocity, U_∞. The different force components are illustrated in Figure 2.2 and are listed here:

- F_L is the lift force perpendicular to U_∞, which is mainly due to pressure imbalance

- F_D is the drag force parallel to U_∞, which is mainly due to pressure and shear imbalance
- F_N is the normal force perpendicular to the chord
- F_A is the axial force parallel to the chord

The relationship between these two sets of components is:

$$\begin{aligned} F_L &= F_N cos\alpha - F_A sin\alpha \\ F_D &= F_N sin\alpha + F_A cos\alpha \end{aligned} \tag{2.1}$$

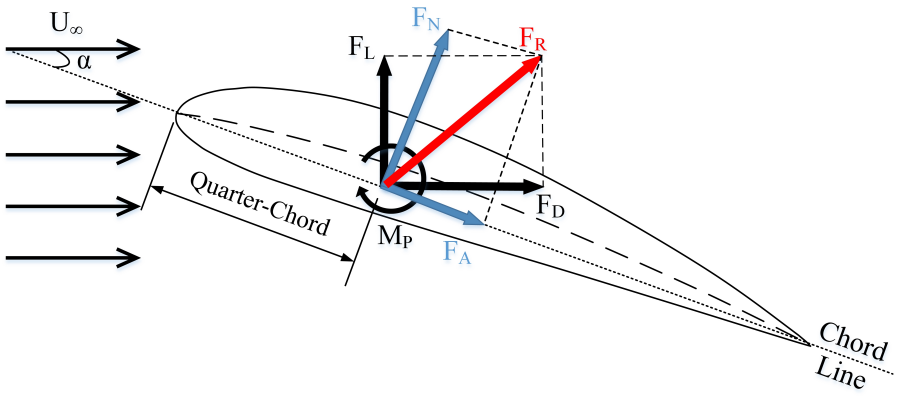


Figure 2.2: A sketch (not to scale) showing the aerodynamic forces and moments acting on an airfoil

One of the most important parameters used to characterize the fluid dynamics over a body is the Reynolds number (Re). It is the physical ratio between inertial and viscous forces and is defined for airfoils as [19]:

$$Re = \frac{U_\infty c}{\nu} = \frac{\rho U_\infty c}{\mu} = \frac{Inertial\ force}{Viscous\ force} \tag{2.2}$$

where ρ is the fluid density, ν is the kinematic viscosity and μ is the dynamic viscosity. Two-dimensional (2D) airfoils are assumed to have an infinite span and are purely a concept. Placing the airfoil model inside a wind tunnel such that the tips extend to the wall, is an approximation of the 2D concept. The aerodynamic forces for 2D airfoils are reported as a non-dimensional coefficients. These coefficients are determined through wind tunnel testing and are a function of Re and α. The airfoil coefficients of lift, drag, moment and pressure are described in the following equations:

$$C_L = \frac{F_L/l}{\frac{1}{2}\rho U_\infty^2 c} \tag{2.3}$$

$$C_D = \frac{F_D/l}{\frac{1}{2}\rho U_\infty^2 c} \tag{2.4}$$

$$C_M = \frac{M_P}{\frac{1}{2}\rho U_\infty^2 A c} \tag{2.5}$$

$$C_p = \frac{p - p_\infty}{\frac{1}{2}\rho_\infty U_\infty^2} \tag{2.6}$$

where l is the airfoil span, A is the projected airfoil area (chord by span only for 2D airfoils), p is the perpendicular pressure at the surface of the airfoil and p_∞ is the free stream pressure. A typical coefficient of lift C_L versus α for a two dimensional (2D) airfoil is illustrated in Figure 2.3. For small α the C_L increases until the maximum lift, $C_{L,max}$, at $\alpha_{critical}$ is reached. In this region the fluid over the airfoil is attached to the surface as shown by the streamlines. However, past the stall point C_L drops dramatically. This happens because the boundary layer on the suction side of the airfoil starts to separate starting from the TE [17]. Inside the separated region the flow is recirculating and part of the flow is moving in the opposite direction to the free stream [19]. The flow described here occurs on a static airfoil where α is constant. In some applications, α is dynamically oscillating and that causes a different flow dynamic than the static cases. The next section discusses this scenario where the airfoil is oscillating about an α_{mean}.

2.1.2 2D Dynamic Stall

Most modern fluid dynamic applications encounter unsteady flow behavior, whether intentional or not. These unsteady effects severely impact the forces the airfoil experiences and cannot be ignored [20]. Dynamic stall occurs on any airfoil when it experiences any type of unsteady motion causing α to oscillate past the static stall angle [9]. There are three airfoil parameters that influence the dynamic stall cycle or unsteady loading on a pitching airfoil with a frequency f_p: airfoil shape, mean pitching angle/amplitude and the reduced frequency k, where:

$$k = \frac{\pi c f_p}{U_\infty} \tag{2.7}$$

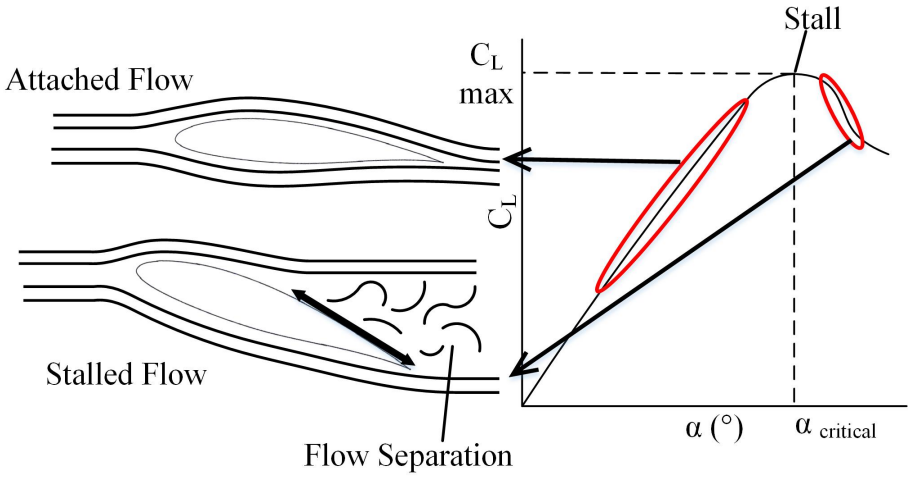


Figure 2.3: A generic C_L versus α plot illustrating attached and separated flow

Corke and Thomas [21] defined the flow field to be unsteady when k is greater than 0.05 otherwise unsteady effects can be neglected as long as the pitch amplitude is not too large. They also explained the reduced frequency by its analogy to a phase lag parameter where the fluid reaction lags behind the pitching motion due to inertial effects.

Dynamic stall is characterized by extreme hysteresis and non-linear cycles in the coefficient of lift (C_L), coefficient of moment (C_M) and coefficient of drag (C_D) [20]. This causes the aerodynamic forces acting on the airfoil to be higher than their static counterparts. The forces on the airfoil are not just higher but dynamic stall generates periodic and oscillatory motion that tends to increase the stress and fatigue levels on the airfoil structure. The dynamic stall cycle could be split into four sections as can be seen in Figure 2.4: a) pitch-up motion, b) flow separation, c) pitch-down motion and d) flow re-attachment. During pitch-up motion the flow remains attached to the airfoil thus C_L keeps increasing past the static stall angle. This is due to the pitching motion and the formation of a leading edge vortex (LEV) or dynamic stall vortex [21]. The LEV brings additional suction to the leading edge and produces values of C_L, C_M and C_D that are much higher than their static counterparts during pitch-up motion [20]. As the airfoil is about to pitch down, the LEV convects downstream over the suction side and once the LEV flows past the trailing edge the flow separates leading to a severe loss in lift, increase in nose-down pitching moment and increase in drag. In some cases a secondary LEV is formed and shed, leading to another C_L peak [22]. Gharali and Johnson [23–25] reported the formation of a secondary LEV and in some cases, smaller vortices after that. The

secondary LEV tends to be weaker in magnitude when compared to the primary LEV. Lee and Gerontakos [26] have also reported the formation of a secondary LEV. Numerical investigations were able to simulate the formation of both the primary and secondary LEV [27]. Typically, during pitch-down, the airfoil is stalled even though α is below the static stall angle. The flow then re-attaches to the surface as α decreases and the cycle starts again [26, 28–30]. Leishman[22] and recently Masdari *et al.*[31] studied the effects of the mean angle of attack, pitching amplitude and reduced frequency on dynamic stall.

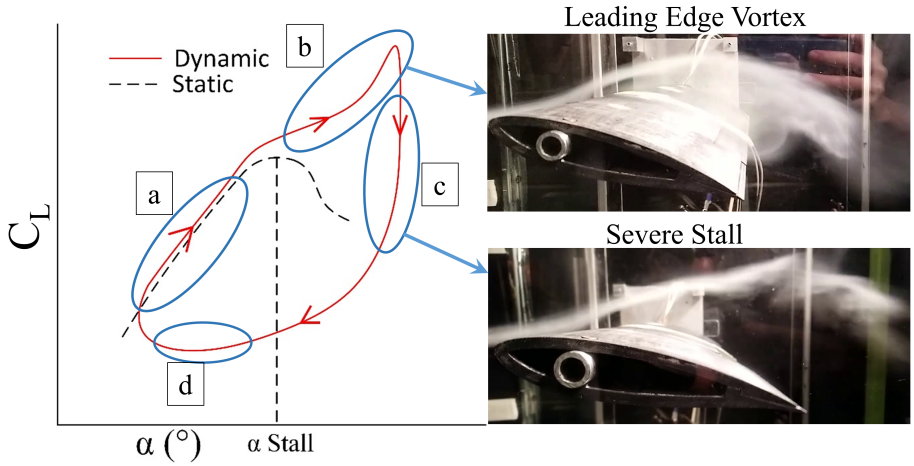


Figure 2.4: A schematic illustrating the influence of the dynamic stall cycle on the airfoil C_L. The cycle is split into four sections: a) pitch-up motion, b) flow separation, c) pitch-down motion and d) flow re-attachment. The pictures, taken during the experimental campaign, help visualize the LEV re-circulation and stall.

While the airfoil is pitching close to the stall point, aeroelastic stability problems could arise. Aeroelastic divergence or stall flutter is promoted when the torsional damping, C_W is negative and is defined by the line integral [9]:

$$C_W = \oint C_M(\alpha) d\alpha \tag{2.8}$$

Damping is positive when it corresponds to a counter-clockwise (ccw) loop while negative for a clockwise (cw) loop in the $C_M - \alpha$ plot [21]. During negative damping, vibration can increase significantly and may lead to structural damage if the structural dynamics permit [32]. Using a TEF to mitigate negative damping without significant loss of lift would benefit the system greatly and would ensure limited flutter on the airfoil structure [32].

2.1.3 Airfoil with Trailing Edge Flap (TEF)

Based on the previous section, the load fluctuation associated with dynamic stall is severe and could be structurally detrimental. It is thus crucial to reduce the impact of the dynamic stall behavior by actively modifying the airfoil aerodynamics. Different control strategies have been developed previously such as leading edge blowing or suction [33, 34], synthetic jets [35], leading edge plasma actuation [36, 37], vortex generators [38, 39] and trailing edge flap (TEF) [40–47]. Barlas and van Kuik [5] summarized and reviewed the different control strategies mentioned to reduce fatigue loading on wind turbine blades. TEF was found to be the most efficient of the control strategies tested because of its control authority over the coefficients of lift and drag, linearity, high frequency response and their simplicity of use. In comparison, they found: microtabs are less efficient for detailed load control due to their on-off characteristics; camber control is expensive, complex to design, and has high power consumption; and boundary layer strategies are limited by their control authority.

The most basic TEF is achieved by hinging the trailing edge about a point typically located between 0.7 to 0.9 of the chord. When the flap is deflected towards the pressure side (negative angle) the C_L increases due to the increase in camber of the airfoil. The opposite is true when the flap is deflected towards the suction side [17]. A schematic showing the flap influence over the lift curve for an ideal case is illustrated in Figure 2.5. This shift in the C_L is very useful in controlling the aerodynamic loads on wind turbines.

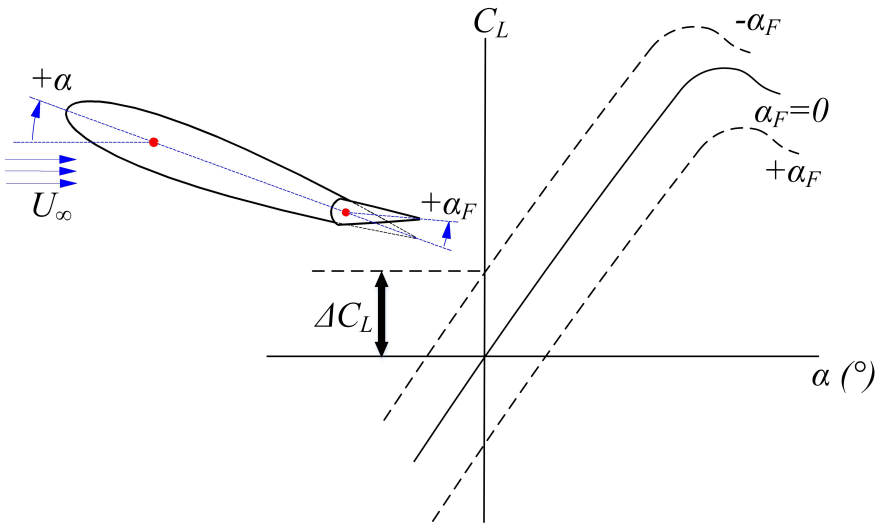


Figure 2.5: Influence of the flap deflection on the lift curve in an ideal case.

Thin airfoil theory has been used to predict the influence of TEF on the lift coefficient and is described in more detail by Houghton and Carpenter [48]. Changing the flap angle is similar to modifying the camber of an airfoil and thus thin airfoil theory could be used to develop an equation for flapped airfoils. More detail about the development of the equations and an in-depth analysis could be found in Houghton and Carpenter [48]. The modified equation derived to predict C_L for different flap angles is:

$$C_L = 2\pi\alpha + 2(\pi - \zeta + sin\zeta)\alpha_F \tag{2.9}$$

where ζ is a constant that is a function of airfoil geometry and α_F is the flap angle as seen in Figure 2.5. The first part, $2\pi\alpha$, accounts for the effect of the angle of attack (α) while the second part accounts for the camber and flap angle of the airfoil. The change in lift due to the flap could then be obtained from Equation (2.9) but with a limited accuracy. Just like with any equation derived from the thin airfoil theory, the viscosity effects that are particularly prominent close to the TE are not accounted for by Equation (2.9). The theory also is limited to small α and small α_F thus experimental data are needed to obtain data on large angles. Experimental data on different airfoils with a TEF could be found in Abbott and Von Doenhoff [49]. The main conclusion to be drawn here is that the relationship between C_L and the flap angle is linear for static α.

2.2 Wind Turbine Aerodynamics

Now that 2D airfoil behavior has been introduced, wind turbine aerodynamics can be discussed. Wind turbines extract mechanical energy from kinetic energy in the atmosphere and this is done through the wind turbine blades. The blades are made from a series of airfoils of different chord lengths and different pitch angles. Throughout this study the focus is on horizontal axis wind turbines (HAWT) where the axis of rotation is parallel to the ground. In this section, wind turbine terminology along with an introduction to the actuator disc and blade element model are presented. Next, different types of blade loading under steady and unsteady conditions are briefly reviewed. Finally, blade aerodynamics when the turbine is yawed or misaligned with the incoming wind are discussed.

2.2.1 Wind Turbine Terminology

The different components that make up the wind turbine and the associated terminology used are now described. A schematic of a typical wind turbine from the front and side

view is illustrated in Figure 2.6. The main sub-components are listed below:

- *Rotor* is the main rotating system consisting of the blades and the hub. It is the most important part from a performance point of view and the main focus of load alleviation since the blades determine the amount of energy captured. U_∞ is the upstream wind speed, h_t is the hub height (from the ground to the rotor center), R is the rotor radius and Ω is the angular speed of the rotor. The blade pitch, β, is the angle between the chord line of the airfoil and the rotor plane. Finally the azimuth position of the blade, ψ, is the angle between the blade and the 6 o'clock position where counter-clockwise rotation is positive viewed from the upwind location.
- *Nacelle and yaw system* The nacelle houses the drivetrain of the wind turbine. It includes a drive shaft connecting the hub to the gearbox driving the generator in a conventional turbine. Some nacelle designs eliminate the need for a gearbox by connecting the hub directly to a specially designed generator. The yaw system lets the rotor axis be aligned with the upstream wind direction. The yaw-offset angle, γ, is the angle between the upstream wind direction and the rotor axis.
- *Tower and Foundation* The tower provides the structural support to the nacelle and rotor. It absorbs all the thrust load from the blades. In most modern wind turbines the tower is typically made from steel tubes, lattice structures or cement.

2.2.2 Actuator Disc and Blade Element Model

A wind turbine converts the kinetic energy from the incoming wind to rotational energy to drive a generator. A simplified method often used to analyze wind turbines is the actuator disc model [18]. It analyzes the aerodynamic behavior without any specific turbine design or geometry just by studying the energy extraction process. Some of the assumptions that are made in this model: incompressible steady state flow, infinite number of blades and non-rotating wake [19]. This is an oversimplification but by doing so a few major aspects of wind turbine performance are determined. The most commonly used parameter in industry that characterizes a wind turbine is the power coefficient, C_{power}. It is the ratio between power produced by the rotor and the power available in the wind as illustrated in Equation (2.10). The actuator disc model is characterized by the axial induction factor (or the inflow factor), a, which quantifies the decrease in air velocity passing through the rotor. By creating a control volume around the wind turbine and applying the conservation of momentum, the net forces on the turbine could be correlated to a and its relationship to C_{power} is [7]:

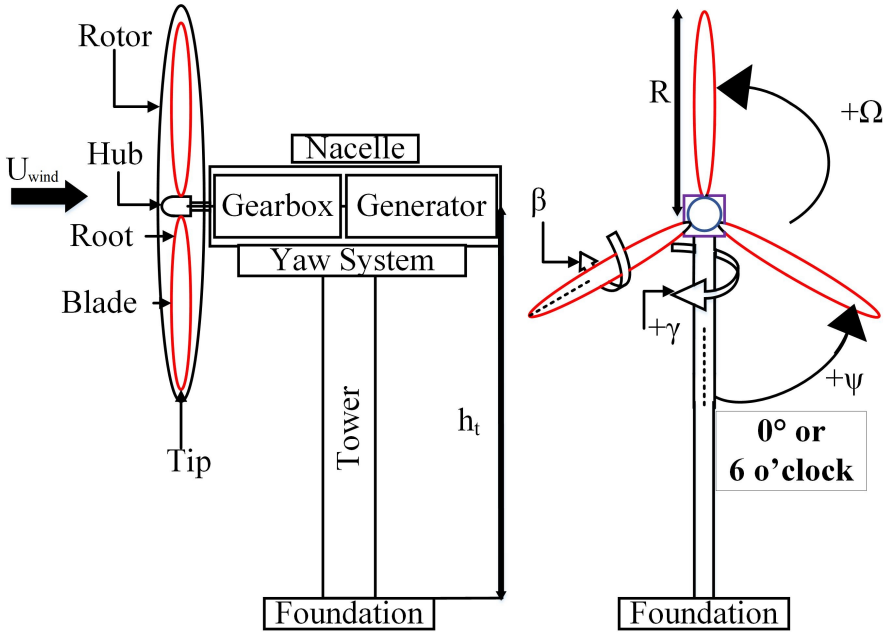


Figure 2.6: A diagram illustrating the terminology of an upwind horizontal-axis wind turbine (a) side view (b) upwind front view

$$C_{power} = \frac{P}{\frac{1}{2}\rho U_\infty^3 A} = 4a(1-a)^2 \tag{2.10}$$

where P is the power captured by the rotor and A is the rotor swept area which is equal to πR^2. The coefficient of thrust, C_T, is the non-dimensional force perpendicular to the rotor and could be related to a by the following equation:

$$C_T = \frac{F_T}{\frac{1}{2}\rho U_\infty^2 A} = 4a(1-a) \tag{2.11}$$

where F_T is the axial force of the wind acting on the wind turbine. The tip speed ratio, λ, characterizes the wind turbine operating condition and is equal to the ratio between the blade tip speed and the free stream velocity as indicated by:

$$\lambda = \frac{\Omega R}{U_\infty} \tag{2.12}$$

The actuator disc model discussed does not account for several things including the flow

variation in the radial direction along the blade span. To better analyze the load variation along the blade span which gives rise to thrust and torque (power), the blade element model (BEM) is used. The BEM divides the blade into smaller sections, typically between 10 and 20 elements [18]. The lift and drag forces on each element are then calculated based on the geometric α and the incident resultant velocity [7]. The flow over each element is assumed to be 2D thus allowing the use of 2D airfoil coefficients obtained from wind tunnel testing. The main assumption in BEM is that the velocity component in the spanwise direction is ignored as well as the 3D effects. There are two velocity components acting on each element that determine α and they are the angular speed of the rotor and the incoming wind speed that form the velocity triangle as illustrated in Figure 2.7. The main forces, velocity components and the angles formed on each element are listed here:

- F_L is the lift force perpendicular to W
- F_D is the drag force parallel to W
- U_{rot} is the tangential velocity component produced by the blade's rotation
- U_{wind} is the upstream velocity component perpendicular to the rotor when the yaw-offset is zero
- W is the relative velocity equal to the root sum squared of U_{rot} and U_{wind}
- β is the blade pitch angle formed between U_{rot} and the airfoil chord
- α is the AOA of the airfoil forming between the airfoil chord and W
- φ is the sum of β and α

The three components of the velocity triangle could be obtained from the following equations:

$$\begin{aligned} U_{wind} = U_2 = U_\infty(1-a) \\ U_{rot} = \Omega r \\ W = \sqrt{U_{wind}^2 + U_{rot}^2} \end{aligned} \tag{2.13}$$

Another assumption made by the BEM is that the upstream wind velocity is homogeneous. However, this is not the case as the wind shear typically created by the earth's roughness creates an atmospheric boundary layer where the air velocity slows down as it gets closer to the ground. The rotor plane is often placed in this boundary layer creating uneven velocity distribution along the rotor plane leading to load fluctuation on the blades. These fluctuations are cyclic in nature and have a frequency of 1P (where P is once per revolution). This cyclical loading creates fatigue and wear on the root of the blade [7]. The next section discusses the different types of loads wind turbines experience during normal operating conditions.

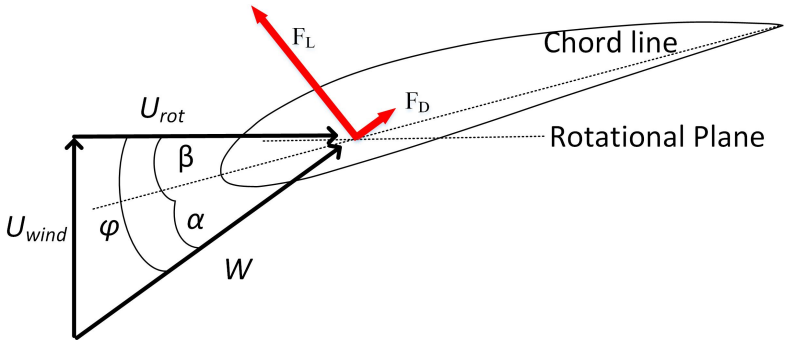


Figure 2.7: 2D airfoil showing the velocity triangle and the forces

2.2.3 Blade Loading During Operation

Wind turbines experience a variety of different loads and stresses during operation. At a first glance, the high loads from heavy storms and hurricanes seem to be the main problem. However, a more detailed consideration reveals that continuous alternating loads on the blades govern the structural design factors for large wind turbine blades [5]. Alternating loads under normal operating conditions cause material fatigue [50]. A typical multi-mega-watt wind turbine will rotate some 10^8 times during a 20 year lifespan [16]. Most blade loading is due to aerodynamic forces but some are due to inertial and gravity forces. It is best to lay out a common coordinate system for the forces on the wind turbine blades at the beginning. It is a common practice to group the loads on the blade in the flapwise and edgewise directions [7]. The forces perpendicular to the rotor plane that tend to deflect the blades in the out-of-plane direction (such as the thrust forces) are in the flapwise direction. The flapwise moment is caused by the axial forces in the flapwise direction. The flapwise moment tends to cause the highest stress on the root of the blade and it is an important parameter for this research. The forces that create a moment to rotate the blades, act in the edgewise direction. The edgewise direction acts in the same direction of the rotor plane. The edgewise moment is usually caused by the tangential load distribution and gravitation forces on the blade. The coordinate system is illustrated in Figure 2.8. Some of the loading on HAWT blades are illustrated in Figure 2.9 and detailed in the list below [7, 50]:

- *Gravity forces* are the result of the deadweight of the blades themselves. This generates an alternating edgewise moment at the root of the blade with a frequency of 1P (once per revolution). There is really very little that can be done to mitigate this moment other than reducing the weight of the blades.

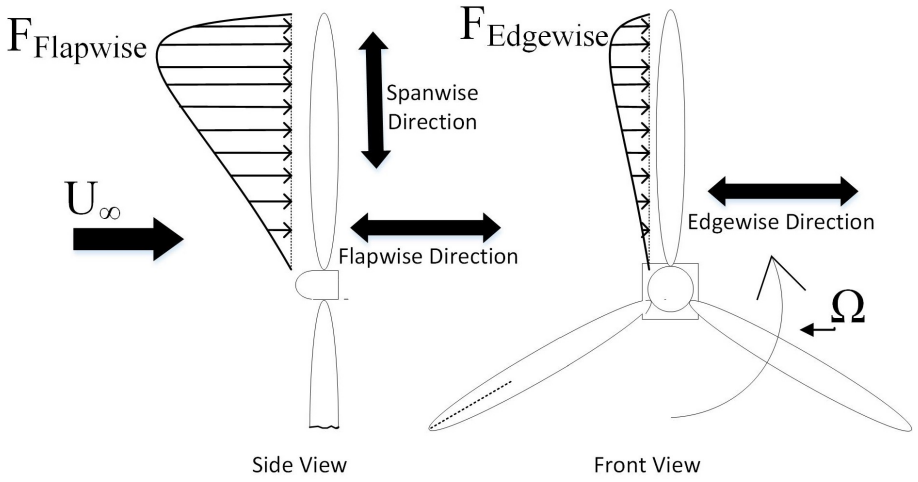


Figure 2.8: The coordinate system used to identify the idealized load distribution on the turbine blades as adapted from [7, 50].

- *Centrifugal forces* are not a major source of fatigue or loading because large wind turbines have a slow rotational speed. The rotational speed increases as the diameter of the wind turbine decreases. So these forces become more dominant for smaller wind turbines. In some cases the centrifugal forces have been used to reduce the aerodynamic loading on the blades [50].
- *Steady mean wind speed* is an idealization that rarely occurs in the open atmosphere. The load distribution along the blade depends on the chord and twist through the spanwise direction. The wind speed has to be monitored to set the appropriate blade pitch to avoid excessive loading on the blades and hub. Under this condition, the idealized load distribution on the turbine blades is illustrated in Figure 2.8. Typically the forces on the blade in both directions increase in the spanwise direction because the velocity, W from Figure 2.7, increases and that in turn increases the lift and drag forces. In most cases, the flapwise forces are higher than the edgewise forces because C_L is much higher than C_D. The forces at the tip are typically diminished due to tip losses.
- *Vertical wind shear* is caused by the earth's boundary layer due to a velocity gradient. This results in having higher loads on the blade in the upper rotational region than in the lower region nearer to the ground. The frequency of occurrence is 1P.
- *Cross wind (yaw-offset)* Most modern wind turbines incorporate an automated yaw system to make sure that the turbine rotor is perpendicular to the incoming wind. If

the wind direction changes rapidly there would be a lag until the yaw system adjusts the nacelle. This could cause cyclic loading on the turbine with a frequency of 1P. More details about yaw-offset are discussed in the next Section 2.2.4.

- *Wind Turbulence* accounts for turbulence in the wind that is usually unpredictable but has to be taken into account when designing for material fatigue. These loads are non-cyclic and always fluctuating.

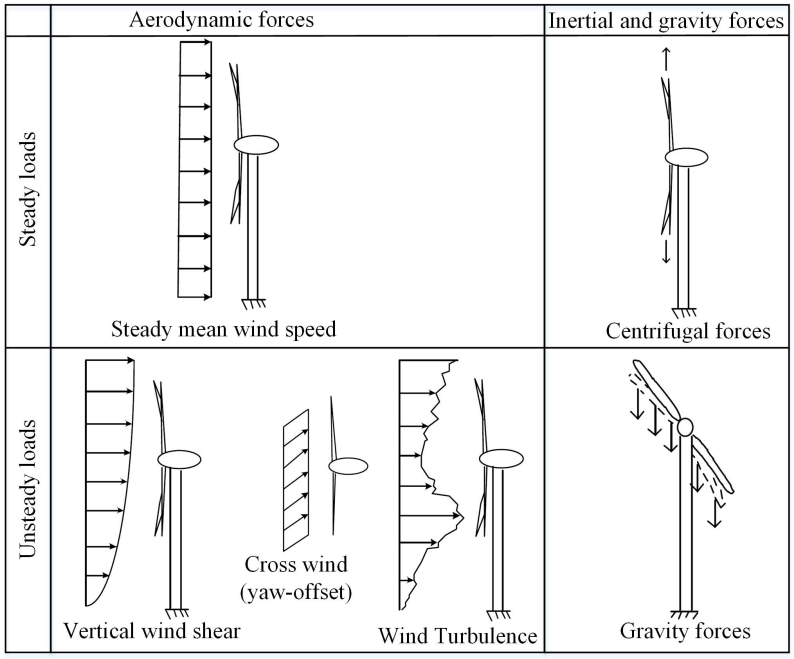


Figure 2.9: The different types of loading on HAWT blades; adapted from [50]

2.2.4 Blade Aerodynamics in Steady Yaw

Wind turbines spend most of the time operating in a relatively unsteady flow conditions [9]. This could be due to many factors, including wind shear, rotor misalignment (yaw) and turbulence of the wind resource. In real environmental conditions wind turbines experience yaw-misalignment on a regular basis because the rotor is not always capable of following the continuously changing wind direction. The turbine, then, spends most of its time in yawed conditions. Also, in recent years, wind farm operators intentionally yaw turbines to redirect the wake away from downstream turbines to increase the efficiency of the entire wind farm

[51]. When a wind turbine is yawed, the angle of attack (α) is constantly changing on each of the blades, thus causing load fluctuation and ultimately fatigue damage [7]. Figure 2.10 is presented to better understand how α changes with azimuth position. When the turbine is yawed, the incoming wind speed (U_∞) is no longer perpendicular to the rotor plane and the blade rotational velocity vector $U_{rot} = \Omega r$ (where r is the local radius of the turbine blade). The rotational velocity vector (U_{rot}) and the free stream incoming velocity vector (U_∞) form the wind velocity vector (W) based on Equation (2.13). When the blade is rotating away from the wind ($90° < \Psi < 270°$) the yaw angle causes α to increase while, in contrast, when the blade is rotating towards the wind ($270° < \Psi < 90°$), the yaw angle causes α to decrease. At 6 and 12 o'clock ($\Psi = 0°$ or $180°$) α is at its minimum and maximum respectively. As the blade rotates and cyclically moves away and towards the upstream wind, α oscillates causing load fluctuations. For this reason and similar situations, it is then vital to understand and reduce the impact of yawed conditions on wind turbine blades.

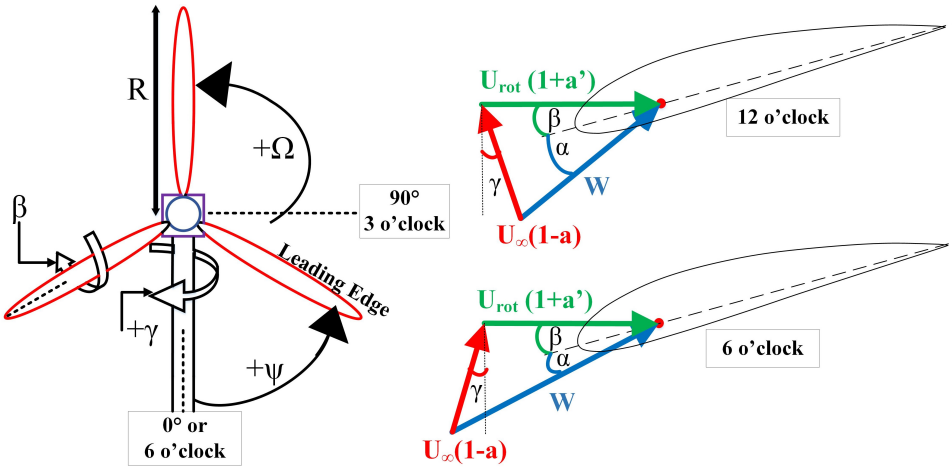


Figure 2.10: A diagram of a horizontal-axis turbine with labels and a schematic of the velocity triangle for a yawed turbine

The yawed rotor not only increases load fluctuation at the root of the blade, but also is less efficient at capturing energy from the wind than the non-yawed rotor. It is then crucial to assess, calculate and model the variation of blade loading in steady yaw. Based on the actuator disc theory discussed, it is possible to modify equations 2.10 and 2.11 to estimate the average C_T and C_P on a yawed rotor as [7]:

$$C_{power} = 4a(cos\gamma - a)^2$$
$$C_T = 4a(cos\gamma - a) \tag{2.14}$$

2.3 Aerodynamic Modeling Tools

This section gives a brief overview of the different design codes used throughout this thesis to model different aspects of the turbine. XFoil, presented first, was extensively used to find the 2D airfoil coefficients. PROPID and OpenFast, presented next, are both wind turbine modeling tools and are used to simulate wind turbine aerodynamics operating in different conditions.

2.3.1 XFoil Code

XFoil [52] is an open-source program that analyzes the viscous/inviscid flow over airfoils. The panel method is used to simulate various airfoil shapes based on thin airfoil theory. XFoil could be used to calculate the 2D coefficients of lift, moment and drag for various airfoils at the specified α. XFoil also provides the capability to add and change the angle of the TEF which is very useful for this study. The experimental data collected in this study are compared to XFoil predictions when other experimental data is lacking in the literature. It is often found that the results match the experimental data for low Reynolds number. Berg *et al.* [53] used XFoil to estimate the torque needed to overcome the aerodynamic loads on a TEF.

2.3.2 PROPID Code

PROPID (PROP Inverse Design) is a wind turbine BEM design code that is capable of providing turbine loading under different input parameters [54, 55]. This design code is capable of calculating the blade lift coefficient distribution, axial induction factor, blade moment and geometric α. The results from the code could then be compared to experimental data. Its main weakness lies in the fact that it cannot simulate a yawed turbine and does not solve for variables in the time domain. Abdelrahman and Johnson [56] used PROPID to design and optimize a single bladed turbine with a constant pitch and chord. The data from the model was then used to build and test the turbine in a large-scale wind tunnel. Gallant and Johnson [57] also used this software to model the same single bladed wind turbine and compared the predictions with experimental data.

2.3.3 AirfoilPrep Code

AirfoilPrep [58] is a useful spreadsheet that allows the user to extend the $C_L - \alpha$ relationship from the usual limited range to the entire $\pm 180°$ range needed by OpenFast using the Viterna method [59]. The main benefit is the ability to generate lift and drag coefficients that are corrected and adjusted for 3D delayed stall at different spanwise locations by using the Du and Selig[60] method to augment the lift and the Eggers [61] method to modify drag. The stall angle is delayed to a higher α and that tends to produce much higher C_L values when compared to 2D flow.

2.3.4 OpenFast Code

The OpenFast (Fatigue, Aerodynamics, Structures and Turbulence) is an open-source design code that simulates the dynamic response of wind turbines using multi-physics and multi-fidelity tools [15]. It was first developed in the very early 2000s but through the years it has been improved and enhanced based on new aerodynamic models and different experimental data that made it more accurate and reliable. The main advantage of OpenFast is that it can simulate wind turbine aerodynamics and structural dynamics in the time domain. The main reason this design tool was used is because it could simulate a wind turbine in yawed condition and produce load fluctuations with azimuth position where PropID failed to do so. The OpenFast tool enables the analysis of a wide range of wind turbine configurations such as the number of blades, pitch regulation, aeroelastic dynamics and many others. OpenFast was designed and created to be used by developers, research laboratories, academia and industry and thus it is a medium-complexity code. OpenFast is very reliable, well tested and widely used by industry and the academic community alike and that makes finding information about this tool easier. OpenFast is also always being updated and is supported by a large community of academics.

Hayman *et al.* [62] discussed the improvements made to the newest version of OpenFast. These improvements produced more accurate predictions when compared to experimental data. Damiani *et al.* [63] recently developed a new unsteady airfoil aerodynamic model that could be used within the OpenFast platform to simulate dynamic stall on the turbine blades. The developed model is based on an extension of the Leishman-Beddoes model [9]. The model first develops the unsteady behavior for a 2D airfoil and then extrapolates it for a 3D blade. Damiani *et al.* compared the model to experimental data for various airfoil shapes, reduced frequencies k and amplitudes of oscillation in a 2D setting. They found good agreement between the model predictions and experimental data. Since the model is based on semi-empirical equations, its accuracy is highly sensitive to the model

parameters chosen. They recommend that the user fine tunes these parameters based on 2D experimental dynamic stall data before simulating unsteady aerodynamics on 3D blades. For this reason, these parameters were tuned and compared to the data collected from the 2D experimental campaign in Chapter 5 and the results are shown in Section 5.3.

Another important benefit is that OpenFast or some version of it has been used extensively in the academic community as a comparison tool to experimental data. Here are some examples where OpenFast has been used. Jonkman [64] modeled and simulated the UAE Phase VI project that is discussed in more detail in Section 2.4.3. The MEXICO project [14] was also modeled using the OpenFast code and is presented in Section 2.4.3. Damiani *et al.* [63] also compared the newest version of the OpenFast model (Aerodyn15) to the UAE set of experiments. They found that even with the new updated unsteady aerodynamic model, discrepancy was still observed but it was improved. Damiani *et al.* [11] recently compared OpenFast models to a utility-scaled instrumented wind turbine that was operating with a yaw offset. They found that the model's prediction matched at times but in some cases discrepancies still existed. Through extensive analysis of the turbine and model, they highlighted the strengths and weaknesses of OpenFast.

2.4 Previous Studies

This section highlights the small number of related studies and limited data found in the literature that have been used throughout the results chapters of this thesis. This is relevant because this study is built on the knowledge found in previously conducted research but also to emphasize the need for more experimental data. Dynamic stall studies that have been conducted on a 2D airfoil equipped with TEF are presented first. This is followed by experiments on full-scale wind turbines in a wind tunnel setting. Next, 3D flow effects that are dominant on wind turbine blades are discussed. Finally, studies on wind turbines equipped with individual pitch control or TEF are introduced.

2.4.1 Dynamic Stall on 2D Airfoil Equipped with TEF

TEF, also known as plain flap or aileron, have been used in the past in the aviation industry to modify the aerodynamic characteristics and obtain higher C_L values [49]. A plain flap is described as a relatively crude device and is likely to lead to some form of boundary layer separation [48]. This means that there is always a possibility of partial separation when the flap is deflected. Abbott and Greenberg [65] studied a plain flap of 20% chord

on a static NACA 23012 airfoil with a large range of flap and pitch angles. They found that the TEF was capable of shifting the entire $C_L - \alpha$ trend up and down in stall and pre-stall conditions alike. The stall angle was also shifted slightly to a lower or higher angle depending on the flap position. The flap not only has influence over C_L, but also a large impact on C_M and C_D. Their results showed that a positive flap angle, defined in this paper as deflection towards the suction side (See Figure 3.1), increased C_D significantly but a negative flap angle only has a slight impact on C_D. Jacobs and Pinkerton [66] showed that the TEF changes the static surface pressure distribution not only at the TE but at the LE as well. Most of the prior research regarding flaps is focused on negative flap angles to achieve higher C_L values in relation to the aviation industry. When applying flaps on wind turbines it is as important to understand the aerodynamics of the airfoil in positive and negative flap angles alike to reduce the load fluctuation on the blade. A section of this study focuses on understanding how high flap angles influence the aerodynamics of a wind turbine-specific airfoil in static conditions.

Surface pressure measurements have been used in the past to determine the magnitude and development of dynamic stall and the LEV by Leishman [22], McCroskey *et al.* [67] and others. These studies show how the LEV could be identified using surface pressure measurements alone. Surface pressure could also be used to determine the location of the laminar-turbulent transition point and the laminar separation bubble. The transition point is associated with high pressure fluctuations that could be measured through surface pressure. Boutilier and Yarusevych [68] showed that the maximum root-mean-square (RMS) in surface pressure corresponds to a location between the mean transition and reattachment point. Raiola *et al.* [69] was able to determine the transition from the standard deviation (STD) in C_p contour plots while the airfoil was pitching.

In recent years, TEF has been investigated and used to manipulate or reduce the impact of dynamic stall on airfoils. Lee *et al.* [70, 71] produced several papers investigating how a TEF can influence the formation and detachment of LEV. They concluded that the TEF was not capable of controlling the formation and detachment of the LEV but the TEF was capable of controlling the LEV magnitude. Green *et al.* [32] discuss the benefit of TEF and how it can influence dynamic stall behavior. They reported that flap deflection was capable of reducing the hysteresis cycle in the lift and moment curves. Furthermore, the flap was also capable of reducing negative damping due to stall vortex deflection or a weaker and thinner LEV. Raiola *et al.* [69] showed that a TEF on a NACA0015 airfoil was capable of controlling the loads generated by dynamic stall and the LEV. Troldborg [72] was able to use the TEF motion to counteract the oscillating pitch motion and obtain a smooth lift curve on the airfoil. Feszty *et al.* [43] and Shehata *et al.* [73] showed that pulsing the TEF was capable of reducing the negative effects of dynamic stall. Zanotti and

Gibertini [74–76] investigated the use of an active gurney flap for dynamic stall control on a pitching airfoil and found that the flap was capable of reducing the amplitude of dynamic stall. Most of the papers and references presented so far study the dynamic stall cycle where the maximum pitch angle is 25°. Only a few select papers investigate deep dynamic stall on a cambered airfoil and present data for pitch angles past 25° [22, 75–78].

2.4.2 3D Flow Effects

The flow dynamics on a rotating blade are different than on a 2D airfoil segment. This difference is an active area of research that is continuously being analyzed and thus finding a comprehensive review of this topic in one source is rather difficult. A review of 3D flow effects on wind turbines is presented in this section because most of the information is found in an array of papers and reports.

One of the main differences between 2D airfoil measurements in a wind tunnel and an airfoil blade section measurements on a rotating turbine are the 3D flow effects. These effects are induced by the rotation of wind turbine blades and could be split into different sections and sources. Blade rotation develops a pressure gradient across the blade span that creates a spanwise velocity component on the blade delaying stall and increasing lift [64]. The spanwise velocity component is significant for the inboard blade element (close to the blade root) but for the outboard element (close to the blade tip) the effect is much smaller because the rotational velocity component is dominant. Du and Selig [60] developed the most frequently used stall delay model and it is adopted in AirfoilPrep [58]. It was reported by the MEXICO project [14] and UAE project [13] that the maximum value of the normal force coefficient, C_n, on a rotating blade is about twice as much as in the regular 2D measurements close to the root of the blade. It was found that the 2D lift curve is significantly smaller than 3D lift curves close to the root of the blade but as r/R increases to one, 2D and 3D lift curves converge [7]. This highlights how the magnitude and flow behavior change on 3D blades. Schreck *et al.* [79] studied the difference between 2D and 3D aerodynamics by looking at the surface pressure and C_n from the UAE and MEXICO projects. They found that blade rotation steepens the C_n lift curve and significantly delays stall and these variations change for different blade spanwise locations. They also reported that the difference was present in both mean and time varying statistics indicating that the flow dynamics are much more complex in 3D. Schreck *et al.* [14] also suggested that the choice of airfoil geometry has a strong influence on the strength and characteristics of the 3D stall effect [14].

A rotating blade also experiences tip loss caused by a leakage of flow from the pressure to the suction side. This introduces downwash which reduces the effective α near the blade

tip and results in a reduced lift and increased drag compared to 2D airfoils at the same α and Re [64, 80]. The tip loss also causes a streamwise vorticity wake behind the wing tip known as trailing vortices. The tip loss factor developed by Prandtl and summarized by Burton *et al.* [7] is the most common adjustment to account for a finite number of blades on wind turbines and the tip losses mentioned. These losses could be approximated and predicted but they also are a source of error when simulating wind turbines. A similar process also occurs at the blade root and the corrections mentioned could be extended to account for these blade root losses.

When the turbine is yawed it causes unsteady flow conditions that could lead to dynamic stall similar to what was discussed in Section 2.1.2. The Beddoes-Leishman dynamic stall model or some iteration of it has been used to simulate dynamic stall on a 2D airfoil and a rotating blade. This model was used in the MEXICO project and a good agreement was found between the experimental and predicted results [81]. They also found that there is a significant difference between 2D and 3D dynamic stall behavior and an empirical correction is used to improve model predictions. They also found that due to large yaw angles the model did not capture experimental trends due to the increased unsteadiness in yawed conditions that delayed separation. Even though details in the experimental trends are not always captured, the magnitude of the loading was reasonably predicted and that is important because it could be used to calculate blade fatigue.

2.4.3 Wind Turbine Measurements in a Wind Tunnel

There have been only two large experimental campaigns in the last two decades aimed at understanding unsteady wind turbine aerodynamics in wind tunnels and both are briefly presented. The widely known UAE Phase VI by NREL project is introduced first followed by the MEXICO project.

UAE Phase VI by NREL

The main objective of the Unsteady Aerodynamics Experiments (UAE) was to investigate and quantify the full-scale 3D aerodynamic behavior of HAWT in steady and unsteady conditions [13]. The acquired experimental data represent an accurate and complete set of wind turbine aerodynamic measurement in a controlled environment that is representative of full-scale machines. The experimental data has paved the way to validate and develop more accurate predictive models that could simulate the highly dynamic load fluctuations that wind turbines could experience as a result of turbulent inflow and shear across the

rotor plane. The tests were conducted on a 10 m diameter 2-bladed HAWT inside the enormous NASA-Ames wind tunnel with a 24.4 m by 36.6 m test section. At the heart of the experimental setup lies three measurement techniques: surface pressure along the chord, angle of attack and inflow dynamic pressure at five span locations (30, 46.7, 63.3, 80, 95% span) as well as blade root bending moment on one blade. The complexity of such a large-scale experimental campaign required a lot of resources, planning and personnel to accomplish. It could be argued that the data obtained from this campaign is the most accurate and comprehensive to date and it was conducted in 2001. This shows that experimental data are very rare, complex and require tremendous amount of resources. The data presented in this thesis, although on a small diameter turbine with fewer measurements, are of similar quality and importance.

Jonkman [64] used the data provided by the UAE Phase VI campaign to validate and test the OpenFast wind turbine design code discussed in Section 2.3.4. The lift data for the airfoil used in the model was modified significantly to account for 3D and spanwise effects using AirfoilPrep. The load discrepancies found between the model and experiments were caused by two sources. The first source is due to inconsistencies in the input file parameters such as aerodynamic airfoil performance. The second source is weakness in the aerodynamic models such as tip loss, stall delay, dynamic stall and unsteady aerodynamic behavior. Although the discrepancies uncovered flows and limitations in OpenFast, the comparison was used as an opportunity to improve the models. This improvement in modeling will ultimately lead to a more cost-effective way of designing turbines and give the modeler more confidence in the results obtained. The data available in this thesis will be an extra resource for modelers to further improve the models and achieve greater accuracy.

Mexico Tunnel Measurements

The Model Rotor EXperiments In COntrolled conditions also known as 'MEXICO' is a large-scale wind turbine experimental campaign conducted in the Large Low-speed Facility (LLF), the largest European wind tunnel [14, 82]. The focus and objective of the well documented and controlled experimental campaign was improving the uncertainty in the aerodynamic calculation models as they are the backbone of every computer program for the design of wind turbines. Having high quality measurements could be used to validate and improve aerodynamic wind turbine models in the fields of 3D stall effects, tip effects and yaw cases. The measurements were conducted on a 4.5 m diameter wind turbine inside a 9.5 m x 9.5 m square wind tunnel. Surface pressure distribution along the blade were collected at 5 locations (25, 35, 60, 82, 92% of blade span) to produce the normal (F_n)

and tangential (F_t) force variation with azimuth angle. Different wind and rotor speeds were tested yielding a tip speed ratio between 3.3 and 10. The results and data from the experimental campaign were so vast and complex that it was not possible for a single country to analyze the data alone. For this reason 20 different institutes from 11 different countries cooperated to produce the IEA Task 29 report, Mexnet (Phase1). Even though meticulous planning and world-renowned groups worked on designing the experimental setup, some of the instrumentation failed to produce reliable data and some results are questioned in the report. For instance strain gauge measurements at the root of the blades were reported to be unusable due to unforeseen error and some of the surface pressure sensors appeared to be malfunctioning. This goes to show that experimental campaigns on a full-scale turbine are very complex and require lots of resources. In this thesis, a similar size diameter wind turbine was tested and very reliable data were obtained even though the budget and personnel resources are minuscule when compared to the MEXCIO project.

The Mexnet report published in 2012 [14] compared F_n and F_t versus azimuth at 5 spanwise sections to OpenFast, an open source BEM code discussed in Section 2.3.4. It is important to note that the OpenFast code they used has changed and improved over the years. Figure 2.11 shows F_n versus azimuth at two different locations: the first, at r/R=0.35 near to the root while the second, at r/R=0.82 near to the tip of the blade. The turbine is yawed to 30° to simulate unsteady blade dynamics. Even though two different institutions used the OpenFast code (CENER_FAST and INTA_FAST in the figure) to simulate the yawed turbine, the trends they produced are different especially at r/R=0.35. This is due to how each group modeled dynamic stall on the blade. When comparing the experimental results (MEXICO) to the OpenFast code, the trend in the data is very different at r/R=0.35. At r/R=0.82 the trend in the data is somewhat similar but not close enough to represent actual flow dynamics. This shows that OpenFast could not accurately simulate dynamic stall on a rotor blade in yawed condition.

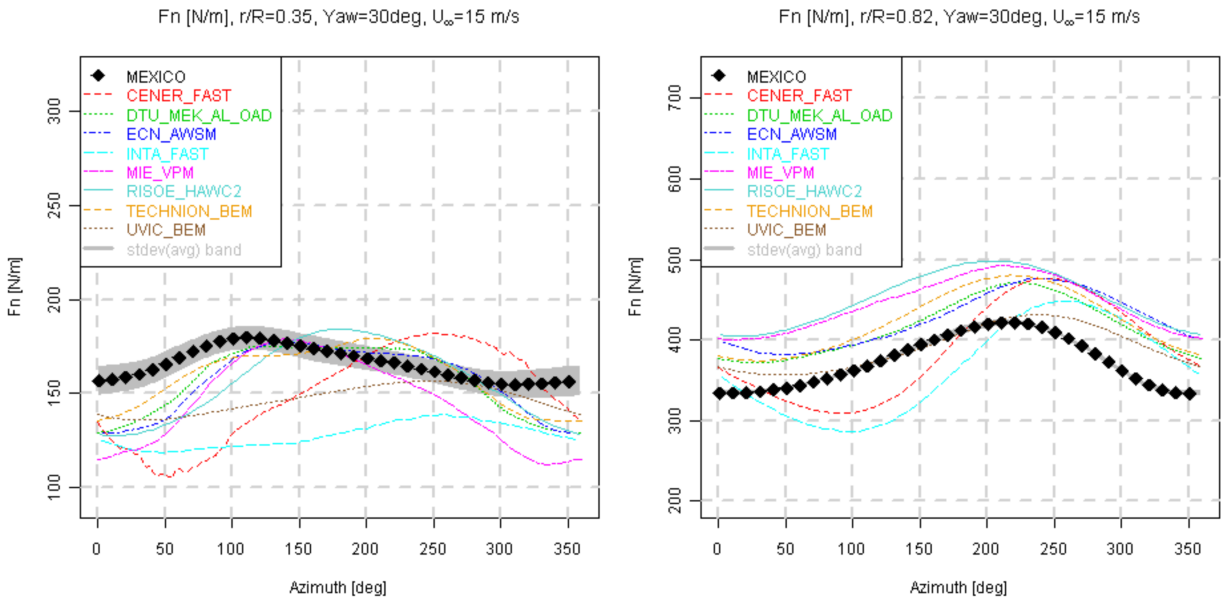


Figure 2.11: Experimental and OpenFast models showing the normal force (F_n) versus azimuth at r/R=0.35 and 0.82 obtained from the MEXICO project [14].

One of the main recommendations from the MEXICO project is that aerodynamic validation is far too limited and that much more detailed aerodynamic measurements are needed in both full-scale and wind tunnel tests. They also highlighted the need for pressure distribution and loads on a turbine operating in yawed conditions to capture the unsteady dynamic behavior. This thesis addresses some of these recommendations and provides detailed experimental work on yawed turbines in a wind tunnel.

2.4.4 Wind Turbine with Individual Pitch Control

Individual pitch control is the most advanced technique used to reduce load fluctuation on wind turbines to date in wind farms [5]. It is basically controlling the pitch of each blade separately and not collectively. This technique is tailored to alleviating the dominant forces with a frequency of once-per-revolution (1P) such as wind shear, tower shadow and yaw misalignment. This control strategy originated from helicopter research known as 'cyclic pitch' which is a matured technology. Larsen *et al.* [83] proposed individual pitch control based on inflow angle of attack and velocity on each of the blades using a pitot tube. Using this method faster variation in inflow could be monitored and compensated by the pitch

angle. Fatigue reduction at different locations on the turbine are in the range of 9% to 31%. Bossanyi *et al.* demonstrate that load reduction could be achieved through individual pitch control given a suitable sensor that could measure the asymmetric loading on the blades [84]. Simulations show the fatigue load on the blades around the 1P peak is reduced without compromising energy capture. This load reduction is also seen in the drive-train, nacelle and tower. Many research groups have proven that individual pitch control can reduce fatigue loads on the wind turbine blades. Nevertheless, this technique is limited by the speed and reliability of pitch actuation, specially for large utility-scale wind turbines. Excessive use of the pitch mechanism could lead to wear on the actuator and bearings which tend to be very expensive parts [5]. High fluctuation load reduction in turbulent areas would require high pitch angles and rates which most standard pitch actuators cannot handle. To achieve a more detailed and fast load reduction due to turbulent flow and unsteady wind speeds another technique is required. Changing the aerodynamic forces locally along the blade would allow for a more accurate load reduction with a much faster response time. This is the main focus of this research.

2.4.5 Wind Turbine with TEF

Barlas and van Kuik [5, 85] and Johnson *et al.* [86, 87] produced several review papers to summarize and review the different technologies that have been used in reducing fatigue loads on wind turbine blades. The 'Smart Rotor' refers to real-time control of blade loading and is composed of four main components: an aerodynamic control surface to influence the aerodynamic forces on the blade, a sensor to measure the load on the blades, an actuator to control the aerodynamic control surface and a controller to link the sensor to the actuator. This research focuses on all the components except the controls aspect of the 'Smart Rotor'. Barlas and van Kuik evaluated the different options for each of the four components and provided feasibility studies. A comparison chart was presented to compare all the technologies with advantages and disadvantages. TEF were found to have the most control authority of the aerodynamic lift forces compared to other aerodynamic control devices. The simplicity, linearity and bandwidth of lift control provided by the TEF makes it attractive and efficient for load control. The aeroelastic response of TEF is within the appropriate range needed to alleviate load fluctuation on utility scaled turbines. One of the main advantages of TEF is that it can control load at a specific r/R location allowing for localized load control. Although TEF are expensive and adds complexity to the blades, it is the most feasible of the active control strategies as illustrated by Barlas and van Kuik [5]. This section briefly presents different studies where the TEF has been simulated on a wind turbine followed by the only six experimental studies found in literature where the

TEF has been installed on a wind turbine.

Simulations with Trailing Edge Flap

Berg *et al.* [12] used the OpenFast code to quantify how the fatigue changes on a large-scale wind turbine with the use of a TEF. The TEF was simulated on a 3 bladed 1.5 MW turbine with a diameter of 65.9 m. A piezoelectric morphing TEF was located on the outer 25% of the blade and composed 10% of the chord with a $\pm 20^{\circ}$ deflection. With a TEF control, the fatigue at the blade root flap moment decreased by 34%. To decrease the cost of energy, the authors recommend increasing the rotor diameter to increase the power capture of the wind turbine. They suggested increasing the diameter until the fatigue level is equivalent to what it was before introducing TEF. The length of the blades were increased by 10% and the fatigue level about the blade root flap moment was still below baseline. In conclusion the TEF was able to significantly decrease the fatigue level on the wind turbine and allow for a larger diameter rotor to capture more power.

Lackner *et al.* [88, 89] simulated the use of TEF on a 5 MW reference wind turbine [90] using an aero-elastic simulation code. The TEF was capable of reducing the fatigue damage between 12 % and 20 % depending on the wind speed. Similar to the previous study, Anderson *et al.* [91] performed simulations to measure the load reduction on the same reference turbine using TEF but using a different code. Instead of using a classic TEF that moves rigidly around its hinge point, a continuous, smooth and deformable TEF was used to reduce drag and noise. The length of the flap was 10 % of the blade (6.3m) while the chord-wise length was 10 % of the chord. The TEF was able to reduce the blade root moment fatigue by 17 % to 25 %. When the TEF were twice or three times as long the fatigue loads decreased to 34 % and 37 % respectively. In another paper by the same group, one differential pressure measurement between the suction and pressure side of the airfoil was used to control the position of the flap [92]. Differential pressure measurement was a more accurate way of measuring the load on the blade compared to strain gages or pitot tubes. It was found that this technique enhanced the load reduction and the most optimal location for the pressure transducer was at 12.5 % from the leading edge.

TEF as Aerodynamic Brakes

Miller and Quandt [93] designed and conducted a series of experiments on a full-scale instrumented wind turbine to test the possibility of using TEF as aerodynamic brakes for over-speed protection. Some other benefits they reported include attenuating structural

loads and increasing wind turbine efficiency in unsteady conditions. They tested three types of flap designs at three different span lengths (7.5%, 15% and 22.5%) and large flap angles (0, 10, 30, 60, 90 degrees). Strain gages were used to measure loading at the root of each blade in the flapwise and edgewise direction. The flap angles were manually set and were constant during a single test unlike this research where it was automated. Their findings suggest that the TEF could then be used to assist or even replace the pitch control of utility-scale turbines. The removal of the pitch control could offset the cost of TEF on the blades as flaps could be more reliable and effective at controlling the loads on the blades locally.

They compared wind tunnel data (2D infinite span) to rotating turbine blade data and found that a reduction in model span or aspect ratio results in "softening" or less abrupt stall behavior. They attributed some of the differences they found between the 2D airfoil and the 3D blade to the fact that a new shed vortex is forming at the TE between the clean blade and the TEF section as shown in Figure 2.12. This vortex is capable of significantly reducing the effective α leading to a reduction in blade loading and performance. The load reduction could wrongly be attributed to the TEF aerodynamics when, in fact, it is occurring on the inboard section of the blade. They did not provide a quantitative effect of this newly formed vortex. This reduction was also reported by Abdelrahman and Johnson [56].

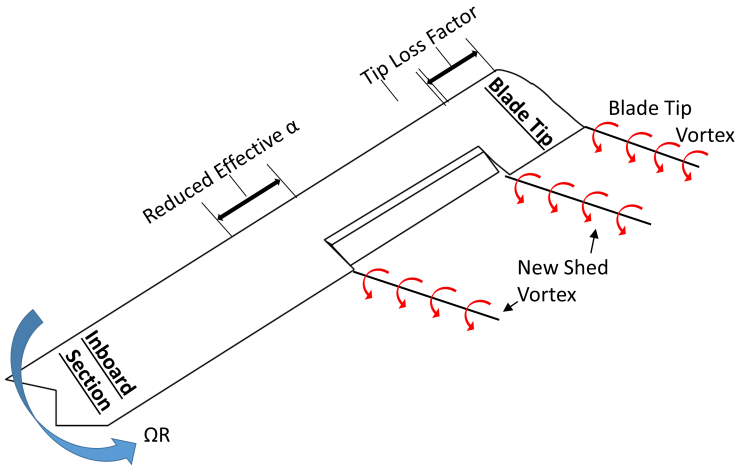


Figure 2.12: The location of the newly developed vortex at the TEF where it reduces the effective α at the inboard section of the blade. Adapted from [93].

.

Controllable Free-Floating Flap

Navalkar *et al.* [94] incorporated blade pitch control and a free floating flap on a small-scale two-bladed wind turbine with a diameter of 2 m. The 0.75 m blade was 3D printed with PC-ABS in one piece. The flap was placed in a way that was free to rotate within ± 30 degrees. The flap covering 15% of the aerodynamic blade span was made of a thin metal sandwiched between two piezobenders that could deform the entire flap. The authors found that the reduction in blade root bending moment was in the order of 40% to 85% depending on whether the rotor is operating in steady or unsteady conditions. Their research was mostly focused on the controls aspects of the TEF unlike the study presented in this thesis which is more focused on the aerodynamics aspect of the TEF.

Full-Scale TEF on Vestas Wind Turbine

Castaignet *et al.* [95, 96] studied the influence of a TEF on full-scale Vestas V27 wind turbine with a rotor diameter of 27 m. One blade was equipped with three 70 cm spanwise length TEF with a chord ratio between 13 % and 18 %. During the experimental campaign only the outer flap worked (5 % of the blade span) while the other two did not function. The turbine was instrumented with strain gages at the root of the blade, two accelerometers at the tip of the blade, three 5 hole pitot tubes and three pairs of pressure tabs at the leading edge of each the three TEF sections. Different tests were conducted on the turbine and the TEF was capable of reducing the load fluctuations on average by 14 % to 20 % of the 1P loads. The main instrumentation lacking was surface pressure measurements along the blade chord but in this thesis it was collected for the different cases.

Piezoelectric based benders

Hulskamp and Wingerden *et al.* [97–99] used piezoelectric based benders to actuate the TEF to control blade loading. Initially the blade segment was tested in a 2D setting where it was only supported on one side. The blade was equipped with two TEF and the width of each flap was 10.5 cm and covered half the chord (6 cm) and could be deflected to ±2°. To obtain feedback for the controller, the blade was equipped with two strain gages placed at the root to measure the strain. A sinusoidal signal was applied to the pitch and flap mechanism with different amplitudes and phases. The reduction in strain for this control scenario was close to 90 % from the uncontrolled case. The TEF were then mounted on a two-bladed 1.8 m rotor diameter wind turbine. There were two TEF which covered 60 % of the chord and 27% of the aerodynamic blade span. To simulate a variation in the angle

of attack, the wind turbine was yawed to 10°. The closed-loop controller was capable of reducing the load fluctuation between 34% and 58% depending on the yaw angle.

Design and Testing of TEF on 9m Blades

Berg *et al.* [53, 100–103] designed, fabricated and tested a TEF on a wind turbine with a blade length of 9 m. The width of the TEF was 20 % of the chord while the length was 20 % of the blade span located between r/R=0.78 and r/R=0.98. The flaps were designed to have a deflection of ±20° and they were 3D printed out of ABS. The flap hinge moments were estimated through XFoil for different α and flap angles. The sensors used to instrument the blades included 2 accelerometers and 4 strain gages at different spanwise locations and a five-hole Pitot tube at 7.9 m blade span. The results showed that the load was decreased by 20% using TEF. The time delay between the flap actuation and the instrumentation response was calculated to be 0.024 seconds. They attributed this delay to the time it took for the airflow around the local blade section to adjust to blade geometry change. The power from the wind turbine for different flap angles was compared to the unmodified wind turbine blades. The results show that the power output changed with flap angles for all wind speeds. This utility-scale test lacked surface pressure measurements along the blade and active control of the TEF to reduce load fluctuation. The study was mainly aimed at the design and mechanical components of the TEF and less on the aerodynamic aspects. The study presented in this thesis uses the knowledge obtained by Berg *et al.* and focuses more on TEF aerodynamics and its capability at reducing load fluctuation.

Wind Turbine S833 Airfoil Trailing Edge Flap

Abdelrahman and Johnson [56] investigated the influence of TEF on a 3.4 m diameter wind turbine in a controlled environment. The blades consisted of a steel tubular spar with 3D printed S833 airfoil sections attached to it. The blades were of constant chord (178 mm) and constant pitch (6°) with a length of 1.7 m. The wind turbine was tested inside the UWaterloo Wind Facility. The length of the TEF was 20 % of the chord and was capable of deflecting within ±25°. Strain gages were installed at multiple places along the spar to measure the flapwise moment. The TEF was placed at different locations along the blade radius and the results showed that the TEF influence over blade load control is largest when r/R=0.89. It was concluded that the flap was capable of manipulating the flapwise moment and the relationship was relatively linear. Even though the experimental campaign was successful, a few key parameters were missing: the TEF was not automated and it

was deflected manually, the data acquisition system was not capable of phase averaging the data to study load fluctuation with azimuth and surface pressure measurements were not measured. More details about this experimental setup and the corresponding results can be found in this thesis [104].

Chapter 3

Experimental Setup

The experimental setup is split into three sections. First the airfoil geometry, surface pressure measurements, TEF actuation and load sensing on the airfoil are presented. The second section introduces the setup of the airfoil with a TEF inside a 2D wind tunnel. Finally, the setup of a 3.5 m diameter wind turbine equipped with a TEF is presented.

3.1 TEF Airfoil Design

This section provides details about airfoil geometry and the dimensions used. The design and build of the 3D printed airfoil is discussed. Selection of the pressure transducers and other design parameters are justified. Finally, detailed information about the flap actuation system is presented.

3.1.1 Airfoil Geometry and Selection

The NREL S833 airfoil was chosen to conduct all the experiments in this thesis. The NREL S833-4-5 family series are designed specifically for 1 to 3 meter diameter HAWT. The two main characteristics of these airfoils is that the maximum lift achieved by the airfoil is relatively uninfluenced by the surface roughness. The second characteristic is having a low profile-drag coefficient [105]. The availability and free access to the airfoil performance data on wind turbines is one reason to why this family was used. The other reason was because the Wind Energy Group have used them for different projects in the past.

Gertz *et al.* [106] used the S83X family to build a 3-bladed, 3.3 diameter wind turbine with variable chord and pitch. For the blade design, Gertz placed the S835 at 40%, S833 at 75%, S834 at 95% and a linear blend in between; this was also recommended by NREL [105]. Johnson *et al.* plotted the power output for each blade segment and concluded that the peak power intensity was located at r/R=0.77 corresponding to the S833 airfoil [107]. For this reason the S833 profile was used to manufacture the entire blade and for simplicity it was decided to make the new blades with constant pitch and chord for testing the influence of TEF at different r/R locations. Abdelrahman *et al.* made the same argument and used the same blades with constant pitch and chord [56].

S833 Dimensions

The airfoil chord was chosen based on the experimental setup of Abdelrahman and Johnson [56]. This was because the experiments were a success and their data could be used for comparison and reference. PropID software, discussed in Section 2.3.2, was used to find the optimal chord and pitch based on a blade length of 1.7 m, wind speed of 8.5 m/s and a rotation speed of 200 rpm. The results suggested using a chord of 178 mm and a pitch of 6°. More details could be found in Abdelrahman [104].

S833 Trailing Edge Flap

The flap width was chosen to be 20% of the chord based on simulations and experimental results found in the literature review in Section 2.4. For the entirety of the project, flap deflection towards the suction side of the airfoil is defined as positive flap angle as shown in Figure 3.1.

3.1.2 3D Printed Airfoil

3D Printed Blades

Different research groups used 3D printing techniques to manufacture small-scale wind turbine blades. Navalkar *et al.* 3D printed 1 m long blades in one piece with reinforced unidirectional carbon fiber spar caps [94]. Sandia National Labs also used 3D printing techniques to print the TEF [53]. Abdelrahman *et al.* 3D printed 1.7 m long blades in 5 pieces, and attached them together by a steel spar at the quarter chord of the airfoil [56]. The latter method was used in this experimental setup because it was more modular

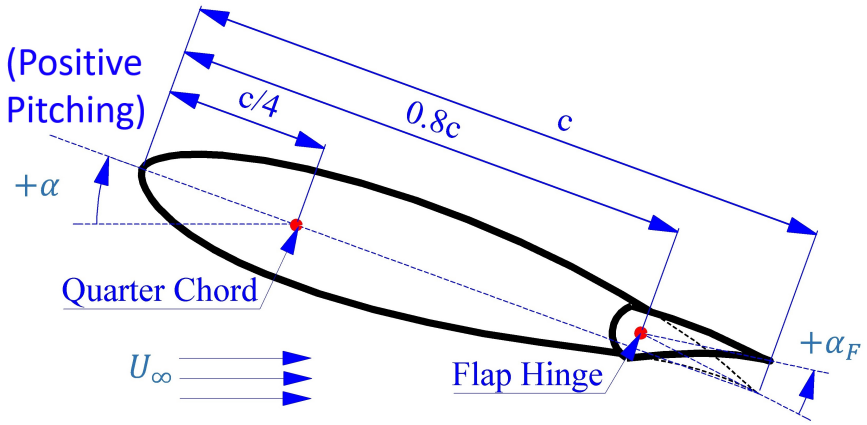


Figure 3.1: A sketch illustrating the airfoil and flap degrees of freedom $+\alpha$ positive AOA; $+\alpha_F$ positive flap angle; U_∞ free stream velocity

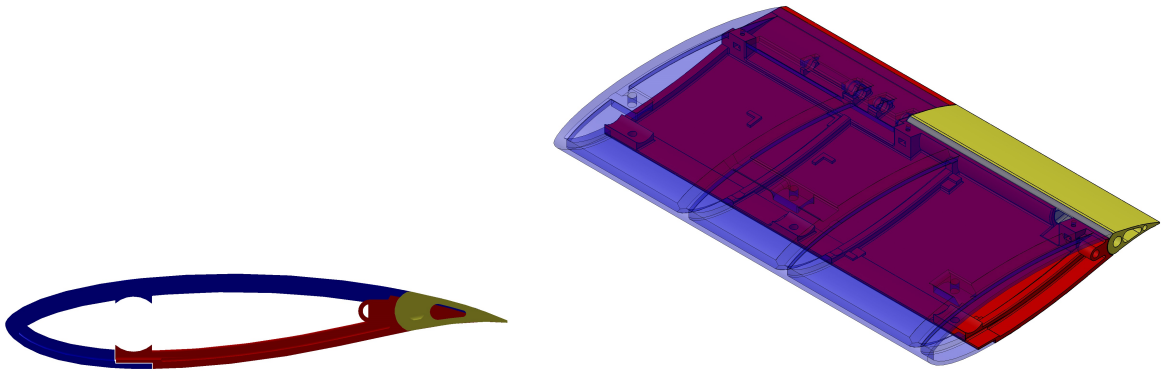
and easier to build. Some of the advantages of 3D printing the blades are: high level of complexity, high accuracy and repeatability, high speed production with no need of a mold, and high strength material.

To 3D print the airfoil section, the Fortus 360mc rapid prototyping machine manufactured by Stratasys [108] was used because it was accessible to students in the 3D print center on the UWaterloo campus. The 3D printer uses Fused Deposition Model or FDM to make 3D models from thermoplastic materials. There were three thermoplastics materials that could be chosen to 3D print the parts. Based on a recommendation from the UWwaterloo 3D print center and experimentation, the ABS-M30 was chosen because of its smooth finish and high strength. The ultimate tensile strength is 28 MPa, and the Izod impact resistance test is 128 J/m [109].

3D Printed Design

One of the main requirements during the design stage is that the 3D printed airfoil model would house the different actuators and sensors. The model went through multiple iterations of failed print jobs and fixes. Based on the requirements and design constraints, it was determined that the airfoil must be constructed from three different parts: the suction side, pressure side, and the flap. To make sure that the suction side and leading edge were smooth they were 3D printed in one part. The connection line between the two 3D printed airfoil pieces is along the quarter chord of the pressure side. Refer to Figure 3.2

for more clarification. Those three sections were printed and sanded down to achieve a smooth surface finish.



(a) 3D model side view

(b) 3D model isometric view

Figure 3.2: 3D model of the airfoil with the three different sections. Blue part: Suction side; Yellow part: Flap; Red part: Pressure side. (a) side view (b) isometric view.

There were multiple features that made this section of the airfoil unique and tailored for this project, see Figure 3.3. Here is a list of the main features:

- The outer shell airfoil thickness was set to 3/32" (2.4 mm). This gave the airfoil surface enough rigidity.
- **Webs**: There were 4 cross-sectional webs that supported the shell from surface pressure and pitching moments and adds stiffness to the model.
- **3 main compartments** to house the pressure transducers, Maxon Controller and Maxon motor adapter.
- **Spar pillow blocks** were used to mate the airfoil to the tubular spar.
- **Flap pressure tap access** was used to route the tubing from the flap to the pressure transducer.
- **Bearing support** was used to accurately place and support the 2 bearings used to align the TEF shaft to the actuator.
- **Motor support** was used to align the Maxon motor with the shaft.

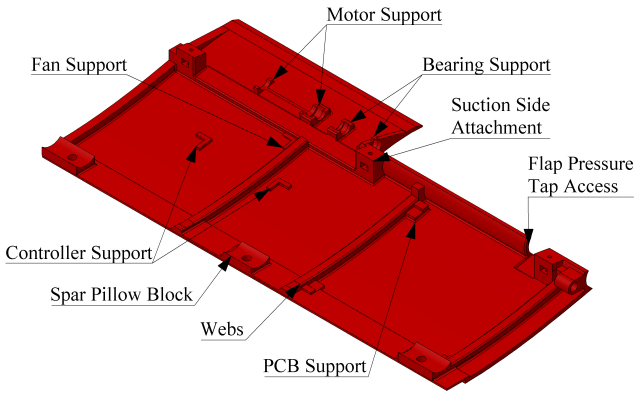


Figure 3.3: Different features of the 3D printed model

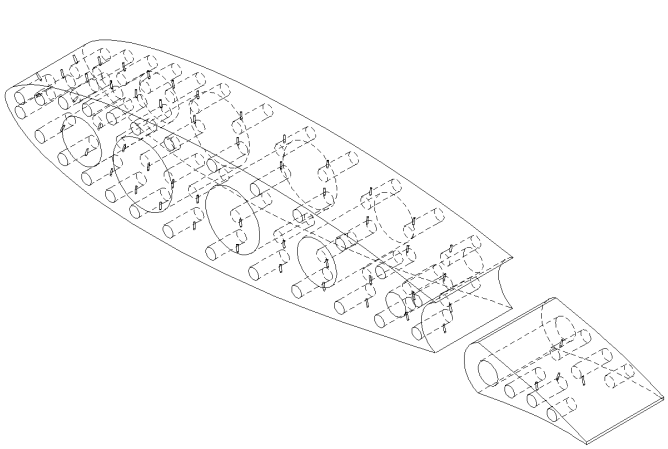
3.1.3 Surface Pressure Measurements

This section provides details about the design of the surface taps and the pressure transducers chosen. A custom-built board was used to organize the pressure transducers and connect them to the data acquisition system. Finally, calibration and uncertainty analysis is presented for the given setup.

Pressure Taps Design

To measure the surface pressure on the airfoil, pressure taps were drilled along the pressure and suction side of the airfoil. As mentioned in section 3.1.2, the airfoils were 3D printed. 3D printing does not provide enough accuracy for surface pressure measurements. A greater accuracy was achieved by CNC machining the airfoil from 6061 aluminum block. There were two parts that were machined, the main airfoil body and the flap that goes with it. Both parts were made at the UWaterloo machine shop using a 4-axis Haas VF4 machine with an accuracy of less than 0.025 mm [110]. A 3D model of the CNC machined part and the layout of the surface pressure taps is shown in Figure 3.4. The tap locations are shown

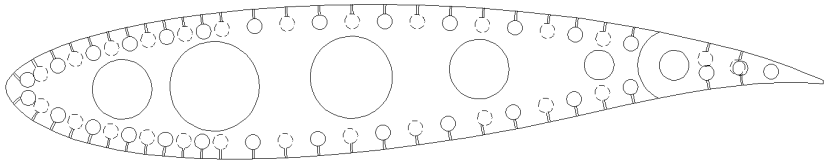
in the appendix in Table B.1.



(a) 3D model wire frame



(b) Final CNC part



(c) S833 airfoil with the pressure tap layout

Figure 3.4: S833 section with the pressure taps along the suction and pressure side

The top and bottom taps were placed at the same x/c location. There were two chord wise planes that the pressure taps were laid on. Each plane is 4 mm from the middle of the aluminum airfoil and 8 mm away from each other. The bottom and top taps are always on the same plane except for the last 2 taps on the TEF (geometric restriction). All the odd number taps are on one plane and all the even number taps are on the other plane. It was not possible to place all the pressure taps on one plane due to geometric constraints. The distance between the two planes is 8 mm, a negligible distance (at 200 rpm and a span wise location of 1.7 m that would lead to a velocity of 35.60 and 35.77 m/s for each of the 2 planes). The pressure taps are denser closer to the leading edge than the trailing edge because most of the lift force is concentrated on the leading edge. The distance between pressure taps is 4 mm at the leading edge and it goes to 7 mm at the trailing edge. The trailing edge flap has 2 pressure taps at the top and 2 at the bottom. The tubing for this section was routed through the 3D printed flap on either side.

An important design factor in installing pressure taps on an airfoil is the size and length of the hole and tube connecting it to the transducer. The pressure taps were directly drilled on the surface of the airfoil to avoid any errors and ensure a smooth surface. To connect the pressure taps to the transducers, 1/8 inch holes were drilled to either side of the airfoil connecting them to the taps as shown in Figure 3.4. Tubing was then used to connect the taps to the transducers.

To get the most accurate pressure measurements without disturbing the flow, the tap size was carefully determined. Typical hole sizes range from 0.4 mm for intricate and small objects to 3 mm for bigger and bulkier objects. To get a reasonably fast response time it is common to connect the tap to a larger diameter cavity. The tap diameter plays an important role in determining the error between the actual and measured pressure at the surface. An important dimensionless tap diameter is defined in Equation (3.1) [111]:

$$d^+ = \frac{d\sqrt{\frac{\tau_w}{\rho}}}{\nu} \tag{3.1}$$

where d is the tap diameter, ν is the kinematic viscosity, τ_w is the wall shear stress. d^+ is also described as the friction Reynolds number of the tap. Most error measurements are graphed versus this dimensionless number. To avoid considerable error it would be good to maintain the l/d (l being the tap length) ratio between 5 and 15. After careful consideration of the different parameters, the ID or tap diameter was chosen to be 0.4 mm. The length of the pressure taps is 2 mm. This combination results in a $l/d = 5$ within the acceptable range mentioned.

Another important factor that was checked is the dynamic response of the pressure taps. In this experiment the chamber of the pressure transducer is extremely small, and the volume inside the tubing is more significant. The equation used to define the natural frequency is based on a Helmholtz resonator and shown in equation (3.2) [112].

$$\omega_n = \sqrt{\frac{\pi r^2 c_{sound}^2}{V(L + \frac{1}{2}\sqrt{\pi^2 r^2})}} \tag{3.2}$$

where ω_n is the natural frequency, r and L are the radius and length of the pressure transmitting tube, V is the volume of the pressure transducer, and c_{sound} is the speed of sound. To increase the natural frequency, the length of the tube was decreased and diameter of the tube was increased. Based on 1/16 inch (1.59 mm) ID tube with a length of 0.15 m and atmospheric pressure, the natural frequency is 15 kHz. The rotor speed

in this case is around 200 rpm or 1200 degrees per second, much lower than the natural frequency of the pressure taps.

Pressure Transducers

In the previous section (3.1.3) the number of taps was 27 along the top and bottom surfaces for a total of 54. To measure the surface pressure on the airfoil while being rotated on the wind turbine with the frequency desired, the pressure measurements had to be simultaneous. To achieve this, 27 differential pressure transducers were used to measure the differential pressure between the suction and pressure side of the airfoil at the same x/c location. This way the number of transducers was 27 instead of 54. This technique was successfully used in Raiola *et al.* [69]. Additional experiments were conducted to study the difference between single-ended and differential pressure measurements in Section 4.4.1.

To determine the pressure range needed, XFoil was used to calculate the coefficient of pressure, C_p, for the S833 airfoil. The pressure taps were located around 1.5 m from the center of rotation. The wind turbine rotational speed was set to 200 rpm. Based on the section of interest, the total incoming wind velocity was 33 m/s due the blade's rotation and wind speed of 10 m/s from the wind tunnel. From this velocity, the Reynolds number was 450,000. The static C_p from XFoil close to the leading edge is 6 when $\alpha = 17°$ and the flap angle is 15°. Dynamic stall could produce much higher C_p values when compared to the static cases as Raiola *et al.* [69] reported that C_p could be as high as 10. With $C_p = 12$, the highest pressure is 8.5 kPa. This number determined the range of the pressure transducer. The differential pressure transducers chosen for this project were manufactured by All Sensors (model number of 120 cmH2O-D1-4V-MINI) with a pressure range: -10 cmH_2O to 120 cmH_2O (approximately from -0.1 kPa to 11.8 kPa) [113]. The response time for the pressure to reach 90 % is 0.5 ms.

Pressure PCB

To connect the 27 transducers to the DAQ card and to mount them inside the airfoil, a custom-built printed circuit board (PCB) was designed and built at UWaterloo. The two PCBs were placed on either side of the pressure taps. There were 14 pressure transducers on each board; the extra transducer was kept free. It was used to measure the influence of temperature and tangential acceleration on the transducer signal. A picture of the PCBs and pressure transducers is shown in Figure 3.5. The details concerning data acquisition are discussed later in Section 3.2.5.

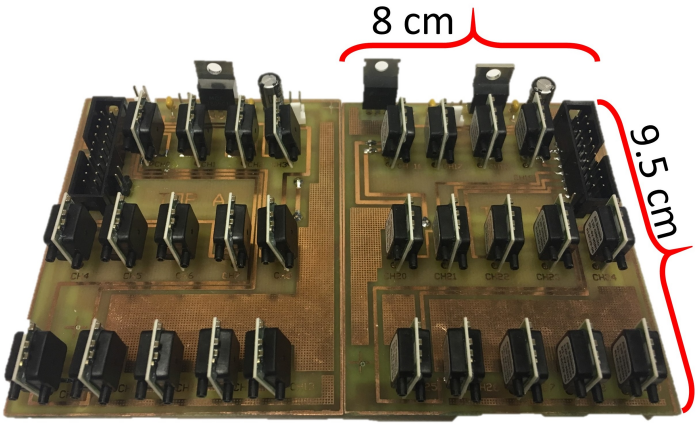


Figure 3.5: The layout of the pressure transducers on the PCB

Pressure Calibration

To ensure that the voltage from the pressure transducer was converted to the pressure accurately, a calibrator was used to calibrate each individual transducer. The Druck DPI 610 pressure calibrator was used with a range of ± 5 inH2O (± 1244 Pa) and accuracy of 0.05 % FS [114]. The range of this calibrator was smaller than the actual range of the transducer but this was the only calibrator the author had access to. The transducer was calibrated between -3 cmH_2O to +5 cmH_2O in increments of 0.5 cmH_2O. Over 4000 data points were collected for each pressure setting. For each transducer a linear regression fit was used to extract the slope and y-intercept. To measure the linearity of the transducer, the coefficient of determination (R-squared) was calculated and it was found to be equal to 0.999 which is approximately 1. This implies that the transducers were linear and the first-order polynomial equation could be used to convert the voltage to pressure. The coefficients of the polynomial and R-squared values are found in Appendix C.1. The slope calculated for each transducer was used for the entire pressure range. The transducers used were brand new and the manufacturer stated that they were all calibrated and linear across the entire pressure range. This provided extra confidence that the transducers were linear.

Pressure Uncertainty

The uncertainty in pressure is calculated in Appendix D.4 and found to be ± 18 mV. This was based on the bias error in the pressure transducer and the uncertainty in the DAQ

card. Precision error depends on the data collection and it was found to be negligible compared to the bias error for the calibration data because the number of samples was well over 4000. Based on the calibration of the transducers, ± 18 mV was equivalent to ± 51 Pa.

3.1.4 Flap Actuation

Flap Hinge Moment Calculation

There were three main force components that the flap actuator had to resist. First was the center of gravity (COG) offset which gives rise to a gravity force acting on the flap due to its weight. This was the smallest resistance and was negligible. The second was the moment that arises from the moment of inertia of the flap while oscillating. This resistance is dependent on the speed of oscillation. The frequency of oscillation chosen for the flap was that of the rotor speed, which in this case was 3.33 Hz. The semi-amplitude of the flap was 20°. The moment of inertia of the flap was acquired through Solidworks software. The torque needed by the motor to overcome the moment of inertia was 0.022 N.m. Another force that was not accounted for and assumed to be negligible is the torque required to overcome the friction created by the TEF bearings. Future studies should try to quantify this torque and include it in the calculations.

The third moment was due to the aerodynamic flow around the airfoil. To predict the moment, the S833 airfoil data points were imported into XFoil, more information can be found in section 2.3.1. Berg *et al.* [53] used XFoil to predict the moment on the TEF. Different simulations were conducted for different AOA and for a flap angle of 20° and -20°. The flap hinge was set to 0.8 in the chordwise direction, and 0.026 in the airfoil thickness direction. From the simulations it was seen that the maximum moment was around 0.1 N.m. The Reynolds number for the simulations was set to 500,000 while the flap length in the spanwise direction was 0.33 m. Accounting for the three moments discussed the motor had to overcome a total torque of 0.122 N.m. The dominant force in this case was due to aerodynamic forces (0.1 N.m).

Maxon Servo Motor Assembly

The main requirement for the flap motor was to deliver a torque of 0.122 N.m with a speed of 160 rpm. One other geometrical requirement was to have a diameter of less than 10 mm. Maxon motors supplies motors of different sizes and combinations. The manufacturer

recommended the Maxon ECX series because it had state-of-the-art technology and was both reliable and powerful. The 8 mm diameter motor was the most suitable size for this experimental setup. Based on many discussions with the manufacturer, it was decided that the motor most suitable for the torque requirements was the package described in Appendix B.3 [115]. The servo motor was attached to a 256:1 gearbox with a 4,096 count encoder attached to the motor side. The weight of the motor was negligible when compared to the rest of the blade. A small fan was installed next to the motor assembly to cool it down and prevent overheating.

Maxon Controller

The controller used in this study was the Maxon EPOS2 24/2 (Part number: 390003) [116] as it was compatible with the mentioned motor. One of the main advantages of the controller was that it could be programmed to actuate the motor according to an analog input. Another advantage of the controller was its small physical dimensions and negligible weight. Some of the specifications of the controller are summarized in Appendix B.3. Another micro-controller adapter was needed for the controller to communicate with the encoder and motor [117]. Both boards were small enough to be placed inside the airfoil.

Maxon Actuation Assembly

A lot of care and effort was exercised to integrate the motor and controllers in the airfoil and flap section. From the start, it was intended to place all the components inside the airfoil. All the components were then chosen to satisfy this requirement. The Maxon motor was connected to the flap shaft directly to reduce the backlash in the assembly as much as possible. To support the flap, 2 ball bearings were installed on either end of the flap (4 bearings in total). The two controllers boards were attached to the pressure side of the airfoil. All the cable connections were incorporated within the airfoil profile. RS232 communication was used to connect the controller to the main computer. A picture of the setup is shown in Figure 3.6.

3.1.5 Internal Organization

To summarize this section and bring together all the different pieces, a picture of the internal organization of the airfoil with the cover off is presented in Figure 3.7. The pressure transducers were placed on either side of the pressure taps located at the middle

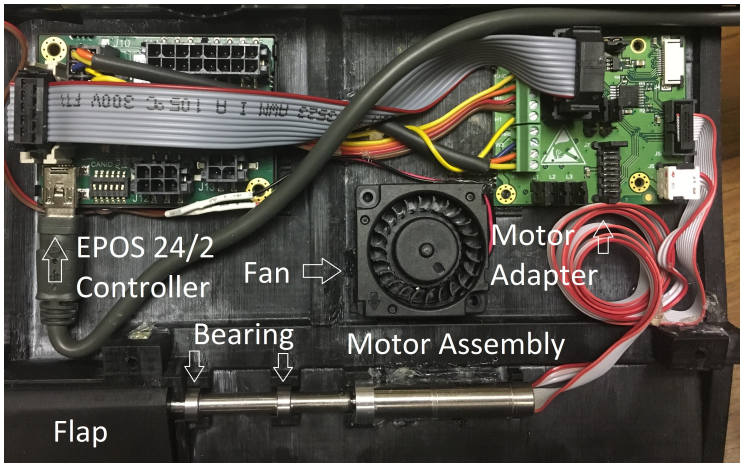


Figure 3.6: Maxon motor and controller assembly inside the airfoil

of the airfoil section. The motor and controller were placed on one side of the airfoil. The stainless steel spar that connected all the pieces together is 3/4" (19 mm) in diameter.

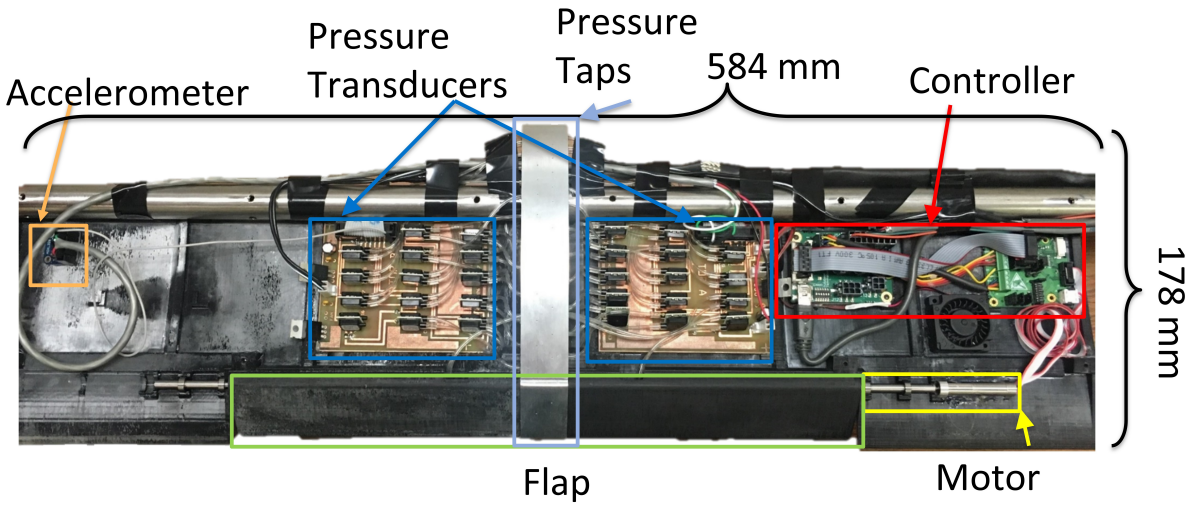


Figure 3.7: Internal organization of the airfoil section with cover removed

3.2 2D TEF Experimental Campaign

The different components of the 2D TEF experimental campaign are presented in this section. First the wind tunnel used to conduct this campaign is discussed. This is followed by introducing the pitch actuation system and stain gage measurements. Finally, the data acquisition system is discussed.

3.2.1 Closed-Loop Wind Tunnel Specifications

The closed-loop wind tunnel at the University of Waterloo was used to conduct the 2D TEF experimental campaign. The wind tunnel has a contraction ratio of 9:1 and a cross section of 0.61 m square. The uniformity was found to be within $\pm$ 0.4% in the spanwise and vertical direction. The turbulence intensity is 0.1%. The free-stream velocity was set by the static pressure drop across the contraction with an uncertainty of less than 2.5%. More information about the wind tunnel calibration can be found in [118].

3.2.2 Small-Scale Wind Tunnel Setup

The setup described here was designed to represent the blade on a wind turbine. The tubular spar was cantilevered and supported on the drive side to resemble a blade. The gap between the airfoil and the wind tunnel was 1.3 cm on either side. The strain gages were attached on the spar and located outside the wind tunnel. More details about the stepper motor and its controller can be found in Section 3.2.3. The aluminum airfoil section that contains the pressure taps was placed at the center of the wind tunnel section sandwiched between the 3D printed airfoil pieces. A schematic of the experimental setup is illustrated in Figure 3.8.

3.2.3 AOA Actuation

For the wind tunnel setup, a stepper motor was used to control the airfoil pitch and provide airfoil oscillation. The Superior Electric Stepper Motor (model number: M093-FD07E) was used in this setup. The motor has a maximum holding torque of 3.6 Nm and has a total of 200 steps/rev. A quadrature encoder with a resolution of 16,384 counts was attached to the back side of the motor to confirm the position of the stepper motor. The Galil Motions controller (model number: DMC-31017-BOX-2PB) [119] was used to drive the

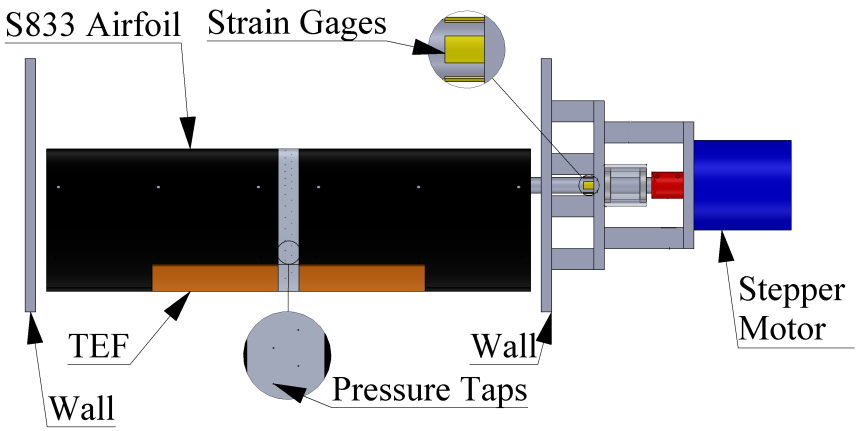


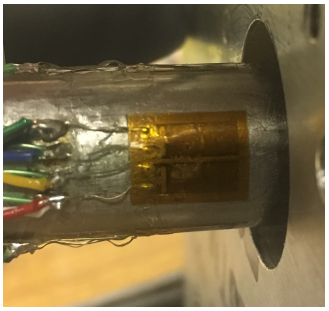
Figure 3.8: Wind tunnel experimental setup with the airfoil and actuation. Strain gages and pressure taps are magnified

stepper motor. More information about the controller setup is found in Appendix B.4. The controller was programmed to actuate the motor according to an analog input.

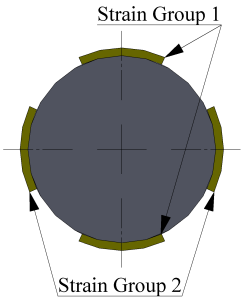
3.2.4 Strain Measurements

Omega precision strain gages (model number: SGD-7/1000-DY11) [120] were used to measure the surface strain of the stainless steel spar at the root of the airfoil. One of the reasons why this specific strain gage was chosen is because it was successfully used to measure the strain on a similar experimental setup by Abdelrahman [56]. The strain gages were connected in a full-bridge configuration with a nominal resistance of 1000 Ω and tolerance of ±0.35%. The uncertainty in the strain gage was calculated to be ± 0.35 % of measured value in Appendix D.3. The two sets of full-bridge strain gages were used to measure the bending strain on the shaft in two directions. The lift and drag on the airfoil were measured simultaneously while the AOA was changing. A full-bridge configuration was used to amplify the signal from the strain gages and to minimize the impact of temperature. A picture of the strain gage and orientation is shown in Figure 3.9.

To ensure that the output from the strain gages was meaningful, they were calibrated by applying known loads at a specific location along the shaft. The main purpose of calibration was to relate the strain from the gages to the moment experienced by the shaft and this relationship should be linear. A linear regression was used to fit the data and the coefficient of determination (R-squared) for both strain gage groups was around 0.999.



(a) Strain gage adhered to stainless steel shaft



(b) The two full-bridge strain groups

Figure 3.9: Strain gage setup and position along the shaft

During the experimental campaign, the strain output was used to calculate the moment based on the linear fit that was established. More information about the calibration is found in Appendix C.2.

3.2.5 Data Acquisition System

There were two separate experimental setups, one in the 2D wind tunnel with an airfoil section while the other was on a wind turbine in the Controlled Wind Research Facility. The DAQ system setup was the same in both experiments to eliminate any discrepancy that could arise from having two different DAQ systems. For this reason, part of the DAQ system was tailored to accommodate both experimental setups. In the current setup there were two inputs (pressure transducers, strain gages) and 2 outputs (flap actuation and AOA actuation). In the second experiment, all the inputs and outputs were placed inside the rotating blade and wireless technology was used to connect the rotating side to the stationary side. Three cDAQ NI 9191 [121] were used to transmit the signal wirelessly from the hub to the stationary computer. The NI 9237 [122] and NI 9205 [123] were used to measure the signal from the strain gages and pressure transducer respectively, while the NI 9263 [124] was used to generate an analog signal to control the flap and pitch actuation. All the cDAQ cards connect to a wireless network that connects to the desktop computer in the control room. An Ethernet cable was then used to connect the router to the main computer. The stepper motor controller was also connected to the router via an ethernet cable. Finally the flap actuation motor was connected to the main computer via a RS232 cable. To illustrate all the inputs and outputs Figure 3.10 shows a sketch of the setup.

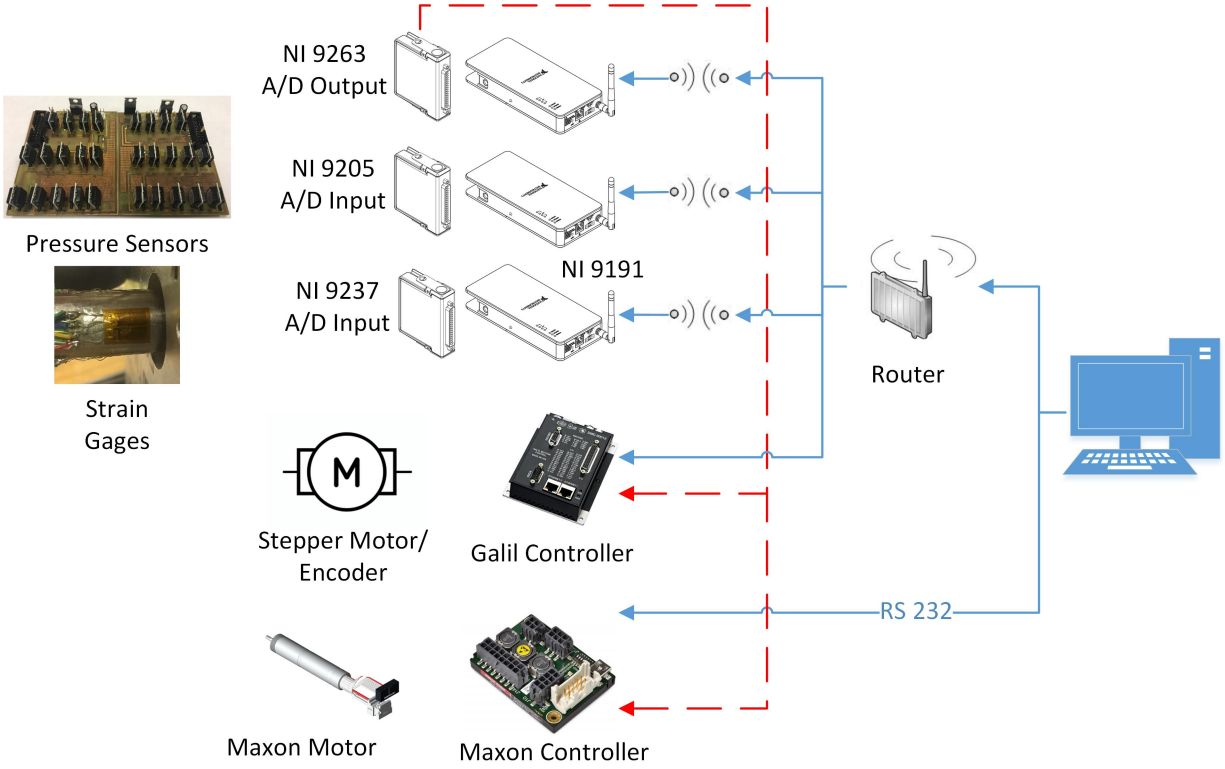


Figure 3.10: A map illustrating the data acquisition system and communication lines between systems for the wind tunnel setup

3.3 Wind Turbine Experiment

This section discusses the characteristics and dimensions of the UWaterloo wind generation facility. Details of the Wind Energy turbine and dimensions are presented. The design of a new hub and pitch control are discussed. Finally, the data acquisition system is shown.

3.3.1 UWaterloo Wind Generation Research Facility

Facility Specification

The UWaterloo wind generation research facility is a large-scale open circuit wind tunnel located off campus in Waterloo, Ontario. The flow is driven by a bank of 2 high by 3 across

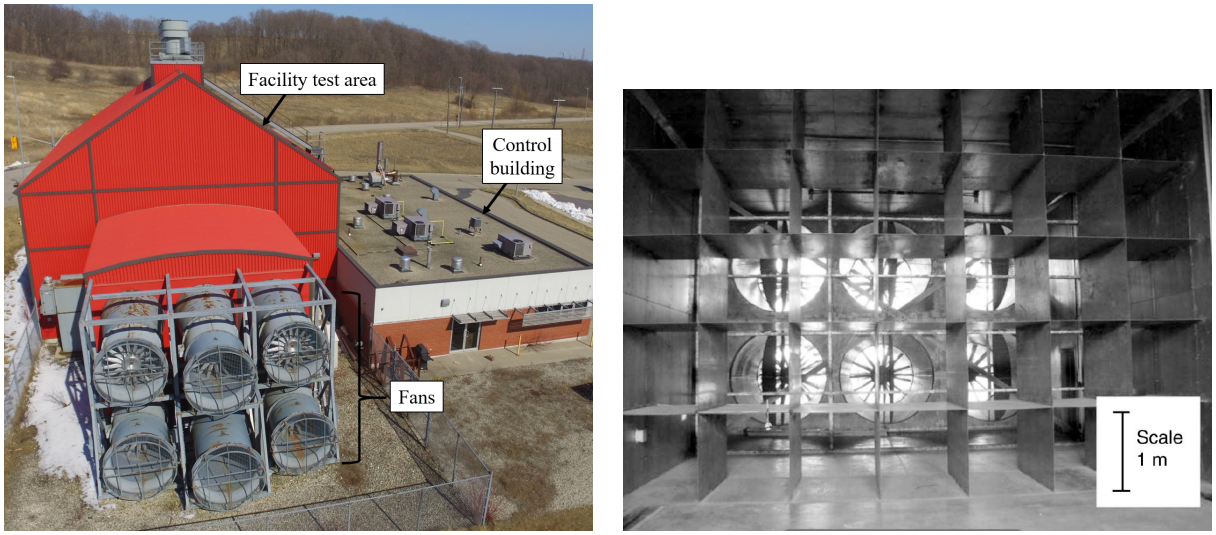
1.98 m diameter fans that are individually controlled by a variable frequency drive (VFD) to control the wind speed in the wind tunnel. The fans are followed by a large plenum with limited flow conditioning including settling screens and flow-straightening ducts. Tables 3.1 and 3.2 summarize the fan specifications and the wind tunnel facility geometry. Figure 3.11 provides a view of the fan banks from inside and outside of the facility. The wind facility can generate wind speeds between 0 and 11 m/s with a turbulent intensity in the range of 5% to 7% [125]. The UWaterloo wind turbine test rig creates a blockage ratio of approximately 7% and is located 7.96 m downstream of the fan exit plenum. The hub height of the tower is 3.05 m. The high turbulence intensity and low blockage ratio creates an ideal environment to test wind turbines as it is representative of the environmental conditions experienced in the field. More information about the facility in terms of geometry and flow characterization can be found in Johnson *et al.* [107], Devaud *et al.* [126], Gaunt [127], and Best [128].

Table 3.1: UWaterloo Wind Facility fan specifications [126]

Specification	Value	Details
Type	Vane axial fans	Howden-Buffalo Model 78-26 Series 1000
Size	1.98 m	Diameter
Number (arrangement)	6 (3 x 2)	-
Volume Flow Rate	78.7 m^3/s	Maximum per fan
Pressure	413.5 Pa	At maximum flow rate
Control	VFD	Individual operation

Table 3.2: UWaterloo Wind Facility geometry specifications [126]

Area	Geometry Details
Fan discharge plenum	8.23 m long, 8.54 m wide, 5.9 m high
Plenum exit plane	Rectangular 8.0 m wide, 5.9 m high
Flow conditioning	Two settling screens and a 7 x 5 array of steel flow-straightening ducts in the discharge plenum
Test area	15.4 m wide, 19.5 m long, 7.8 m high along the sides and 13 m high at the peak
Flow exit	Squared, 7.9 m x 7.9 m



(a) Aerial view of the facility

(b) Fan bank and flow-straightening duct

Figure 3.11: Photographs of UWaterloo Wind Generation Research Facility

Wind Characterization

To characterize the incoming wind in the wind tunnel, 16 pitot tubes were used to measure the velocity simultaneously at the hub location. More information about the setup used to measure the velocity can be found in McKinnon [125]. The non-dimensional velocity contour plots at 0.3 D (wind turbine diameter) upstream of the turbine are plotted in Figure 3.12 for an average velocity of (a) 7.1 m/s (b) 9.4 m/s(c) 11.8 m/s respectively. From the three plots, it is seen that there exists a non-uniformity of the velocity at the turbine hub location. There are multiple peaks and troughs in the contour plots that have a significant impact on the results as later seen in the results chapters. The largest peak is at z/D=0.25 and y/D=0.25 where a 10% velocity increase was noted in all three plots presented. This non-uniformity was also found by Gallant [129] during previous experiments conducted in the same facility. This velocity increase is consistent for different velocity settings and different days of operation. This non-uniformity was also seen in the research of Weisinger and Best [128, 130] spanning an interval of 20 years.

McKinnon [125] tried extensively to adjust the fan speeds individually to attempt to obtain a uniform profile. He concluded that the desired uniformity could not be completely achieved. Although there was improvement in adjusting the fan frequencies individually, it may not be completely beneficial to divert from running all the fans at the same frequency.

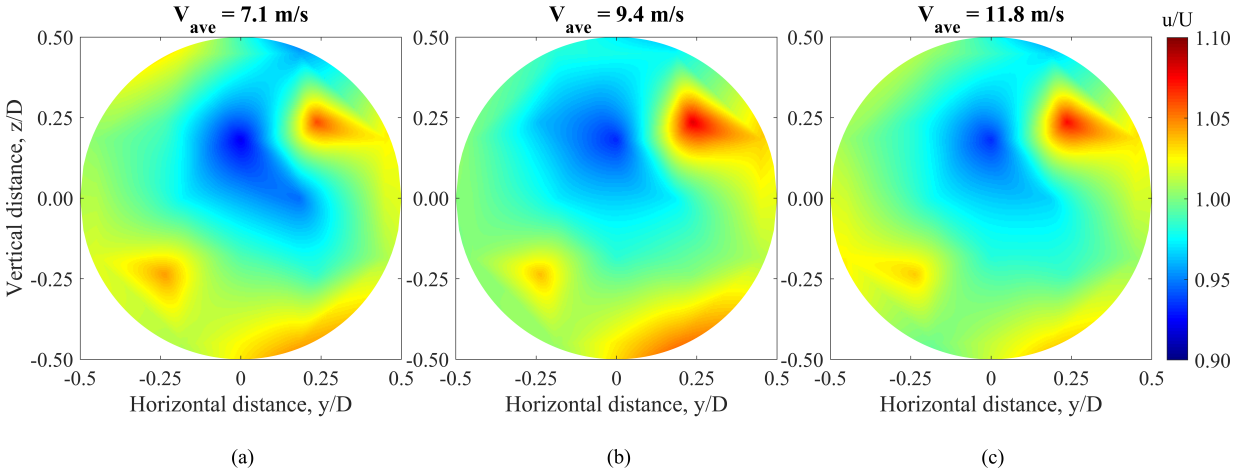


Figure 3.12: Non-dimensional velocity profile at 0.3 D upstream of the turbine with an V_{ave} of (a) 7.1 m/s (b) 9.4 m/s(c) 11.8 m/s

Based on his conclusion, the tests conducted in this thesis were all done without adjusting the fan frequencies and running them all at the same frequency. Instead of adjusting the speed of the fans, additional flow-straightening screens were placed at the straightening ducts to achieve higher uniformity. For further discussion, see the following section.

Improving Wind Uniformity

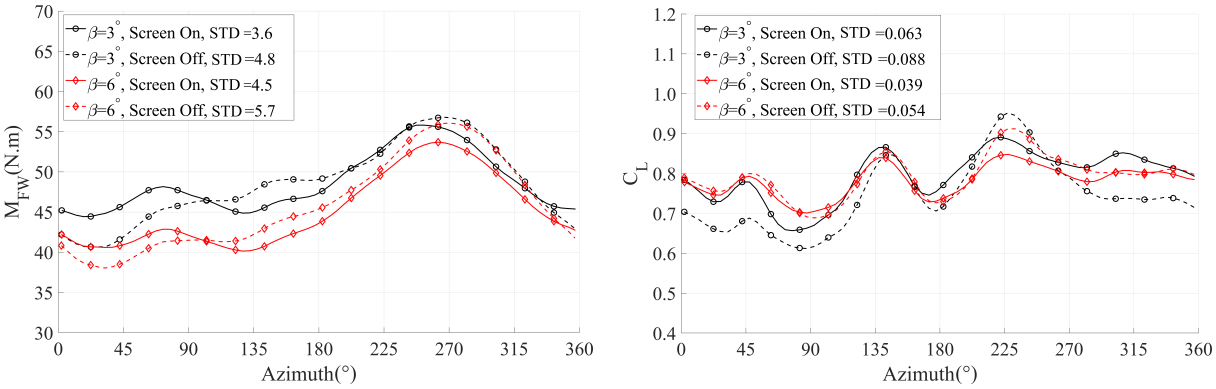
One way to reduce spatial flow velocity fluctuations is to place screens in the area affected. By adding screens, the velocity fluctuations is reduced and the velocity spatial distribution becomes more even. Based on the results from Figure 3.12, four screens were placed at the entrance of the flow-straightening ducts. These four ducts supply the flow for the top right quarter (z/D=0.25 and y/D=0.25) of the turbine rotor. Figure 3.13 shows the screen and the placement location. To test the impact of the screens on the turbine performance, tests were conducted with and without screens and the results are summarized in Figure 3.14.



(a) Screen Location (b) Screen Layout

Figure 3.13: Placement of additional screens at the flow-straightening ducts to improve flow uniformity in the wind tunnel.

The blade flapwise moment (M_{FW}) is plotted with azimuth position (Ψ) when the turbine was operating at zero yaw offset and a tip speed ratio (λ) of 3.5 for blade pitch, $\beta = 3°$ and $6°$. In an ideal case when the wind speed is uniform with no turbulence, the loading on the turbine is constant and does not change with azimuth position. Looking at the dotted lines ("screen off") in Figure 3.14a, there is a significant increase in M_{FW} at $\Psi = 270°$. This increase corresponds to an increase in velocity found in the contour plots in Figure 3.12. There exists a delay of $\pi/4$ between the velocity increase and the moment increase at the root of the blade. This delay does not appear in the $C_L - \psi$ plot in Figure 3.14b indicating that the C_L response to wind speed change is more instantaneous. The spike in C_L happens at $\Psi = 225°$ the exact location of the wind speed increase. Now comparing the "screen on" data (solid line) to the "screen off" data (dotted line), it can be seen that the variation in M_{FW} and C_L decreases indicating better wind uniformity in the wind tunnel. This improvement is clearly seen between $\Psi = 180°$ and $270°$ where the screens are located. To quantify the improvement in load uniformity on the turbine, the standard deviation (STD) is provided in the legend of each plot. These values indicate that the velocity spatial variation decreased when the screens are added. For this reason the screens were installed during the entire experimental campaign.



(a) Flapwise Moment (out-of-plane)

(b) C_L at r/R=0.82

Figure 3.14: Additional screen impact on M_{FW} and C_L. Solid line: Screen on. Dotted line: Screen off. Black line: $\beta = 3°$. Red line: $\beta = 6°$.

3.3.2 Wind Energy Group Test Turbine

The wind turbine blades with the integrated TEF were tested on the custom-designed and -built wind turbine rig owned by the Wind Energy Group of UWaterloo. The turbine is an upwind 3-bladed horizontal-axis design with a hub height of 3 m. The maximum rotational speed is 230 rpm, while the power capacity is 3 kW and the nacelle can be yawed between ±40°. The nacelle included a Marathon Electric Y287 184TC frame vector motor, a 3.7 kW motor, which functions as a generator or motor depending on the controller setting. The motor was equipped with an encoder to accurately control the rotational speed using a closed-loop controller. A coupler brake was face-mounted to the motor for emergency braking and for parking the rotor. To reduce the motor speed to the desired rotor speed the Nord helical in-line gearbox SK572.1 was used with a reduction ratio of 7.49:1 and was face-mounted to the coupler brake. Figure 3.15 shows a picture of the test rig with all the different components.

The motor, encoder, and the brake were controlled by an SP2203 Control Techniques Vector Drive to provide a closed-loop control to accurately set the speed of rotation. The drive was capable of running a 5.6 kW motor via a variable frequency drive (VFD). A dynamic brake resistor was used to dissipate the power generated by the wind turbine. An additional communications sub-panel was located in the control room to set the rotational speed of the rotor. The sub-panel also provided real-time feedback from the motor to show the actual rotational speed and power output. The proportional-integral (PI) controller

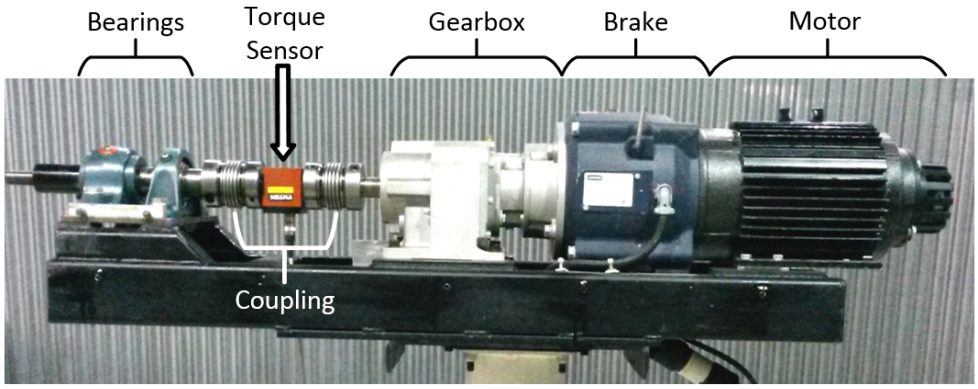


Figure 3.15: Wind Energy Group test rig drive-train with labels

tries to match the rotational speed set by the user. The two couplings in Figure 3.15 were attached to the Futek TRS 605 torque/encoder sensor [131]. It is a non-contact shaft to shaft rotary sensor with a 200 Nm torque capacity and a 1440 counts/rev encoder. The encoder provided position and can be synchronized with the torque sensor to provide power output. More information about the test rig can be found in Abdelrahman [104].

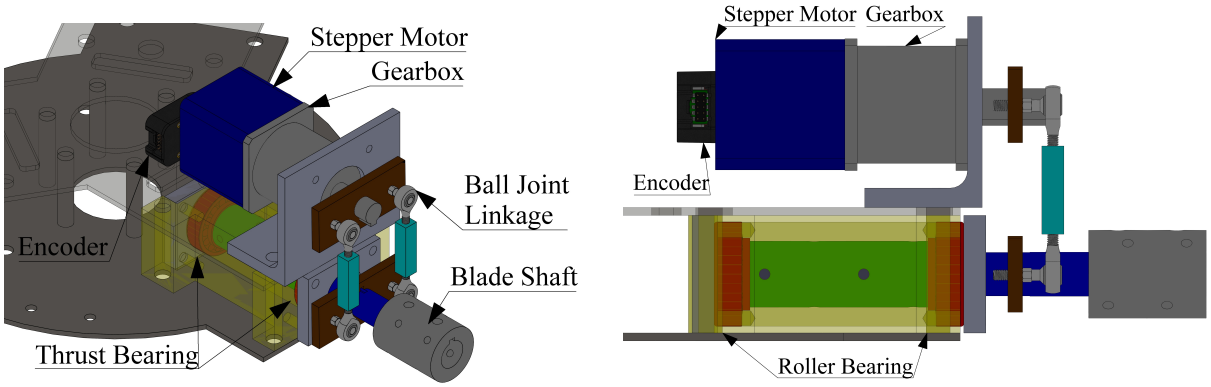
3.3.3 Wind Turbine Rotor Setup

The current wind turbine had fixed blade pitch and it could only be changed manually. To control the blade pitch from the control room and during operation a new mechanism was designed to support and actuate the blade. In this section the blade support is illustrated followed by pitch actuation selection, and hub assembly.

Pitch Control Setup

Part of the changes to the wind turbine setup required a new mechanism to pitch the blade while in operation. To do so a stepper motor was incorporated inside the wind turbine hub. A 3D model of the design is provided in Figure 3.16. A pair of tapered roller bearings was used to support the wind turbine blade and also to provide smooth rotational freedom. The bearings were rated to absorb all the loads that the wind turbine blade would experience while in operation. Having the motor and the main shaft in line was impossible due to geometric and space restriction. So the motor/gearbox assembly was placed above the blade shaft as seen in Figure 3.16. Ball joint linkages were used to connect the motor output shaft to the blade shaft. The ball joint linkages were used because they are capable

of handling a large missalignment and yet provide very minimal backlash in the system. The aerodynamic forces are very sensitive to the blade pitch so keeping the backlash in the system minimal was a very important requirement. An encoder with a high resolution (16,384 counts/rev) manufactured by US Digital Encoder was connected to the motor to insure an accurate control over the pitch angle. The encoder was connected to the stepper motor controller. In this mechanism, full rotation of the blade was not possible but it was also not needed. The blade pitch rotational freedom is between ±30°.



(a) Isometric View

(b) Side View

Figure 3.16: A 3D model of the connection between the motor and the blade shaft. Different views are shown for clarity.

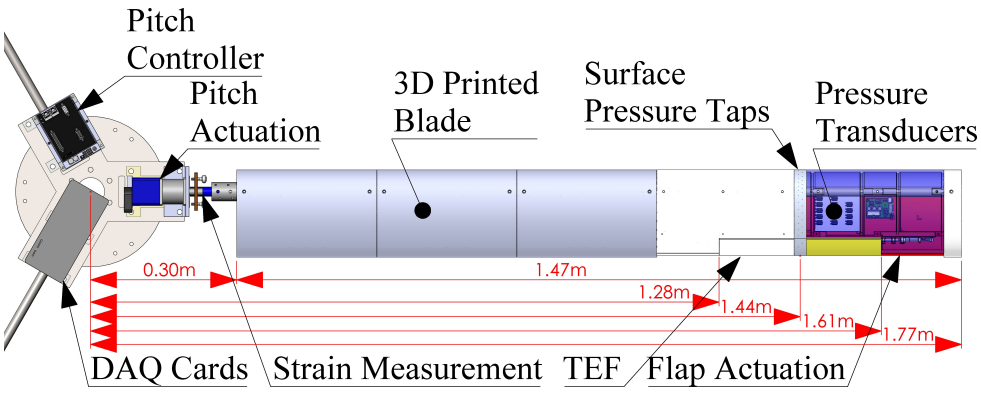
To select the appropriate motor, the torque and speed requirements were determined first. The motor had to overcome the forces created by the aerodynamic moment coefficient (C_m) and the resistance from the mass moment of inertia. The maximum C_m was determined using XFoil for different AOA and flap angles [52]. The mass moment of inertia and other properties were determined using SolidWorks. The total torque needed by the motor was estimated to be 5 Nm.

The 2 phase hybrid stepper motor with a NEMA 23 frame by Sumtor (model number: 57HS7630A4) was chosen and has a holding torque of 1.8 N.m. The motor was coupled to a single-stage planetary gearbox with a gear ratio of 10:1 with a backlash of 15 arcmin (0.25°). The gearbox/motor assembly produced a holding torque 16 Nm more than three times the maximum torque that was required.. The stepper motor was controlled by the same Galil controller discussed in Section 3.2.3. The stepper motor was controlled in a closed-loop system where the encoder provides feedback to the controller to ensure that the desired motion or pitch angle was always achieved. The controller was located at the

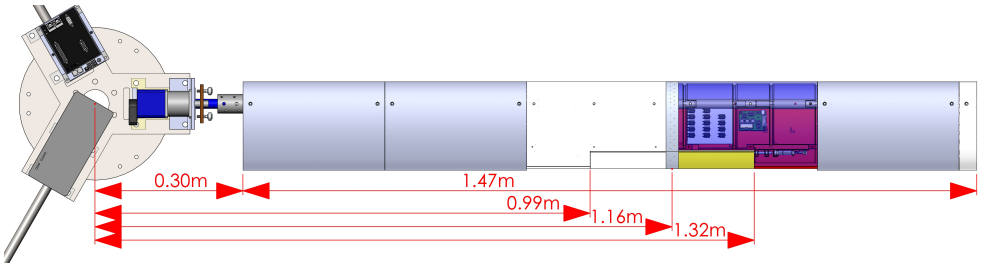
hub, and the power was transferred through the slip ring. Communication between the controller inside the moving hub and the stationary computer was done over a WIFI bridge created by two D-link DWL 810 routers. This allowed wireless communication and control of the controller and the motion of the pitch.

Hub/Blade Assembly

To test a TEF system on a wind turbine the rotor was designed to have a single-blade with a constant pitch and chord. A 3D model of the airfoil with labels and dimensions is shown in Figure 3.17. The blade consists of 4 modular sections that allowed the surface pressure section and the TEF to be placed at r/R=0.66 or r/R=0.82 as shown in the figure. The flap span is 22% of the 1.47 m aerodynamic blade span. A stainless steel spar at the quarter chord that runs along the total length of the blade was used to support the 3D printed blades and hold all the components together. The designed blade was capable of housing all the instrumentation and the flap actuation system.



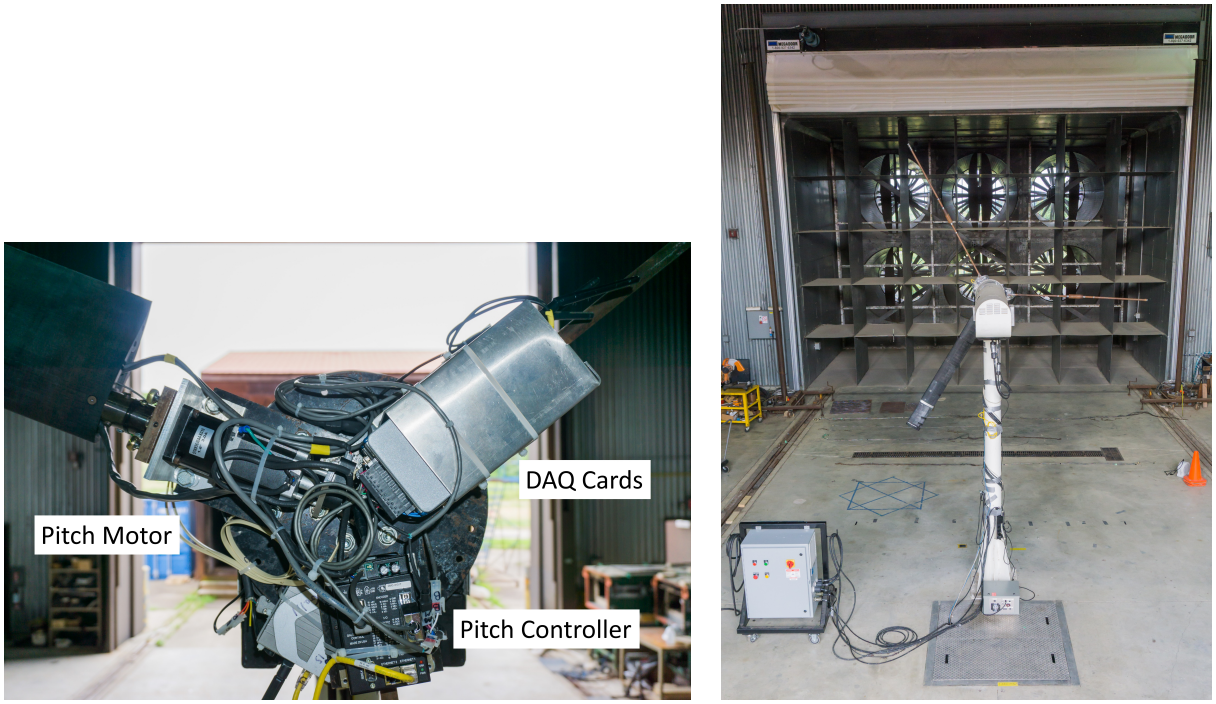
(a) TEF at r/R=0.82



(b) TEF at r/R=0.66

Figure 3.17: Layout of the hub, aerodynamic blade and the TEF flap at a) r/R=0.82 and b) r/R=0.66

One of the important aspects of the experimental campaign was to acquire surface pressure measurements on the blade while it was rotating in different conditions. Transferring the analog signal from the pressure transducers to the computer through slip-rings would require a very large channel count and would introduce noise to the signal. One innovative way of transferring the data to the computer was through a wireless signal. Three cDAQ-9191, a Wi-Fi chassis that houses the 3 DAQ modules mentioned in Section 3.2.5, were used to transfer data to and from the computer through a wireless router. The DAQ cards and stepper motor controller were all placed on the hub of the turbine. Figures 3.17 and 3.18a illustrate the layout of the hub and the instrumented blades.



(a) Instrumented Hub (b) Wind Turbine

Figure 3.18: Pictures of the (a) wind turbine hub and (b) wind tunnel layout.

Full Turbine Assembly

After the hub was fully assembled, it was attached to the Wind Energy Group test rig. To transfer power and communication from the rotating hub to the stationary group a slip ring was used (more details in the following section). The slip ring was placed between the bearings and downstream of the rotor. The wind turbine was composed of one aerodynamic blade and two counter-weights to balance the rotor. The counter-weights were made of tubular spar with a cylindrical weight placed at a specific location to match the exact weight and center of gravity of the aerodynamic blade. This way, counter-weights and the aerodynamic blade had the same length, weight and center of gravity to produce a rotor with minimal imbalance. A 3D model and a picture of the entire turbine with the aerodynamic blade are presented in Figures 3.19 and 3.18b.

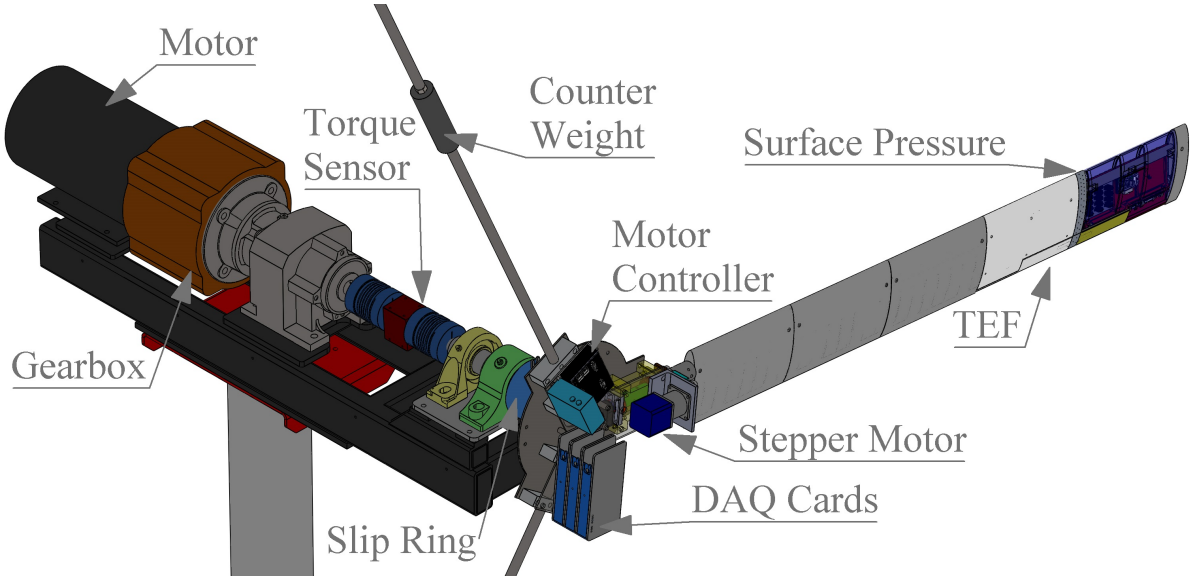


Figure 3.19: 3D model of the wind turbine assembly showing the main components

Slip Ring

The slip ring was needed to supply power to the instrumentation and flap/pitch actuation. A through bore shaft slip ring was required so it could be placed downstream of the rotor plane. The only available location to place the slip ring was between the bearing and the rotor plane. Table 3.3 shows the number of channels needed to connect the instrumentation on the moving hub to the stationary ground. Based on the physical dimensions and the required channels a through bore slip ring by Senring (model number: H50119-1210 Series) [132] was chosen with 12 channels.

Strain Gage

Two strain gage groups were installed at the root of the blade to measure the edgewise (in-plane) and flapwise (out-of-plane) direction root bending moments. The same type of strain gages were used on the wind turbine as the ones used in the 2D TEF experimental campaign. More information about the strain gages can be found in Section 3.2.4. The location of the gages are marked in Figure 3.17. The strain gages were calibrated to convert strain into root moment in both directions. More information about the calibration can be found in Appendix C.2.

Table 3.3: Slip ring channel layout and description of the connections between the static nacelle and the rotating hub

Item	Description	Number of Channels
1	Power for DAQ cards	2
2	Power for Flap Motor	2
3	Power for Stepper Controller	2
4	Power for WIFI Controller	2
5	RS 232 connection for Flap Motor	3
	Total	11

Data Acquisition System

The data acquisition system and motion actuation was a very crucial and important part of the setup. An essential requirement was that the motion of the flap and pitch should be synchronized with the rotation of the rotor. Furthermore the data acquired (surface pressure, root strain, and rotor torque) should all be synchronized with respect to the azimuth position. The DAQ system for the wind turbine was a continuation of the DAQ system designed for the wind tunnel experiments, as described in Section 3.2.5. The main difference between the two systems was the addition of a rotary encoder and torque sensor in the nacelle of the turbine. To illustrate all the inputs and outputs Figure 3.20 shows a sketch of the setup. All the connections between the rotor side and the stationary ground were carried out via a wireless connection or through the slip ring.

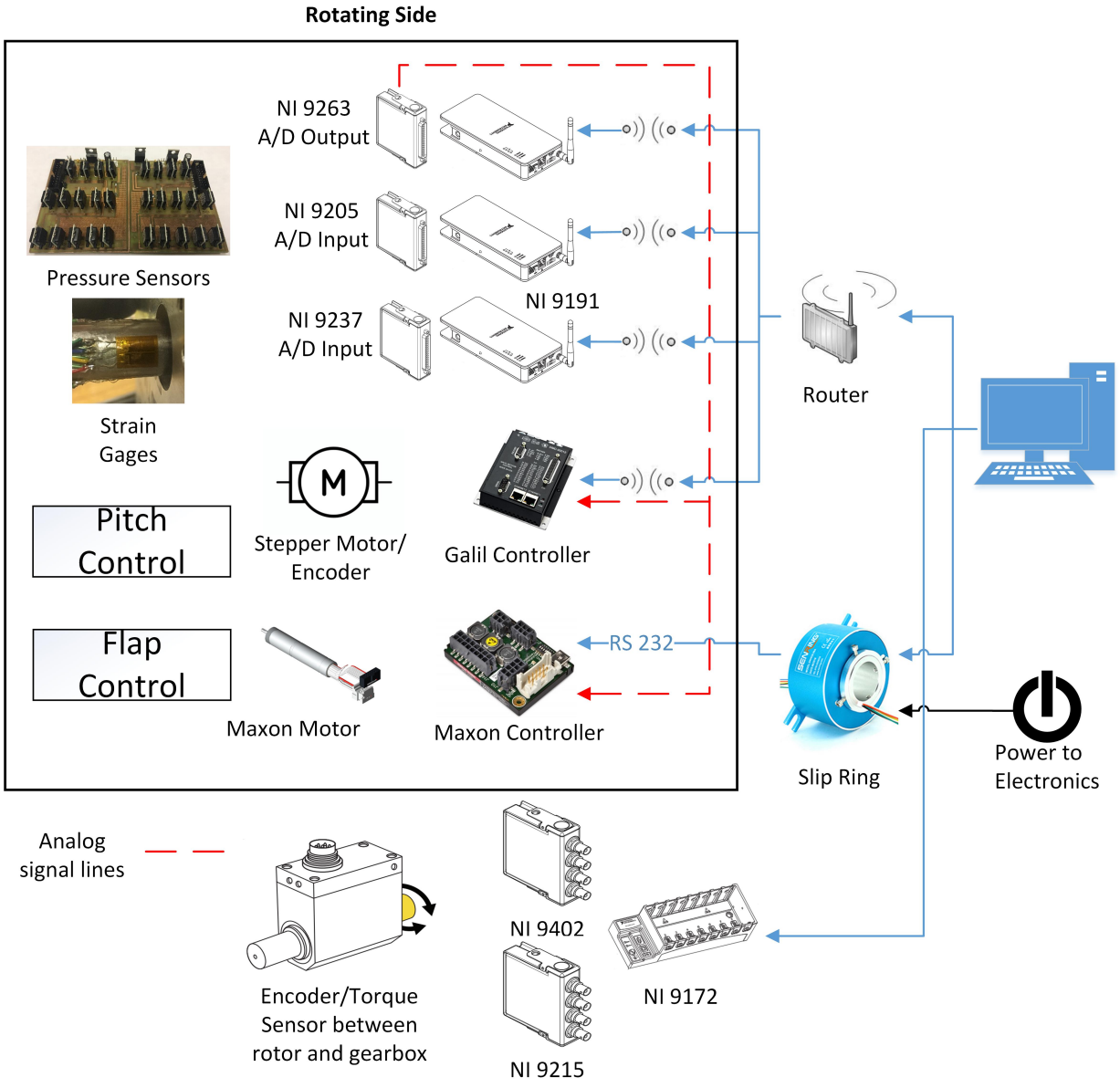


Figure 3.20: A map illustrating the data acquisition system and communication lines between systems for the wind turbine setup

Chapter 4

Experimental Procedure and Verification

Before presenting the experimental data, this Chapter describes the different experimental cases that were conducted. The experimental plan was split into two major campaigns. The first campaign was used to test the TEF in a 2D environment in a 0.61 m square wind tunnel. The second campaign was used to test the TEF on a full-scale 3.5 m diameter wind turbine in a controlled wind generation facility. A convergence study was also conducted for both campaigns to ensure that the phase-averaged data presented is reliable and the number of cycles is sufficient. A few key experimental parameters are also validated in this Chapter to increase confidence in the data collected. The OpenFast setup is presented next to highlight the important input parameters used in this model. The final section indicates how the wind turbine performance parameters were derived and calculated.

4.1 2D TEF Experimental Campaign

The two main objectives of this campaign were to characterize the lift coefficient on the S833 airfoil for different pitch and flap angles. The second objective was to discuss how a TEF could influence the development of dynamic stall on a 2D airfoil. To do so, the most optimal environment was in a 0.61 m square wind tunnel where the wind speed could be controlled accurately. The experimental setup for the wind tunnel is discussed in Section 3.2.2. This campaign consisted of two main subsections: airfoil characterization and dynamic airfoil oscillation.

4.1.1 Static Airfoil Characterization

Static airfoil characterization is an important first step as it creates a baseline matrix that is used for reference and to compare trends in data from different experimental campaigns. The coefficient of lift, C_L and the coefficient moment at the quarter chord, C_M are plotted against a wide range of pitch angles, α and for different flap angles, α_F. The measured α ranged from -5° to 50° in steps of 1° and α_F ranged from -20° to 20° in steps of 10°. This wide range of α in comparison to typical smaller angle range testing was chosen to replicate the same range that wind turbine blades experience [57, 133]. This experiment basically measures the static forces on the airfoil while α and α_F are constant. C_L and C_M presented in the results sections are determined by integrating the differential coefficient of pressure ($\Delta(\mathrm{C_p})$ expressed in Equation (2.6) along the chord of the airfoil from the 27 differential pressure transducers. Corrections due to wind tunnel blockage and sidewalls were calculated to be around 4% and 2% for $\mathrm{C_L}$ and $\mathrm{C_M}$, respectively [134, 135]. The wind speed of operation was set to 15 m/s resulting in a chord-based Reynolds number (Re) of 170×10^3. This velocity was based upon a compromise between a high Reynolds number and an achievable pitch frequency to obtain dynamic stall behavior on the airfoil at the desired reduced frequency k. For reference, this velocity corresponds to a radial location of r/R=0.35 on the wind turbine discussed in Section 3.3.

To study how the TEF influences C_L and C_M, it is much easier to plot these two variables against α_F instead of α. For this reason another set of experiments was conducted where α_F ranged from -40° to 60° in steps of 10° and α ranged from 0° to 25° in steps of 5°.

4.1.2 Dynamic Airfoil Oscillation

On a rotating wind turbine blade the effective angle of attack (α) varies as the blade rotates for a yawed turbine. Morote [136] and Burton *et al.* [7] modeled the α variation as a function of azimuthal position. Gallant and Johnson [57] compared those previous two models to experimental data on a 3.5 m HAWT. From the models and experiments it was found that the α variation is very similar to a sinusoidal path when the turbine is yawed. To simulate the dynamic forces on a yawed wind turbine blade, α will follow a sine path similar to that described in Gharali and Johnson [25] and shown in Equation (4.1) ($\alpha(\mathrm{t})$). The motion for the flap angle $\alpha_F(\mathrm{t})$ is described in Equation (4.2). To study the influence that the TEF has on the aerodynamic forces on the airfoil, the flap angle oscillation frequency, f_F, is the same as the pitch frequency, f_p.

$$\alpha(t) = \alpha_{mean} + \alpha_{amp} sin(2\pi f_p t) \tag{4.1}$$

$$\alpha_F(t) = \alpha_{amp,F} sin(2\pi f_F t + \phi_F) \tag{4.2}$$

where α_{amp} is the semi-amplitude for the pitch, α_{mean} is the mean geometric angle of attack of the airfoil, $\alpha_{amp,F}$ is the semi-amplitude of flap angle and ϕ_F is the phase shift with respect to the pitch motion. Unsteady flow behavior on pitching airfoils, with a frequency of f_p, is quantified by the reduced frequency, k, described in Equation (2.7). Corke and Thomas [21] suggested that the flow field is unsteady when $k \geq 0.05$ otherwise the unsteady effects are minor and can be neglected as long as the pitch amplitude is not too big. They also explained the reduced frequency by its analogy to a phase lag parameter where the fluid reaction lags behind the pitching motion due to inertial effects.

The system is operated at two different reduced frequencies, k, being 0.06 and 0.1 to represent the α variation at two different spanwise locations on a yawed wind turbine blade. The wind turbine blade element tested in this section was subsequently installed on a wind turbine with a 3.5 m diameter and a rotational speed of 200 rpm in the next section. On the turbine, the reduced frequency, k, will decrease when the blade element is moved away from the hub. A k value of 0.06 would occur closer to the blade tip while k of 0.1 would occur closer to the hub. To match the behavior of the airfoil between the wind turbine campaign and the 2D campaign, the reduced frequency has to be matched. The frequency of oscillation on the wind turbine (3.33 Hz) is too high to be matched in the wind tunnel due to motor limitations. To produce the same reduced frequency in the wind tunnel with a smaller actuation frequency the velocity had to be reduced thus changing the Reynolds number from the wind turbine to the 2D experiment. The free steam velocity for all test cases was set to 15 m/s (Re=170×10^3). Table 4.1 summarizes all the dynamic airfoil oscillation test cases. Test cases a and b represent a reduced frequency of 0.06 and 0.1, respectively. Test cases 1, 2, 3 and 4 represent a mean angle of attack of 0°, 10°, 20° and 25°, respectively, promoting onset and deep stall. Four different flap phases $\phi = 0\pi$, $\phi = \pi/2$, $\phi = \pi$ and $\phi = 3\pi/2$ are also tested.

To better understand the motion of the airfoil and flap with different flap phases, Figure 4.1 graphically depicts the kinematic motion along with airfoil/flap positions for case 1 where $\alpha_{mean} = 0°$. The four different flap phases are plotted along with the airfoil motion schematics at four instances in the cycle. The arrows on the airfoil motion schematic show the direction of motion of the airfoil and flap.

Table 4.1: Wind tunnel dynamic airfoil oscillation test cases

Test No	α_{mean} (°)	f_p (Hz)	k	f_F (Hz)	α_{amp} (°)	$\alpha_{amp,F}$ (°)	ϕ_F
Case 1a	0	1.61	0.06	[0, 1.61]	10	20	[0:0.5:1.5] π
Case 1b	0	2.68	0.1	[0, 2.68]	10	20	[0:0.5:1.5] π
Case 2a	10	1.61	0.06	[0, 1.61]	10	20	[0:0.5:1.5] π
Case 2b	10	2.68	0.1	[0, 2.68]	10	20	[0:0.5:1.5] π
Case 3a	20	1.61	0.06	[0, 1.61]	10	20	[0:0.5:1.5] π
Case 3b	20	2.68	0.1	[0, 2.68]	10	20	[0:0.5:1.5] π
Case 4	25	2.68	0.1	[0, 2.68]	5	20	[0:0.5:1.5] π

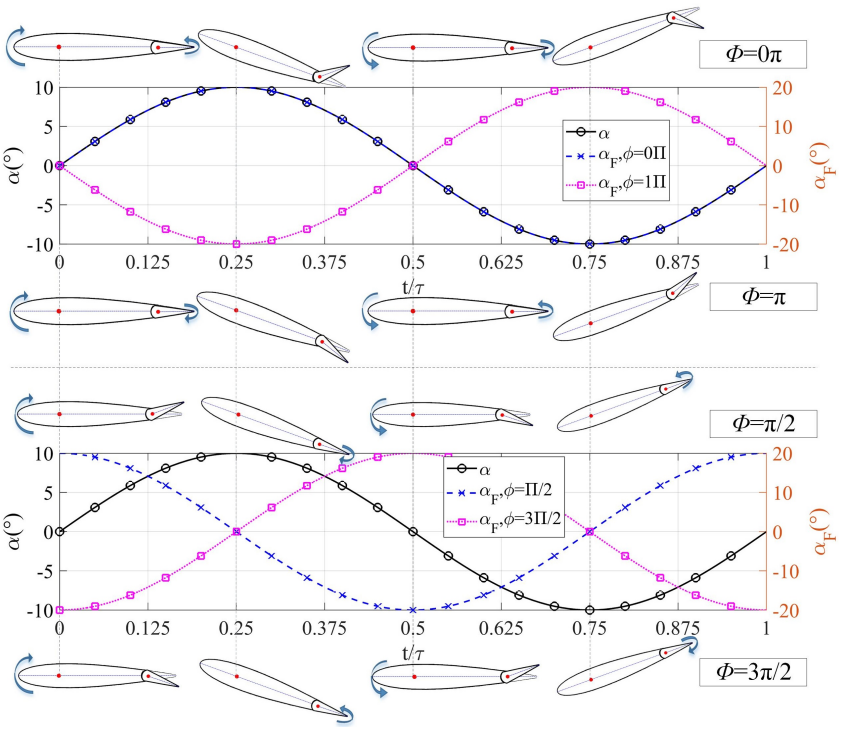


Figure 4.1: Kinematics of the airfoil and TEF motion for $\alpha_{mean} = 0°$ and different ϕ for case 1

4.2 Wind Turbine TEF Experimental Campaign

In this campaign the focus was testing the TEF on the 3.5 m diameter wind turbine (Section 3.3.2) in the controlled wind generation facility (Section 3.3.1). For all the experiments conducted in this campaign, three measurements were recorded at all times: surface pressure measurements, strain measurements at the blade root (in the flapwise and edgewise directions) and the torque produced from the rotor. The campaign is divided into three main sections: Base loading, dynamic flap cases and dynamic pitch cases.

4.2.1 Wind Turbine Base Loading

The first step of this campaign was to measure the base loading on the wind turbine rotor. These tests were crucial in understanding the aerodynamics of the wind turbine and in creating a rotor load baseline that will be used for reference. Two yaw angles, $\gamma = 0°$ and 30°, were tested to simulate steady and unsteady wind turbine aerodynamics. The unsteady case was used to determine the load fluctuations experienced by the rotor and used to determine the pitch and flap amplitude of oscillation for load alleviation for subsequent sections. Wind turbine base loading was split into two experimental sections where the pitch angle was varied first and then the flap angle was varied next. Table 4.2 illustrates the complete range of variables tested. The combination of all the variables presented in the tables were tested and that is equivalent to 48 and 120 tests for experiments 1 and 2, respectively. This large number of tests (168 in total) provided more detailed insight into wind turbine aerodynamics under a wide range of operating conditions. The three different tip speed ratios, λ, are equivalent to a free stream velocity, U_∞, of 10.5, 8.7 and 7.3 m/s, respectively. These λ values were chosen to study the wind turbine under a wide range of operating conditions and to match the experiments conducted by Gallant [137]. The flap angle, α_F, ranged from -20° to 20° in steps of 10° to study how the TEF influences the aerodynamic forces on the blade.

The radial location (r/R) of the surface pressure measurements and the TEF were changed from 0.82 to 0.66 to study how the TEF location impacts loading on the rotor. This also provides insight into how the normal force coefficient, C_n, changes for the two radial locations. Andersen *et al.* [91] numerically simulated a wind turbine with a TEF to find the optimal location to place the flap where it could reduce load fluctuation the most. They concluded that depending on whether the blades are stiff (rigid in structure) or elastic (allowing the blade to slightly deform under load) the TEF should be located at r/R=0.96 and r/R=0.73, respectively. Usually beyond 90% the tip losses would dominate.

This shows that the ideal location to place the TEF is dependent on the elasticity of the blade and in this case, the blade is elastic. Thus placing the TEF around r/R=0.73 is ideal and so is what was done here.

Table 4.2: Wind turbine base loading test cases

Experiment No	λ	$\beta(^\circ)$	$\alpha_F(^\circ)$	$\gamma(^\circ)$	TEF r/R Location
1	[3.5, 4.2, 5]	[0, 3, 6, 9]	0	[0, 30]	[0.82, 0.66]
2	[3.5, 4.2, 5]	[3, 6]	[-20:10:20]	[0, 30]	[0.82, 0.66]

4.2.2 Dynamic Flap Cases

One of the main objectives of this research is to decrease the load variation on the wind turbine blades that could be due to many things including rotor yaw misalignment. For this reason and for all the experiments conducted in this section, γ was set only to 30°; this way the wind turbine was operating in unsteady conditions. Only the lowest λ (highest free stream velocity) was used in this set of experiments because it produced the largest load fluctuations on the turbine. A β of 6° was tested because it is the analytical design condition and a β of 3° because it produced higher rotor load fluctuations and the blade was not entirely stalled. The flap motion in this set of experiments follows a sinusoidal wave expressed in Equation (4.2). The flap oscillation frequency, f_F, was set to 3.33 Hz (based on rotor speed of 200 rpm). The flap phase, ϕ_{Flap}, is the phase offset between the flap motion and the azimuth position, ψ, of the blade. When $\phi_{Flap} = 0\pi$ or in-phase the load fluctuations theoretically should decrease and the opposite is true for $\phi_{Flap} = \pi$ or out-of-phase. The flap motion semi-amplitude, $\alpha_{amp,F}$, was set to 10° at first to test small oscillation of the flap. The amplitude was then increased to 20°, the design condition of the flap motion. Finally, the amplitude was increased to 27°, the maximum amplitude allowed by the motor controller. This amplitude was tested last because it was operating outside the design conditions and it was feared that this test condition might damage the flap actuation system. After all the test cases were conducted, there was no damage on the flap actuation system; for further details, see Chapter 8. The different test cases that were conducted are listed in Table 4.3. A total of 7 distinct cases were conducted to show how the TEF could potentially reduce load fluctuation under different operating conditions.

Table 4.3: Test matrix for dynamic motion for flap cases

Case	λ	$\beta(^\circ)$	$\alpha_{amp,F}(^\circ)$	$\gamma(^\circ)$	TEF r/R Location	ϕ_{Flap}
1	3.5	[3, 6]	10	30	0.82	[0:0.5:1.5] π
2	3.5	[3, 6]	20	30	[0.82, 0.66]	[0:0.5:1.5] π
3	3.5	3	28	30	0.66	[0:0.5:1.5] π

4.2.3 Dynamic Pitch Cases

In this section the flap was fixed but the blade pitch was oscillating in an attempt to reduce rotor load fluctuations. The pitch actuation, $\beta(t)$, followed the motion prescribed in Equation (4.3) where β_{mean} is the mean pitch of the blade and β_{amp} is the semi-amplitude of the motion which was set to 5° for all cases. The pitch phase, ϕ_{Pitch}, is the phase offset between the pitch motion and the azimuth position, ψ, of the blade. The frequency of pitch oscillation f_B was set to 3.33 Hz, which is similar to the experimental plan outlined in the previous section for the flap oscillation. Table 4.4 illustrates the different experiments that were conducted. A combination of four distinct tests were carried out to show how the pitch system could control load fluctuations on the rotor blade.

$$\beta(t) = \beta_{mean} + \beta_{amp} sin(2\pi f_\beta t + \phi_\beta) \tag{4.3}$$

Table 4.4: Test matrix for dynamic motion for pitch cases

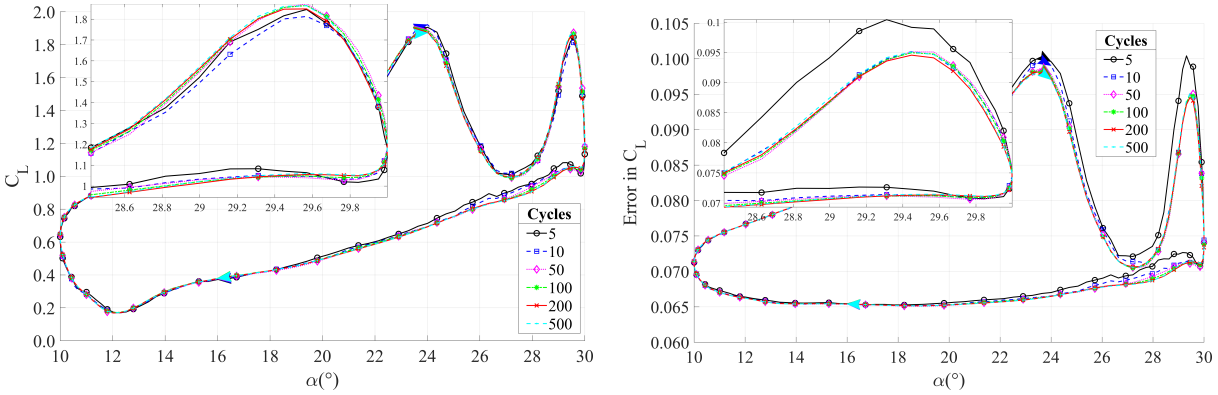
Case	λ	$\beta_{mean}(^\circ)$	$\beta_{amp}(^\circ)$	$\gamma(^\circ)$	TEF r/R Location	ϕ_{Pitch}
1	3.5	[3, 6]	5	30	[0.82, 0.66]	[0:0.5:1.5] π

4.3 Convergence Study

A convergence study is imperative to ensure the phase-averaged data presented is reliable and the number of cycles is sufficient. First, this study was conducted on the 2D TEF experimental campaign and then on the wind turbine experimental campaign.

4.3.1 2D TEF Convergence Study

The results presented in Figure 4.2 show the convergence study on the phase-averaged C_L and uncertainty in C_L for case 2b (refer to Table 4.1) where k=0.1 and the airfoil is undergoing deep stall for the FixedFlap case. In this convergence study the phase-averaged data is presented for 5, 10, 50, 100, 200 and 500 cycles. The loop for 5 cycles is presented to show that even at a low cycle number the results are representative of the converged results. This shows repeatability and instills high confidence in the results. The phase-averaged data starts to converge at 100 cycles. This shows that the use of 200 cycles is sufficient to accurately determine the phase-averaged data for C_L and uncertainty in C_L. The uncertainty gets smaller as the number of cycles increases until it converges after 200 cycles.



(a) Coefficient of lift

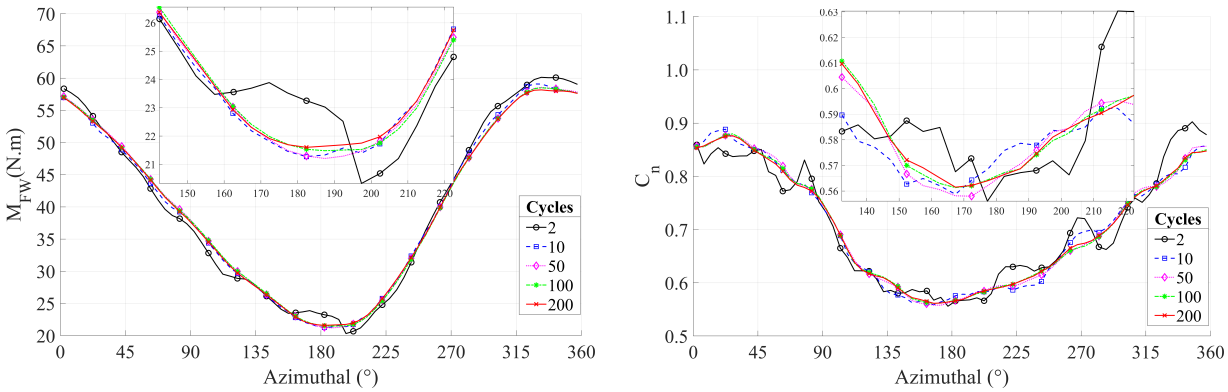
(b) Uncertainty in Lift

Figure 4.2: Coefficient of lift (C_L) and uncertainty for different cycle counts for case 1b where k=0.1 and $\alpha_{mean} = 20°$ while the flap was fixed. The data is magnified between $\alpha = 28°$ and $\alpha = 30°$.

4.3.2 Wind Turbine Convergence Study

Similar to the convergence study done in the previous campaign, the same study was done to the wind turbine campaign on C_n and M_{FW}, the two crucial variables. Figure 4.3 shows the convergence study for cycle counts 2, 10, 50, 100 and 200 where $\lambda = 3.5$, $\beta = 6°$ and $\gamma = 30°$. These parameters were chosen because the turbine would be operating at design pitch angle at the highest wind speed and when the turbine is yawed. This operating condition produces the highest load fluctuations on the turbine. A low cycle count of

2 is presented to show that even at such a low number of cycles the data is very much representative of the converged data. This is also indicative that the method used to collect and bin the two variables is reliable. It is seen that M_{FW} converged much faster than C_n due to the inherit uncertainty and noise in the surface pressure data. The data converged after 100 cycles indicating that having a larger cycle count should not change the results. For all the experiments done in the wind turbine campaign, 1000 cycles were collected for each case to eliminate any uncertainty in the data.



(a) Flapwise Moment (out of plane)

(b) C_n at r/R=0.82

Figure 4.3: Wind Turbine convergence study on (a) C_n and (b) M_{FW} for various cycle counts when $\lambda = 3.5$, $\beta = 6°$ and $\gamma = 30°$. The data is magnified around $\Psi = 180°$.

4.4 Experimental Validation

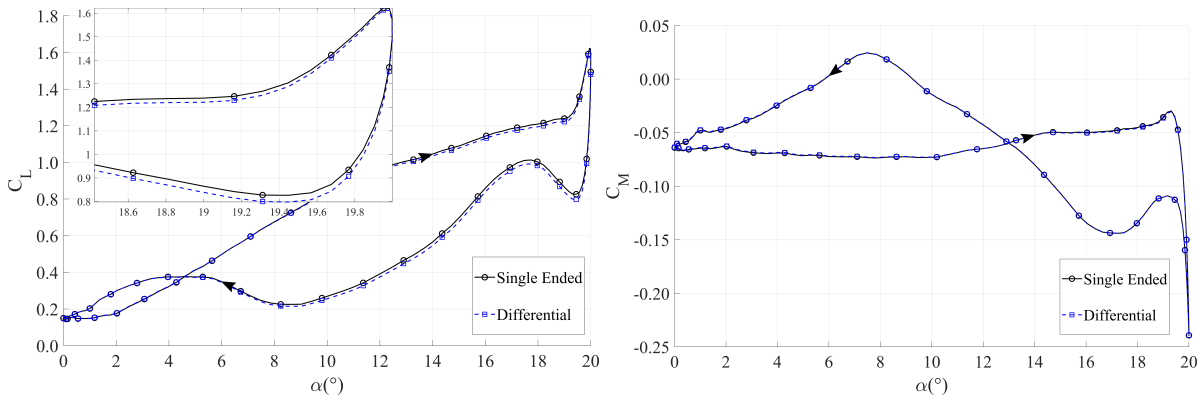
It is important to validate the measurement techniques that were used in this experimental setup. Initially the difference between differential pressure measurements and single-ended pressure measurements is studied to quantify any possible discrepancy between the two techniques. Second, a small experiment was conducted to correlate the azimuthal angle on the wind turbine to the sensor output data.

4.4.1 Differential Pressure Measurement Validation

In order to validate the approach of using a differential pressure measurement to determine C_L and C_M on a cambered airfoil, independent single-ended pressure measurements of the

suction and pressure sides were compared with the differential measurements. The tubing inside the airfoil was modified to conduct single-ended pressure measurement and then modified again to conduct differential pressure measurements. The validation was done for case 2b where k=0.1 and $\alpha_{mean} = 10°$. This case was chosen because of its higher α_{mean} and high reduced frequency that produced the highest cyclic loading.

Figure 4.4 compares the C_L and C_M cycles while the airfoil is operating in the dynamic stall regime using two approaches: single-ended surface pressure measurements and differential surface pressure measurements. The difference between the two cases is very small in magnitude while the patterns are exactly the same. The difference in C_L (Figure 4.4a) between the two cases is negligible for lower α but increases for higher α. This is because, in the differential pressure measurement, the pressure force from each tap angle is projected to the global y-coordinate using an average angle of the suction and pressure tap. On the other hand, single-ended pressure measurements use each tap angle to project the pressure force to the global y-coordinate producing more accurate results. As for the C_M (Figure 4.4b) calculations, there was no need to project the tap angle to the global y-coordinate. For this reason the C_M values in both cases are very similar and independent of α. The maximum difference is 4% for C_L and less than 1% for C_M. The difference in ΔC_p (that produced both coefficients) between the two cases was also studied and the largest difference was found to be concentrated at the LE and when $\alpha = 20°$. This is because the curvature of the airfoil is most significant at the LE and α is high. These differences are minor and do not significantly change the details including how the LEV is interpreted and studied. Since this study focuses on how the TEF influences surface pressure and the development of the LEV, these constant errors and offsets will be present in all cases and will not affect the comparison. In conclusion, the two methods are both valid because the discrepancy between the two cases is small and could be ignored and because the pattern in C_L and C_M is not influenced by differential pressure measurement.



(a) C_L versus α for both pressure measurement techniques

(b) C_M versus α for both pressure measurement techniques

Figure 4.4: Coefficient of lift (C_L) and moment (C_M) versus α for case 2b (k=0.1 and $\alpha_{mean} = 10°$) to compare single-ended pressure measurements to differential pressure measurements. A plot inset is used to magnify the data around $\alpha = 19°$ for C_L .

When using the differential pressure measurement technique (plotting only ΔC_p) it would be impossible to know with 100% certainty if the formation of any sort of aerodynamic structure is occurring on the pressure side or suction side. The structure of interest in this study is the formation of a leading edge vortex (LEV) on the suction side of the airfoil. Most of the references in the literature review such as Leishman [22] and McCroskey *et al.* [67] show that the LEV occurs on the suction side of the airfoil and no such vortices occur on the pressure side. To insure that the LEV is occurring on the suction side on this airfoil and in this experimental setup, C_p data from the single-ended measurements are plotted in Figure 4.5. The C_p contour plots prove that the LEV is only occurring on the suction side while no fluid structure is impacting the pressure side. From here on forth, ΔC_p and not C_p is plotted and more discussion about surface pressure patterns are presented in Chapter 5.

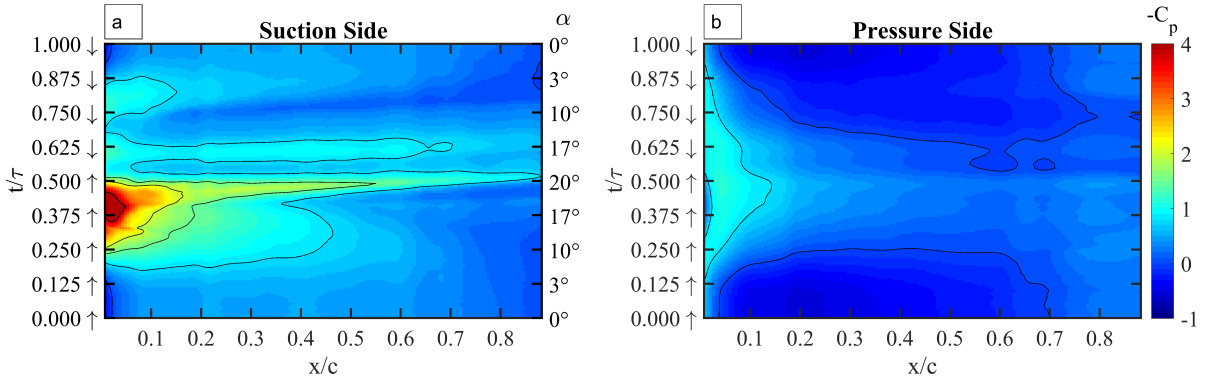


Figure 4.5: Contours of ΔC_p versus x/c versus α for (a) the suction side and for (b) the pressure side for the single-ended pressure measurement technique. This test is conducted for case 2b (k=0.1 and $\alpha_{mean} = 10°$). The iso-lines on the plot represent constant ΔC_p values=[0, 0.8, 1.5, 2, 4, 5].

4.4.2 Azimuth Angle Validation

To validate the correlation between the pressure measurements that produce C_n and azimuthal position, a validation test was conducted. An air compressor and a nozzle were used to create an air jet at r/R=0.82 and $\Psi = 0°$ (when the blade is vertically downwards or at the 6 o'clock position). Data was then collected from the on-board sensors just like any other experimental test while the turbine was operating at design speed with the wind tunnel off. The pressure from the pressure tap closest to the leading edge was analyzed and is plotted in Figure 4.6 against azimuth position using 1° bins. The pressure shows that there is a distinct spike at $\Psi = 0°$ with a width of less than 2° proving that the data acquisition of the pressure and rotor encoder readings is synchronized. This small experiment provides confidence in the data acquisition system and synchronization. No additional experimental validation was needed for the blade root moment measurements because it could be validated from any of the data sets collected. The edgewise blade root moment is dominated by gravitational forces as the blade rotates around its axis. The maximum and minimum edgewise root bending moment has to occur when the blade is at $\Psi = 90°$ and $\Psi = 180°$ or at the 3 and 9 o'clock position. For example, looking at Figure 6.7e the maximum and minimum edgewise moment occur at $\Psi = 90°$ and $\Psi = 180°$, respectively, as predicted and validating the moment measurements against azimuthal position.

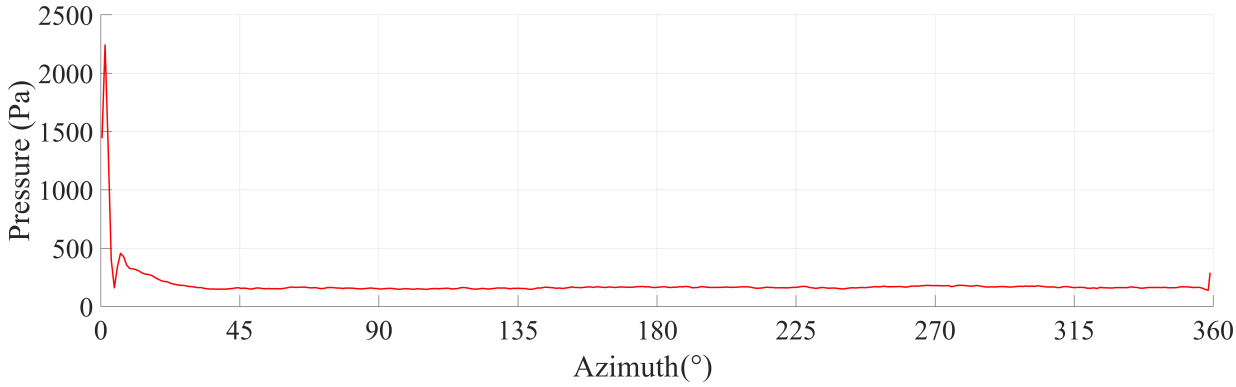


Figure 4.6: Surface pressure at x/c=0.01 versus azimuth when an air jet was created at r/R=0.82 and $\Psi = 0°$ while the turbine is operating at the design rotational speed with the wind tunnel off

4.4.3 Step Response

A step response experiment is conducted by sending an impulse unit step function to the input while studying the response of the output. The inputs in this case are the pitch and flap systems while the outputs are C_n at r/R=0.82 and M_FW. By sending a unit step function to the pitch and flap controllers while studying the time behavior of C_n and M_FW, important characteristics could be measured such as the blade time response. The experiment was conducted while the turbine is operating at the design tip speed ratio of $\lambda = 4.2$ and blade pitch angle of $\beta = 6°$. The magnitude of the pitch and flap unit step functions were $\pm 5°$ and $\pm 20°$, respectively. A unit step actuation in pitch is presented first in Figure 4.7 where the response of ΔC_n and ΔM_{FW} are plotted against time. The time response between actuation and a change in output was found be 0.013 sec or 15° of blade rotation for ΔC_n and 0.035 sec or 42° of blade rotation for ΔM_{FW}. This time delay between actuation and sensor output could be due to the finite time needed by the flow around the blade to adjust caused by a change in blade pitch. The time delay could also be due to the limitations in the experimental setup system. The plots shows that the output from ΔC_n has a faster response time than ΔM_{FW} by almost a factor of two. This was expected because the pressure transducers connected to the surface pressure taps instantly measure a change in pressure when the blade pitch changes. On the other hand, the strain gages at the blade root measure the strain only after the load change occurs due to the pitch change. These set of plots also show that the instrumentation used in this set of experiments is reliable and the time response is relatively quick.

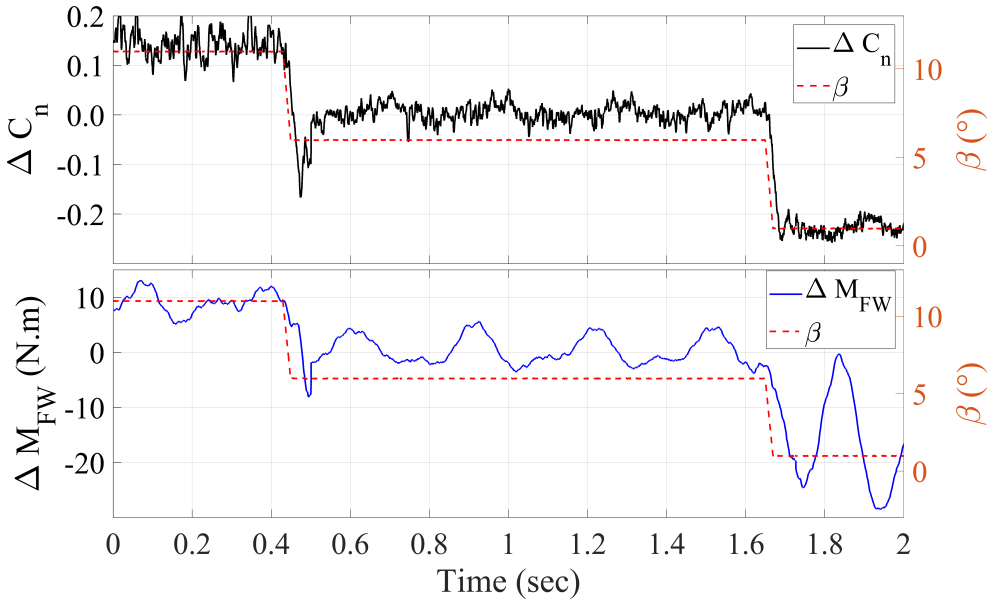


Figure 4.7: Pitch step response for C_n and M_{FW}

The same set of plots are presented again in Figure 4.8 but for flap actuation. The time response between actuation and a change in output was found to be 0.015 sec for ΔC_n similar to what was found for the pitch case. As for ΔM_{FW}, the time response is 0.055 sec or 66° of blade rotation. This is significant because the local change in surface pressure around the TEF section requires a finite time to be transferred and sensed at the blade root where the strain gages are located. Berg *et al.* [103] also observed a similar time delay and attributed it to the time taken for the airflow around the local blade section to adjust to blade geometry change.

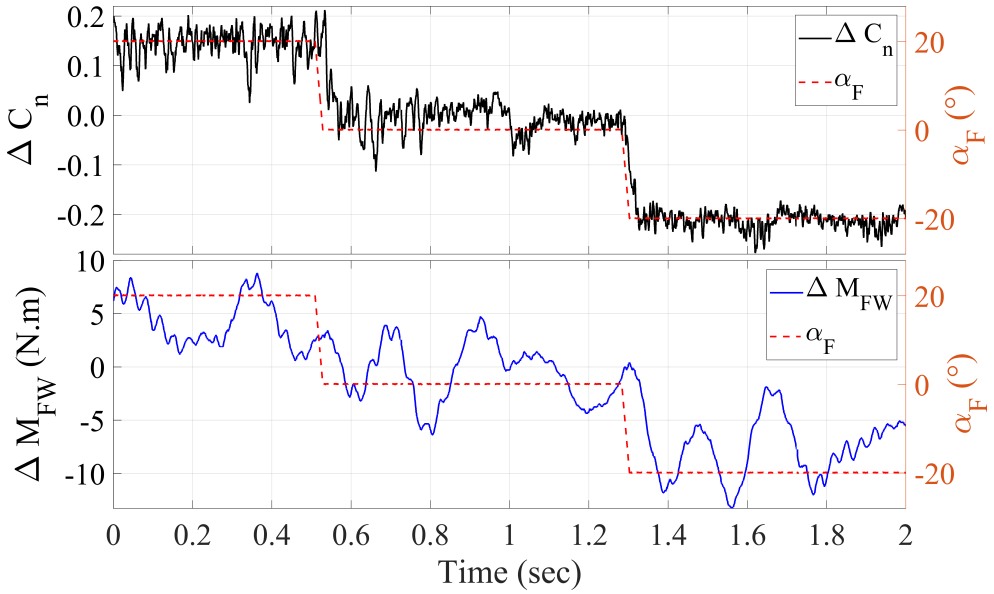


Figure 4.8: Flap step response for C_n and M_{FW}

4.5 OpenFast Setup

The OpenFast design code, introduced in Section 2.3.4, requires many input parameters such as airfoil data, blade geometry and environmental conditions setting to run properly. It is very crucial and important to set the input parameters to resemble the physical model as much as possible because the accuracy of the predicted output variables is only as good as the input parameters used. Through meticulous analysis, the physical properties of the turbine were found and imported into the OpenFast model. The input files are split into three main sections: airfoil parameters, blade properties and running conditions. It is important to note that no input from the wind turbine field measurements was used in any way or form to modify or correct the OpenFast model.

4.5.1 Airfoil Parameters

The airfoil parameter data are one of the more important yet challenging input files to obtain. The lift, moment and drag coefficients for a wide range of angle of attack (-180° to 180°) and for the appropriate Reynolds number must be identified and loaded into the model. The S833 airfoil lift and moment coefficient curves were obtained from the 2D

experiments that are described in Section 5.1.1. The drag coefficient was obtained from XFoil and experimental sources. Before the airfoil coefficients were loaded into OpenFast, AirfoilPrep, which was introduced in Section 2.3.3, was used to modify the lift curves independent of airfoil geometry based on a model developed by Du and Selig [60]. This modification was required to account for the 3D flow effects that the blade experiences on a rotating system. Depending on the r/R location, AirfoilPrep increases C_L and delays stall. This tool also extends the airfoil coefficients from the limited α range available to the entire $\pm 180°$ range required by OpenFast. The lift predictions provided by the model should then accurately resemble experimental data because the same blade segment used on the full-scale wind turbine was also used to obtain the 2D lift curves that were loaded into OpenFast.

Damiani *et al.* [63] suggested that to better simulate unsteady aerodynamics on the turbine model, a few important parameters must be tuned based on 2D dynamic stall hysteresis loops for the same airfoil. To this end, the 2D dynamic stall experimental measurements presented in Section 5.2 were used to tune the OpenFast parameters responsible for simulating dynamic stall. The tuned unsteady aerodynamic parameters and the input file used in OpenFast are documented in Appendix B.5. The results from this unsteady dynamic model were then compared to 2D experimental data and are summarized in Section 5.3. This study is unique because 2D dynamic stall data for the same airfoil and condition were available. In other scenarios, dynamic stall data may not be available for the desired airfoil and operating conditions. Hence, tuning these OpenFast parameters becomes more difficult and that leads to less accurate predictions. This makes OpenFast very reliant on 2D experimental data to produce accurate results.

4.5.2 Blade Properties

There are two input files used to characterize the blades in OpenFast. The first file controls the blade twist, chord and airfoil profile ID used at each blade span section. The second input file controls blade mass density and blade stiffness in the edgewise and flapwise direction along the blade span. The accuracy of the blade mass in the input file is directly linked to the accuracy of the blade edgewise moment prediction by OpenFast. The second file also controls the blade structural damping ratio and blade harmonics and these are used by the code to resolve the interactions between the excitation frequencies and the natural frequencies of the blades. These latter parameters were obtained and extracted from the physical blade and loaded into OpenFast.

As discussed, the turbine being tested is single-bladed with two cylindrical counterweights. The cylindrical rods were also modeled in OpenFast to create a more realistic

model and enhancing the accuracy of the predictions. The drag coefficient of a cylinder with an infinite aspect ratio and the cylinder mass density were loaded into OpenFast to resemble the counterweights. The drag coefficient of the cylinders and airfoil directly controlled the accuracy of the rotor torque predictions. A simple test was conducted in the model and wind tunnel where the wind speed was zero but the turbine was rotating at the desired rotational speed. The results were then compared and the torque measurements from the model and experiment were found to very well match. This indicates that the drag coefficient was set correctly in the model.

4.5.3 Running Conditions

Physical dimensions of the turbine such as rotor diameter, hub diameter, nacelle height and other factors were loaded into the OpenFast input files. Three different wind speeds were simulated to resemble the three tip speed ratios tested in the wind tunnel. The same set of blade pitch angles and yaw angles tested experimentally were also simulated in OpenFast. These parameters were relatively easy to change and modify. One of the strengths of OpenFast is in its capability of simulating a turbine with multiple structural degrees of freedom (DOF). This is particularly important for utility-scale aeroelastic turbines because as the blades bend and deform under load, the aerodynamics changes, influencing the overall blade loading.

Another important reason to enable structural DOF is when there is a potential for the excitation frequencies to coincide with the natural frequencies of the turbine. In this particular experimental setup, blade deflection is not significant due to the short length of the blades (1.4 m). The natural frequency of the blades was measured to be 5.1 Hz and that does not coincide with the excitation of the turbine which is 3.33 Hz (rotating at 200 rpm). For these two reasons, enabling DOF in OpenFast does not provide any additional information and does not change the model prediction. To confirm this hypothesis, two cases were simulated, one with DOF and the other completely rigid. The results were identical indicating no impact from enabling DOF. Running a simulation with DOF requires up to 15 times more computing power. To this end all the simulations presented here are with no DOF. During the entire length of the experimental campaign, no excessive vibration on the blades and turbine occurred. This also shows that the natural frequency of the turbine did not coincide with the excitation frequency.

4.6 Wind Turbine Performance Measurements

This section explains how all the wind turbine performance measurements presented in the results chapters were obtained. The torque, blade moment and normal force coefficient measurements are discussed along with some important analysis that was carried out on th data. An in-depth uncertainty analysis is also presented for the three variables.

4.6.1 Torque Measurements

The torque measurements were obtained from the Futek TRS 605 torque sensor [131] placed in the nacelle as discussed in Section 3.3.2. The torque sensor was independently calibrated to ensure that the analog reading was accurate (more details could be found in Appendix C.3). While only one counterweight rod at the 3 o'clock position was installed on the parked turbine, weights were added at the tip to simulate a torque increase. After calibration, the linear regression was found to be exactly 1 indicating that the relationship is linear. A detailed analysis of the bias uncertainty may be found in Appendix D.2 and was calculated to be ± 0.6 N.m or $\pm 0.3\%$ full-scale. The precision uncertainty was found to be insignificant due to the large number of samples collected (typically higher than 4000 data points).

Since the wind turbine experimental rig only has 1 aerodynamic blade and 2 counterweights, it was not able to produce more power than the resistance of the system. As a result, the rotor required input from the generator in the nacelle to achieve the desired tip speed ratio. The counterweights also produced significant drag while the rotor was rotating at 200 rpm. To clearly show the contribution of the aerodynamic blade towards the torque generated, ΔTorque was determined by taking the difference between the torque generated with no incoming wind speed and the torque generated when the wind speed is set to the desired speed.

4.6.2 Blade Moment Measurements

The blade moment was measured using two sets of strain gages (as discussed in Section 3.3.3) located at r/R=0.14 or the root of the blade. The strain gages measure the blade moment in the edgewise and flapwise direction simultaneously. To correlate the strain measurements to a useful unit, in this case N.m, a calibration was done. A series of weights were added at the tip of the blade to create multiple data points and this was done in both directions. The linear regression in this case was also 1 indicating that the strain gages are

linear for the operational range. During calibration it was noticed that the measurements in both directions are influenced by each other and that effect was caused by how the strain gages were installed as per Section 3.3.3. Thus, based on extra calibration tests and data analysis, this influence between the gages was removed. Based on the uncertainty calculations presented in Appendix D.3, the total uncertainty was found to be ±0.5% of the measured reading and not of full-scale.

Strain measurements have been extensively used in the literature, as was discussed previously in Section 2.4. Cooperman *et al.* [138] reviewed a range of sensors and found that strain gages can accurately measure the blade loading but only do so after the load occurs. So there exists a phase lag between aerodynamic load occurrence and an excitation of the strain sensors. This effect was previously noted in the step response section (Section 4.4.3) and is seen in all the results obtained.

4.6.3 C_n Measurements

The normal force coefficient, C_n, is the most interesting and complex measurement in this study when compared to the other two. It is unusual and impressive to have such a high density of pressure taps (54 taps) on a small airfoil chord of 178 mm including those on the flap. This concentration facilitated excellent resolution and accurate determination of the normal force coefficient. As mentioned in the experimental setup (Section 3.1.3), there was an extra pressure transducer in the blade that was not connected to any of the pressure taps. During the experiments conducted, the signal from this transducer was measured to study how the influence of acceleration and rotation affect the measurements. Based on the results obtained, the mentioned effects were negligible and could be ignored. The first step in obtaining C_n was to convert the differential pressure into coefficient pressure, C_p, using Equation (4.4) where W is the local velocity vector shown in Figure 2.7. If the turbine is not yawed and is operating in steady conditions, then W can be calculated using Equation (2.13). On the other hand, when the turbine is yawed, U_{wind} (equal to $U_2 = U_\infty(1-a)$) changes with azimuth position as depicted in Figure 2.10. Based on Equations (2.13) and the velocity triangle illustrated in Figure 2.10, W was calculated for all the azimuth positions and is plotted in Figure 4.9 for different tip speed ratios, λ. The average axial induction factor, a, was calculated based on the power output measured by the torque sensor. The solid lines in the plot are based on calculations while the dotted line were obtained from the OpenFast model. The maximum difference between any pair of lines on the graph is less than 0.6% indicating that the calculated velocity distribution is reliable. The error is mainly due to the incorrect axial induction factor assumed. In reality the axial induction factor changes with azimuth and in the current calculation it is

assumed to be constant. This observed discrepancy is small because the axial induction factor is small due to the single-bladed turbine.

$$C_p = \frac{\Delta P}{\frac{1}{2}\rho_\infty W^2} \tag{4.4}$$

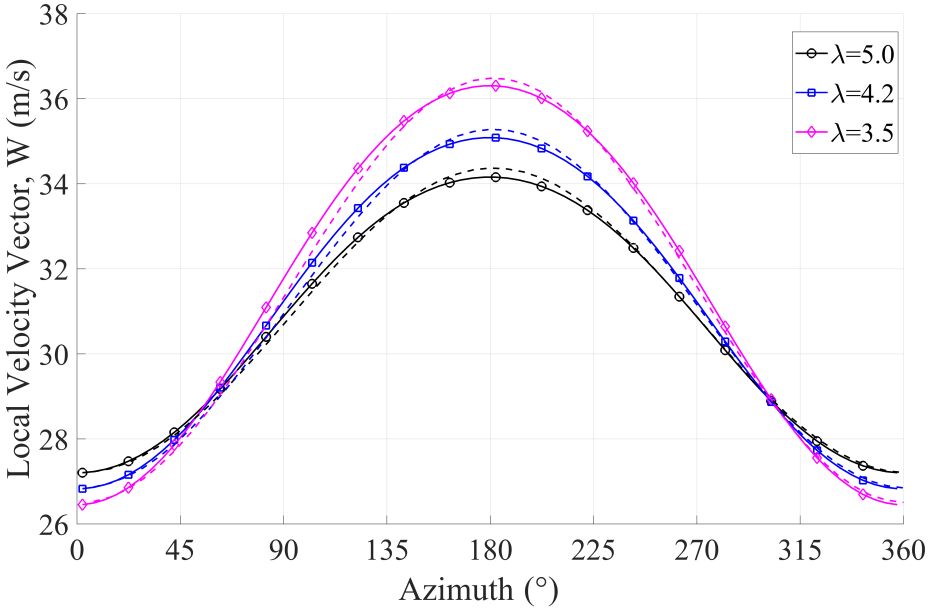


Figure 4.9: Local velocity vector, W, versus azimuth for different λ values when $\gamma = 30°$. Solid lines are based on calculations while the dotted lines were obtained from the OpenFast model.

Finally, after C_p was obtained, C_n was calculated using Equation (4.5). The variable C_n was used in this study and not the more common variable C_L because the geometric angle of attack of the blade was not known and not measured in this case. The uncertainty in C_n measurement was calculated and is evaluated in Appendix D.4. Based on the results obtained from the different campaigns, the uncertainty in C_n was found to be $\pm$ 5% which was consistent for all the cases tested. This uncertainty is based mostly on the bias error as the precision error is negligible due to the large number of samples obtained (more than 4000).

$$C_n = \int_{x/c=0}^{x/c=1} \Delta C_p(x)dx \approx \sum_{n=1}^{N=27} C_p(x)\delta x \tag{4.5}$$

4.6.4 Power Spectral Density (PSD)

The load fluctuations during normal operation of a wind turbine are often cyclic with a frequency of 1P (once per revolution) as discussed in Section 2.2.3. By looking at the data in the time domain or phase average it would be rather difficult to perceive and quantify the cyclic nature of the load fluctuation. To quantify this fluctuation the power spectral density (PSD) is often used in the academic community [88, 96, 98, 99, 139]. When the PSD is used, the reduction in fatigue loads is revealed in the frequency domain for the different load alleviation techniques. The PSD data may also reveal the system harmonics to identify the natural frequency. The PSD is calculated from the time series data to describe the power distribution in the frequency domain.

Chapter 5

2D TEF Experimental Campaign

After describing the experimental setup and the experimental plan in the previous two chapters, the results from the 2D TEF experimental campaign are discussed here in detail. By reviewing the previous studies found in literature in Section 2.4.1, it was concluded that more research was aimed at rotorcraft engineering and less research has focused solely on at wind turbine blades. A few important areas have also not been fully addressed such as the following needs. More experimental data is needed regarding dynamic stall behavior on wind turbine specific airfoils and cambered airfoils with a TEF. Additional analysis and information regarding dynamic stall on an airfoil with a flapping TEF are needed. Data on a cambered airfoil with a TEF pitching past 25° are very limited and more reliable experimental results are required. This chapter builds on prior studies and tries to address some of these issues by conducting experiments on the S833 cambered airfoil by NREL that is designed for small-scale wind turbines [105].

It was found that dynamic stall produces load fluctuations that are cyclic and repetitive in nature. The cyclic loading experienced by airfoils could be characterized by the minimum/maximum load value difference and the hysteresis in the cycle. The main aim of the TEF in this Chapter is to reduce the difference between the minimum/maximum load cycle and reduce the hysteresis cycle while eliminating the negative damping. Ideally, if the cyclic loading was eliminated, the load magnitude on the blade would be quasi-steady. To decrease the cyclic loading caused by dynamic stall, it is important to control the development of the LEV and eliminate or decrease the detrimental hysteresis lift and moment cycle.

This chapter is split into four main sections. Static results are presented first to study how the TEF influences airfoil coefficients in steady conditions. The second section studies

the hysteresis loop occurring due to dynamic stall and how the TEF motion influences this loop. This is followed by a comparison of the experimental dynamic stall cycle to the OpenFast model predictions. Finally, the main conclusions are presented.

5.1 Static Results [1, 2, 3]

The static results are split into two main subsections. The first section characterizes the influence of the TEF on the airfoil coefficients when the flap angle is in the linear range of $\pm 20°$. The second section studies the aerodynamic of the airfoil when the flap angle exceeds the linear range. The experimental plan for this section and the different cases tested are described in Section 4.1.1.

5.1.1 Static Airfoil Characterization

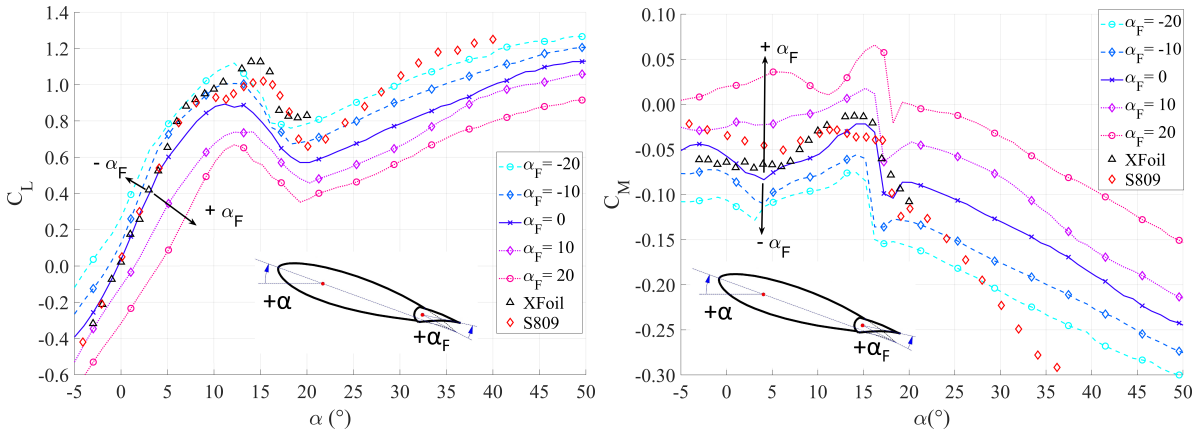
Figures 5.1a and 5.1b show the lift coefficient (C_L) and moment coefficient (C_M) at the quarter chord versus α, respectively. C_M is defined as positive for nose-up pitching moment and negative for nose-down pitching moment as per Figure 3.1. For comparison, results obtained from XFoil [52] with α ranging from -3° to 20° for a clean airfoil ($N_{crit} = 9$) with no flap at the same Re are also plotted on both figures. In Figure 5.1a the experimental values for $\alpha_F = 0°$ match the XFoil results for $\alpha < 5°$. The measurements and the model start to deviate slightly when α is greater than 5° with XFoil predicting higher values. This is possibly due to the discretization of the $-\Delta(C_p)$ measurements obtained from the pressure taps along the chord, the flap/airfoil intersection line on the physical model or incorrect assumptions in XFoil. Although the magnitude does not match, the trend in the data is similar near the stall point and at zero lift. Experimental C_L and C_M measurement data of a S809 airfoil from Ramsay *et al.* [135] are plotted in Figure 5.1. The data for S809 matches well with S833 for $\alpha < 10°$, but diverges for larger values of α. This occurs because Re for the S809 is 750×10^3 while Re for the S833 is 170×10^3. Reported experimental data for the S833 airfoil could not be found in the literature and therefore this data is a

[1] Presented at the WindTech International Conference 2017 Boulder, Colorado, USA. Oral presentation title: In-blade Load Sensing and Control on 3D Printed Wind Turbine Blades Using Trailing Edge Flaps.

[2] Presented at the TORQUE Conference 2018 Milan, Italy. Poster title: In-blade Load Sensing on 3D Printed Wind Turbine Blades Using Trailing Edge Flaps.

[3] Published by Samara, F., & Johnson, D. A. (2018). In-blade Load Sensing on 3D Printed Wind Turbine Blades Using Trailing Edge Flaps. Journal of Physics: Conference Series, 1037, 052023. doi: 10.1088/1742-6596/1037/5/052023

an important contribution. Data from Ramsay *et al.* [135] on the S809 airfoil has been included since it represents the closest match because the airfoils are somewhat similar and data includes larger values of α. This data is shown to compare the dynamics of stall and how C_L increases for $\alpha > 20°$ when the airfoil is stalled. As the flap angle, α_F, decreases (increasing the camber of the airfoil), C_L increases while C_M decreases. The opposite is true for increasing the flap angle and decreasing airfoil camber. For example, at α_F=-20° C_L increased by 23% while for α_F=+20° C_L decreased by 28% based on α_F=0° and α=11°.



(a) Coefficient of lift

(b) Coefficient of moment

Figure 5.1: Measured coefficient of a) lift (C_L) and b) moment (C_M) versus α for several α_F. Only every fourth data point is marked on the plot for clarity. The experimental data is compared to XFoil [52] predictions for a clean airfoil ($\alpha_F = 0$). Experimental C_L and C_M for the S809 airfoil at a higher Re are also plotted from reference [135].

Contour plots of $-\Delta C_p$ for x/c locations versus α at α_F of -20° and 20° are shown in Figures 5.2a and 5.2b. The contour plots are a matrix of 27 averaged pressure points in the x-direction by 55 different α angles in the y-direction with each point being an average of 4000 data points. For some instances of α_F and α angles, $-\Delta C_p$ is plotted in Figure 5.2c. The contour plots clearly show the stall angle occurring when the $-\Delta C_p$ peak close to the LE (0<x/c<0.1) is sharply reduced. From Figures 5.1 and 5.2, the stall angle is 16°, 17° and 18° for $\alpha_F = -20°$, $\alpha_F = 0°$ and $\alpha_F = 20°$ respectively. The flap angle, α_F, thus has influence over the stall angle of the airfoil as the camber of the airfoil changes. The change in α_F increases and decreases the $-\Delta C_p$ peak magnitude in pre-stall conditions thus increasing and decreasing C_L. Changing α_F from $-20°$ to 20° changes the sign of $-\Delta C_p$ values close to the TE from positive to negative as indicated by the marked white dashed line in the figure. This indicates that the suction side of the airfoil has both negative and

positive pressure that causes pressure imbalance on the airfoil, leading to a much larger C_M values. Just after the stall point ($\alpha = 17°$), the $-\Delta C_p$ peak close to the LE ($0<x/c<0.1$) is dramatically reduced but $-\Delta C_p$ over the entire chord is slightly increased (this is more clearly seen in Figure 5.2c). This indicates a movement of the pressure center from the LE to the mid-chord region. The pressure center movement leads to a dramatic change in C_M that was also seen in Figure 5.1b.

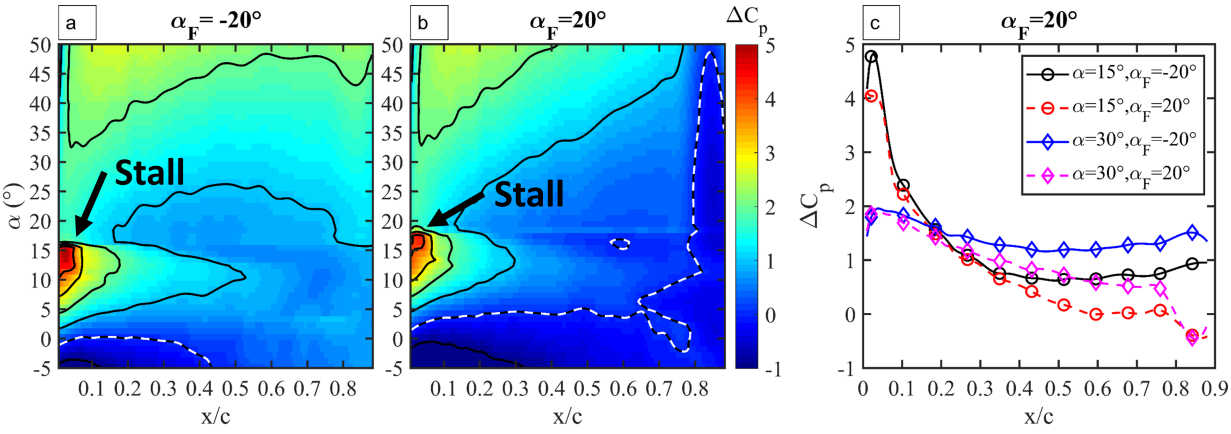


Figure 5.2: Contours of $-\Delta C_p$ versus x/c versus α. **a)** $\alpha_F = -20°$ and **b)** $\alpha_F = 20°$. The location of stall is marked for clarity. The iso-lines on the plot represent constant $-\Delta C_p$ values=[-1 0 1 2 3 4]. The iso-line of $-\Delta C_p$=0 is marked in white dashes. **c)** $-\Delta C_p$ versus x/c for different α_F and α cases.

5.1.2 High Flap Angle Characterization

Instead of typically plotting C_L or C_M versus α for the static cases, these coefficients are plotted against α_F in Figure 5.3. Having α_F on the x-axis clearly shows how the TEF influences the lift and moment for a constant α. To better understand the C_L curves it is important to study the contour plots in Figure 5.4 where $-\Delta C_p$ is plotted against the chord on the x-axis and α on the y-axis ranging from -40° to 60°. Six individual α_F cases are plotted ranging from 0° to 25° in steps of 5°. It is imperative then to draw conclusions from both figures (Figures 5.3 and 5.4) simultaneously as they complement each other.

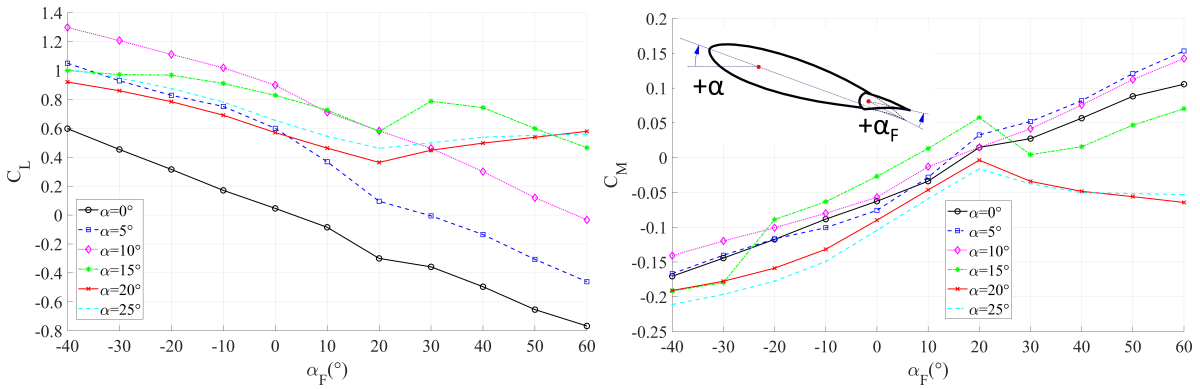
Focusing on Figure 5.3a, as α_F increases (decreasing airfoil camber), C_L decreases as long as $\alpha \leq 10°$ where the flow is attached. When $\alpha = 15°$ the flow over the airfoil seems to be in and out of stall depending on α_F because C_L is greater than the $\alpha = 10°$ case for three α_F values and smaller for the others. In Figure 5.4.d ($\alpha = 15°$) when $\alpha_F = -40°$ or

$-30°$, the flow over the airfoil is completely stalled reducing C_L because the $-\Delta C_p$ peak at the LE is greatly diminished. When $-20 \leq \alpha_F \leq 20°$ the flow is partially attached as evident by the high $-\Delta C_p$ concentration at the LE but not completely attached because C_L is smaller than when $\alpha = 10°$. Lastly, for $\alpha_F \geq 30°$ the flow is completely attached as evident by an increase in $-\Delta C_p$ at x/c=0.3 and C_L is greater than when $\alpha = 10°$. For $\alpha = 20°$ and $25°$, the trends are similar and could be explained in a similar way. For $\alpha_F \leq 20°$ the flow looks to be completely separated because C_L is reduced and the $-\Delta C_p$ peak at the LE is also greatly diminished as seen in Figures 5.4.e and 5.4.f for all α_F values. When $\alpha_F > 20°$ C_L increases instead of decreasing as α_F increases. This could be attributed to the fact that as the flap angle becomes more positive the flow starts to partially reattach increasing $-\Delta C_p$ along the entire length of the chord as seen in the contour plots.

The TEF can significantly influence C_L as long as the airfoil is not stalled but even in stalled cases some influence is still present. For example, C_L changed from 1.3 to 0 for $\alpha = 10°$ by just changing the flap angle. The slope of C_L change ($d(C_L)/d(\alpha_F)$) is then $0.13/10°$ as long as the airfoil is not stalled. This linear slope is similar to what was found by Abbott and Von Doenhoff [49] for most cases. The TEF was capable of reattaching the flow over the airfoil for the $\alpha = 15°$ case and partially reattaching the flow for the $\alpha = 20°$ and $25°$ cases. The TEF is also capable of producing much higher C_L values than by just changing α. This was also observed by Abbott and Greenberg [65] for a different airfoil but they also found that C_D increases significantly for positive flap angles only. The maximum C_L value for any α with a clean airfoil ($\alpha_F = 0°$) is 0.9 but the highest C_L value with the TEF is 1.3 thus 0.4 greater than with no TEF. It is important to note that even though the airfoil is stalled ($\alpha = 20°$or $25°$), the TEF still has significant impact on C_L.

In Figure 5.3b as α_F increases (decreasing airfoil camber) C_M increases except for select cases. From the Figure it is seen that the flap angle has a large impact on the C_M values. This effect can be better explained by investigating the $-\Delta C_p$ contour plots in Figure 5.4. The contour plots show that as α_F changes, the center of pressure of $-\Delta C_p$ moves along the airfoil chord. C_M tends to be more sensitive to the pressure center location than the magnitude of pressure on the airfoil surface. For example, when $-\Delta C_p$ is concentrated at the LE this causes the airfoil to pitch nose-up making C_M positive. In contrast, when $-\Delta C_p$ is concentrated at the TE that causes the airfoil to pitch nose-down making C_M negative. Typically for non-stalled airfoils, positive α_F values decrease $-\Delta C_p$ at the TE and the airfoil is in pitch nose-up leading to a positive C_M. The opposite is also true; negative α_F values increase $-\Delta C_p$ at the TE and the airfoil is in pitch nose-down leading to a negative C_M. When $\alpha = 20°$ and $25°$, the slope in the C_M curve changes at $\alpha_F = 20°$ because $-\Delta C_p$ increases close to the TE as seen in the contour plots and this is attributed

to partial flow reattachment. Changing α_F has a larger impact on C_M when compared to the change in α because the center of pressure does not change with α as was also observed in Abbott and Von Doenhoff [49]. In conclusion, the TEF influence over C_L and C_M does not change whether the blade is stalled or not.



(a) Coefficient of lift versus α_F

(b) Coefficient of moment versus α_F

Figure 5.3: Measured coefficient of lift (C_L) and moment (C_M) versus α_F for several α values

In Figures 5.4a-c the TEF not only changes $-\Delta C_p$ close to the TE but also at the LE as well. This indicates how the TEF influences the airflow over the entire chord and not just where the flap is located. In Figure 5.4.d it can be seen that the flow is separated for $\alpha_F = -40°$ and $-30°$ because the $-\Delta C_p$ peak at the LE is absent. Looking at the same plot, at $\alpha_F = 30°$ there seems to be an increase in $-\Delta C_p$ close to the LE and that increased the C_L value in Figure 5.3a. In Figures 5.4.e-f the trend is similar in both cases and the flow is separated for all α_F. Once the airfoil is stalled, changing the flap angle will not lead to a significant effect on $-\Delta C_p$ close to the LE but still could impact $-\Delta C_p$ in the TE region. The iso-lines in all the plots help show how the TEF impacts $-\Delta C_p$. The iso-line of $-\Delta C_p$=0 is marked in white dashes to better show negative $-\Delta C_p$ regions. The data and patterns in the contour plots are similar to the results obtained by Jacobs and Pinkerton [66] on a RAF 30 airfoil.

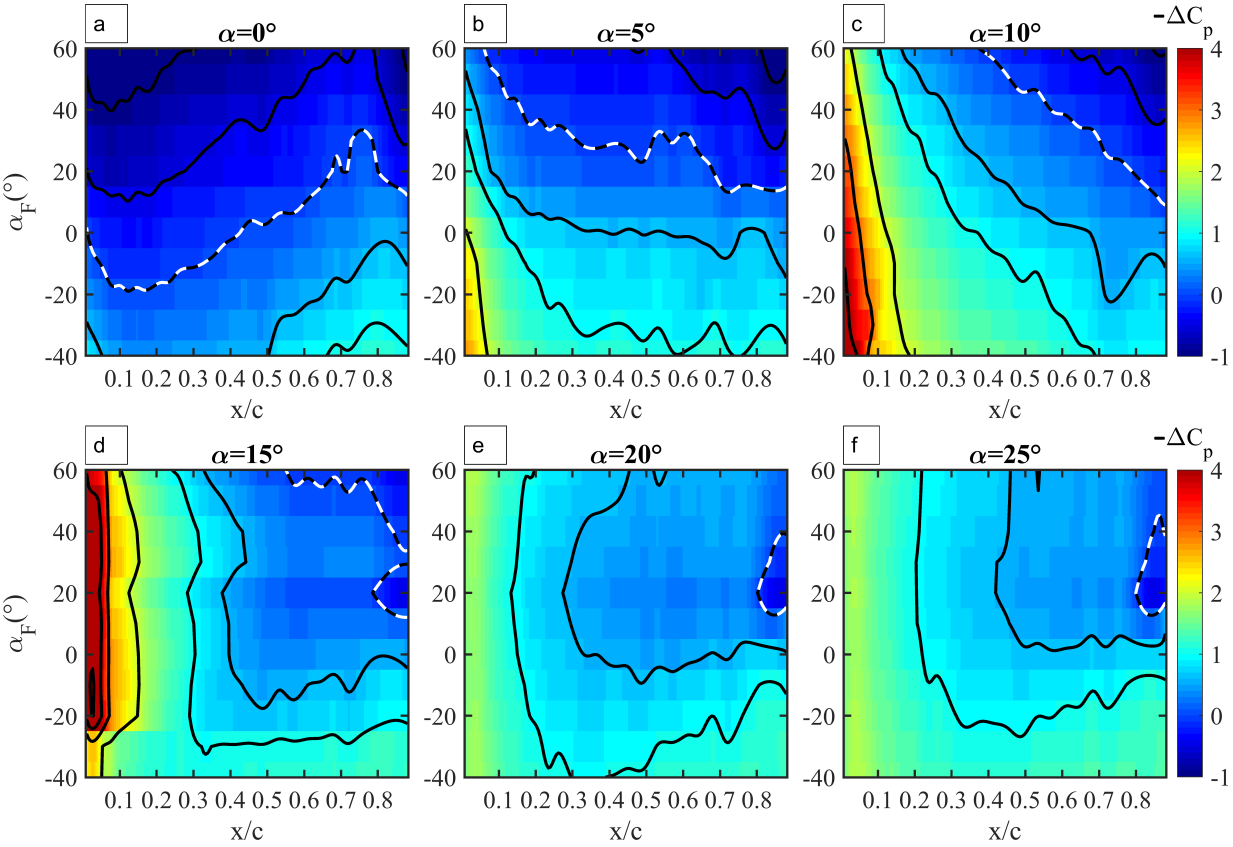


Figure 5.4: Static contours of $-\Delta C_p$ versus x/c versus α_F. a) $\alpha = 0°$, b) $\alpha = 5°$, c) $\alpha = 10°$, d) $\alpha = 15°$, e) $\alpha = 20°$ and f) $\alpha = 25°$. The iso-lines on the plot represent constant $-\Delta C_p$ values=[-1, -0.5, 0, 0.5, 1, 2, 3, 4]. The iso-line of ΔC_p=0 is marked in white dashes.

5.2 Dynamic Pitching [4, 5, 6]

In this section, the dynamic pitching results are presented. The motion of the airfoil and flap are governed by Equations (4.1) and 4.2 while the study parameters are listed in Table

[4]Presented at the CSME Congress 2019 London, Ontario, Canada. Oral presentation title: Dynamic stall on an S833 airfoil with a trailing edge flap.

[5]Presented at the Wind Energy Science International Conference 2019, Cork, Ireland. Oral presentation title: Dynamic stall on an S833 airfoil with a trailing edge flap.

[6]Published by Samara, F., & Johnson, D. A. (2020). Dynamic Stall on Pitching Cambered Airfoil with Phase Offset Trailing Edge Flap. AIAA Journal, (Accepted date: 12-Feb-2020), 1–25

4.1 found in Section 4.1.2. The four cases that were conducted are presented in increasing order of the value of α_{mean} which is equal to 0°, 10°, 20° and 25°.

5.2.1 Case 1 $\alpha_{mean} = 0°$

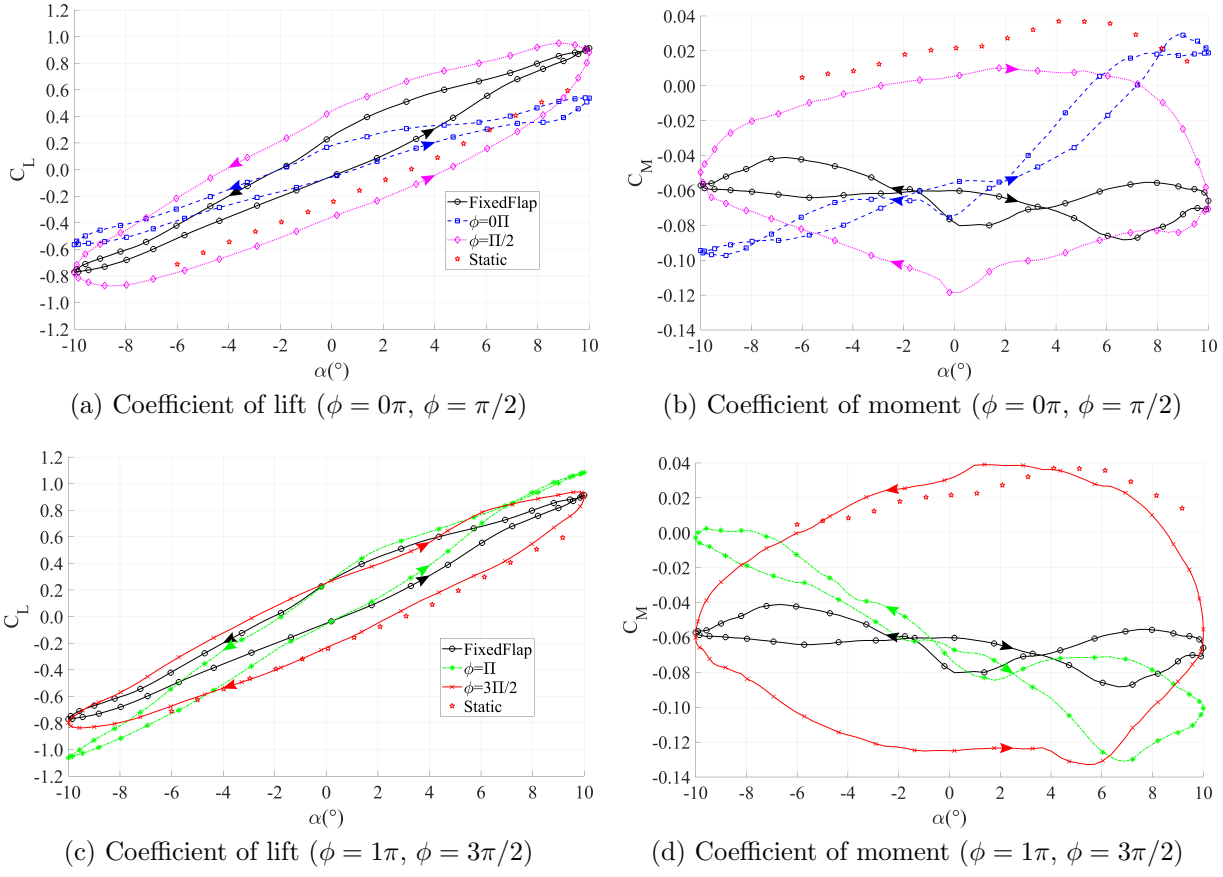
The figures presented in this section belong to cases 1a and 1b where k= 0.06 and 0.1 respectively with $\alpha_{mean} = 0°$. Approximately 600 cycles were collected for each scenario and each cycle was divided into 160 bins based on cycle period. C_L and C_M were then calculated for each of the 160 bins in the cycle. The C_L averaged cycles are presented in two plots, Figures 5.5a and 5.5c, and each plot contains a FixedFlap loop, static airfoil data, and 2 flap phases (first: $\phi = 0\pi$ and $\pi/2$, second: $\phi = \pi$ and $3\pi/2$). The arrows on the plot indicate the direction of airfoil motion,either upstroke or downstroke. The FixedFlap data represents a pitching clean airfoil where the flap is not moving relative to the airfoil. The four phases shown represent the phase shift between the pitch and the flap motion denoted by ϕ in Equation (4.2). The C_M averaged cycles are also presented in a similar fashion in Figures 5.5b and 5.5d.

Looking at Figures 5.5a and 5.5c for case 1a, the dynamic FixedFlap results can be compared to the measured static airfoil C_L marked in red stars (★). The hysteresis cycle due to dynamic motion produces higher C_L values in comparison to the static case as expected. The largest change in C_L for $\phi = 0\pi$ or π, when compared to the FixedFlap case, is found to occur when α is at its minimum (-10°) and maximum (10°). When $\phi = 0\pi$ or π and $\alpha = 0°$ then $\alpha_F = 0°$ producing similar conditions to the FixedFlap case, thus making all three curves align at that α value. When $\phi = 0\pi$ and $\alpha = 10°$ then $\alpha_F = 20°$ and the camber is decreased thus reducing C_L. For the same curve when $\alpha = -10°$ then $\alpha_F = -20°$ and the camber is increased thus increasing C_L. The opposite is true when $\phi = \pi$, C_L increases at $\alpha = 10°$ and decreases at $\alpha = -10°$ compared to the FixedFlap curve. When $\phi = \pi/2$ or $3\pi/2$, C_L is equal to the FixedFlap at $\alpha = 10°$ and $-10°$ due to the fact that $\alpha_F = 0°$ at these points. For $\phi = \pi/2$ and $\alpha = 0°$ during the upstroke motion $\alpha_F = 20°$ decreasing C_L but during downstroke $\alpha_F = -20°$ increasing C_L. This indicates that when $\phi = \pi/2$ or $3\pi/2$, the greatest change in C_L occurs when α is near the mean angle of attack. Based on the four ϕ cases presented, it was conclude that the TEF is capable of changing C_L at any point in the cycle and the variable ϕ determines that location of change. The airfoil and flap kinematics are illustrated in Figure 4.1.

The hysteresis cycle of C_L is counter-clockwise (ccw) for the majority of ϕ values indicating that during downstroke, the lift is greater than the upstroke for the same α. The ccw cycle is due to the nature of dynamic motion and a characteristic of the airfoil. For

example, Raiola *et al.* [69] tested a symmetric airfoil, the NACA 0015, under similar conditions and their results showed that the hysteresis cycle was clockwise. The NACA 0015 is a symmetric airfoil while the S833 airfoil has camber and is thicker. On the other hand, for dynamic cases of cambered airfoils, the hysteresis cycle is counter-clockwise, similar to the results presented in [31, 46, 140]. The counter-clockwise hysteresis cycle could be attributed to a vortex being generated at the LE at higher α that increases lift during the downstroke. The most interesting case is when $\phi = 3\pi/2$, where the direction of the hysteresis cycle is now clockwise (cw). This occurs because when $\alpha = 0°$ and during the upstroke motion, $\alpha_F = -20°$ increasing C_L but during the downstroke $\alpha_F = 20°$ decreasing C_L. So during the downstroke, C_L is smaller than the upstroke just for $\phi = 3\pi/2$.

The TEF also has a significant influence on C_M as seen in Figures 5.5b and 5.5d for the different ϕ cases. For the FixedFlap case, the variation in C_M is the smallest when compared to other flap phases. Any motion of the TEF at any ϕ will lead to either an increase in C_M hysteresis or an increase in minimum/maximum C_M peaks. In most cases, C_M is much smaller than the measured static case, indicating that the airfoil is in constant nose-down pitching moment. For the FixedFlap, $\phi = 0\pi$ and $\phi = 1\pi$ cases, there are some cw and ccw loops occurring in the C_M hysteresis curve. The cw loops in the cases mentioned occupy a small portion of the cycle but nonetheless they lead to negative damping. These small cw loops do not resemble flutter because there is no dynamic stall in this case. Dynamic stall only occurs when the airfoil pitching exceeds the static stall α by few degrees [20, 21], so in this case ($\alpha_{mean} = 0°$) there should be no dynamic stall. The entirety of the $\phi = \pi/2$ loop is cw, producing negative damping that introduces the possibility of aeroelastic problems but may never materialize due to the lack of dynamic stall. On the other hand, for $\phi = 3\pi/2$ the entire loop is ccw, eliminating any possibility of flutter or aeroelastic problems due to the lack of negative damping.



(a) Coefficient of lift ($\phi = 0\pi$, $\phi = \pi/2$)

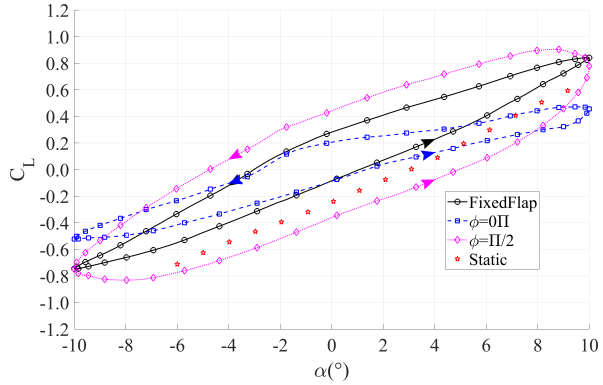
(b) Coefficient of moment ($\phi = 0\pi$, $\phi = \pi/2$)

(c) Coefficient of lift ($\phi = 1\pi$, $\phi = 3\pi/2$)

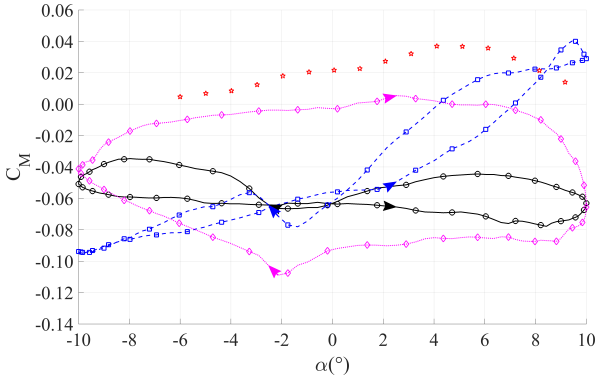
(d) Coefficient of moment ($\phi = 1\pi$, $\phi = 3\pi/2$)

Figure 5.5: Coefficient of lift (C_L), and moment (C_M) versus α for different flap phases (ϕ) for case 1a where k=0.06 and $\alpha_{mean} = 0°$. Only every fourth data point is marked on the plot for clarity.

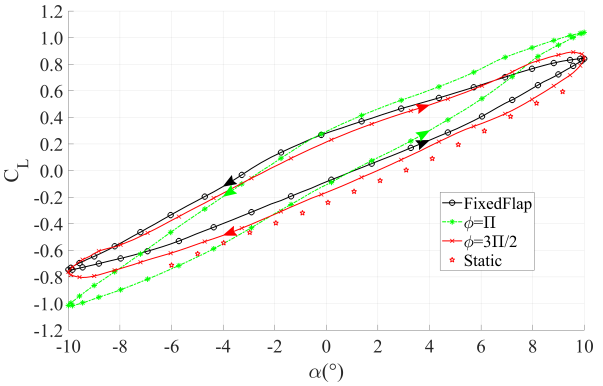
Figure 5.6 shows C_L and C_M for case 1b where k increased from 0.06 to 0.1 and $\alpha_{mean} = 0°$. Since dynamic stall did not occur when $\alpha_{mean} = 0°$ then increasing k does not create a large change in the C_L and C_M cycles. The major difference between case 1a and 1b (increasing k from 0.06 to 0.1) is that the difference between the upstroke and downstroke is wider and C_L and C_M increase by about 6% in extreme values. These differences are due only to an increase in k as all other variables are the same as the previous case. This concludes that k has great influence over the aerodynamic behavior of the flow around the airfoil and that is in alignment with what is presented in Leishman [22] and Masdari *et al.*[31].



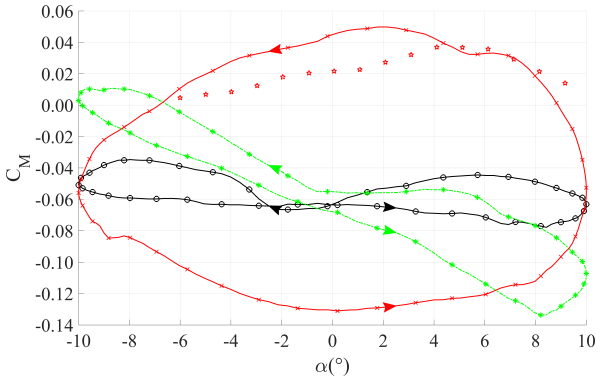
(a) Coefficient of lift ($\phi = 0\pi$, $\phi = \pi/2$)



(b) Coefficient of moment ($\phi = 0\pi$, $\phi = \pi/2$)



(c) Coefficient of lift ($\phi = 1\pi$, $\phi = 3\pi/2$)



(d) Coefficient of moment ($\phi = 1\pi$, $\phi = 3\pi/2$)

Figure 5.6: Coefficient of lift (C_L), and moment (C_M) versus α for different flap phases (ϕ) for case 1b where k=0.1 and $\alpha_{mean} = 0°$. Only every fourth data point is marked on the plot for clarity.

A contour plot of $-\Delta C_p$ is displayed in Figure 5.7 where the chord length is plotted on the x-axis and the period of the averaged cycle is plotted on the y-axis for case 1b (k=0.1 and $\alpha_{mean} = 0°$). The plots correspond to a matrix of 27 differential pressure transducers representing the airfoil chord by 160 bins representing 1 complete period. Each point in the matrix is the average of 4000 data points. The variable t/τ is a dimensionless time unit used to represent a cycle (τ is the period of the cycle). Arrows along the y-axis indicate upstroke or downstroke in the cycle. t/τ could also be associated with α as shown on the right y-axis and the relationship is plotted in Figure 5.7d for $\phi = \pi$. The contour plot is not symmetric about t/τ=0.5 and the $-\Delta C_p$ peak is shifted slightly up. This shift is likely due to the nature of having unsteady flow while pitching. The unsteady flow can create a

phase lag between the fluid reaction and the pitching motion [20]. This $-\Delta C_p$ peak shift leads to higher lift values during the downstroke when compared to the upstroke. This results in the ccw direction of the C_L hysteresis cycle mentioned in Figures 5.5 and 5.6. Comparing $\phi = 0\pi$ (Figure 5.7b) to the FixedFlap case (Figure 5.7a), the $-\Delta C_p$ values are smaller and the constant $-\Delta C_p$ iso-lines are shifted towards the LE. When $t/\tau = 0.5$ and $\phi = 0\pi$ then α_F would be 20°, decreasing airfoil camber and reducing the $-\Delta C_p$ to negative values close to the TE as indicated by the white dashed in the figure. This indicates that there is negative $-\Delta C_p$ (suction side pressure greater than pressure side) around the TEF area thus leading to a nose-up pitching moment as indicated in Figures 5.5 and 5.6. Now comparing $\phi = 1\pi$ (Figure 5.7c) to the FixedFlap case (Figure 5.7a) the $-\Delta C_p$ values are greater and the constant $-\Delta C_p$ iso-lines are shifted away from the LE. Focusing on $t/\tau = 0.5$ again, when $\phi = 1\pi$, then $\alpha_F = -20°$. This increases $-\Delta C_p$ values close to the TE and leads to a nose-down pitching moment.

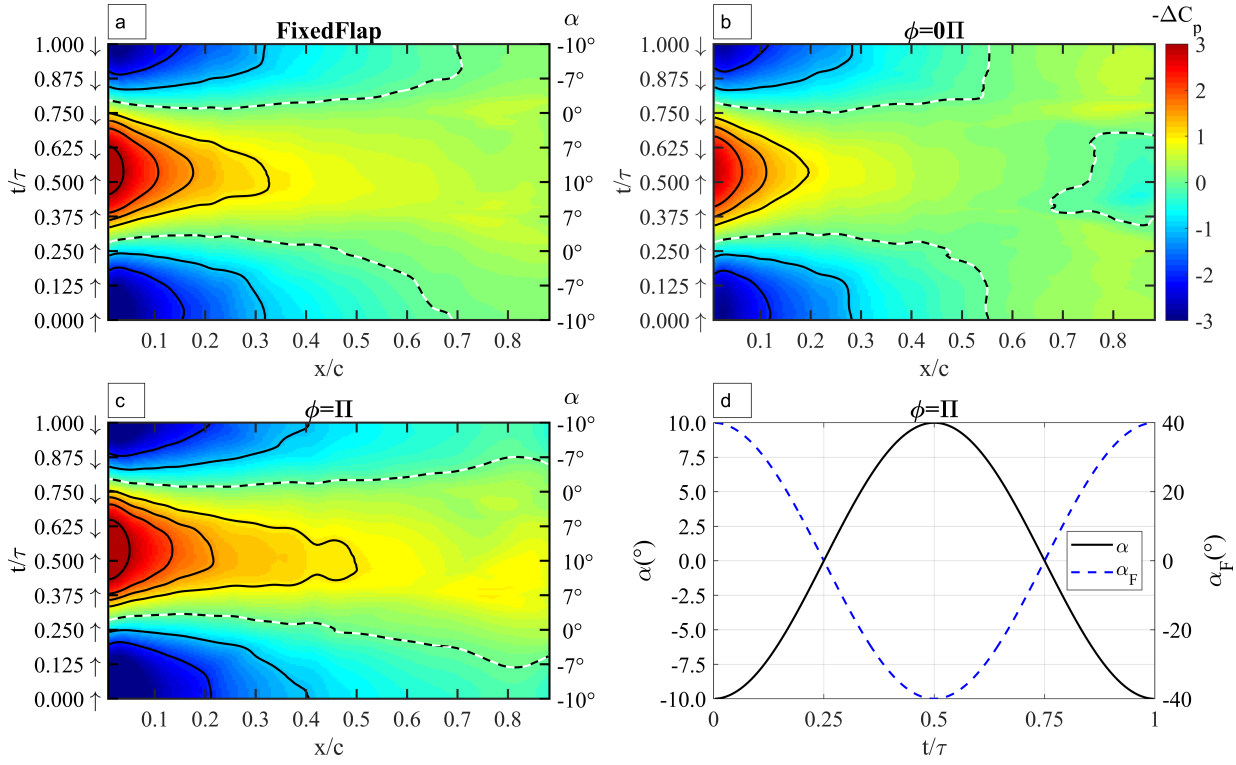


Figure 5.7: Contours of $-\Delta C_p$ versus x/c versus α for case 1b (k=0.1 and $\alpha_{mean} = 0°$). **a)**, **b)**, and **c)** represent FixedFlap, $\phi = 0\pi$, and $\phi = 1\pi$ respectively. The angle of attack (α) is shown on the secondary axis. **d)** α versus pitch period (t/τ), and flap angle (α_F) for phase $\phi = 1\pi$. The iso-lines on the plot represent constant $-\Delta C_p$ values=[-2, -1, 0, 1, 1.5, 2, 3]. The iso-line of $-\Delta C_p$=0 is marked in white dashes.

The ΔC_p standard deviation (STD) contour plots for the same case, 1b, are shown in Figure 5.8. The contour plots are plotted in $\log_{10}$ scale to better show the details at smaller STD values. The transition point from laminar to turbulent flow is determined by locating the maximum value of the STD at each specific point of time along the chord as has been done by Raiola *et al.* [69]. A dashed line is added to highlight the location of the transition point. The pattern highlighted has a frequency twice that of the flapping motion because transition occurs on both sides of the airfoil. Each side of the airfoil acts as both a pressure and suction side. Pressure fluctuations are higher around t/$\tau \approx 0.25$ and 0.75 when $\alpha = 0°$ because the suction and pressure side switch roles. In Figure 5.8.c the STD(ΔC_p) is large around t/$\tau \approx 0.5$ and x/c>0.7 because $\alpha_F = -20°$ and the camber of the airfoil is at its maximum. When $\alpha_F = -20°$ it creates a large angle that forces the airflow close to the TE to separate and this increases the STD value.

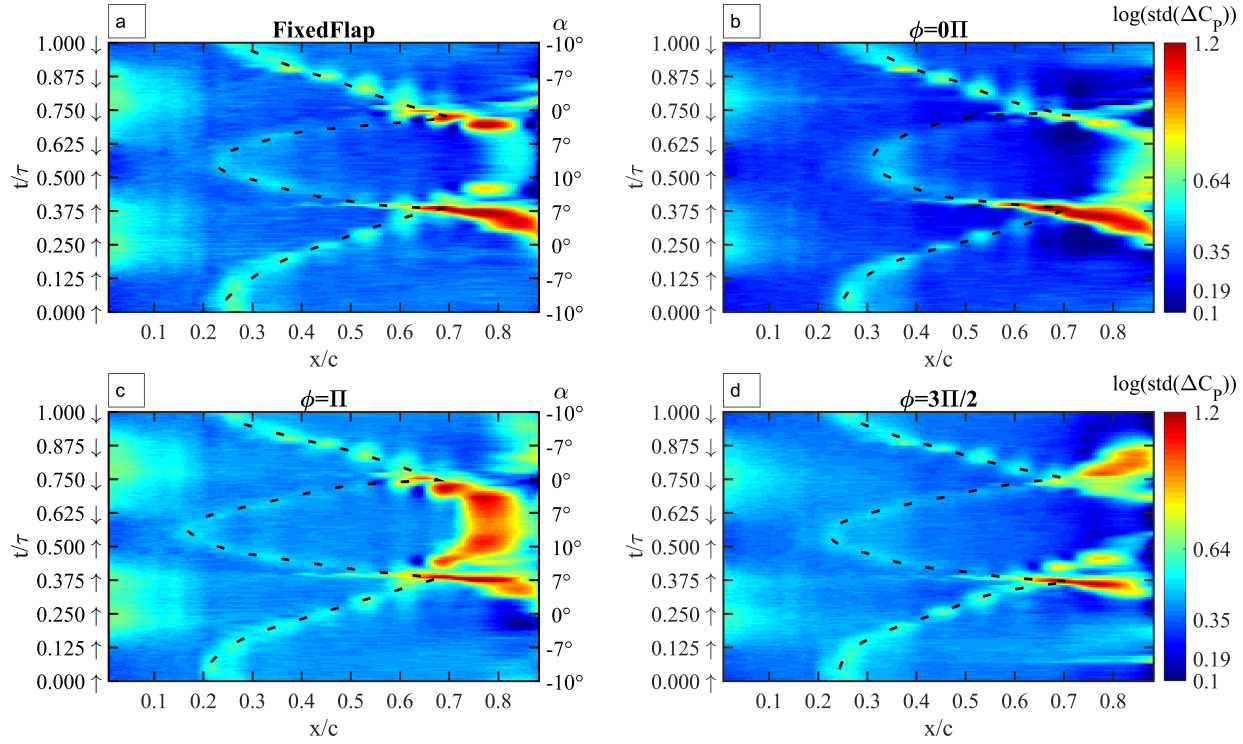


Figure 5.8: Contours of STD(ΔC_p) versus x/c versus t/τ for case 1b (k=0.1 and $\alpha_{mean} = 0°$). **a)**, **b)**, **c)**, and **d)** represent FixedFlap, $\phi = 0\pi$, $\phi = 1\pi$, and $\phi = 3\pi/2$ respectively. The angle of attack (α) is shown on the secondary axis. The dashed line shows the location of the transition point.

5.2.2 Case 2 $\alpha_{mean} = 10°$

The same figures presented in previous Section 5.2.1 are re-plotted for cases 2a and 2b where the only experimental parameter difference is changing α_{mean} from 0° to 10°. The change of α_{mean} alters the cycle loop significantly especially at high α values. The C_L values are approximately double their static counterparts when $18° < \alpha < 20°$ due to dynamic stall occurrence. Looking at C_L in Figures 5.9a and 5.9c, a similar trend can be seen across the different flap phases but with a differing magnitude and location. Starting at $\alpha = 0°$ and for all cases, as the airfoil pitches upward, C_L keeps increasing past the static stall angle. When α is between 17° and 19° there is a sudden sharp increase in C_L. This is likely due to the generation and subsequent shedding of a LEV from the LE as explained in the introduction and noted by Corke and Thomas [21]. The LEV creates

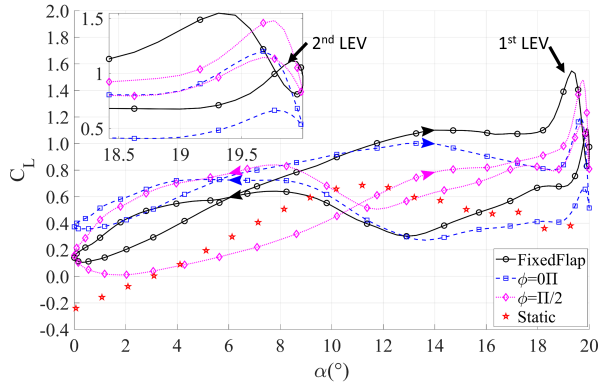
extra suction on the suction side of the airfoil enhancing C_L. While comparing the C_L cycles for the different ϕ cases, it was concluded that the TEF is not capable of controlling the formation of the LEV but rather it delays or promotes the formation of the LEV as was concluded by Lee and Gerontakos [26]. For example, compared to the FixedFlap when $\phi = \pi$ the sharp increase in C_L (or LEV) occurs 1° earlier and when $\phi = 0\pi$ the sharp increase in C_L occurs 0.5° later. As soon as the airfoil reaches α maximum of the upstroke cycle and just before reversing direction C_L drops dramatically due to shedding of the LEV. The shedding location of the LEV is not constant and will change depending on the operating conditions. After the primary LEV is shed, a second C_L peak occurs created by a secondary LEV which is weaker in magnitude. The secondary LEV occurs during the upstroke motion in some cases, and in other cases occurs during the downstroke motion. The formation of multiple LEVs is reported in the literature review by Leishman [22] and Gharali and Johnson [23]. During stall and after the secondary LEV, C_L keeps decreasing as α decreases. The airfoil is stalled even though α is below the stall point which is a characteristic of dynamic stall that delays flow reattachment. At around 8° and during the downstroke cycle, C_L increases to a larger than that observed on the static C_L plot indicating that the flow is beginning to reattach from the LE. Flow reattachment after stall is more clearly seen in the STD(ΔC_p) contour plots in Figure 5.12 and is discussed later in this section.

For all cases except when $\phi = 3\pi/2$ in Figures 5.9a and 5.9c, the C_L loop crosses over itself halfway through the downstroke. This is also seen in other experimental work [31, 135]. When the loop crosses over, it indicates that during upstroke the C_L is smaller than downstroke. This is in agreement with case 1a ($\alpha_{mean} = 0°$) where the loop direction is also ccw. For $\alpha < 6°$ and case 2a, the C_L variation in magnitude and shape is similar to case 1a. Looking at the overall C_L variation it could be noted that when $\phi = \pi$ the lift fluctuation is the largest while when $\phi = 0\pi$ the lift fluctuation is the lowest. In both cases ($\phi = 0\pi$ and π), the variation around $\alpha = 0$ is negligible when compared to the FixedFlap case. For $\phi = \pi/2$ and $\phi = 3\pi/2$, the difference between the upstroke and downstroke is narrower and wider respectively. Based on these four ϕ phases, it could be concluded that the TEF is capable of reducing or increasing the C_L at any specific point along the dynamic stall cycle based on the value of ϕ.

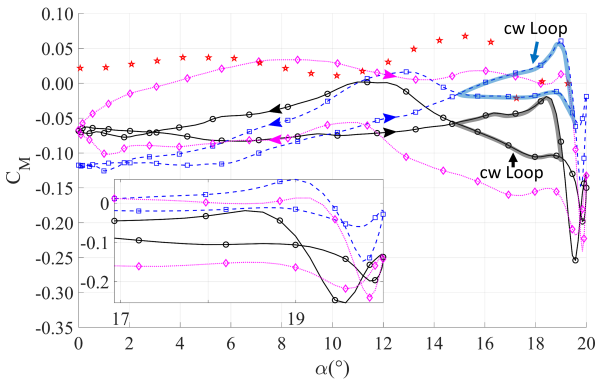
Figures 5.9b and 5.9d show the variation in C_M for different flap phases for case 2a. For $\alpha < 12°$ the variations in C_M for all ϕ cases are relatively flat and on the same scale as in case 1a with $\alpha_{mean} = 0°$. The C_M static values are also shown in the plot for comparison. During the upstroke motion (for all ϕ cases) and just when the pitching motion is about to reverse, the LEV formation and shedding causes a rapid and severe increase in nose-down pitching moment (negative C_M) at about 19°. The peak in C_M always occurs after the

peak in C_L. The vortex starts at the LE and passes along the airfoil exiting at the TE. While the vortex sweeps over the airfoil, it produces a rapid aft movement of the center of pressure from the LE towards the TE resulting in a large nose-down pitching moment on the airfoil [9].

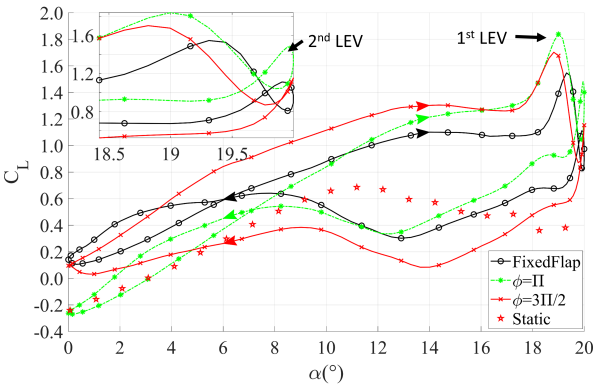
Another important factor to look for in the C_M plots is the formation of negative damping as discussed in the introduction. Negative damping occurs when $C_M - \alpha$ creates a clockwise (cw) cycle and that promotes flutter and instabilities and would not be a good choice for operation. The cw loop (highlighted and labeled in Figures 5.9b and 5.9d) could be seen in the FixedFlap case, $\phi = 0\pi$, and $\phi = \pi$. In these particular cases the cw loops are likely to produce airfoil flutter due to the existence of dynamic stall and a LEV [21, 32]. For $\phi = \pi/2$ the entire loop is negatively damped while $\phi = 3\pi/2$ produces no negative damping. The TEF was capable of reducing and increasing the minimum C_M peak and was also able to remove negative damping effects and reduce flutter for specific flap phases.



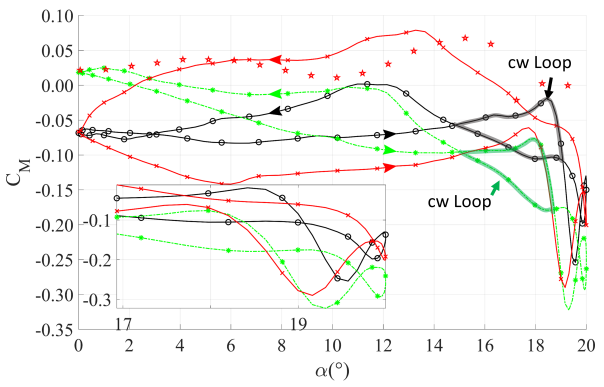
(a) Coefficient of lift ($\phi = 0\pi$, $\phi = \pi/2$)



(b) Coefficient of moment ($\phi = 0\pi$, $\phi = \pi/2$)



(c) Coefficient of lift ($\phi = 1\pi$, $\phi = 3\pi/2$)



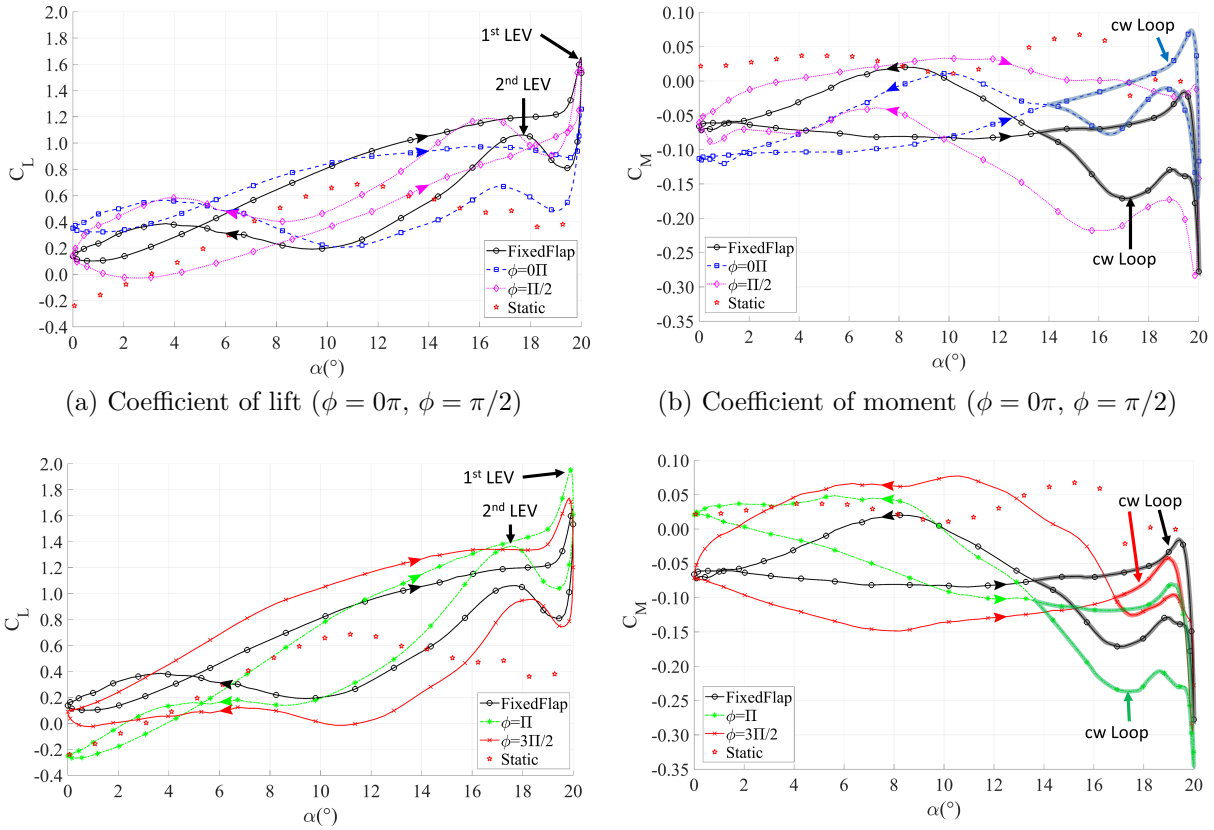
(d) Coefficient of moment ($\phi = 1\pi$, $\phi = 3\pi/2$)

Figure 5.9: Coefficient of lift (C_L), and moment (C_M) versus α for different flap phases (ϕ) for case 2a where k=0.06 and $\alpha_{mean} = 10°$. Only every fourth data point is marked on the plot for clarity. A plot inset is used to magnify the data around $\alpha = 19°$. The 1^{st} and 2^{nd} LEV and the cw loops are marked in each plot.

C_L and C_M are plotted in Figure 5.10 for case 2b with a reduced frequency of 0.1. When comparing case 2b to 2a (Figure 5.9) where k increased from 0.06 to 0.1, a few significant differences arise. These differences include an increase in the C_L peak indicating a larger and stronger LEV as seen in Figures 5.10a and 5.10c. The LEV onset is also delayed by 1° pushing the peak location to the right from 19° (case 2a) to 20° (case 2b). The secondary LEV onset is also delayed by 2° and occurs at about 18° during the downstroke. Increasing k is then found to delay the onset of flow separation and dynamic stall to a greater value of α. Reattachment is also delayed by 4°. The difference between the upstroke and downstroke is larger slightly widening the hysteresis loop. Comparing C_M for case 2b (Figure 5.10)

against case 2a (Figure 5.9) a few notable changes are worth mentioning. The negative damping loops are longer and larger in magnitude and negative damping now occurs for $\phi = 3\pi/2$. $\phi = \pi/2$ is the only case where negative damping occurs during the entire cycle. It was found that when k increased from 0.06 to 0.1, the negative damping loop increased.

Now that the plots for cases 2a and 2b are presented for different ϕ cases, a conclusion could be made about the influence of ϕ. If the aim is to reduce the C_L fluctuations around the mean angle then it would be best to set $\phi = \pi/2$. On the other hand, if the aim is to reduce C_L fluctuations at the minimum and maximum then it would be best to set $\phi = 0\pi$. Now focusing on the C_M plots, it was found that $\phi = 0\pi$ decreases the peaks and reduces the negative damping loop in size. For $\phi = \pi/2$ it was found that the entire C_M loop causes negative damping possibly promoting stall flutter. It is recommended then to use $\phi = 0\pi$ because it reduces the minimum/maximum of the C_L and C_M cycle and reduces negative damping.



(a) Coefficient of lift ($\phi = 0\pi$, $\phi = \pi/2$)

(b) Coefficient of moment ($\phi = 0\pi$, $\phi = \pi/2$)

(c) Coefficient of lift ($\phi = 1\pi$, $\phi = 3\pi/2$)

(d) Coefficient of moment ($\phi = 1\pi$, $\phi = 3\pi/2$)

Figure 5.10: Coefficient of lift (C_L), and moment (C_M) versus α for different flap phases (ϕ) for case 2b where k=0.1 and $\alpha_{mean} = 10°$. Only every fourth data point is marked on the plot for clarity. The 1^{st} and 2^{nd} LEV and the cw loops are marked in each plot.

To understand the importance of the formation and shedding of the vortices, the temporal change in $-\Delta C_p$ is plotted in Figure 5.11 for case 2b just as case 1b was plotted in Figure 5.7. $-\Delta C_p$ for case 2a is not shown here because the trends are very similar. The FixedFlap case, $\phi = 0\pi$ and $\phi = 1\pi$ are presented along with a plot showing the correlation between the period (τ) and α and α_F for $\phi = 1\pi$. During the upstroke motion (as indicated with the arrows on the left axis) and for all cases, a large $-\Delta C_p$ peak is present at the LE after t/τ=0.25 that gets stronger with increasing α. When the pitch motion is about to reverse, the LEV is shed increasing $-\Delta C_p$ along the entire chord. This is seen in the plots at t/τ=0.45 where the LEV is clearly seen moving from the leading to the trailing edge. Even though the $-\Delta C_p$ peak at the LE is smaller, $-\Delta C_p$ on the entire chord increases thus

increasing the total lift as indicated in the C_L versus α plots in Figures 5.9 and 5.10. The contour plots reveal that as the vortex sweeps over the airfoil, it produces a rapid aft movement of the center of pressure from the LE towards the TE resulting in a large nose-down pitching moment on the airfoil. After the LEV is shed indicated by a decrease in $-\Delta C_p$, $-\Delta C_p$ increases slightly at t/τ=0.625 indicating the formation of the secondary LEV. Full reattachment takes place at about t/τ=0.75 where the highest suction is located at the LE. The major difference between the three plots is the variation in $-\Delta C_p$ magnitude for the different flap phases. The constant $-\Delta C_p$ iso-lines clearly show how ϕ influences the pressure over the airfoil. The magnitude of the LEV is decreased for $\phi = 0\pi$ and increased for $\phi = \pi$ and that is in agreement with $C_L - \alpha$ (Figures 5.9 and 5.10). To conclude, these plots clearly show the temporal change of $-\Delta C_p$ and clearly show the importance of the LE region and the impact of the dynamic motion.

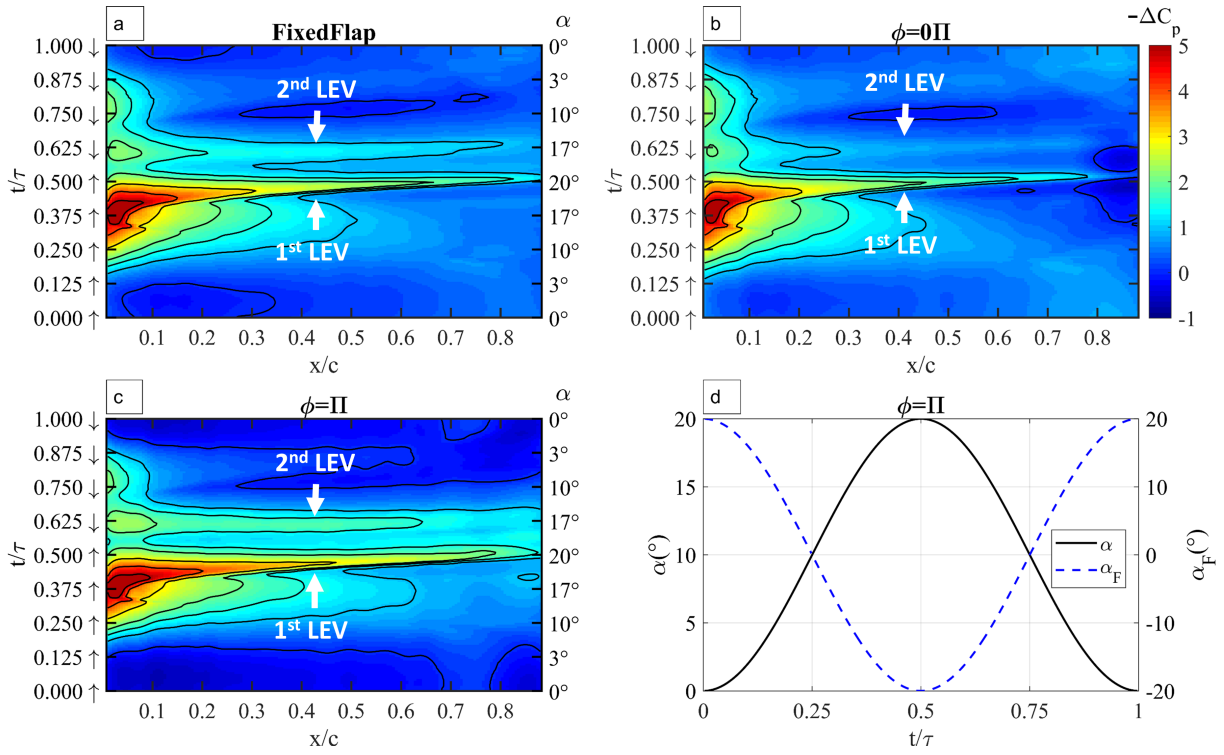


Figure 5.11: Contours of $-\Delta C_p$ versus x/c versus α for case 2b (k=0.1 and $\alpha_{mean} = 10°$). **a)**, **b)**, and **c)** represent FixedFlap, $\phi = 0\pi$, and $\phi = 1\pi$ respectively. **d)** shows α versus the pitch period, t/τ, and flap angle, α_F , for phase ϕ= 1π. The angle of attack (α) is shown on the secondary axis. The iso-lines on the plot represent constant $-\Delta C_p$ values=[-1, 0, 1, 1.5, 2, 3, 4, 5] . The 1^{st} and 2^{nd} LEV are marked in each plot.

Another way to visualize airfoil stall and vortices is by looking at the standard deviation in ΔC_p in Figure 5.12 for case 2b. The STD is plotted in $\log_{10}$ scale to show the small changes at lower values. Vortices and stall are associated with large pressure fluctuations and can be clearly seen in the figure. The high STD(ΔC_p) streak at $t/\tau = 0.45$ is associated with the LEV being shed and the direction of movement is from the LE to the TE because the pressure center in the plot moves from x/c=0 to x/c=1 and at the same time moves up along the y-axis. At t/τ=0.5 the magnitude decreases indicating stall but then increases again at t/τ=0.625 indicating the formation of the secondary LEV. After the secondary LEV, the airfoil is completely stalled until $t/\tau \approx 0.75$ where the STD(ΔC_p) is greatly reduced indicating airflow re-attachment on the airfoil. The patterns in STD(ΔC_p) do not change significantly for the different flap phases apart from the magnitude.

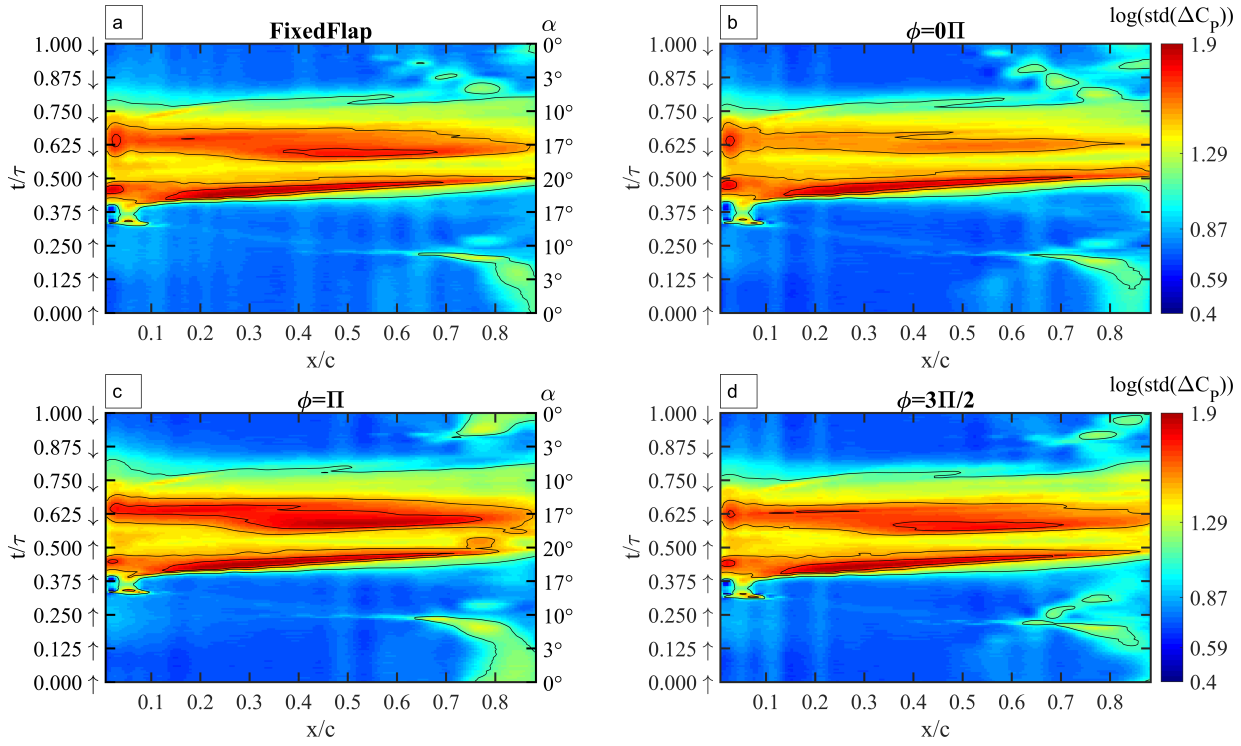


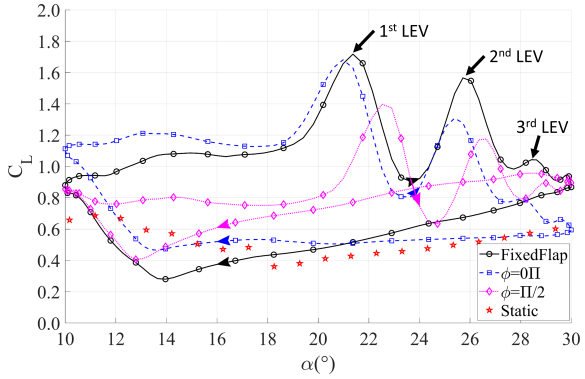
Figure 5.12: Contours of log(STD(ΔC_p)) versus x/c versus α for case 2b (k=0.1 and $\alpha_{mean} = 10°$). **a)**, **b)**, **c)**, and **d)** represent FixedFlap, $\phi = 0\pi$, $\phi = 1\pi$, and $\phi = 3\pi/2$ respectively. The angle of attack (α) is shown on the secondary axis. The iso-lines on the plot represent constant log(STD(ΔC_p)) values.

5.2.3 Case 3 $\alpha_{mean} = 20°$

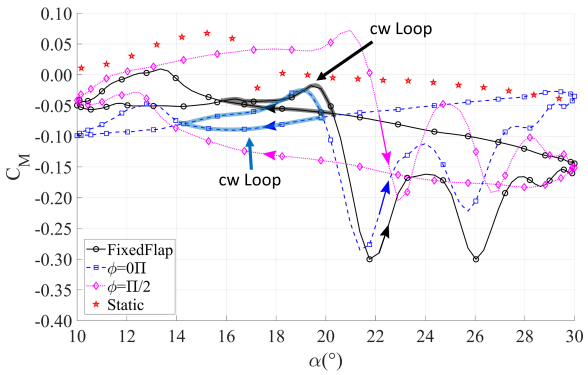
In this subsection cases 3a and 3b for k= 0.06 and 0.1, respectively, are considered, with α_{mean} increased to 20° from 10° in previous case. The α_{mean} parameter was chosen so the airfoil is operating in deep dynamic stall and within the static stall angle range so the flow has the opportunity to reattach on the airfoil. This way the airfoil was oscillating back and forth around the static stall angle which is around 16°. The phase-averaged C_L loops are presented in two plots, Figures 5.13a and 5.13c. A similar trend can be observed across the different flap phases but with a slightly different magnitude and location. Starting at $\alpha = 10°$ as the airfoil pitches up, C_L starts to increase but then around $\alpha = 21°$ there is a sudden increase in C_L caused by the primary LEV. After the LEV convects off the airfoil, the flow is separated. Then around $\alpha = 26°$ there is a second sharp increase in C_L; this time it is due to a secondary LEV which tends to be weaker in magnitude as illustrated by a smaller C_L peak. The secondary LEV is followed by a subsequent small LEV before the downstroke portion of the cycle. The formation of multiple LEVs is in agreement with previous experimental works and numerical models [22, 23, 76]. It is interesting to note that all the LEVs occur during the upstroke only as seen in McCroskey [77]. This could be attributed to the low k value of 0.06 and high α_{mean} of 20°. During the downstroke the airfoil is stalled and C_L keeps decreasing until around $\alpha = 14°$ where the flow starts to reattach and C_L starts to increase. It is interesting to note that C_L is greater than the static value even during the downstroke cycle where the airfoil is stalled; this results is due to the nature of dynamic stall. Comparing $\phi = 3\pi/2$ to the FixedFlap, the primary and secondary LEV (which are seen as a spike in the $C_L - \alpha$ plots) occur 1° earlier while for $\phi = \pi/2$ the LEV occurs 1° later. In the other two ϕ cases (0π and π), the LEV location does not change. One interesting point to observe is that when $\alpha = 10°$ and 30° (minimum and maximum), the C_L values at these two points are equal for the FixedFlap case. Out of all the different ϕ tested it could be concluded that when $\phi = \pi/2$, C_L has the least fluctuation. This is because most of the loading occurs halfway through the upstroke portion of the cycle where $\alpha = 20°$. The magnitude of the C_L peaks caused by the LEV are smaller than in the other cases and the hysteresis cycle is narrow.

Figures 5.13b and 5.13d show the C_M hysteresis loops for case 3a. During dynamic stall the LEV starts from the LE and sweeps towards the TE. While the vortex sweeps over the airfoil, it produces a rapid aft movement of the center of pressure from the LE towards the TE resulting in a large nose-down pitching moment on the airfoil [9]. When the LEV is at the LE it increases C_L but when the LEV is shed towards the TE it increases the C_M value. This is why the peak in C_M always occurs after the peak in C_L for all cases. C_M is in constant nose-down pitching (negative C_M value) for the different ϕ cases when compared

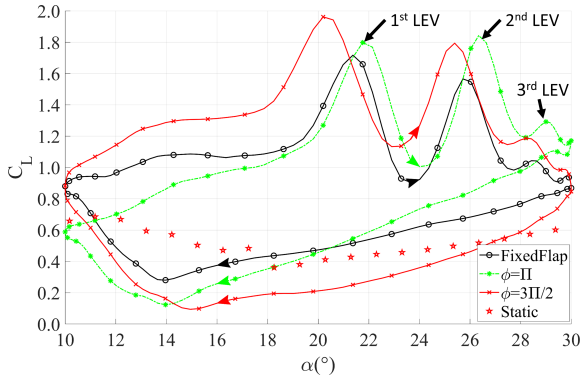
to the static values. This indicates that the center of pressure is always behind the quarter-chord of the airfoil towards the TE. Another important point to notice in the C_M loop is the formation of a clockwise (cw) loop that indicates negative damping. A small cw loop is found in the FixedFlap, $\phi = 0\pi$, and $\phi = \pi$ around $\alpha = 18°$. For $\phi = \pi/2$, the entire loop is cw promoting stall flutter while the entire loop for $\phi = 3\pi/2$ is counter-clockwise (ccw) preventing stall flutter at all times. As discussed in the introduction, negative damping promotes flutter and instabilities that lead to severe vibration and mechanical failure if the structural dynamics permit and would be best avoided at all times [21]. In this experimental setup when negative damping was present, the airfoil section was observed to experience excessive vibration.



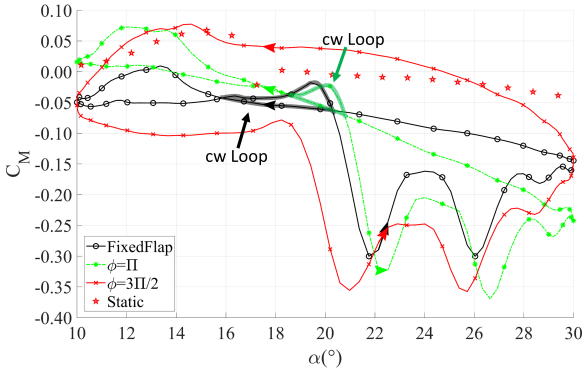
(a) Coefficient of lift ($\phi = 0\pi$, $\phi = \pi/2$)



(b) Coefficient of moment ($\phi = 0\pi$, $\phi = \pi/2$)



(c) Coefficient of lift ($\phi = 1\pi$, $\phi = 3\pi/2$)



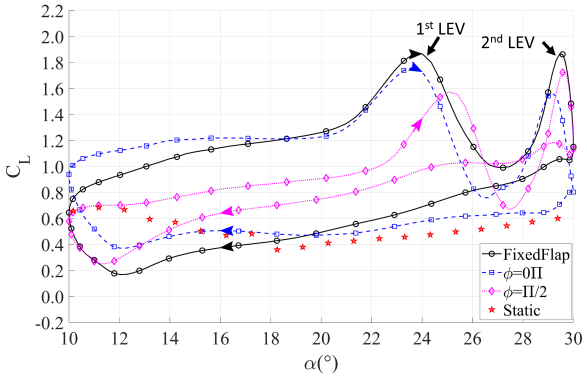
(d) Coefficient of moment ($\phi = 1\pi$, $\phi = 3\pi/2$)

Figure 5.13: Coefficient of lift (C_L), and moment (C_M) versus α for different flap phases (ϕ) for case 3a where k=0.06 and $\alpha_{mean} = 20°$. Every 4^{th} data point is marked on the solid lines for clarity. A plot inset is used to magnify the data around $\alpha = 19°$. The 1^{st} and 2^{nd} LEV and the cw loops are marked in each plot.

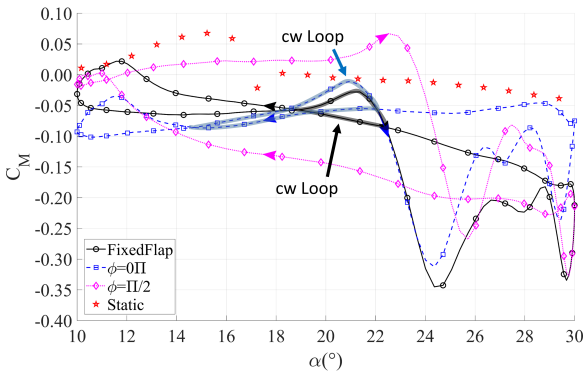
Figure 5.14 shows C_L and C_M for case 3b where k increased from 0.06 to 0.1 and $\alpha_{mean} = 20°$. Focusing on the C_L curves there are few major differences when k increases. First, the amplitude of the C_L peaks caused by the LEV are increased and the occurrence of the LEV is delayed by 3°. The primary LEV occurs around 24° followed by a secondary LEV at 29°. This delay in occurrence of the LEV is mainly due to the increase in k value that tends to delay dynamic stall to a higher α value [21, 22]. The secondary LEV again tends to be weaker than the primary LEV. There is also a very small subsequent LEV occurring during the first part of the downstroke cycle. The difference between the upstroke and downstroke increases, widening the hysteresis loop and increasing cyclic loading when

k increases. These differences mentioned are in agreement with prior studies [9, 26, 77]. The loss of lift after the secondary LEV is much steeper and sudden when compared to the k=0.06 case because the secondary LEV occurs when the airfoil is about to change pitch direction at $\alpha = 30°$. From cases 3a and 3b, it is concluded from the C_L loops that for $\phi = \pi/2$ the load fluctuation is smallest, the hysteresis loops are much narrower and the peaks due to the LEV are less severe. On the other hand, $\phi = 3\pi/2$ has the largest load fluctuations, the widest hysteresis loops and the highest peaks.

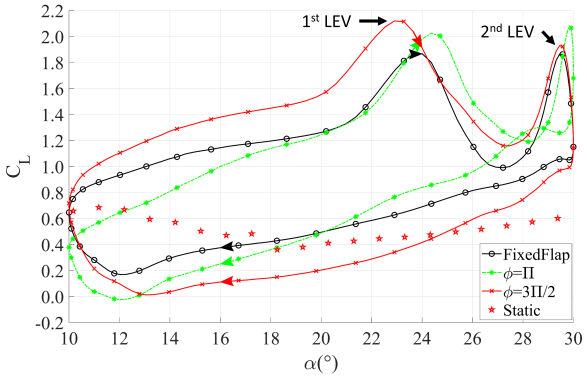
Looking at the C_M hysteresis plots in Figure 5.14 and comparing them to Figure 5.13 where k increased from 0.06 to 0.1 a few differences are apparent. C_M peaks are increased and the LEV formation is delayed as seen in the C_L plots. The cw loops now occur around $\alpha = 21°$ instead of 18°. The magnitude of negative damping is about the same. A similar conclusion to that noted for the C_L loops is reached for the C_M loops, $\phi = \pi/2$ produces the least fluctuations and $\phi = 3\pi/2$ produces the greatest fluctuations. On the other hand, $\phi = \pi/2$ leads to a negatively damped C_M loop promoting flutter while $\phi = 3\pi/2$ leads to positive damping. To conclude which ϕ to use to minimize dynamic stall effects on the airfoil, $\phi = \pi/2$ greatly reduces C_L but at the same time leads to negative damping. Another option is $\phi = 0\pi$ and that reduces C_L peaks slightly but eliminates negative damping. So depending whether to reduce C_L peaks or eliminate negative damping, ϕ should be $\pi/2$ or 0π.



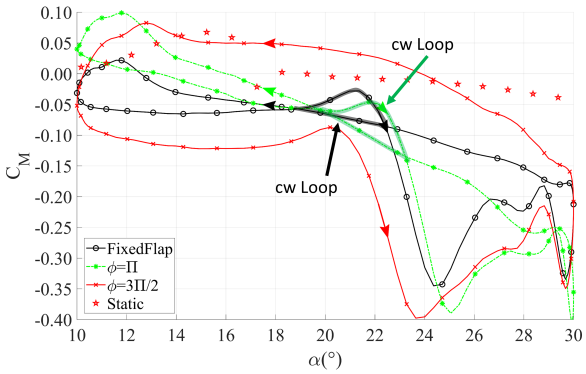
(a) Coefficient of lift ($\phi = 0\pi$, $\phi = \pi/2$)



(b) Coefficient of moment ($\phi = 0\pi$, $\phi = \pi/2$)



(c) Coefficient of lift ($\phi = 1\pi$, $\phi = 3\pi/2$)



(d) Coefficient of moment ($\phi = 1\pi$, $\phi = 3\pi/2$)

Figure 5.14: Coefficient of lift (C_L), and moment (C_M) versus α for different flap phases (ϕ) for case 3b where k=0.1 and $\alpha_{mean} = 20°$. Every 4^{th} data point is marked on the solid lines for clarity. The 1^{st} and 2^{nd} LEV and the cw loops are marked in each plot.

To better understand how the pressure center and magnitude changes over the airfoil surface, the same $-\Delta C_p$ contour plots discussed in the previous two subsections are re-plotted for case 3b. Figure 5.15 shows the $-\Delta C_p$ contour plots for FixedFlap, $\phi = \pi/2$, and $\phi = 3\pi/2$ cases. Starting at $t/\tau = 0$, $-\Delta C_p$ is concentrated at the LE (x/c<0.25) and starts to increase until it reaches its maximum at $t/\tau \approx 0.25$ indicating that the flow is attached. After this point the LEV starts being shed from the LE to the TE. As the LEV is shed it tends to decrease $-\Delta C_p$ close to the LE but increases $-\Delta C_p$ on the rest of the airfoil surface. This increase in $-\Delta C_p$ over the airfoil creates the sudden peak in C_L and C_M as seen in Figures 5.13 and 5.14. After the primary LEV, the $-\Delta C_p$ values are diminished indicating stall until the secondary LEV is formed at $t/\tau \approx 0.45$ but with

a weaker magnitude. After the secondary LEV, $-\Delta C_p$ values are diminished again for the rest of the cycle indicating stall. This phase-averaged pattern in ΔC_p for the pitching cycle and how it shows both LEV was also seen experimentally by Zanotti and Gibertini [75, 76] for a NACA 23012 airfoil without a TEF. Comparing the three different ϕ cases, the magnitude of the LEV is increased for $\phi = 3\pi/2$ and decreased for the $\phi = \pi/2$ when compared to the FixedFlap as seen more clearly through the iso-lines on the plots. This comparison was also noted by Lee and Su [71] from the time history of $-\Delta C_p$ on a NACA 0015 symmetric airfoil. This concludes that the TEF is not capable of eliminating the LEV formation that causes spikes in the $C_L - \alpha$ and $-\Delta C_p$ plots but it could reduce its impact on the airfoil.

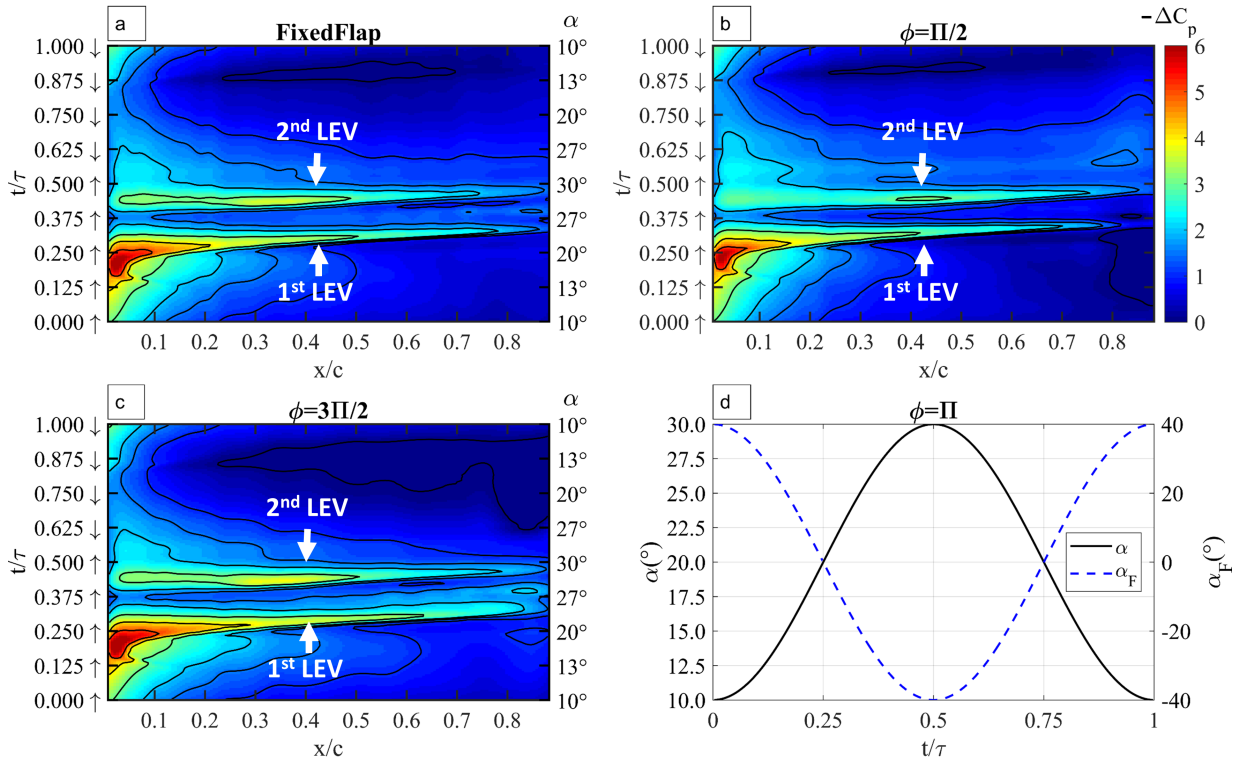


Figure 5.15: Contours of $-\Delta C_p$ versus x/c versus α for case 3b (k=0.1 and $\alpha_{mean} = 20°$). **a)**, **b)**, and **c)** represent FixedFlap, $\phi = \pi/2$, and $\phi = 3\pi/2$ respectively. The angle of attack (α) is shown on the secondary axis. **d)** α versus pitch period (t/τ), and flap angle (α_F) for phase $\phi = 1\pi$. The iso-lines on the plot represent constant $-\Delta C_p$ values=[0, 1, 1.5, 2, 3, 4, 5].

A different way of visualizing the airfoil stall and the vortex structures can be seen by

looking at the standard deviation (STD) in ΔC_p which is plotted in Figure 5.16 for case 1b. The STD is plotted in log scale to show the small changes at smaller values. Vortices and stall are associated with large pressure fluctuations because of the flow dynamics [9]. While $0<t/\tau<0.25$ and for all the cases presented, STD(ΔC_p) values are small indicating that the airfoil is not stalled. The primary and secondary LEV discussed in Figure 5.15 also appear in this figure and are associated with very large STD values at $t/\tau \approx 0.25$ and $t/\tau \approx 0.45$. The time history of the STD(ΔC_p) clearly shows that the movement of the LEV is from the LE to the TE. The observations made here reinforce the discussion made earlier while discussing $C_L - \alpha$ and $-\Delta C_p$ plots. After both vortices flow past the TE, STD is reduced but still greater than the value observed at $t/\tau = 0$ indicating that the flow over the airfoil is stalled between t/τ=0.5 and 1. The STD is then reduced further at $t/\tau = 0$ when the airfoil starts to pitch upwards indicating flow reattachment. This observation is confirmed in the $C_L - \alpha$ plot in Figure 5.14 which shows that during the downstroke cycle, C_L is much smaller than the upstroke cycle until the very end of the cycle. The STD(ΔC_p) patterns do not change significantly between the four ϕ cases presented in the figure other than a slight change in magnitude and location of the peaks.

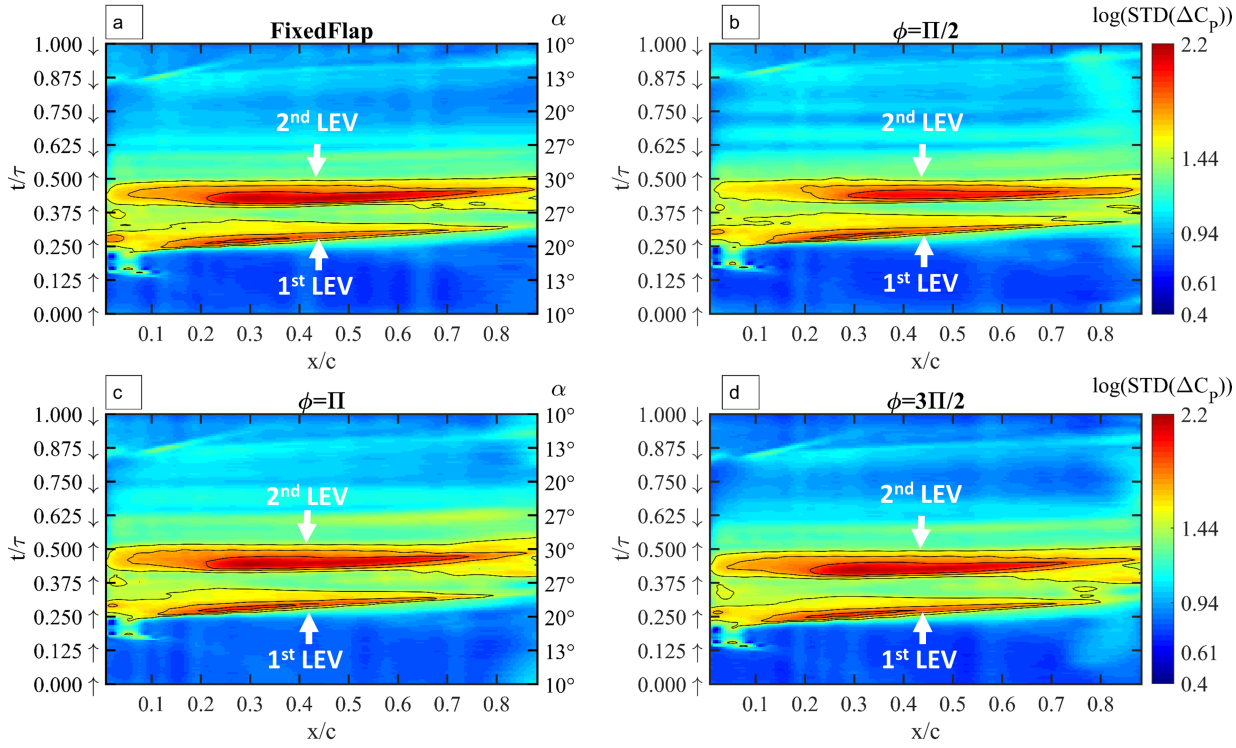
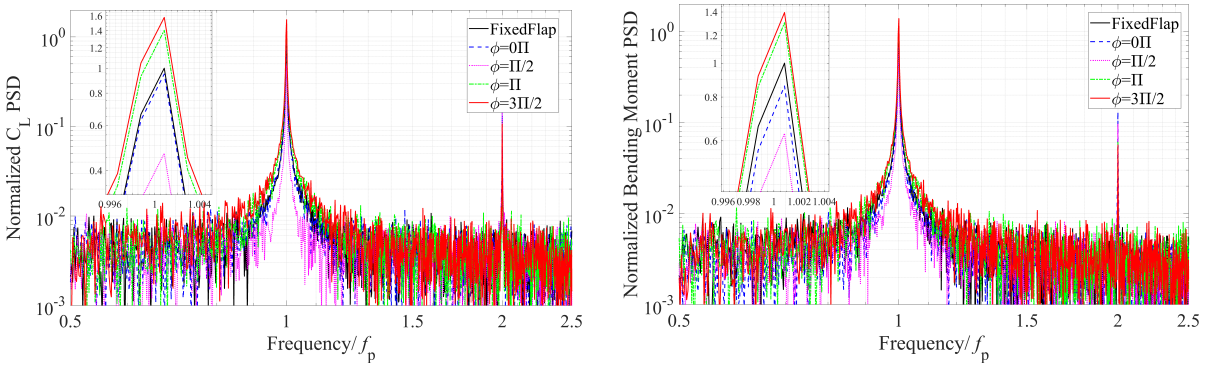


Figure 5.16: Contour plots showing the STD(ΔC_p) versus x/c versus α for case 3b where k=0.1 and $\alpha_{mean} = 20°$. a), b), c), and d) represent FixedFlap, $\phi = \pi/2$, $\phi = 1\pi$, and $\phi = 3\pi/2$ respectively. The iso-lines on the plot represent constant log(STD(ΔC_p)) values.

So far $C_L - \alpha$, $C_M - \alpha$, $-\Delta C_p$, and STD(ΔC_p) have been plotted showing the complexity and behavior of dynamic stall but they do not clearly show with absolute certainty which ϕ case reduces the load fluctuations the most. To simply and effectively measure the impact of a TEF on an oscillating airfoil undergoing dynamic stall, it is deemed more appropriate to analyze the data in the frequency domain by the academic community [96, 98, 139] as was discussed in Section 4.6.4. The power spectral density (PSD) plots for C_L and root bending moment are displayed in Figures 5.17a and 5.17b respectively. The y-axis is normalized with respect to the peak amplitude found in the FixedFlap case while the x-axis is normalized with respect to the oscillating frequency (f_p) and thus the highest amplitude occurs at frequency/f_p =1. There is another peak present at frequency/f_p =2 representing the second harmonic of the oscillation. Both axis of the plot are in $\log_{10}$ scale to better show the frequency and amplitude distribution and an inset is used to magnify the results

around the oscillating frequency. The plots show that for $\phi = \pi/2$, the peak C_L amplitude at the oscillating frequency is reduced by 53% while the root bending moment amplitude is reduced by 37% with respect to the FixedFlap case. This reduction is significant and shows that the TEF is capable of reducing cyclic loading. There is a greater measured reduction in C_L than root bending moment because C_L is measured at the center of the TEF section while the root bending moment measures the lift for the entire airfoil section where the TEF occupies 60% of the airfoil section.



(a) Spectral density for C_L

(b) Spectral density for moment

Figure 5.17: Normalized power spectral density distribution for C_L, and moment for different flap phases (ϕ) for case 3a where k=0.06 and $\alpha_{mean} = 20°$. Frequencies on the x-axis were normalized with respect to the oscillating frequency (f_p). Both axis are log scale and an inset is shown to magnify the results around the oscillating frequency.

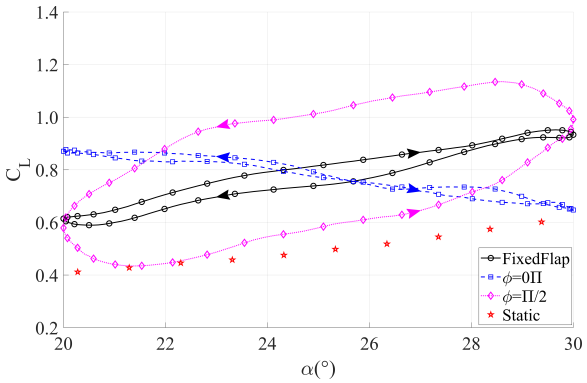
The PSD is also plotted for case 3b but not presented here as no new information could be derived and those plots exhibit trends similar to the ones noted for case 3a. Comparing case 3b to 3a and for $\phi = \pi/2$, the C_L amplitude is reduced by 26% compared to 53% while the root bending moment amplitude is reduced by 24% compared to 37%. The change in % reduction occurs because higher k values produce larger peaks in the $C_L - \alpha$ plots and the TEF influence over the latter variable is the same independent of k.

5.2.4 Case 4 $\alpha_{mean} = 25°$

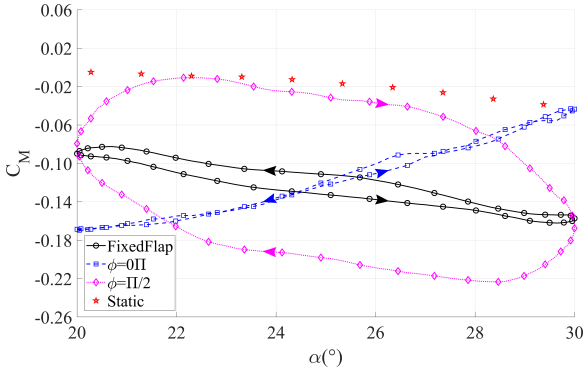
The results published in Gallant and Johnson [57] indicate that when an operating wind turbine is yawed, the mean oscillating α could be as large as 25° while the amplitude could be 5° for certain conditions. Case 4 in this paper aims to simulate a wind turbine

blade under the same conditions that Gallant and Johnson mentioned. Figure 5.18 shows $C_L - \alpha$ and $C_M - \alpha$ for case 4 and for different ϕ cases where k=0.1, $\alpha_{mean} = 25°$, and $\alpha_{amp} = 5°$. Focusing on the C_L plots (Figures 5.18a and 5.18c), the FixedFlap cycle is cw and the hysteresis loop is narrow indicating that the difference between the upstroke and the downstroke motion is minimal. What is most interesting about the different loops is that the airfoil is stalled during the entire cycle but even so, C_L is greater than its static counterpart. There are several aspects that indicate the airfoil is always stalled for all ϕ cases. First, the airfoil motion for case 4 restricts α to a range from 20° to 30° so α is never below the static stall angle and thus reattachment does not occur. Second, the formation of a LEV is not obvious or never detaches in any of the loops indicating that the flow never reattaches on the airfoil. Lastly the $-\Delta C_p$ contour plots presented later in Figure 5.19 show that $-\Delta C_p$ is never concentrated at the LE and the values are smaller than the static case indicating flow separation. When comparing $\phi = \pi/2$ or $3\pi/2$ to the FixedFlap loop it is found that the C_L loop widens significantly but at the same time C_L does not change when α is at its minimum or maximum value. On the other hand, when comparing $\phi = 0\pi$ or $\phi = \pi$ to the FixedFlap loop, it was found that the width of the C_L loops do not change and stay narrow but the C_L minimum/maximum values are altered when α is at its minimum or maximum value. This shows that the TEF can manipulate C_L at any point on the cycle and that point is determined by the variable ϕ. To reduce the C_L fluctuation and keep the value constant for the entire cycle then it is recommended to set $\phi = 0\pi$ and reduce $\alpha_{amp,f}$ from 20° to 15°.

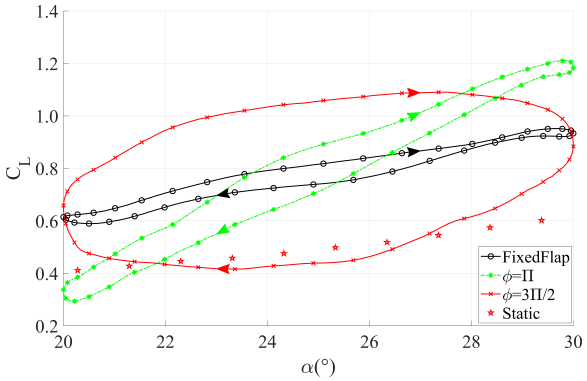
Figures 5.18b and 5.18d represent C_M versus α for the different ϕ loops. For all cases, C_M is smaller than its static counterpart indicating the center of pressure is past the quarter-chord of the airfoil. This is confirmed by the $-\Delta C_p$ contour plots in Figure 5.19. In the FixedFlap, $\phi = 0\pi$, and $\phi = \pi$ the C_M loops are narrow and ccw eliminating the possibility of stall flutter. For $\phi = \pi/2$ the C_M loop widens significantly and is cw promoting stall flutter on the airfoil. As for $\phi = 3\pi/2$, the C_M loop is also wide but the loop is ccw eliminating the possibility of stall flutter. To reduce C_M fluctuations and achieve a constant C_M, it is concluded to use $\phi = 0\pi$ but also reduce $\alpha_{amp,f}$ from 20° to 10°. This conclusion is aligned with the one made for the $C_M - \alpha$ loops.



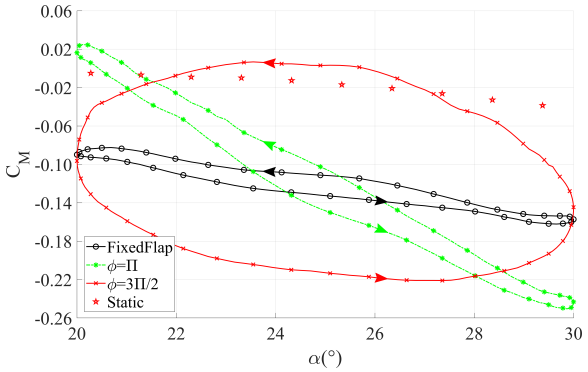
(a) Coefficient of lift ($\phi = 0\pi$, $\phi = \pi/2$)



(b) Coefficient of moment ($\phi = 0\pi$, $\phi = \pi/2$)



(c) Coefficient of lift ($\phi = 1\pi$, $\phi = 3\pi/2$)



(d) Coefficient of moment ($\phi = 1\pi$, $\phi = 3\pi/2$)

Figure 5.18: Coefficient of lift (C_L), and moment (C_M) versus α for different flap phases (ϕ) for case 4 where k=0.1, $\alpha_{mean} = 25°$, and $\alpha_{amp} = 5°$. Every 4^{th} data point is marked on the solid lines for clarity.

To study how the pressure over the airfoil surface changes in distribution and magnitude, $-\Delta C_p$ versus x/c versus t/τ is plotted in Figure 5.19 similar to Figure 5.15. These contour plots show that the airfoil is stalled because the $-\Delta C_p$ values are much smaller and less concentrated at the LE when compared to case 3 in Figure 5.15. This occurs because for case 4, α always exceeds the static angle and the flow does not have the opportunity to reattach over the airfoil surface. Case 4 is stalled during the entire cycle despite the fact that it is oscillating between $20° \leq \alpha \leq 30°$ and within the oscillating bound of case 3 where $10° \leq \alpha \leq 30°$ and the flow was attached during part of the case 3 cycle. When comparing $\phi = 0\pi$ to the FixedFlap case several aspects are noteworthy. At $t/\tau = 0.5$, $-\Delta C_p$ close to the TE (x/c>0.75) becomes negative due to the fact that $\alpha_F = 20°$ is cre-

ating a smaller suction pressure on the suction side. On the other hand, when $t/\tau = 0$ or 1 indicating that $\alpha_F = -20°$, it creates a higher suction pressure on the suction side close to the TE. The opposite is true when $\phi = \pi$; the suction pressure increases at $t/\tau = 0.5$ and decreases at $t/\tau = 0$ and 1 when compared to the FixedFlap case. The TEF did not just have influence on the TE pressure but also on the LE pressure as well as could be seen in the contour plots and the iso-lines. This concludes that the TEF influences the aerodynamics around the entire airfoil when the flow is stalled or attached.

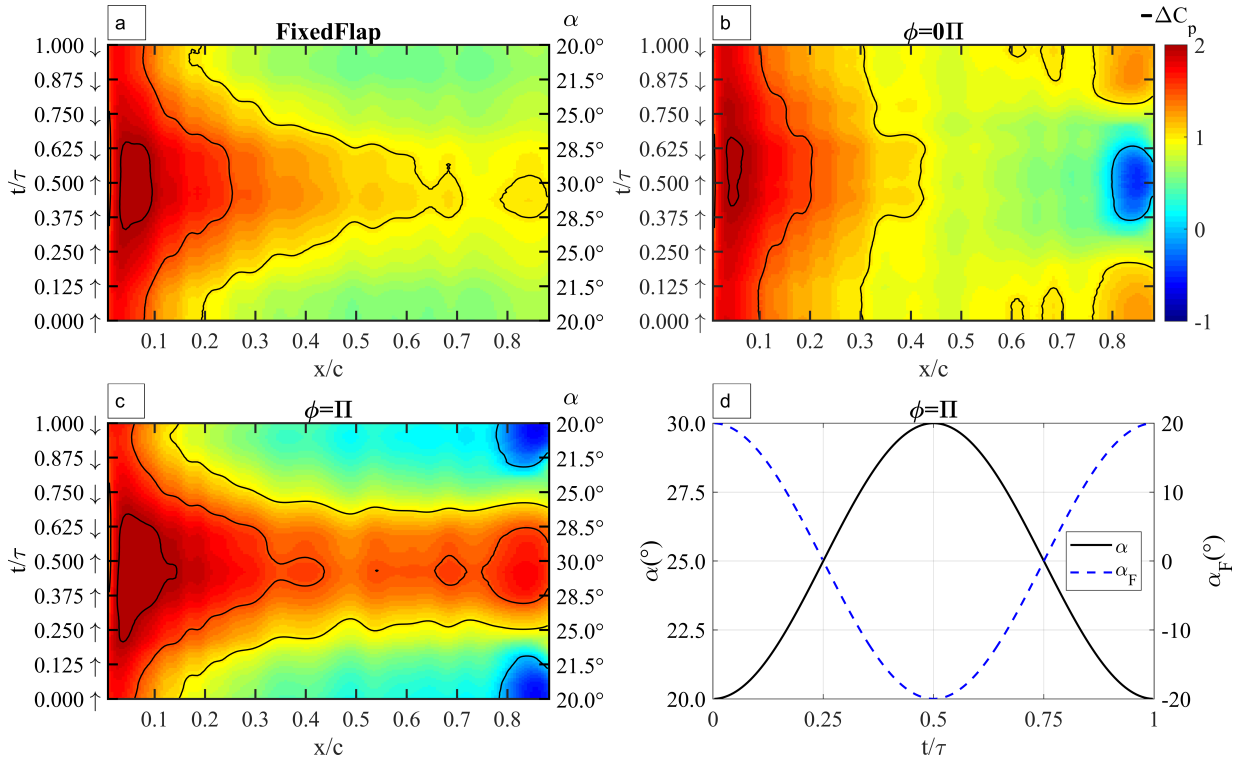


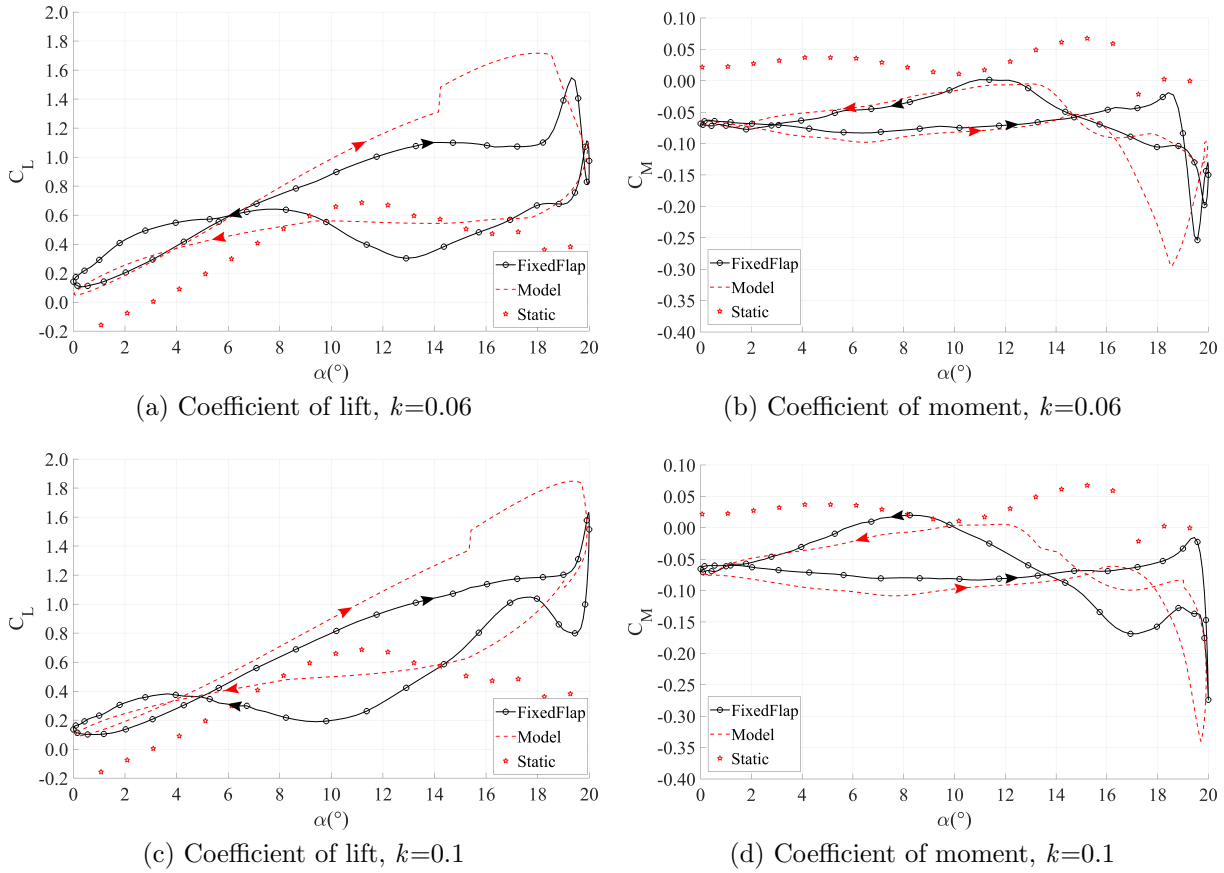
Figure 5.19: Contour plots showing the $-\Delta C_p$ versus x/c versus α for case 4a where k=0.06 and $\alpha_{mean} = 25°$. a), b), and c) represent FixedFlap, $\phi = 0\pi$, and $\phi = 1\pi$ respectively. d) shows the α versus the pitch period and flap angle for phase of 1π. The iso-lines on the plot represent constant ΔC_p values.

5.3 Model Versus Experimental Dynamic Stall

As discussed in the literature review in Section 2.3.4, Damiani *et al.* [63] developed a new unsteady aerodynamic model that could be used to simulate dynamic stall on an oscillating

2D airfoil. It is a semi-empirical model and the unsteady aerodynamic parameters must be tuned to match the experimental data as discussed in Section 4.5. After the parameters were tuned, test cases 2 and 3 were modeled and compared to experimental data. Note that the tuning parameters are presented in Appendix B.5 and were kept constant for all cases simulated.

The experimental data (solid line) and model data (dotted line) are plotted in Figure 5.20 for case 2 where k= 0.06 or 0.1, $\alpha_{mean} = 10^{\circ}$ and $\alpha_{amp} = 10^{\circ}$. The description of the dynamic hysteresis loop will not be repeated in this section and only the important differences or similarities between the model and the experimental data are mentioned. The model predicted the C_L cycle within 13% uncertainty while for the C_M cycle within 12% to 26% uncertainty. The location of the LEV peaks are within $\pm 1^{\circ}$. The peaks in the model are not as sharply defined as the experimental data. The model C_M cycle also predicted a CW loop indicating the occurrence of stall flutter similar to what was found in experimental data. The model was capable of more accurately simulating the cycle for higher k values as mentioned by Damiani *et al.* [63].



(a) Coefficient of lift, k=0.06

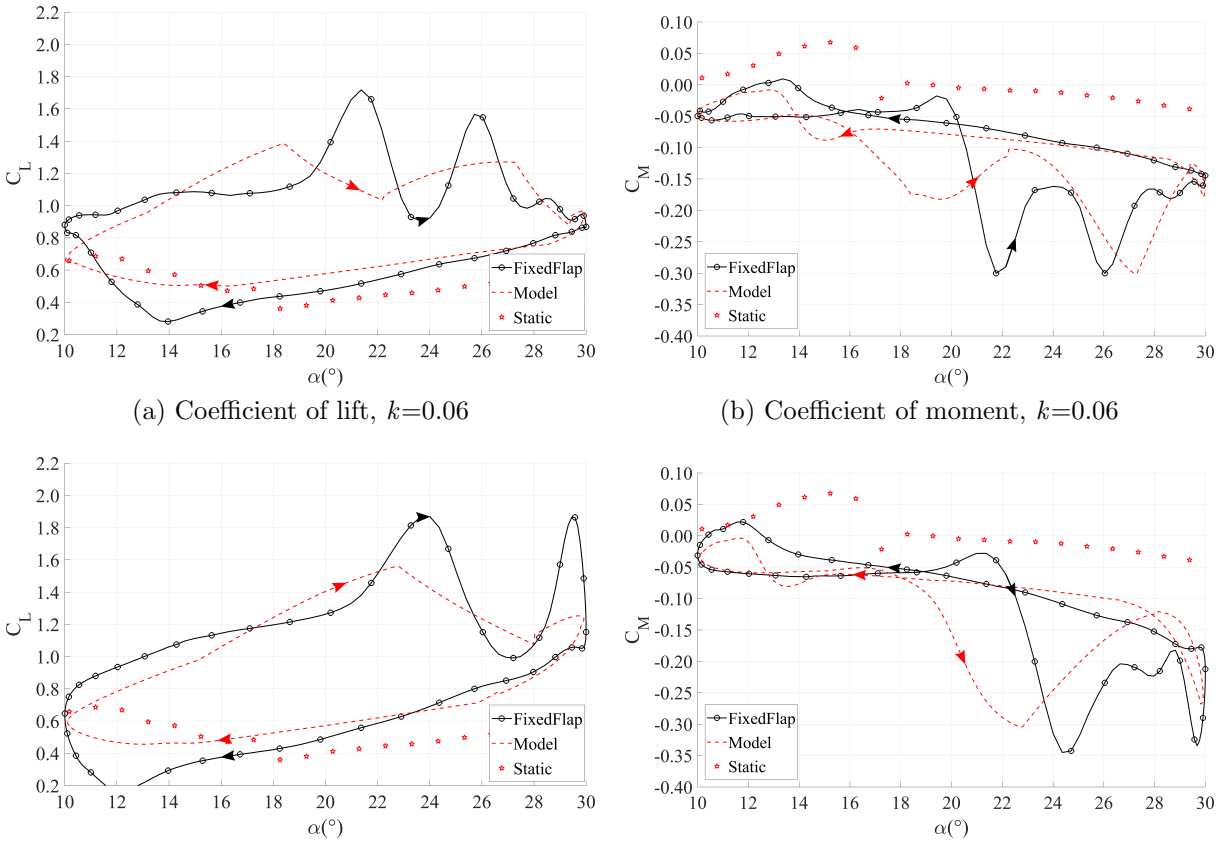
(b) Coefficient of moment, k=0.06

(c) Coefficient of lift, k=0.1

(d) Coefficient of moment, k=0.1

Figure 5.20: Coefficient of lift (C_L), and moment (C_M) versus α comparing the FixedFlap case to the unsteady aerodynamic model for case 2 where k= 0.06 or 0.1, $\alpha_{mean} = 10°$ and $\alpha_{amp} = 10°$.

Moving on to the more challenging cases to simulate, case 3 is plotted in Figure 5.21 where $\alpha_{mean} = 20°$. There are more discrepancies in this case and the uncertainty values for C_L and C_M are within 15%-18% and 14%-33% respectively. Although the model was capable of predicting multiple LEVs, they are not sharply defined as the experimental results and the peaks are within ±3°. It is possible to tune the model parameters further to reduce discrepancy in the magnitude and location of the LEV but for the purposes of this study the results are acceptable. The parameters could be tuned for every case separately but that is unreasonable since there is only one airfoil input file. The parameters were tuned to satisfy all cases equally.



(a) Coefficient of lift, k=0.06

(b) Coefficient of moment, k=0.06

(c) Coefficient of lift, k=0.1

(d) Coefficient of moment, k=0.1

Figure 5.21: Coefficient of lift (C_L), and moment (C_M) versus α comparing the FixedFlap case to the unsteady aerodynamic model for case 3 where k= 0.06 or 0.1, $\alpha_{mean} = 20°$ and $\alpha_{amp} = 10°$.

All the conditions that are presented so far are rather challenging because the airfoil is operating in the deep stall region. Even so, the model was capable of predicting the multiple LEV in the cycle and the uncertainty in magnitude is within 12% to 33%. Damiani *et al.* [63] also compared the model to different experimental results for different airfoils and conditions. The discrepancies they noted, match and resemble the discrepancies mentioned in this section. They argued that the discrepancy between experimental and model predictions could be due to the limitations of the code especially in deep stall. They concluded that the accuracy of the model is heavily dependent on the availability of experimental data and better tuning the unsteady aerodynamic parameters. The experimental data presented here will make a contribution to refine or provide validation data to the model. The author was in contact with the NREL group who are currently refining and building the OpenFast

model. Based on that correspondence, they stressed the need for more experimental data to tune the parameters in OpenFast to achieve smaller uncertainty values.

5.4 Conclusions

Static measurements of C_L and C_M for different α_F and a wide range of α from $-5°$ to $50°$ are briefly presented at Re of 170×10^3. They show that a TEF is capable of increasing and decreasing C_L and C_M for all the α range tested. This is important because it shows that the TEF is capable of equally manipulating airfoil coefficients when the airfoil is attached or stalled. The surface pressure contour plots showed that even though the flap is capable of changing $-\Delta C_p$ over the entire chord, most of the change is concentrated at the LE.

The hysteresis curves for C_L and C_M versus α were presented for a pitching airfoil with reduced frequencies of 0.06 and 0.1 and for α_{mean} of $0°$, $10°$ and $20°$. When $\alpha_{mean} = 0°$, the airfoil is pitching well below the static stall angle and the hysteresis cycle follows the static coefficients indicating no dynamic stall. As α_{mean} increases from $0°$ to $10°$, the C_L and C_M curves are altered significantly. The C_L values are approximately double their static counterparts for high α due to dynamic stall occurrence. There is a presence of multiple sudden peaks in the C_L data indicating the formation of multiple LEVs. The TEF was able to decrease the magnitude of negative damping and in some cases completely eliminating it as was seen in the $C_M - \alpha$ plots. As α_{mean} increased further from $10°$ to $20°$, the dynamic stall created two very noticeable LEVs and minor subsequent LEVs. It was found that changes in ϕ were responsible for promoting or delaying the occurrence of the LEV in the cycle by $1°$. The formation of multiple LEVs is in agreement with previous studies.

The unique $-\Delta C_p$ contour plots presented in this chapter showed a clearer picture of where the high suction peaks occur, flow separation on the airfoil and the formation of the primary and secondary LEV and how it moves along the airfoil. It was found that as the LEV is shed it tends to decrease $-\Delta C_p$ close the LE but increases $-\Delta C_p$ on the rest of the airfoil surface thus moving the center of pressure. In some cases, it was possible to locate the boundary layer transition points and stall area from the STD(ΔC_p) contour plots.

When k increased from 0.06 to 0.1 a few significant differences arose in the hysteresis loops: the amplitude of the C_L peaks increased indicating a larger and stronger LEV; there is a delay in the formation of LEV and flow reattachment; the difference between the upstroke and downstroke is increased, slightly widening the hysteresis loop and increasing load fluctuations; and the negative damping loops are longer and larger in magnitude. Based on the different cases tested it was concluded that the flap phase, ϕ, should be

determined based on α_{mean} and k because the load peaks occur at different locations. The TEF can manipulate airfoil coefficients and loads at any point on the cycle and that point is determined by ϕ. All the plots show how a TEF can influence C_L, C_M, $-C_p$, LEV, and stall. Based on the PSD plots, it was found that for the appropriate ϕ, C_L amplitude is reduced by at least 26% while the root bending moment amplitude is reduced by at least 24%. It can be concluded that the TEF is not capable of eliminating the LEV completely but it can reduce its impact on the airfoil.

The data presented throughout this chapter is a contribution to the academic community as more experimental data and analysis are needed to determine the influence of a TEF over the dynamic stall cycle for a cambered airfoil. The deep dynamic stall cases presented where the pitch angle reaches 30° are specially unique and novel since they have never previously been investigated. The data presented here for the different cases will be very useful for modelers to improve the uncertainty of dynamic stall models.

Chapter 6

Full-Scale Testing on a Wind Turbine

The wind turbine operated by the Wind Energy Group was upgraded to include an actuation system that controls the blade pitch and flap angle independently from the control room as presented in the experimental setup Section 3.3.3. This allowed the wind turbine to be operated in a wide range of test conditions where previous researchers couldn't. More sensors were included to measure the coefficient of power (C_{power}), flapwise bending moment (M_{FW}), and C_n through surface pressure measurement. The C_n measurements are a major contribution as it has never been measured before on a wind turbine equipped with TEF and individual pitch control (IPC). All the measurements could be averaged and investigated in relation to the azimuth position to study the cyclic variations on yawed turbines. This is another major contribution when compared to the average data published by Abdelrahman [104]. The wind turbine is operated in a controlled large-scale wind tunnel facility with high turbulence intensity which is more representative of the environmental conditions that wind turbines typically would be exposed to in the field. Previous studies mentioned in the literature review include turbines being operated in small-scale wind tunnel with negligible turbulence intensity, a misrepresentation of real environmental conditions, or turbines being operated in the field where there was no control over incoming velocity or environmental conditions. The setup presented in this study is ideal in the sense that the wind tunnel captures environmental conditions while the wind speed and other parameters are controlled.

This chapter consists of three major sections. The first section includes an overview and high-level discussion on how the pitch and flap system influences the three measured parameters (C_{power}, M_{FW}, and C_n). A comprehensive data matrix for different pitch angles, flap angles, tip speed ratios, and yaw angles is investigated in an averaged form to reveal high level or macro patterns. The second section takes individual data points from the

first section and dissects it to plot the data against azimuth for various constant pitch angles and tip speed ratios. By doing so, the impact of unsteady flow behavior on turbine loading is studied. The same data are also compared to OpenFast predictions to highlight the strengths and weakness of the model. Finally, the third section discusses how the TEF can manipulate blade loading under different operating conditions.

6.1 Pitch and Flap System Overview [1, 2]

A series of tests were conducted and outlined in the experimental setup to study the influence of pitch and flap on the turbine loading. The load was measured at three different locations: at the rotor, at the root of the blade, and at a blade segment. The influence of the pitch system on the turbine loading will be discussed first, followed by the flap system. Analysis and comparison of the two systems will be studied in detail for non-yawed and yawed turbines. This section provides a comprehensive study on how the pitch and flap influence turbine loading at different wind speeds. A direct and unique comparison between the pitch and flap systems is provided. Each data point presented in this section is the average of 1000 rotational cycles of the rotor and each cycle contains 600 data points.

6.1.1 Pitch Outline

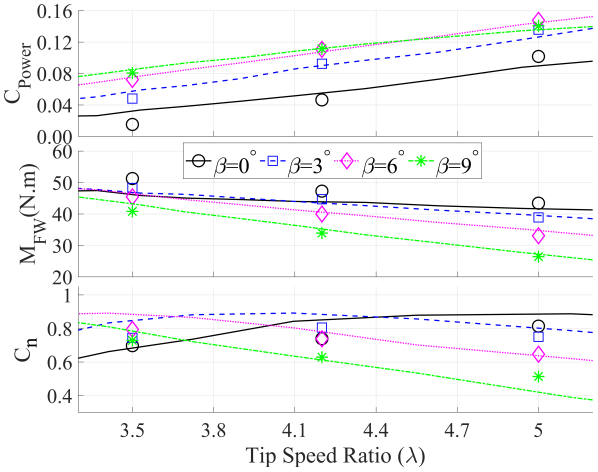
To measure the base loading of the present wind turbine, the turbine was run under different tip speed ratios and pitch angles. The coefficient of power (C_{power}), flapwise bending moment (M_{FW}) and C_n are plotted for different λ and β conditions in Figure 6.1 for $\gamma = 0°$, $\gamma = 30°$. C_{power} shows the performance of the entire turbine and M_{FW} shows the loading on a single-blade, while C_n shows the forces on a small segment of the blade. These three load measuring techniques provide insight at three different levels to paint a full picture of the loads on the entire turbine. PROPID [141], a blade element method software, was used to predict the three variables mentioned and they are plotted for comparison with the experimental data. The lines in Figure 6.1a are from PROPID while the markers represent experimental data. PROPID data for yawed conditions was not available.

[1] Presented at the NAWEA/WindTech International Conference 2019, Amherst, Massachusetts, USA. Oral presentation title: Influence of pitch and flap system on turbine loading

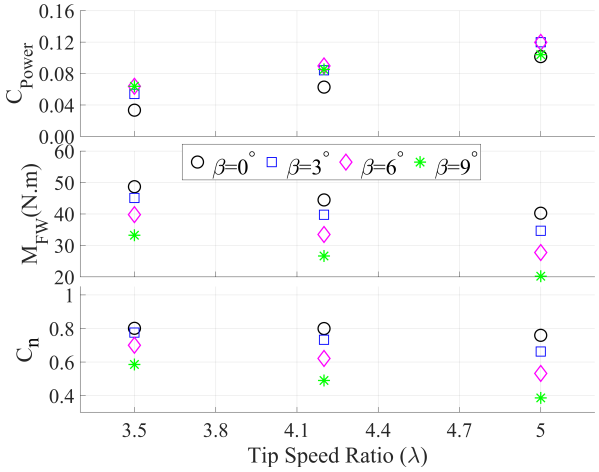
[2] Published by Samara, F., & Johnson, D. A. (2020). In-Blade Measurements of Cyclic Loading on Yawed Turbines with Trailing Edge Flap. Journal of Physics: Conference Series, 1452, 012061. doi.org/10.1088/1742-6596/1452/1/012061

Both plots in Figure 6.1 reveal, that C_{power} increases as λ increases or U_∞ decreases for the small range tested. For $\beta = 6°$, the analytical design condition, C_{power} is greater than the other three β cases indicating better performance. Both experimental and PROPID data exhibit the same trend and show that $\beta = 6°$ leads to a more optimal running condition for this turbine, specially for lower wind speeds. When $\beta = 0°$, α increases to such high angles of attack that the airfoil is then stalled decreasing lift while increasing drag and ultimately decreasing C_{power} when compared to the $\beta = 6°$ case. As expected for all cases C_{power} is small given the fact it is a single-bladed turbine with a constant pitch and chord. Both M_{FW} and C_n exhibit the same trend and decrease when β and λ increase. The distribution of both M_{FW} and C_n reveal that β tends to have a larger influence on the loading at higher λ and smaller influence at lower λ. This is because as λ decreases, U_∞ increases and that in turns increases the geometric angle of attack, α, based on the blade velocity triangle in Figure 2.7. When α is higher and the blade operates at the onset of stall, C_n is no longer linear and the airfoil is about to stall. The C_n values for both experimental and theoretical cases matched because the lift data for the airfoil were imported into PROPID from wind tunnel experiments for the S833 airfoil presented by Samara and Johnson [142].

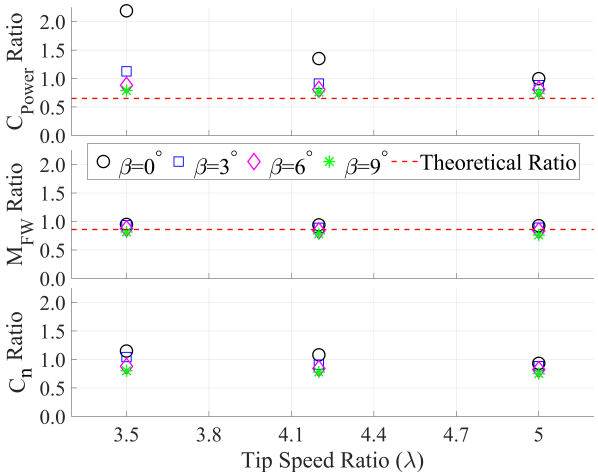
When the turbine is yawed to $\gamma = 30°$, C_{power} decreases except when $\beta = 0°$ where the C_{power} increased when the turbine is yawed. This could be explained by the fact that the blade is stalled during the entire rotation cycle for the non-yawed case but for the yawed case the blade goes in and out of stall, increasing the average power output. Based on the momentum theory for a turbine rotor there exists a relationship between yawed and non-yawed turbines for C_{power} and M_{FW} as outlined by Burton *et al.* [7] and expressed in Equation (2.14). This relationship is based solely on momentum theory and does not account for blade aerodynamics or blade stall. To compare this theoretical relationship to experimental, the ratio between $\gamma = 30°/\gamma = 0°$ for the three variables are presented in Figure 6.1c. The theoretical ratio line is overlaid on the C_{power} and M_{FW} plots for comparison. The biggest outlier from the theoretical ratio occurs when $\beta = 0°$ because the blade is mostly stalled and the momentum theory does not account for stall. For $\beta = 6°$ and 9° the ratio is the same across different λ and greater than the theoretical value. The slight mismatch could be attributed to rotor aerodynamics. On the other hand the experimental M_{FW} ratio is much closer to theory.



(a) $\gamma = 0°$ (Markers are experimental data while lines are theoretical data from PROPID)



(b) $\gamma = 30°$

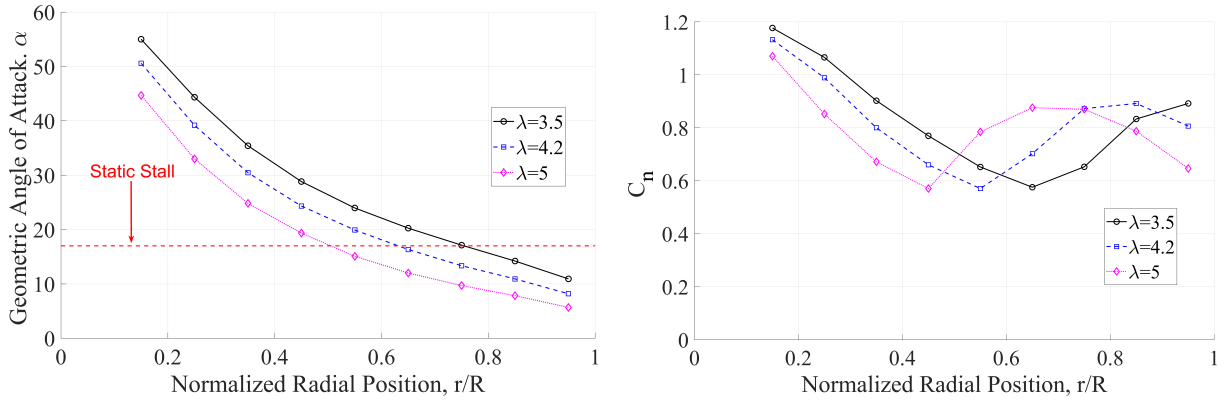


(c) Ratio between $\gamma = 30°/\gamma = 0°$

Figure 6.1: C_{power}, M_{FW}, and C_n (at r/R=0.82) for different β angles and tip speed ratios. (a) $\gamma = 0°$, (b) $\gamma = 30°$, (c) $\gamma = 30°/\gamma = 0°$

To better understand the aerodynamic behavior of the blade with constant pitch and chord, the geometric angle of attack (α) and C_n spanwise distribution are plotted in Figure 6.2 for $\beta = 6°$ for the three tip speed ratios. The static stall angle is marked by a dotted red line in Figure 6.2a. Due to the constant pitch, the blade is stalled for r/R<0.5 and as λ decreases a larger portion of the blade is stalled. Angle of attack could reach values as large

as 55° close to the root of the blade. Such high angles were also found by Abdelrahman [104] and Gallant and Johnson [57]. Figure 6.2b shows that C_n is higher at the root of the blade even though the blade is stalled. This is a characteristic feature of the S833 airfoil and is seen in the static lift data presented in the previous chapter. The trend in lift decreases after stall but then increases again for high α. Moving from the root of the blade to the tip, C_n first decreases and then starts to increase when the static stall angle is reached, then it decreases again when the angle is lower than the static stall point. On the other hand, C_D is much greater when the blade is stalled and the power output is drastically reduced.



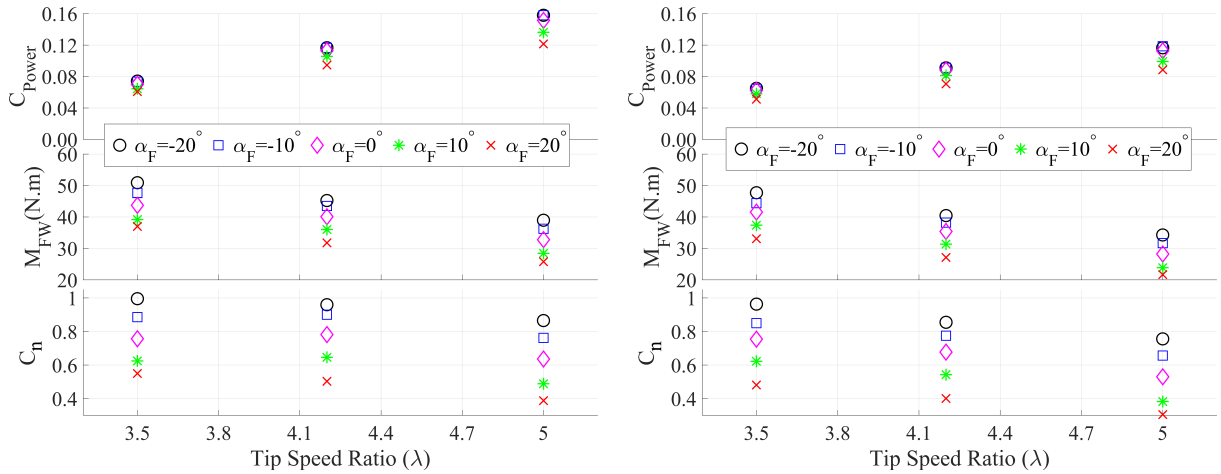
(a) PROPID Geometric angle of attack, α (b) PROPID C_n

Figure 6.2: (a) Geometric angle of attack, α, and (b) C_n distribution along the spanwise of the blade for $\beta = 6°$ from PROPID

6.1.2 TEF influence on turbine loading

The same parameters plotted in Figure 6.1 are presented in Figure 6.3 but instead of varying β, the flap angle, α_F changes. It is noted that C_{power} has a smaller change when α_F is varied in comparison to β changes especially at lower λ. This is because the TEF alters only 22% of the aerodynamic blade span while preserving the rest of the blade. The pitch system, changing β, on the other hand alters the entire aerodynamics of the blade. When β is altered it also changes the percentage of the blade that is stalled for a constant λ value. Unlike the pitch system, the rate of change in M_{FW} with respect to α_F is the same for different λ. This indicates that the linearity of the flap system is not influenced by λ. When compared to the pitch system, the change in C_n with α_F variation is much more significant and linear. This is because experimental data showed that the influence

of the TEF on C_n is linear for the entire range of α and is not affected by the stall angle [142]. The data in Figure 6.3b is mostly shifted slightly lower when compared to Figure 6.3a because the turbine blade is partially stalled when the turbine is yawed to 30°. Figure 6.3b for $\gamma = 30°$ also shows that the flap system does influence the three variables equally for yawed and non-yawed conditions.



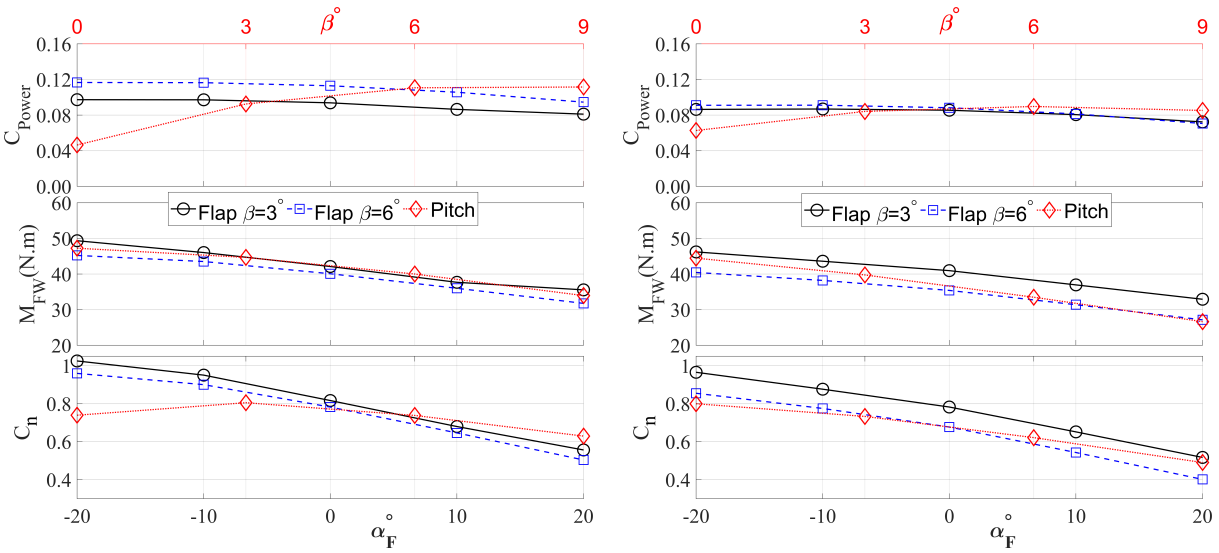
(a) $\gamma = 0°$ (b) $\gamma = 30°$

Figure 6.3: C_{power}, M_{FW}, and C_n (at r/R=0.82) for different α_F angles at $\beta = 6°$. (a) $\gamma = 0°$, (b) $\gamma = 30°$.

6.1.3 Pitch and Flap Comparison

To better illustrate the differences between the pitch and flap system, the influence of β and α_F on C_{power}, M_{FW} and C_n are plotted on the same graph for $\lambda = 4.2$ in Figure 6.4. The value of α_F is shown in the bottom x-axis while β is displayed on the top x-axis. The plot clearly shows that the pitch system has a greater influence on C_{power} than the flap system as concluded earlier. The slopes of the pitch and flap results show that their influence over M_{FW} is very similar. This is significant as it indicates that the TEF is capable of manipulating M_{FW} better than or equal to pitching the entire blade and without influencing the power output. As expected the flap system has a greater influence over C_n because C_n is measured at midspan of the TEF. The TEF can increase or decrease C_n in a linear fashion unlike pitching the entire blade. The TEF only occupies 22% of the aerodynamic blade span or about 4% of the blade surface area but its control authority is very similar to that of pitching the entire airfoil, but without the negative impact of

decreasing C_{power}. This could be explained by the fact that most of the power produced by the blade is located around r/R=0.77, as shown by Johnson *et al.* [107]. Placing the TEF at that location has the largest impact on the loading of the blade. This indicates that the TEF has a great deal of influence over the bending moment on the entire blade using only 4% of the surface area. The TEF can increase or decrease M_{FW} by about 15%, which aligns with what was found in the literature review. Based on the M_{FW} plot in Figure 6.4a, the slope of the flap influence is 0.325 Nm/° while the slope of the pitch is 1.44 Nm/°. There is an order of magnitude difference between the two, but changing the pitch angle is much more difficult than changing the flap angle. Another important benefit favoring the TEF is that the load control is localized whereas the pitch system changes the loading on the entire turbine blade. It is important to re-iterate that the TEF is tested on a single-bladed turbine with constant chord and pitch. The control authority of the TEF may be different for a twisted blade with variable chord.



(a) $\gamma = 0°$ (b) $\gamma = 30°$

Figure 6.4: C_{power}, M_{FW}, and C_n (at r/R=0.82) for different α_F (bottom axis) and β (top axis) angles for $\lambda = 4.2$. (a) $\gamma = 0°$, (b) $\gamma = 30°$.

6.2 Steady Pitch and Tip Speed Ratio Cases [3]

Averaging loads on the turbine for the entire azimuth or rotational cycle does not provide insight into how the load fluctuates with rotor rotation, specially for yawed cases. Beginning with section, ΔTorque, M_{FW}, and C_n are plotted against azimuth position (ψ) to better understand and study the forces and aerodynamics of the blades as they rotate. In this section the influence of pitch and tip speed ratio on the wind turbine performance are studied.

6.2.1 Outline

The complete wind turbine base loading test configuration was introduced earlier in Section 4.2.1. Out of the numerous tests conducted, only the most interesting and relevant cases are plotted in this section. Table 6.1 organizes the test cases together with the different variables and figure references. Initially, different wind speeds were tested on a yawed and non-yawed turbine to determine how the performance of the turbine changes. This provided insight into how the aerodynamics of the turbine differ for the various tip speed ratios tested. Subsequently, different blade pitch angles were tested to study how it influences cyclic loading on a turbine under steady and unsteady conditions. The normal force coefficient, C_n, was measured at two r/R locations, 0.66 and 0.82, by moving the blade section that houses the pressure transducers. For all the cases presented in this section, the experimental data was compared to the NREL OpenFast code described in Section 2.3.4. After all the cases are discussed, a brief list of conclusions are made about the accuracy of OpenFast and the important findings from this section.

OpenFast was used in two different capacities. Initially, it validated the steady experimental results; subsequently, the unsteady experimental data presented was used to identify possible limitations in OpenFast. The OpenFast code is based on the BEM approach and has been adjusted and validated against prior experimental data and that makes its prediction useful, particularly when the turbine is operating in steady and non-yawed conditions [14, 64]. As a result, the experimental data were expected to somewhat match OpenFast predictions in steady and non-yawed conditions. In more challenging conditions where dynamic stall occurs, OpenFast has been noted to perform poorly when compared to the limited experimental data available in the academic community [11, 63]. For this reason, and after increasing confidence and reliability of the experimental data, the role

[3] Accepted at the TORQUE 2020 International Conference 2020, Delft, Netherlands. Accepted oral presentation title: Experimental Load Measurement on a Yawed Wind Turbine and Comparison to FAST

was switched and experimental data in unsteady cases were capable of identifying the inaccuracies in how the wind turbine was setup or the inherit limitations of the OpenFast code.

Table 6.1: Test matrix for pitch cases in steady conditions

Case	λ	$\beta(^\circ)$	$\alpha_F(^\circ)$	$\gamma(^\circ)$	Variables Presented	Figure Reference
1a	[3.5, 4.2, 5]	6	0	0	Torque, M_{FW}, C_n	Figure 6.5
1b	[3.5, 4.2, 5]	6	0	30	Torque, M_{FW}, C_n	Figure 6.6
1c	5	[0, 3, 6, 9]	0	0	Torque, M_{FW}, C_n at r/R=0.82 and 0.66, ΔC_p	Figure 6.7, and 6.8
1d	3.5	[0, 3, 6, 9]	0	30	Torque, M_{FW},{C_n, ΔC_p, $STD(\Delta C_p)$} at r/R=0.82 and 0.66	Figure 6.9, 6.11, and 6.12

6.2.2 Tip Speed Ratio Influence

Non-Yawed Turbine

The wind speed is one of the most important parameters when studying the aerodynamics of a wind turbine. Wind speed determines the geometric blade angle of attack (α), tip speed ratio, power output and most importantly in this study, the magnitude of blade loading. Thus it is important to study how the change in wind speed (change in λ) influences the turbine performance parameters: ΔTorque, M_{FW} and C_n. These variables are plotted against azimuth, ψ, for λ=3.5, 4.2 and 5 as per Table 6.1. The same test matrix discussed was simulated in the OpenFast semi-empirical model (dotted lines in the figures) and compared to the experimental data (solid lines in the figures). Refer to Section 4.5 for more information about OpenFast and settings. Focusing on the non-yawed case in Figure 6.5, it is noted for all cases that the pattern in the performance variables does not change with wind speed but only the magnitude is altered. The pattern in the data is the same even though each data set was collected on different dates. This consistency demonstrates repeatability in the measurements and increases confidence in the results. As the wind speed increases or λ decreases, the turbine loads increase as indicated by the three plotted variables but the increase is not linear. This is because as the incoming velocity vector (U_∞) increases, the geometric angle of attack (α) also increases according to the relative

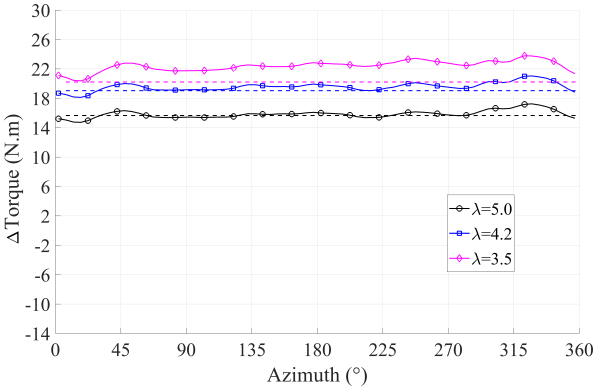
velocity triangle in Figure 2.7. The α increase is also seen in the OpenFast results and the values are identified in the legend of Figure 6.5. The variation in α versus azimuth is constant as expected because $\gamma = 0°$.

The torque measurements appear first in Figure 6.5a since torque a measure of performance of the entire rotor. The measurements are phase-averaged from 1000 cycles into bins of 5°. The ΔTorque measurement displayed here is the difference between the torque generated with an incoming wind speed of 0 and the torque generated when the wind speed is set to the desired speed as discussed in Section 4.6.1. This approach was done to the experimental and model data alike to highlight the torque generated by the single-blade and eliminate the drag generated by the counterweight cylinders. The torque generated with incoming wind speed of 0 was measured to be 29 Nm while OpenFast prediction was 28.9 Nm. This means that if ΔTorque is greater than 29 Nm then the rotor torque is positive but if it is less than 29 Nm then the rotor torque is negative and the motor in the nacelle is driving the rotor. Since ΔTorque in all the cases presented is less than 29 Nm, this indicates that the single-bladed rotor is not capable of providing sufficient rotational force to overcome drag at the operated rotational speed. This observation is repeated in OpenFast as both experimental and model results are very similar. At λ=5, ΔTorque from OpenFast and experimental data accurately matched but when λ increased to 3.5, OpenFast under-predicted by 5%. This difference is acceptable and could be due to uncertainty in experimental results, model input parameters and OpenFast model predictions. The small variations in ΔTorque are mainly due to the wind tunnel non-uniformity.

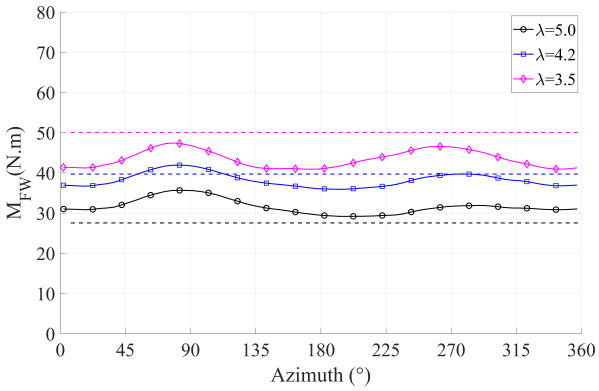
Focusing on the M_{FW} plots in Figure 6.5b, there is an increase in bending moment for the three λ cases at $\Psi \approx 90°$ and 270°. This is due to an increase in the incoming velocity (U_∞) at that location and is characterized and discussed in Section 3.3.1. This non-uniformity was also observed by Gallant [129] and McKinnon [125] and is found in all data sets for the same reason previously mentioned. The OpenFast model produced values that were very comparable to the experimental results but the non-uniform velocity field from the wind tunnel were not simulated. The discrepancy between OpenFast and experimental data is mainly due to the discrepancy in C_n and is discussed in the next paragraph.

In Figure 6.5c, C_n exhibits both a non-uniformity and a minor oscillation with azimuth but the pattern is the same across different λ. This oscillation is mainly due to the non-uniformity in wind speed from the wind tunnel. OpenFast was able to reproduce constant C_n values versus azimuth that are very representative of the experimental data. This results was expected because the aerodynamic data of the S833 airfoil from the experimental campaign in Chapter 5 were imported into the model. The difference between OpenFast and the phase-averaged experimental data is 4%, 2% and 7% respectively for $\lambda = 3.5$, 4.2

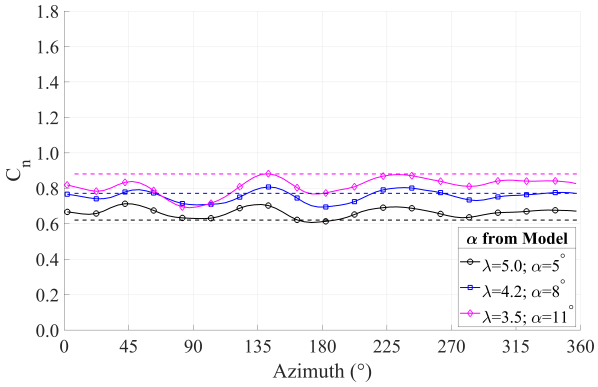
and 5.0. These minor discrepancies are mainly due to experimental and model uncertainties that were discussed in Section 4.6. Based on the α values at r/R=0.82 obtained from the model, the airfoil section is not stalled for any of the λ cases. Typically, non-stalled cases are not challenging to predict and that is why OpenFast produced relatively accurate C_n values.



(a) Rotor Torque



(b) Flapwise Moment (out of plane)



(c) C_n at r/R=0.82

Figure 6.5: Turbine performance for various λ values for case 1a where $\beta = 6°$ and $\gamma = 0°$. Solid lines represent experimental data while dotted lines represent OpenFast model data. Every 4$^{\text{th}}$ data point is marked on the solid lines for clarity.

Yawed Turbine

Wind turbine aerodynamics in yawed conditions, which were discussed in Section 2.2.4, are very different than non-yawed operation. Due to yaw angle, γ, the incoming wind speed and the induced velocity both vary as a function of azimuth position and that dependence leads to a geometric change in angle of attack, α. The induced velocity, discussed in more detail in Section 2.2.4, is defined as the velocity decrease at the rotor plane and its magnitude is a function of the axial induction factor, a, in Equation (2.13). Unlike the case in the previous section where the theoretical velocity triangle was constant during rotation, in yawed flow the angles and velocity vectors in the velocity triangle are constantly changing with azimuth position producing cyclic loading on the blades. The variation in ΔTorque, M_{FW}, C_n and α are plotted in Figure 6.6 for different λ values and for yaw angle, $\gamma = 30°$.

Focusing on Figure 6.6a, experimental ΔTorque measurements slightly vary with azimuth position and the trough and crest are located at $\psi \approx 155°$ and 320°, respectively. On the other hand, OpenFast predictions show significant ΔTorque variations with ψ but the crest and trough locations match the experimental data. This difference between experimental and OpenFast data is attributed to two main factors: angular momentum, and physical nacelle rig characteristics. Due to blade rotation and weight of the blades/hub, the momentum and inertia of the rotor significantly dampens out the torque variation with azimuth similar to what was reported by Gallant [129]. The angular momentum of the rotating blades was calculated to be 230 kg m^2/s based on a rotation of 200 rpm, a blade mass of 5 kg and a blade length of 1.77 m. On the other hand, the angular momentum change due to ΔTorque of 30 Nm from OpenFast is about 0.23 kgm $^2/s$ or 0.1%, which is insignificant. More detailed calculations may be found in Appendix D.5. Thus the torque sensor mounted to the wind turbine shaft does not see a significant change in torque despite a force increase on the blades because of the large angular momentum inherent in the rotor. OpenFast does not seem to model angular momentum; to be certain that was correct, the blade mass was increased by tenfold but the predicted ΔTorque did not change. Angular momentum is also found in the shaft, gearbox, and generator that could further dampen out the ΔTorque variations even further. Another less significant reason as to why ΔTorque is different between the model and experiments is due to the proportional-integral controller (PI) that controls the motor in the nacelle described in more detail in Section 3.3.2. Due to the single-bladed rotor, the motor provides power to the rotor and not the other way around as previously mentioned. If the rotor experiences a change in load then the PI controller senses that change and sends more or less power to the rotor to keep the rotational speed constant, thus dampening out the measured torque fluctuation. Since the torque sensor measures the torque difference between the rotor and generator, it cannot

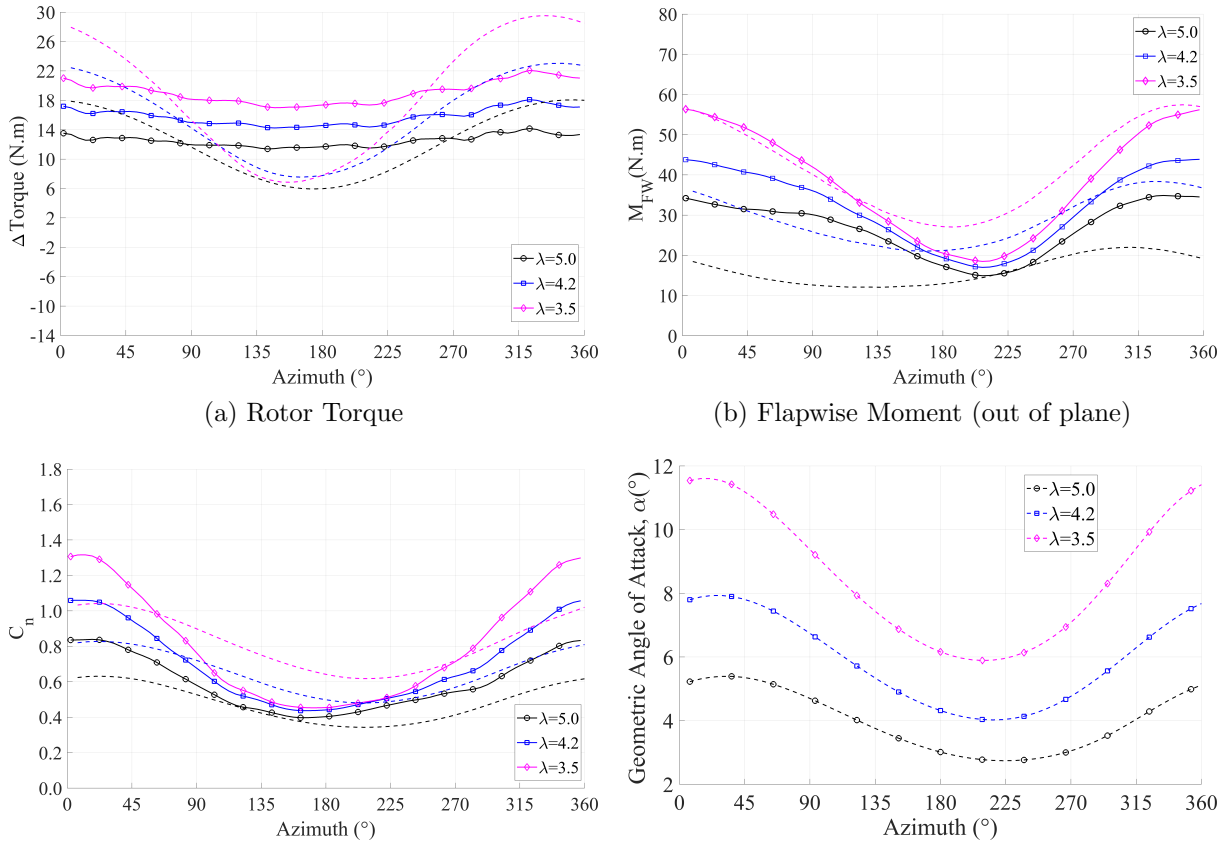
measure the change of torque from the rotor alone.

Looking at the M_{FW} variation in Figure 6.6b, the experimental data for the three different λ cases converge around the cycle center ($\Psi = 180°$) and diverge at the cycle ends ($\Psi = 0°$ or $360°$). This pattern indicates that the blade load fluctuation increases as λ decreases. This trend is supported by the OpenFast model but is not as explicit. The trough in the experimental data is not located $\Psi = 180°$ but shifted to the right to $\Psi \approx 220°$. When the trough is at $\Psi = 180°$ this indicates that the load variation is dominated by the fluctuation of wind velocity relative to the blade. On the other hand, when the trough is shifted from the center, it indicates that the induced velocity component variation with azimuth is significant as explained in Section 2.2.4. The magnitude of the induced velocity is dependent on a, which in turn is dependent on C_{power} derived from the rotor torque. Even though rotor torque increases with an increase in free stream velocity, C_{power} decreases as seen in Figures 6.1b and 6.6a. A reduction in C_{power} leads to a smaller axial induction factor, a, according to Equation (2.10). This shows that as λ decreases so does a and that reduction, in turn, reduces the effect of the induced velocity. For this reason the trough for $\lambda = 3.5$ is located closer to $\Psi = 180°$ than $\lambda = 5$ as seen more clearly in the OpenFast model and supported by Burton *et al.* [7]. The OpenFast model is very comparable to experimental data for $\lambda = 3.5$ but when $\lambda = 5$, the difference is more significant. These differences are due to the discrepancy in C_n and are discussed in more detail in the next paragraph. Blade loading is determined by integrating C_n across the blade span so any discrepancy in C_n causes error in blade loading.

The C_n variation at r/R=0.82 for the different λ cases is plotted in Figure 6.6c. For all three cases, the troughs are located in the same position at $\Psi = 180°$ unlike the M_{FW} data. The α-azimuth distribution at r/R=0.82 was obtained from OpenFast and plotted in Figure 6.6d. This plot indicates α does not exceed the stall angle for all cases displayed and it also suggests that dynamic stall does not occur. The cyclic variation in C_n is mainly due to α (plotted) and velocity vector (W) change with azimuth when the rotor is yawed. The importance of this velocity change is discussed and plotted against azimuth in Section 4.6.3 and is used to calculate C_p and C_n. The variation in W with azimuth is significant and causes large cyclic variation in C_n.

There is a significant discrepancy between the experimental data and the model, and there are multiple sources of errors, some more significant than others. One of the main sources of discrepancy is based on how the physical model programmed in OpenFast and what parameters were chosen to simulate unsteady wind turbine behavior. Even though OpenFast is a medium complexity source code it requires tremendous effort and expert knowledge of rotor theory to set the model up, from obtaining accurate airfoil coefficients to tuning dynamic stall parameters to understanding the limits of the predictions. OpenFast

setup is discussed in more detail in Section 4.5. One of the main uncertainties in blade aerodynamics lies in the effects blade rotation has on the airfoil coefficients specially for high λ values [14]. These coefficients are the most important input parameter that determines accuracy of the model and they should be corrected for 3D flow effects. These 3D flow effects are induced by the rotation of wind turbine blades and significantly alter the stall angle and slope of the $C_n - \alpha$ data as discussed in Section 2.4.2. The stall angle and $C_n - \alpha$ slope also change for different blade spanwise locations because 3D flow effects are more significant closer to the root of the blade than to the tip area. AirfoilPrep, which was described in Section 2.3.3, was used to modify the lift data independent of airfoil geometry based on a model developed by Du and Selig[60]. There is an inherent error associated with this modification because each airfoil may perform differently in 3D flow as reported by Schreck *et al.* [14, 79]. There are many other 3D flow effects on the blade such as tip/root losses discussed in Burton *et al.* [7] and post stall dynamics [64]. It was suggested that the choice of airfoil geometry has a strong influence on the strength and characteristics of 3D stall effect [14]. So even though OpenFast implements corrections to simulate 3D flow, these corrections are dependent on airfoil geometry and thus become the inherent error associated with these corrections. Errors could also arise from the different aerodynamic models OpenFast uses in predicting wind turbine loads [64]. OpenFast is based on a BEM model that is executed independently of airfoil geometry or aerodynamics. Another major source of error is OpenFast's inability to predict an accurate α distribution over the blade span and that weakness is a fundamental fault in the classic BEM aerodynamic models. Even if accurate airfoil coefficients that take into account 3D flow behavior are used, having the incorrect α distribution leads to inaccurate turbine loading and can influence subsequent predictions of the rotor performance. Another unique source of error in this project is related to the single-bladed rotor with constant pitch and chord. The lack of twist in the blade, to make it modular, forces a large section of the blade to operate in stall and unsteady aerodynamics that are generally more difficult to predict and model. The final cause of error is due to experimental uncertainties, which are discussed in more detail in Section 4.6. All the sources of discrepancies just mentioned are found in the data presented in this section and subsequent sections.



(a) Rotor Torque

(b) Flapwise Moment (out of plane)

(c) C_n at r/R=0.82

(d) α distribution based on the OpenFast Model

Figure 6.6: Turbine performance for various λ values for case 1b where $\beta = 6°$ and $\gamma = 30°$. Solid lines represent experimental data while dotted lines represent OpenFast model data. Every 4^{th} data point is marked on the solid lines for clarity.

6.2.3 Pitch Angle Influence

Non-Yawed Turbine

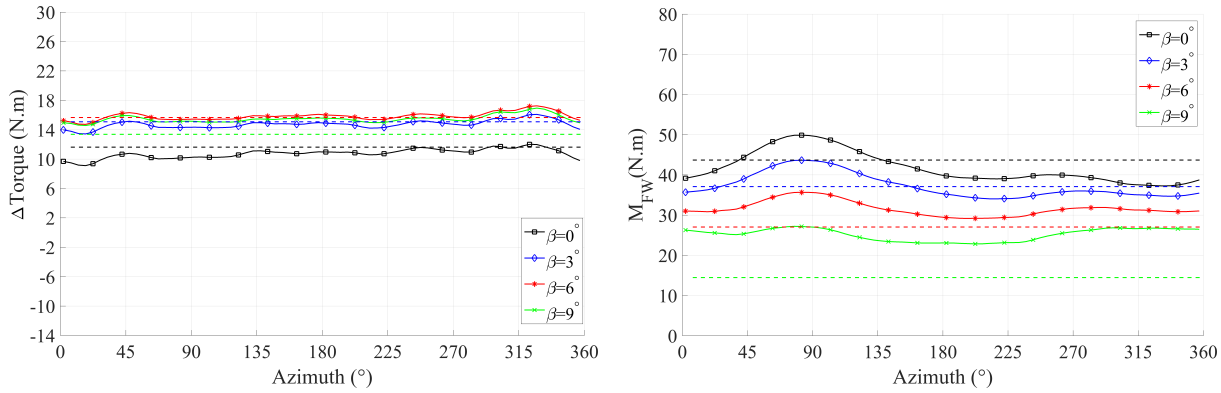
After studying the influence of changing wind speed on turbine performance, the influence of changing the pitch angle, β, is studied in this subsection. The same performance parameters are plotted versus azimuth in Figure 6.7 for a constant $\lambda = 5$, $\gamma = 0°$, and $\beta = [0°, 3°, 6°, 9°]$. The blade pitch angle is an important parameter to study because it is one of the parameters that determines whether the flow over the blade is stalled or

attached. Blade pitch angle also determines the efficiency of the turbine rotor because it allows the blade to operate at the $C_L - \alpha$ peak. At first, ΔTorque is plotted in Figure 6.7a for different β cases. Experimental and model data both show that when $\beta = 6°$, the analytical design condition, the most power is produced similar to the conclusion made in Section 6.1.1. This also illustrates that blade pitch determines the entire wind turbine efficiency. OpenFast predictions matched experimental torque measurements with a maximum discrepancy of less than 6%, which is considered a very good agreement.

Focusing next on the flapwise moment (M_{FW}) plots in Figure 6.7b, the moment increase at $\psi = 80°$ is due to the non-uniformity in wind speed from the wind tunnel, which becomes more apparent as β decreases. This effect arises because at lower β angles, the blade would be operating close to the stall region where small wind velocity variations could lead to blade stall, thereby significantly altering the loads on the blade. The discrepancy between the OpenFast model and experimental data becomes more significant as β increases. This discrepancy is due to a smaller lift prediction by the model as seen in the C_n plots in Figures 6.7c and 6.7d. The α values from the model are identified in the C_n plot legend and indicate that at r/R=0.82 and 0.66 the blade segment is not stalled for the model. There is no indication of stall in the experimental data either and that is based on the $-\Delta C_p$ contour plots presented in Figure 6.8. OpenFast C_n predictions accurately resemble experimental data in some β cases because the same blade segment used on the full-scale wind turbine was also used to obtain the 2D lift data that were imported into OpenFast. The discrepancy in C_n between the model and experiment is most likely due to the 3D flow effects of the blade, which were discussed in greater detail in the previous subsection. As mentioned, AirfoilPrep was used to modify and correct the airfoil coefficients to account for 3D flow effects based on Du and Seling[60]. The model predicts that at r/R=0.82, in Figure 6.7c, the 3D flow effects are negligible and no substantial modification to the lift coefficient is required. On the other hand, experimental data indicate that the 3D flow effects are not negligible as modeled but rather are significant and the lift is enhanced due to 3D flow effects. For C_n at r/R=0.66, in Figure 6.7d the discrepancy between OpenFast and experimental data is much smaller because AirfoilPrep altered the airfoil coefficient significantly to account for 3D flow effects. The experimental data indicate that 3D flow effects are present along the entire span of the blade. Jonkman [64], using the UAE data, and Schreck *et al.* [14], using the MEXICO data, both found that OpenFast under predicted the 3D flow effects on the turbine rotor, especially at the outboard section of the blade.

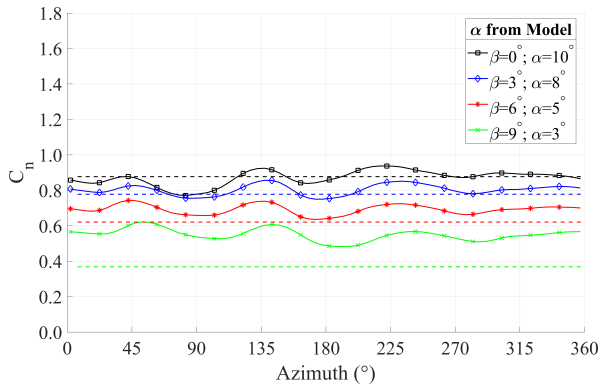
Finally, the blade edgewise moment or in-plane moment (M_{EW}) is plotted in Figure 6.7e. The in-plane moment is dominated by gravity forces as the blade is rotating thus producing the highest peaks at $\psi = 90°$ or $270°$ (when the blade is at 3 or 9 o'clock

position). The shift in moment along the y-axis as β changes is mainly due to the change in drag coefficient as α changes. The Wind Off case is included when the turbine is being rotated with the wind tunnel off to measure the drag on the cylindrical counterweights and the aerodynamic blade while $\beta = 0°$. This is why for this case only, the M_{EW} cyclic average is about 0 Nm. As the drag on the blade increases the moment cycle is shifted downward. The model's accuracy in predicting M_{EW} that matches experimental data is highly dependent on the blade input files to OpenFast especially the weight and drag coefficient values. Experimental data show that for all β cases, the M_{EW} data are very similar to each other with slight variation in the y-axis due to an increase in drag on the blade. For this reason $\beta = 0°$ produces the lowest mean in M_{EW} because a large section of the blade is stalled increasing drag. OpenFast predictions matched experimental data for all cases with a discrepancy of less than 5%.

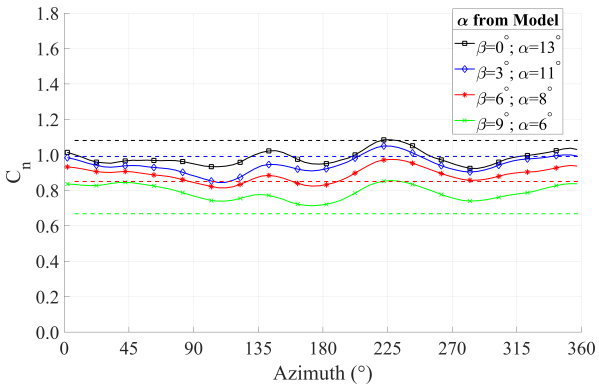


(a) Rotor Torque

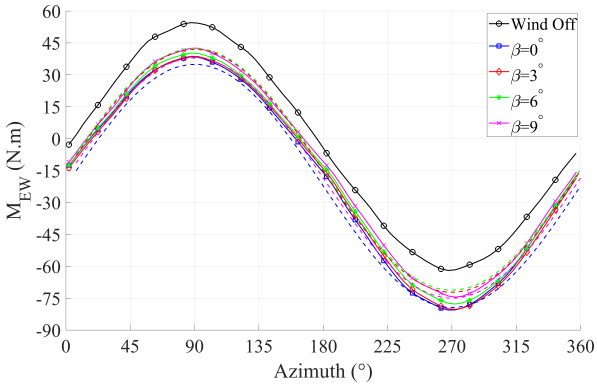
(b) Flapwise Moment (out of plane)



(c) C_n at r/R=0.82



(d) C_n at r/R=0.66



(e) Edgewise Moment (in-plane)

Figure 6.7: Turbine performance for various β for case 1c where λ=5 and $\gamma = 0°$. Solid lines represent experimental data while dotted lines represent OpenFast model data. Every 4^{th} data point is marked on the solid lines for clarity.

To study the surface pressure distribution of the 3D blade at a more detailed level along the blade chord, contour plots of $-\Delta C_p$ against the chord on the x-axis (x/c) and azimuth angle on the y-axis (ψ) are displayed in Figure 6.8. The plots are a matrix of 27 differential pressure measurements along the airfoil chord by 72 bins, which each corresponding to 5° of rotation. Each point in the matrix is the average of 8000 data points. Out of the four β cases tested, only $\beta = 0°$ and 6° are presented because the other two cases look very similar. Focusing on the $\beta = 0°$ case, ΔC_p is concentrated at the LE indicating that the blade section at r/R=0.82 is not stalled. This result is in agreement with OpenFast because it predicted $\alpha = 10°$ and smaller than the stall angle. There are small variations with azimuth position that lead to small changes in C_n as seen in Figure 6.7c. As β increases, α decreases thus diminishing the ΔC_p peak at the LE as seen in the contour plot in Figure 6.8.b. The STD in ΔC_p was also studied but not included here because the STD values were very small and negligible, indicating no significant pressure fluctuations.

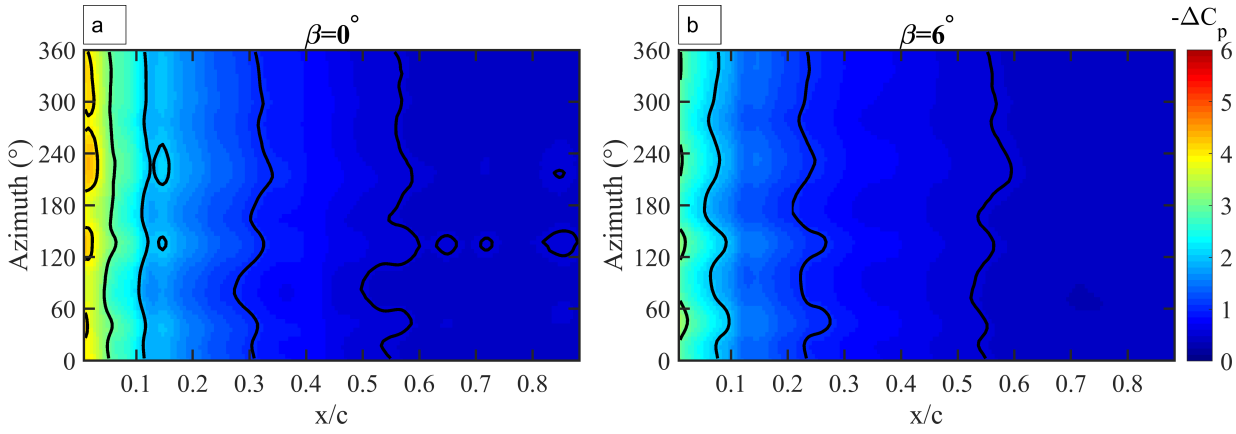


Figure 6.8: Contours of $-\Delta C_p$ versus x/c versus ψ at r/R=0.82 for a) $\beta = 0°$ and b) $\beta = 6°$ for case 1c where $\lambda = 5$ and $\gamma = 0°$. The iso-lines on the plot represent constant $-\Delta C_p$ values=[0 0.5 1 2 3 4].

Yawed Turbine

The same series of plots displayed before for the non-yawed turbine are now presented for $\gamma = 30°$ and $\lambda = 3.5$ in Figure 6.9. The ΔTorque data in Figure 6.9a reveal that the highest power produced by the rotor is when $\beta = 6°$ or 9°, which parallels the observation and conclusion based on Figure 6.1b. Smaller β angles produce less power because a larger section of the blade is stalled. The discrepancy between OpenFast and experimental data is very significant and this is caused by the angular momentum in the rotating rotor

that dampens out rotor torque variations similar to what was discussed in Figure 6.6 and the calculations are shown in Appendix D.5. That being said, both OpenFast and experimental ΔTorque data exhibit very similar trends as β changes and the troughs and crests are located at $\psi \approx 160°$ and 320° respectively. Focusing on the flapwise moment (M_{FW}) versus azimuth plot in Figure 6.9b, as β decreases the load variation increases. One of the reasons this happens is because the loading on the blade is higher when β is smaller as seen in Figure 6.7 for the non-yawed case. Another reason is that as β decreases, a larger portion of the blade span would be operating in the dynamic stall region causing a larger load fluctuations as was concluded from Figure 6.2a. For example, the $\alpha - \psi$ distribution at r/R=0.82 and 0.66 from OpenFast in Figures 6.9d and 6.9f shows that as β decreases the blade section starts to operate past the static stall point where unsteady dynamic may occur. Unsteady dynamics and dynamic stall are discussed in more detail in the next few paragraphs when looking at the C_n plots. For smaller β angles, the OpenFast model prediction for M_{FW} is very close to the experimental data. On the other hand, as β increases the discrepancy between the model and experimental data increases. This is attributed to the discrepancy in C_n and is discussed next.

Lastly, the C_n azimuth variation at r/R=0.82 and 0.66 for different β cases is plotted in Figures 6.9c and 6.9e. Interestingly, all the experimental β cases converge at the cycle trough or at $\psi = 180°$. This happens even though there is an 8° difference in α between the highest and lowest β case. The α variation with azimuth obtained from OpenFast at r/R=0.82 and 0.66 is plotted in Figures 6.9d and 6.9f because these patterns assist in explaining the pattern in C_n. At both radial locations, the trend in C_n indicates that there is a significant unsteady aerodynamic behavior occurring and in some cases dynamic stall may be present. A few important differences arise when comparing C_n variation at r/R=0.82 and 0.66. The fluctuations in C_n are increased significantly indicating a stronger unsteady aerodynamics behavior and a strong dynamic stall. From Chapter 5 it was concluded that dynamic stall and unsteady aerodynamics are influenced by three main parameters: reduced frequency (k), α oscillation amplitude and α oscillation mean. As r/R decreases from 0.82 to 0.66 all these parameter change: k increases from 0.057 to 0.076, α amplitude increases from 7° to 9.5° and α_{mean} increases by 4°. It was concluded from Section 5.4 that increasing all these parameters was found to increase dynamic stall behavior leading to a larger fluctuation in C_n. This explains why the fluctuations in C_n at r/R=0.66 are much more significant than r/R=0.82. As the blade section r/R decreases or moves closer to the root of the blade, the amplitude/mean of oscillation and the reduced frequency k both increase leading to a more significant dynamic stall cycle.

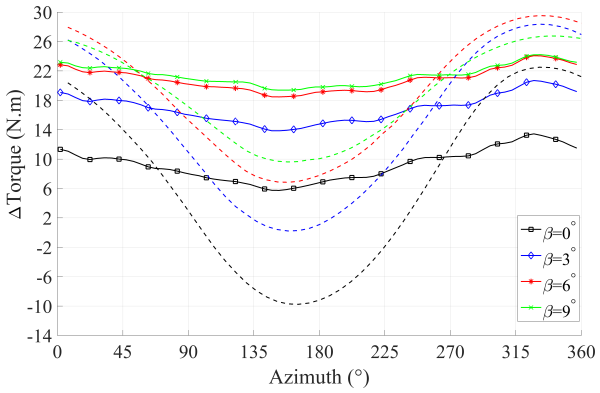
All the data presented here are phase-averaged with azimuth and by doing so, it is possible that some important detail was lost. For this reason, instantaneous and individual

C_n data points that have not been averaged are plotted in Figure 6.10 for select cases. This way, if certain details were obscured in the averaged data, they will hopefully appear in the individual data. Dynamic stall behavior seen here is somewhat different than what was discussed in Chapter 5 and this could be due to 3D flow effects and increased turbulence. One of the main differences seen is the lack of a sudden increase or decrease in C_n as was observed for the 2D airfoil. A similar observation was noted by Jonkman [64] and Schreck *et al.* [14]. By looking at the C_n data alone, it is rather difficult to draw conclusions on whether the blade is stalled or not. For this reason contour plots of ΔC_p are plotted for select cases in Figure 6.11 and are discussed in more detail later. This way blade stall can be studied with more certainty and without assumptions. In the next paragraph, OpenFast is compared to experimental data.

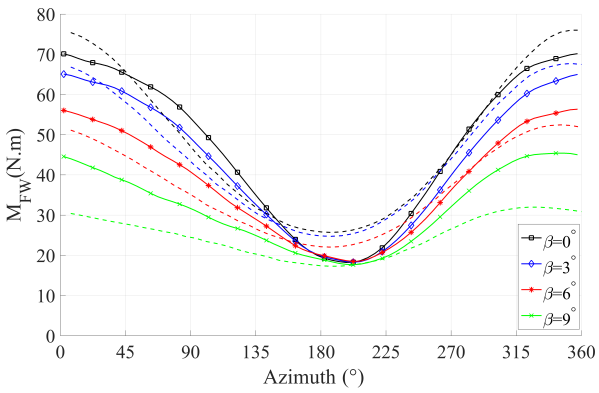
Some of the differences between OpenFast predictions and experimental data can be explained by understanding how OpenFast predicts dynamic stall. There are two main sources of error that could lead to a discrepancy between OpenFast and experimental data. The first one has been discussed numerous times throughout this section and is due to the 3D flow effects. AirfoilPrep has been used to modify the airfoil coefficients to correct for some of these effects however it was found so far that some of these corrections did not improve the accuracy of the predictions. If discrepancies in C_n were found in the steady non-yawed case, then they will appear in the yawed cases considered here. The second source of discrepancy is found in how OpenFast models dynamic stall on a wind turbine and that was developed by Damiani *et al.* [63] and described in Section 2.3.4. They suggested that to better predict dynamic stall in OpenFast, some important parameters must be tuned, which was carried out and also described Section 4.5. The newly developed dynamic stall model was compared to 2D dynamic stall in Section 5.3 and it was concluded that the model predicted dynamic stall in 2D but did not accurately predict the magnitude. However, the dynamic stall model parameters were tuned based on 2D data and that may lead to the discrepancy seen here. Pereira *et al.* [81] argued the 3D effects due to rotation alters dynamic stall behavior and was discussed more in Section 2.4.2. The C_n discrepancy seen at r/R=0.82 and 0.66 are due to the dynamic stall model and the inaccuracy in correcting the airfoil coefficient for 3D flow effects. Damiani *et al.* [63] found similar discrepancies between the OpenFast model and the UAE results even though they were using the newest version of OpenFast and tuned the unsteady dynamic parameters to 2D experimental data. They argued that some of these discrepancies could be explained by uncertainties in the measurements and the airfoil input files used in OpenFast. Better accuracy in the model could be achieved by better tuning the unsteady aerodynamic model and using 3D airfoil lift data instead of 2D. Jonkman [64] and Damiani *et al.* [63] both used 3D airfoil coefficients to simulate the UAE results and their predictions better matched

experimental data. In another study, Damiani *et al.* [11] recently compared OpenFast models to a utility-scaled instrumented wind turbine that was operating with a yaw offset. They found that the model's prediction matched at times but in some cases discrepancies still existed.

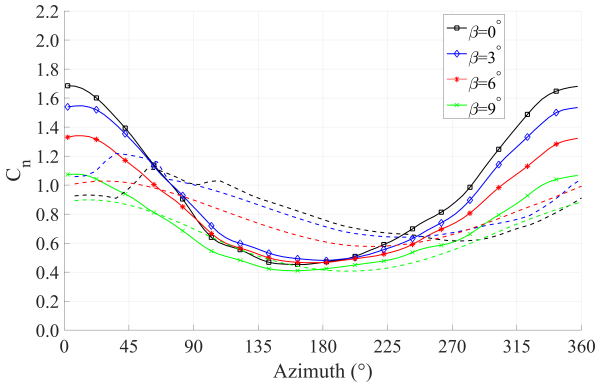
OpenFast predicted that the blade section at r/R=0.82 is undergoing dynamic stall for $\beta = 3°$ and $0°$ only and that is indicated by the steep increase in C_n at $\psi \approx 45°$. As for r/R=0.66, OpenFast predicted dynamic stall for all cases considered and the steep increase in C_n is located at $\psi \approx 60°$. The amplitude of α oscillation at r/R=0.82 is only 3.5° (from Figure 6.9d) and likely does not lead to a significant dynamic stall cycle. On the other hand at r/R=0.66 the amplitude is 5° (from Figure 6.9f). Based on the literature review and Chapter 5, dynamic stall is significant when the amplitude is greater than 5°. Experimental C_n data do not clearly indicate dynamic stall occurrence. The phase-averaged data could possibly hide the dynamic stall behavior and for this reason individual data points are plotted and discussed next in Figure 6.10. Dynamic stall is associated with unsteady flow behavior over the airfoil surface that leads to larger standard deviations (STD) in the surface pressure measurements as seen and discussed in Chapter 5. For this reason the $STD(\Delta C_p)$ contour plot are plotted and discussed later in Figure 6.12. Another possible reason for the discrepancy between experimental results and OpenFast is concentrated at $\Psi = 0°$ or 360° could be due to rotational stall delay. Jonkman [64] argued that most models under predict stall delay on a rotating blade.



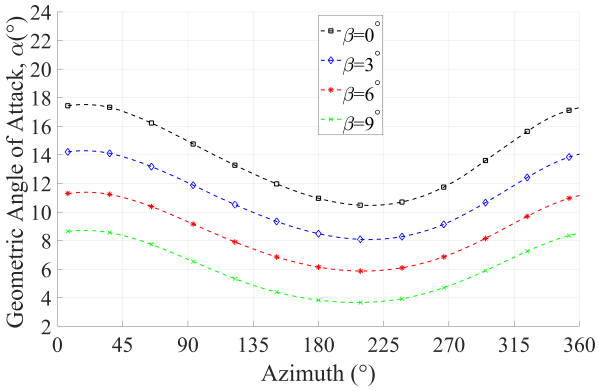
(a) Rotor Torque



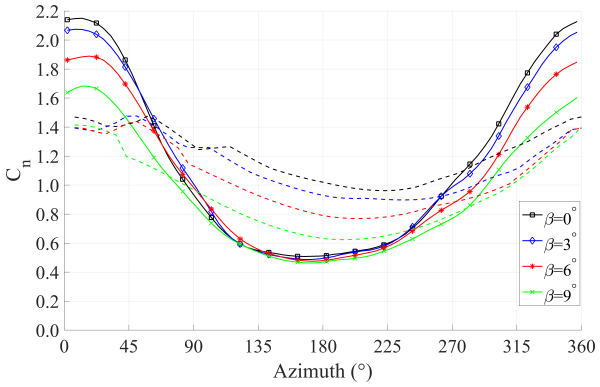
(b) Flapwise Moment (out of plane)



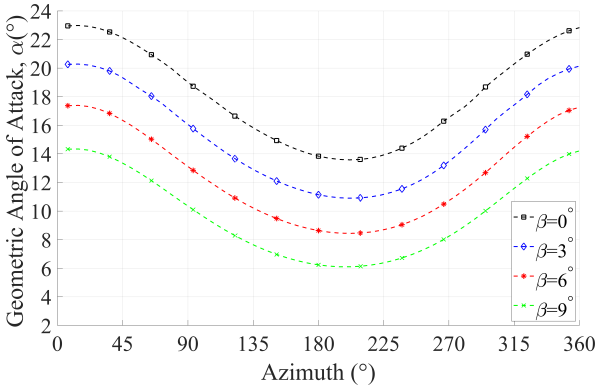
(c) C_n at r/R=0.82



(d) α distribution from OpenFast at r/R=0.82



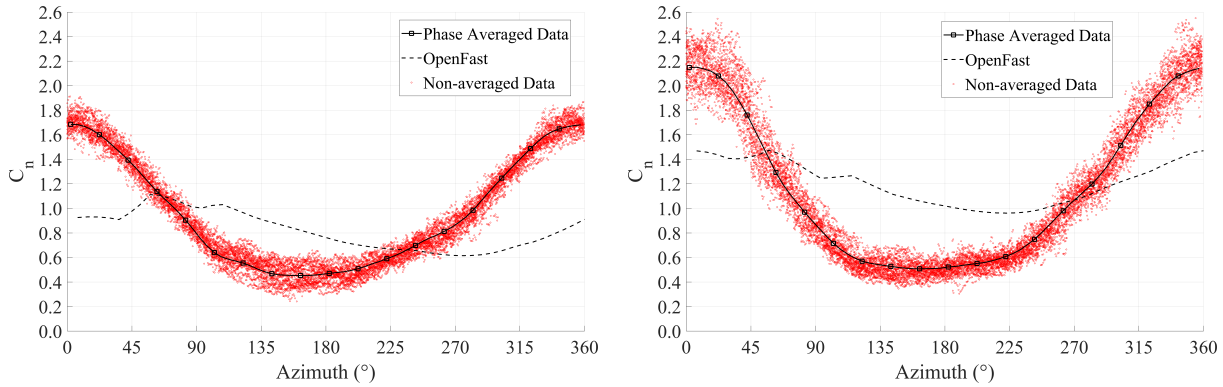
(e) C_n at r/R=0.66



(f) α distribution from OpenFast at r/R=0.66

Figure 6.9: Turbine performance for various β for case 1d where λ=3.5 and $\gamma = 30°$. Solid lines represent experimental data while dotted lines represent OpenFast model data. Every 4^{th} data point is marked on the solid lines for clarity.

To ensure that the C_n phase-averaged data does not exclude information about dynamic stall, Figure 6.10 is plotted where individual data is plotted separately. The same $\beta = 0°$ case displayed in Figures 6.9c and 6.9e also plotted here, together with the OpenFast prediction. The individual data have not been modified and none of the data outliers have been removed. This shows that the data collected is very repeatable and the phase-averaged data is statistically representative of the individual data. In Figure 6.10a, there is a slight increase in C_n variation around $\psi \approx 145°$ which is indicative of stall, but that condition will be subsequently confirmed in the ΔC_p contour plots. This increase in variation occurs just after dynamic stall is predicted by OpenFast. In Figure 6.10b, there is a significant increase in C_n variation across the entire cycle, which is due to a stronger dynamic stall cycle. This occurs due an increase in reduced frequency (k), α oscillation amplitude and α oscillation mean as r/R decreases from 0.82 to 0.66 as discussed previously. These plots do not provide significant insight on the formation of dynamic stall. Most of the information presented here could be seen in the contour plots presented next, in Figure 6.11.



(a) C_n at r/R=0.82 (b) C_n at r/R=0.66

Figure 6.10: C_n versus α for case 1d where λ=3.5, $\gamma = 30°$ and $\beta = 0°$. Non-averaged data are plotted individually along with its phase-averaged curve. OpenFast prediction for the same case is also plotted in the dotted line.

Similar to the ΔC_p contour found in Figure 6.8 for the non-yawed turbine, Figure 6.11 is presented for $\gamma = 30°$ and r/R=0.82 and 0.66. Focusing first on r/R=0.82, as β decreased from 6° to 0° a few important differences are worth mentioning. The pattern in both cases are very similar but only the magnitude of ΔC_p changes. In the region of $\psi = 0°$ or 360°, ΔC_p increases noticeably as β gets smaller because α increases and the unsteady behavior is more significant. The more interesting region to study occurs around $\psi \approx 180°$

because from this region it could be clearly determined if dynamic stall is occurring. As was concluded from Chapter 5, if ΔC_p is not concentrated at the LE indicating that the airfoil is stalled and this is also applicable to 3D flow. When $\beta = 6°$ and $\psi \approx 180°$, ΔC_p is concentrated at the LE indicating that the flow is attached and no dynamic stall is occurring in the cycle. On the other hand, even though as β decreases (α increases), ΔC_p is reduced at the LE and $\psi \approx 180°$. This indicates that ΔC_p is not concentrated at the LE any longer indicating dynamic stall is occurring in the cycle. OpenFast predictions from Figure 6.9c showed that dynamic stall is occurring for $\beta = 0°$ but not when $\beta = 6°$ similar to what is seen and concluded from the contour plots presented here. As for the r/R=0.66 cases in Figures 6.11.c and d, a similar conclusion could be made. At $\psi \approx 180°$, ΔC_p is not concentrated at the LE and that indicates that the blade is stalled and dynamic stall is occurring for all the β cases considered. This result was also simulated by OpenFast and observed in the $C_n - \alpha$ plot found in Figure 6.9e.

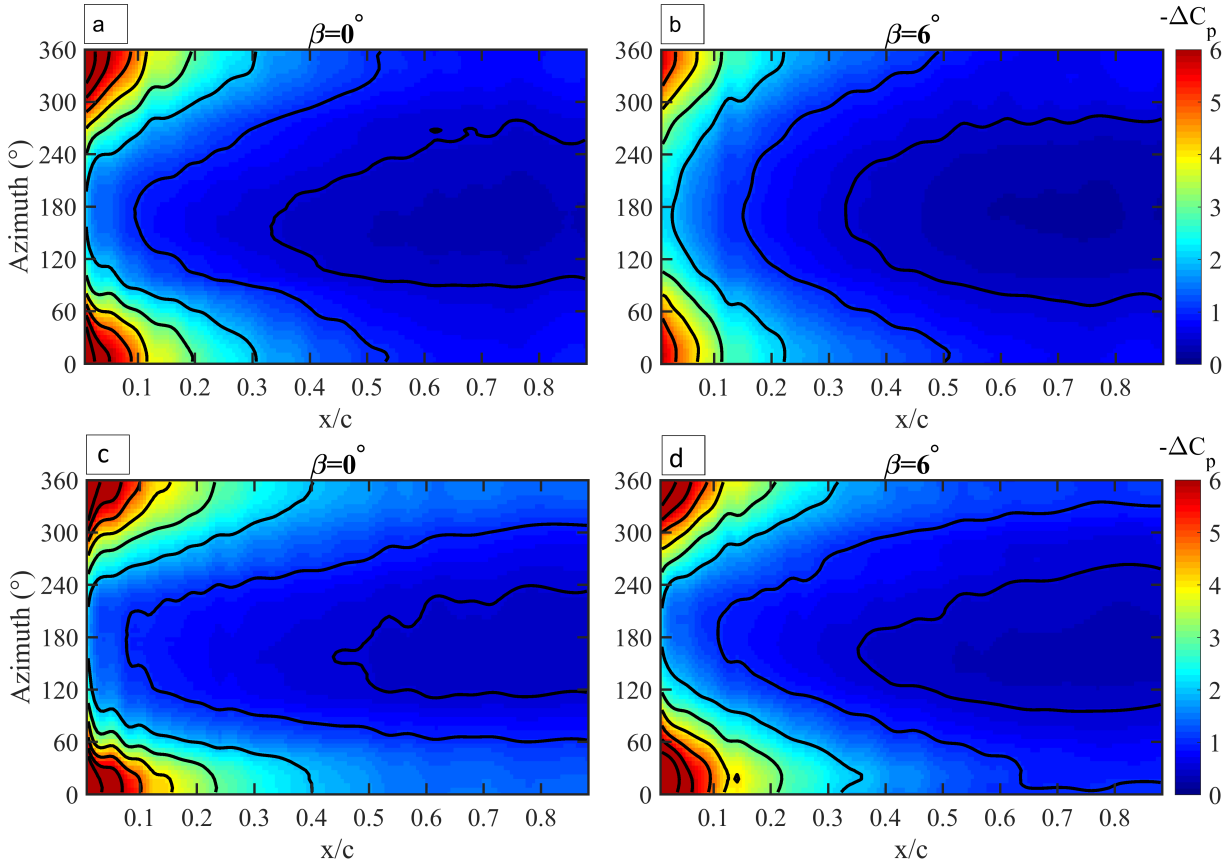


Figure 6.11: Contours of $-\Delta C_p$ versus x/c versus ψ for a) $\beta = 0°$ at r/R=0.82, b) $\beta = 6°$ at r/R=0.82, c) $\beta = 0°$ at r/R=0.66 and d) $\beta = 6°$ at r/R=0.66 for case 1d where $\lambda = 3.5$ and $\gamma = 30°$. The iso-lines on the plot represent constant $-\Delta C_p$ values=[0 0.5 1 2 3 4 5 6 7].

To better understand and visually present the pressure fluctuation over the airfoil surface, $STD(\Delta C_p)$ contours are displayed in Figure 6.12 for two β angles and two r/R locations. High $STD(\Delta C_p)$ values are associated with flow instabilities and separation and could indicate whether the blade is stalled or dynamic stall is occurring as discussed in Chapter 5. When $\beta = 6°$ and r/R=0.82, $STD(\Delta C_p)$ is small and does not change with ψ indicating no dynamic stall is occurring during the cycle. This conclusion agrees with the insights that were reached in the discussion of the $-\Delta C_p$ contour plots found in Figure 6.11. This is also confirmed by showing that α variation during the entire cycle is lower than stall from the $\psi - \alpha$ distribution in Figure 6.9d. However, when $\beta = 0°$ and r/R=0.82, α is oscillating around the stall angle as seen in Figure 6.9d. The different

contour plots confirm that as β decreases at both r/R location, $STD(\Delta C_p)$ is significantly increased indicating the occurrence of dynamic stall. This is also in agreement with the conclusion made in the previous Figure 6.11. When $\beta = 3°$ and at both r/R locations, there is a distinct peak in $STD(\Delta C_p)$ at $\psi \approx 60°$ and that coincides with the C_n peak predicted by OpenFast in Figure 6.9. Such behavior is part of the dynamic stall cycle. A higher $STD(\Delta C_p)$ value indicates a larger unsteadiness in the flow, leading to a stronger dynamic stall cycle. Out of the four contour plots presented, only plot b indicates a steady flow over the blade section. There is a slight increase in $STD(\Delta C_p)$ for plot d indicating a small dynamic stall cycle. As for plots a and c, $STD(\Delta C_p)$ is noticeably larger, indicating a much stronger dynamic stall cycle and that shows in the $-\Delta C_p$ plots presented in Figure 6.11.

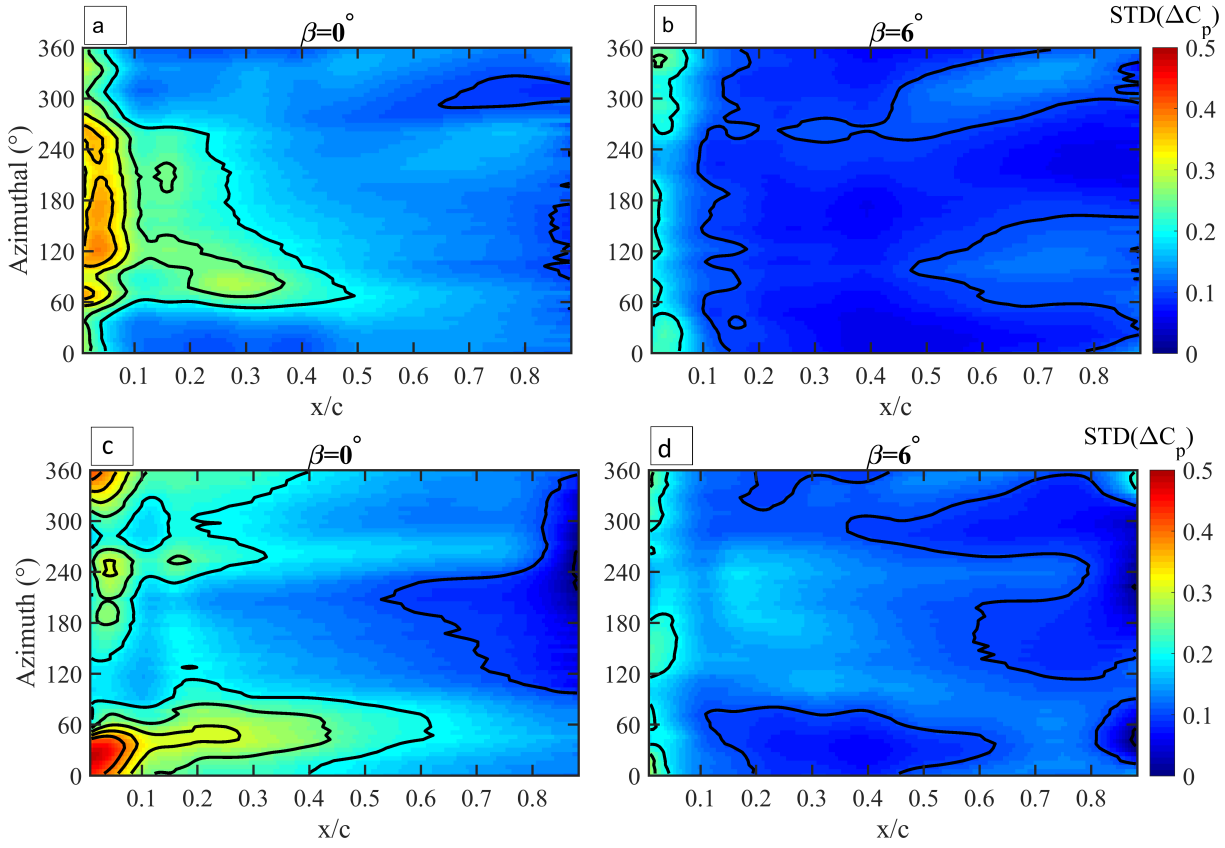


Figure 6.12: Contours of $STD(\Delta C_p)$ versus x/c versus ψ for a) $\beta = 0°$ at r/R=0.82, b) $\beta = 6°$ at r/R=0.82, c) $\beta = 0°$ at r/R=0.66 and d) $\beta = 6°$ at r/R=0.66 for case 1d where $\lambda = 3.5$ and $\gamma = 30°$. The iso-lines on the plot represent constant $STD(\Delta C_p)$ values=[0 0.1 0.2 0.25 0.3 0.35 0.4 0.5].

6.2.4 OpenFast Model Conclusion

OpenFast has been used extensively in this section as a comparison tool for the experimental data. After simulating the turbine under different wind speeds, blade pitch angles and yaw angles a few important conclusions about the OpenFast model that was used can be identified. However, before summarizing a list of strengths and weaknesses of OpenFast, it is important to note that the model's performance is only as good as the input parameters used. For this reason, the physical properties of the turbine were found and imported into OpenFast; see Section 4.5 for additional details.

Discrepancies between OpenFast predictions and experimental data highlight model weaknesses in stall delay, post stall and 3D flow effects. These losses could be approximated and predicted using different corrections and models but they could also be a source of error. Even though OpenFast is a medium complexity code it requires an expert in the field of wind turbine aerodynamics to understand the predictions and the limitations of the source code.

OpenFast Strengths:

- **Simulation length** was in the order of minutes and can be run on any desktop computer. That is a huge benefit and the operator can run hundreds of different scenarios relatively quickly.
- OpenFast is a very **modular tool** that can easily be adapted to simulate any turbine. For example, it was capable of simulating a 3-bladed turbine with 2 of these blades being cylindrical counter-weights.
- OpenFast is capable of obtaining many **different aerodynamic output variables** at any desirable location on the turbine. That feature is helpful in analyzing the load distribution at any location on the wind turbine.
- In steady **non-yawed cases**, OpenFast was capable of **accurately predicting** the rotor torque, flapwise/edgewise moment, and lift coefficient for different tip speed ratios and blade pitch angles.
- OpenFast is capable of simulating a turbine with an elastic blade, a feature is particularly important for larger turbines or when the turbine is operating close to the natural frequency of the blades.

OpenFast Weaknesses:

- OpenFast **requires 2D experimental data** to obtain the lift data and to tune the unsteady aerodynamic model. In some cases it is difficult to obtain experimental data for the desired airfoil and operating conditions thus ultimately leading to less accurate predictions.
- One of the main sources of discrepancy found, occurs in the process of correcting the airfoil coefficients to account for 3D effects using AirfoilPrep. The experimental data show that AirfoilPrep under-predicted 3D flow effects, specially in the vicinity of the blade tip.
- OpenFast did not seem to model or account for angular momentum while predicting rotor torque as discussed in Section 6.2.2. For this reason OpenFast simulated much greater variation in rotor torque compared to the experimental data that were observed.
- OpenFast predicted dynamic stall behavior in some cases where it did not appear experimentally. This discrepancy is mainly due to stall delay and rotational effects.
- Variation in C_n was under-predicted by the model in yawed cases due to 3D flow effects and the various reasons mentioned and discussed.
- OpenFast is a medium complexity code when compared to SOWFA, computational fluid dynamic software by NREL [143]. Even so, OpenFast still requires tremendous effort and expert knowledge of rotor theory to set the model up from obtaining accurate airfoil coefficients to tuning dynamic stall parameters.
- OpenFast still is not as reliable as experimental data. The main benefit is derived after the model has been validated and the turbine can be simulated in different conditions. For this reason the experimental data reported here could be used to improve these models and create more reliable predictions.

In conclusion, modeling tools and experimental data complement each other and are both equally valuable. Experimental data are used to strengthen and validate the aerodynamic physics in the model, while the model in turn enhances the reliability of the experimental data.

6.2.5 Pitch and Tip Speed Influence Summary

After testing different tip speed ratios (λ), blade pitch angles (β) and yaw angles (γ) a few important conclusions are summarized here. In the non-yawed experimental data, the

C_n data at r/R=0.82 and 0.66 strongly indicate that 3D flow effects are present along the entire span of the blade. Experimental data in yawed conditions showed that the induced velocity component variation with azimuth that shifts M_{FW} data away from $\psi = 180°$ is significant only at higher λ. On the other hand, at lower λ the induced velocity is less significant and the M_{FW} data are centered around $\psi = 180°$. By plotting the individual data separately, it is concluded that the phase-averaged data is statistically representative of the individual data and the data collected is very repeatable. It was found that as β or λ decreases, the load variation in ΔTorque, M_{FW} and C_n increases. One of the reasons for this dependence is because a larger portion of the blade span would be operating in the dynamic stall region that causes larger load fluctuations.

For the yawed cases, experimental data show that dynamic stall behavior on a rotating blade is very different than that exhibited on a 2D airfoil segment, and this difference could be due to 3D flow effects, increased turbulence or unsteady effects. One of the main differences seen is the lack of a sudden increase or decrease in C_n, such as was observed on the 2D airfoil. From the C_n data alone it was not possible to determine if dynamic stall is present. On the other hand, contour plots of ΔC_p were able to show clearly and with certainty the location of dynamic stall. The same contour plots can also indicate whether the blade is stalled or not. If ΔC_p is not concentrated at the LE then the blade is stalled and the opposite is also true. Contour plots of $STD(\Delta C_p)$ also proved very useful in determining the dynamic stall location and magnitude, since dynamic stall is associated with unsteady flow behavior over the airfoil surface. As the instrumented blade section moves closer to the root of the blade, the amplitude/mean of oscillation and the reduced frequency k both increase, leading to a more significant dynamic stall cycle.

6.3 Steady Flap Cases

This section focuses on developing an understanding of how TEF influences a wind turbine under different blade pitch angles, yaw angles, tip speed ratios and r/R locations to simulate different operating conditions. Experimental data on a full-scale instrumented turbine with a TEF are scarce. This chapter tries to provide important information to improve aerodynamic understanding of a wind turbine equipped with a TEF using experimental data. Having a complete and comprehensive set of experiments helps to shed some light on how a TEF manipulates rotor power, blade loading and forces on a blade segment. Furthermore, the experimental data will be an excellent resource for modelers to develop new models to simulate TEF on a wind turbine or to validate existing models. The results here are not compared to the OpenFast model because it is not capable of simulating a

TEF on a wind turbine. However, the results are compared to other experimental work when data is available. An overview that summarizes and introduces the different test cases conducted in this section is presented first. This is followed by a complete set of plots showing how the wind turbine performance parameters change with fixed flap angles for yawed and non-yawed turbines to simulate steady and unsteady conditions. The TEF was then tested at two different spanwise locations r/R=0.82 and 0.66 to find the optimum and most efficient location for the TEF. Finally a summary of the findings and conclusions from this section are presented.

6.3.1 Outline

The complete set of experiments conducted during the wind turbine campaign (discussed in Section 4.2.1) are not all reported here. Out of the 120 tests conducted, only the most interesting and informative cases are plotted. To better understand and more effectively highlight the TEF impact, a matrix is created grouping the different tests into 5 cases and are listed in Table 6.2. For all the cases, the flap angle ranged from -20° to 20° in steps of 10°. The single-bladed turbine has only one TEF section that occupies 22% of the 1.47m aerodynamic blade or 19% of the 1.77m rotor radius. Since the blade design is modular, the TEF center section could be placed at two r/R locations, 0.82 and 0.66. The TEF is manually moved from one location to the other. When the TEF is centered at r/R=0.82, the flap is located between r/R=0.73 and 0.91. On the other hand, when the TEF centered at r/R=0.66, the flap is located between r/R=0.56 and 0.75 (refer to Figure 3.17 for more dimensions). The center of the TEF segment was changed to study how the change in TEF location influences blade loading and to determine the most efficient location for the TEF to alleviate cyclic loading on the blade. For case 2b.R2, the TEF was deflected to large angles of ±80° to study how a TEF could force the blade section to stall and how that influences blade loading. The influence of TEF on a non-yawed wind turbine under different wind speeds and blade pitch angles is presented first followed by the same set of conditions but on a yawed turbine. The three variables that are studied and plotted against azimuth are: rotor Torque, flapwise root bending moment (M_{FW}) and normal force coefficient (C_n). The figure reference link in the table is added for organizational purposes.

Table 6.2: Test matrix for flap cases in steady condition

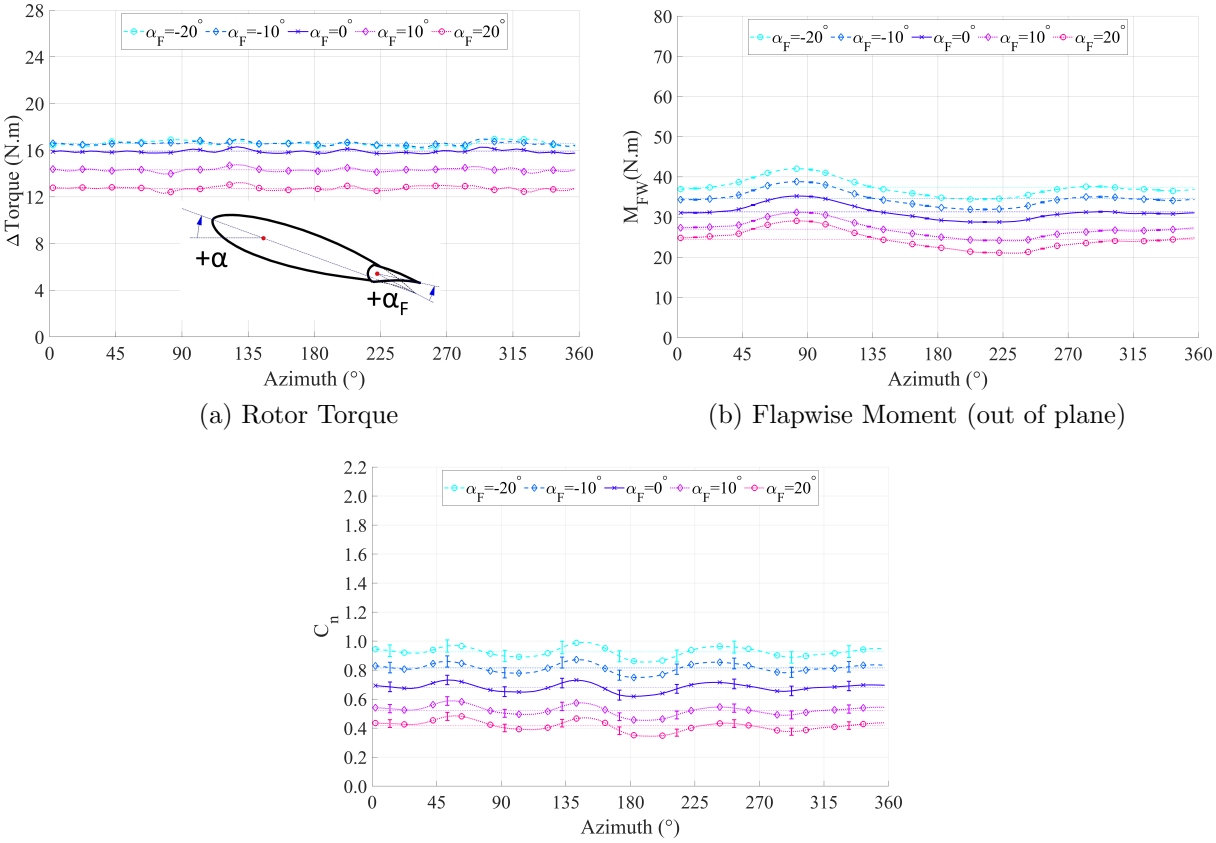
Case	λ	$\beta(^\circ)$	TEF r/R Location	$\alpha_F(^\circ)$	$\gamma(^\circ)$	Variables Presented	Figure Reference
2a	5	6	0.82	[-20:10:20]	0	Torque, M_{FW}, C_n	Figure 6.13
2b.R1	3.5	3	0.82	[-20:10:20]	0	Torque, M_{FW}, C_n , ΔC_p	Figure 6.14 and 6.16
2b.R2	3.5	3	0.66	[-80:20:80]	0	average{Torque, M_{FW}, C_n} , ΔC_p	Figure 6.17 and 6.18
2c	3.5	3	0.82	[-20:10:20]	30	Torque, M_{FW}, C_n, ΔC_p	Figure 6.19 and 6.20

6.3.2 Yaw=0° Flap at r/R=0.82

First, case 2a is presented where the turbine performance parameters are plotted against azimuth in Figure 6.13 where $\beta = 6^\circ$, $\gamma = 0^\circ$, λ=5 and the flap is centered at r/R=0.82. Focusing on the ΔTorque measurements in Figure 6.13a, negative α_F slightly increased rotor power while positive α_F substantially decreased rotor power. Apart from the change in lift coefficient as the flap angle changes, the drag coefficient plays an important role in controlling rotor torque. This is because, as mentioned in Section 2.4.1, Abbott and Von Doenhoff [49] showed that positive flap angles increased C_D significantly but negative flap angles has only a slight impact on C_D. As discussed earlier, the torque measurements are highly sensitive to C_D. This means that positive flap angles produce lower torque because of the higher drag coefficient created by the TEF blade segment. Berg *et al.* [103] reported the same findings on a utility-scaled turbine for the same flap angle deflections and for the same wind speed. They found that for high tip speed ratios, positive flap slightly increased turbine power output while negative flap angles significantly reduced power output. This shows that positive power augmentation from positive α_F angles is very useful in low wind speed conditions because it increases the efficiency of the wind turbine as noted in the average C_{Power} plot in Figure 6.3.

The blade flapwise moment, M_{FW}, is presented next in Figure 6.13b where positive α_F reduces blade loading while negative α_F does the opposite. The increase in M_{FW} at $\psi \approx 85^\circ$ is due to the non-uniformity in wind speed from the wind tunnel as mentioned in the previous section and is evident in all the data collected and presented. The change in M_{FW} for $\alpha_F = -20^\circ$ and 20° relative to 0° is 19% and -22%, respectively. The control capability of negative α_F is then found to be less than the control capability of positive α_F

due to the upper limit in the lift coefficient and the tendency for the airfoil to stall for high negative values of α_F. Berg *et al.* [103], measuring only M_{FW} and not C_n, found a similar trend in their data. This effect is also seen in the C_n plots in Figure 6.13c, where the change in C_n for $\alpha_F = -20°$ and $20°$ relative to $0°$ is 36% and -39%, respectively. A more detailed discussion about the difference between positive and negative α_F is presented later in Figure 6.15. There is a larger change in C_n than in M_{FW} because the latter measures loading on the entire blade where the TEF only occupies 22 % of the blade span, while C_n measures the forces at the midspan of the TEF segment. The slight variation in $C_n - \psi$ is due to the non-uniformity in wind speed in the wind tunnel that was also noted in the previous section. In all cases, this non-uniformity appears in the same location.



(a) Rotor Torque

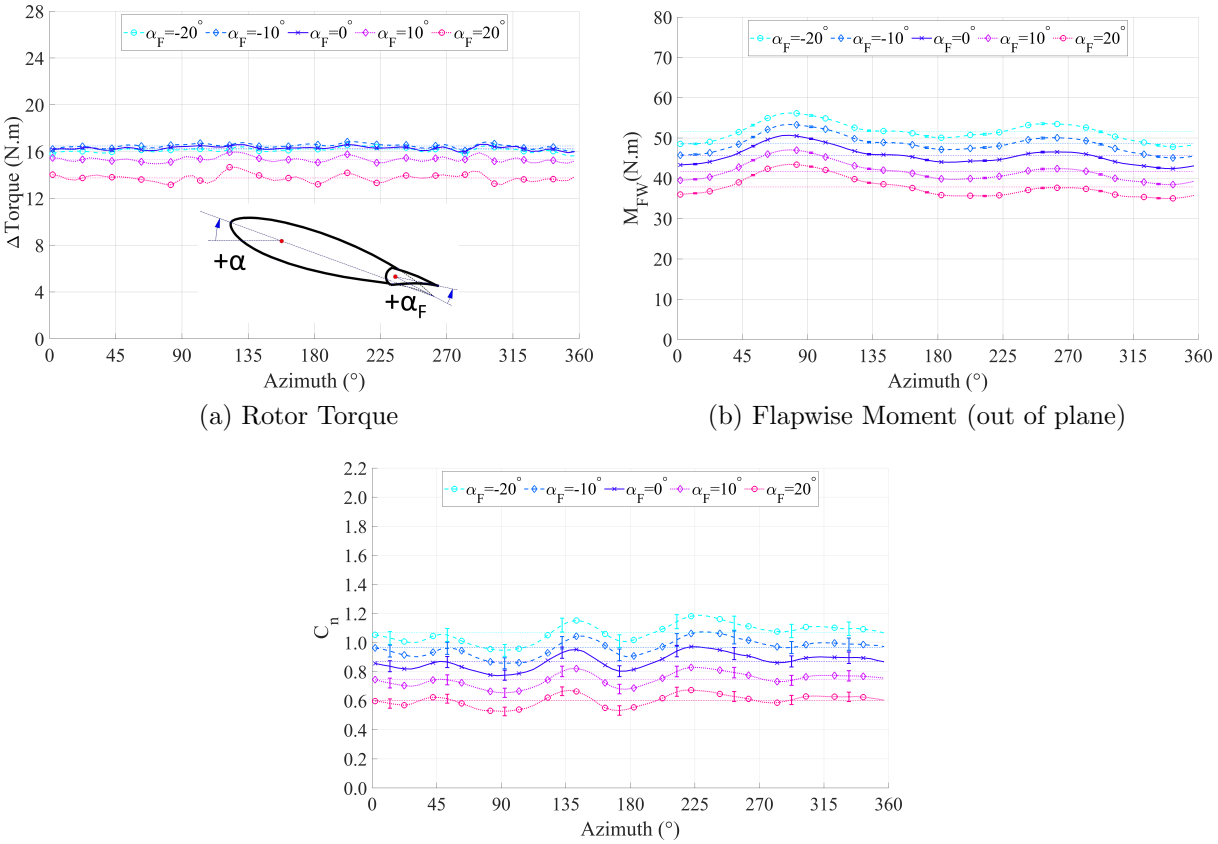
(b) Flapwise Moment (out of plane)

(c) C_n at r/R=0.82

Figure 6.13: Turbine performance for various α_F for case 2a where $\beta = 6°$, $\gamma = 0°$, λ=5 and the flap is centered at r/R=0.82. Solid lines represent experimental data while dotted lines represent the cycle-average. Every 4^{th} data point is marked on the solid lines for clarity.

To study how the blade pitch and wind speed change the flap control capability, case 2b.R1 is displayed in Figure 6.14 where β decreased to 3° and λ decreased to 3.5 from the previous case. Figure 6.14a shows that there was no increase in rotor torque at all for negative α_F but for positive angles the same reduction shift is still present when compared to case 2a. This result could be due to the larger forces experienced by the rotor when the wind speed increased. Decreasing the blade pitch from 6° to 3° also forces a larger section of the blade to stall, significantly increasing the drag coefficient. The results from Berg *et al.* [103] also show that at lower wind speeds negative α_F slightly increases rotor power but for higher wind speeds there is no change in rotor power. From the M_{FW} and C_n data

(Figures 6.14b and 6.14c), similar conclusions can be drawn. The absolute shift in value of these two variables for different α_F angles did not change (within uncertainty values) from case 2a to 2b.R1 but the percentage change did differ. A more detailed comparison between case 2a and 2b.R1 is presented next in Figure 6.15. Another important observation to note is that the TEF shifted the turbine loading for the entire cycle and all azimuth positions equally. This observation demonstrates that the methodology used to collect turbine performance parameters is reliable and repeatable even though some of the data were collected on different days.



(a) Rotor Torque

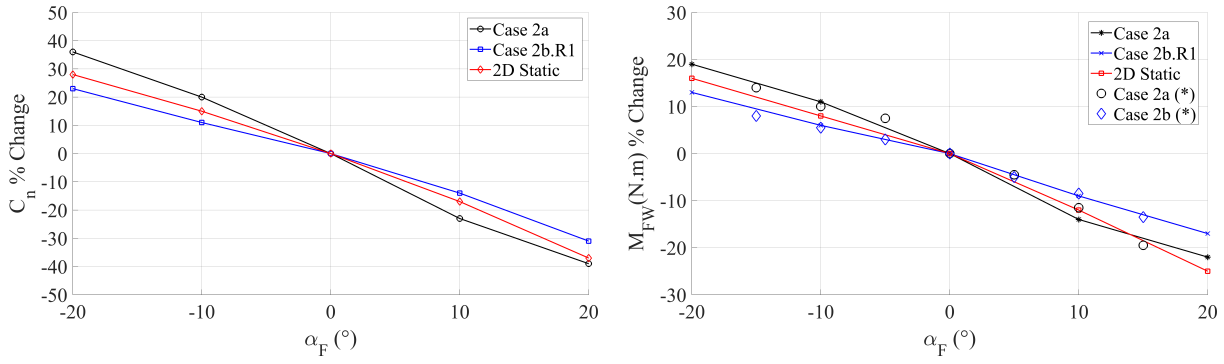
(b) Flapwise Moment (out of plane)

(c) C_n at r/R=0.82

Figure 6.14: Turbine performance for various α_F for case 2b.R1 where $\beta = 3°$, $\gamma = 0°$, λ=3.5 and the flap is centered at r/R=0.82. Solid lines represent experimental data while dotted lines represent the cycle-average. Every 4^{th} data point is marked on the solid lines for clarity.

To better understand how α_F influences the aerodynamics of the blade and how it compares to a 2D airfoil section, Figure 6.15 plots the percentage change in M_{FW} and C_n relative to $\alpha_F = 0°$. The 2D static data is from the wind tunnel experimental campaign described in Section 5.1.1. Both plots clearly show that the change in turbine loading is reduced as wind speed increases or β decreases (going from case 2a to case 2b.R1) because the aerodynamic loading on the turbine increases with the latter two variables. The TEF could manipulate loading by a certain amount and that loading is not influenced by a change in λ or β. So when turbine loading increases due to the latter two variables, the influence of the TEF decreases because the change in load due to the TEF becomes less significant. The control capability for positive α_F is less than that for negative α_F due to the upper limit on the lift coefficient and the tendency for the airfoil to stall for high negative α_F as discussed earlier and is seen on the turbine blade and 2D static cases. Abdelrahman and Johnson [56] conducted a very similar experiment on the same single-bladed turbine using the same airfoil and dimensions but they only reported cycle-averaged values for M_{FW}. The main difference between their experiment and this experiment is the added value of phase-averaging of the current data and collecting surface pressure measurements to obtain C_n. Their results are also plotted in Figure 6.15 for comparison. The trends in their data align very well with the data collected in this experiment. This increases confidence in the data and conclusions made. Some of the differences between the two experiments could be due to the location and length of the flap or experimental uncertainties. The flap length they used was 0.25 m centered around r/R=0.89 whereas the flap length in this project was 0.33 m, centered around r/R=0.82.

Another important note to emphasize is that the data is almost linear as evident in all cases presented, both for M_{FW} and C_n. This was expected based on the discussion in Section 2.1.3 and Equation (2.9) which shows a linear relationship between C_L and α_F. C_n and M_{FW} on a wind turbine are not influenced solely by the TEF but also by the shed vortex forming at the inboard (towards hub) section of the TEF as explained by Miller and Quandt [93] and shown in Figure 2.12 from Section 2.4.5. The vortex occurs where the flap separates from the blade, reducing the effective α on a small section of the inboard blade and reducing overall blade loading. This reduction could explain the smaller slope in the M_{FW} % change data presented in Figure 6.15, particularly for negative α_F. This argument was also reported by Abdelrahman and Johnson [56]. Negative α_F tends to create a stronger vortex at the edges of the flap, which results in a smaller % change in loading when compared to positive α_F.



(a) % Change in C_n (b) % Change in Flapwise Moment (out of plane)

Figure 6.15: Percentage change in a) M_{FW} and b) C_n relative to $\alpha_F = 0°$ for case 2a and 2b.R1 versus α_F where the flap is centered at r/R=0.82. (*) refers to experimental data points from Abdelrahman and Johnson [56].

To obtain M_{FW}, C_n is integrated along the entire blade span and the latter variable in turn is determined by integrating surface pressure along the chordwise direction. Thus it is important to study how the flap changes surface pressure in the chordwise direction. To do so a contour plot is used to present ΔC_p for $\alpha_F = -20°$ and $20°$ in Figure 6.16. As expected ΔC_p is uniform versus azimuth apart from few variations due to the non-uniformity in wind speed from the wind tunnel. This non-uniformity and trend was also seen in the C_n plots in Figure 6.14c. The more interesting aspect of these plots is that the flap has more influence over ΔC_p close to the TE than the LE. This is aligned with the results and conclusions made from the 2D static results in Section 5.1.2. All the iso-lines are shifted towards the TE as α_F decreases indicating that the flap does influence the aerodynamics along the entire chord-length of the blade. In both contour plots, ΔC_p is concentrated at the LE indicating that the blade segment at r/R=0.82 is not stalled. In Figure 6.16.b, there exists a negative $-\Delta C_p$ region as indicated by the iso-line marked in white dashes at x/c=0.82. This occurs because as α_F is deflected to 20°, it creates a pocket around the flap hinge where the pressure is positive on the suction side of the airfoil. When $\alpha_F = -20°$ the pocket disappears so does the negative $-\Delta C_p$ values.

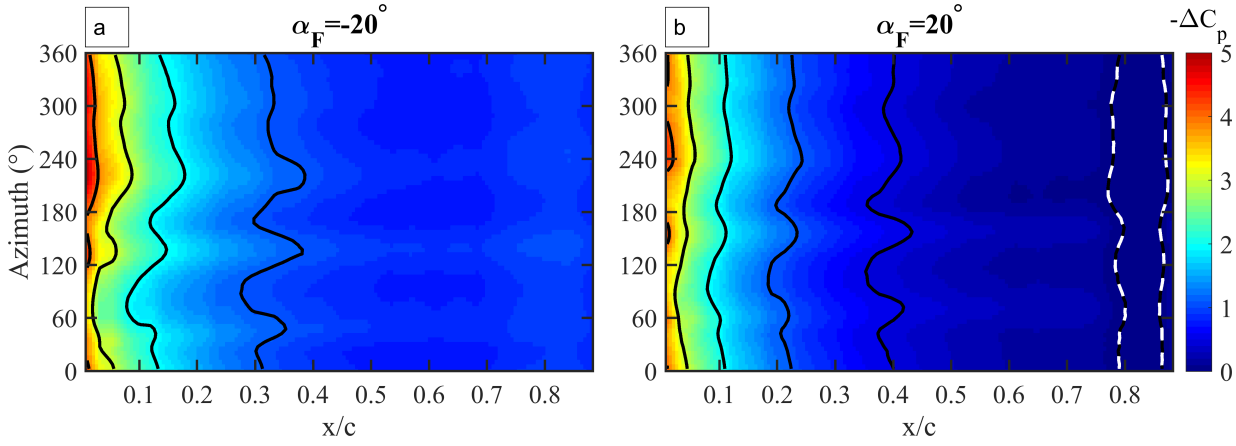


Figure 6.16: Contours of $-\Delta C_p$ versus x/c versus ψ at r/R=0.82 for a) $\alpha_F = -20°$ and b) $\alpha_F = 20°$ for case 2b.R1 where $\lambda = 3.5$, $\gamma = 0°$, and $\beta = 3°$. The iso-lines on the plot represent constant $-\Delta C_p$ values=[0 0.5 1 2 3 4 5]. The iso-line of $\Delta C_p = 0$ is marked in white dashes.

6.3.3 Yaw=0° Flap at r/R=0.66

In this section the flap location has been moved from r/R=0.82 to 0.66 to study how changing the flap location influences blade loading. From the previous section, it was concluded that the load variation with azimuth is negligible when $\gamma = 0°$. For this reason, the turbine performance parameters are averaged for the cycle and are plotted versus α_F and not versus azimuth. The performance parameters were plotted versus azimuth but not presented here to make sure that the variation with azimuth is indeed negligible as predicted even when r/R has changed. Due to this technique of plotting, different cases could be presented in the same plot and could be compared to each other. The three performance parameters presented in Figure 6.17 are for four distinct cases identified in the plot legend where $\gamma = 0°$ and λ=3.5. The red and black lines represent $\beta = 3°$ and 6°, respectively while the solid line and the dotted line represent r/R=0.66 and 0.82, respectively. For all the cases presented, α_F ranged from -20° to 20° in steps of 10° but for r/R=0.66 and $\beta = 3°$ (case 2b.R2) additional α_F were tested from -80° to 80° in steps of 20°. This was conducted to investigate how extreme large α_F influences turbine loading. The two main discussion points are: how varying the TEF location changes its control capability; and how deflecting the flap to such high angles influences blade loading.

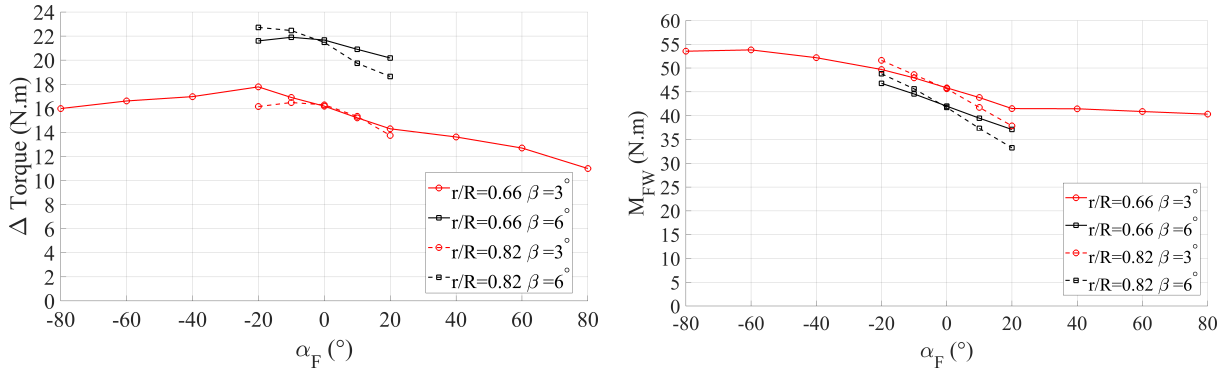
First, ΔTorque is presented for the four cases in Figure 6.17a. Based on the α_F range of -20° to 20°, there is no clear trend or relationship between α_F and ΔTorque. The relationship is highly dependent on λ as seen in Figures 6.13 and 6.14 and is also dependent

on β and r/R as seen in this figure. From the data discussed so far, it could be concluded that α_F influence over ΔTorque is not linear and the relationship is dependent on multiple external factors such as blade stall. A similar conclusion was also made in Section 6.1, which showed that the TEF was not capable of controlling rotor torque as effectively as blade pitch. Beyond $\alpha_F = \pm 20°$, ΔTorque is reduced in both directions because large values of α_F increases the drag coefficient at the blade section. Positive α_F produced the smallest ΔTorque values because the flow over the TEF blade section is severely stalled, significantly increasing th drag coefficient. Abbott and Von Doenhoff [49] clearly showed that positive α_F does lead to higher drag coefficient compared to negative α_F and that in turn leads to lower ΔTorque values. The idea of using TEF as an aerodynamic brake has been discussed and tested by Miller and Quandt [93]. The plot presented here supports the concept where a TEF can in fact be used as an aerodynamic brake but this is not the focus of this study. When $\alpha_F = -80°$, ΔTorque is reduced by 37% and there should be an even greater reduction when r/R increases to 0.82 because the moment arm and the relative velocity to the blade segment are increased making the drag force even larger and more significant. Johnson *et al.* [107] experimentally found that the highest power production area (area producing the most torque) is located at r/R=0.77 for the different cases they tested. This also shows that when the TEF is centered at r/R=0.82 (flap located between r/R=0.73 and 0.91), is a better location to control ΔTorque than when the TEF is centered at r/R=0.66 (flap located between r/R=0.56 and 0.75). If ΔTorque is reduced to zero, that indicates that the aerodynamic blade is not producing power. The results presented here support the idea that the TEF can then be used to assist or even replace the pitch control of utility-scaled turbines. The removal of the pitch control could offset the cost of TEF on the blades as flaps could be more reliable and effective at controlling the aerodynamic of the blades locally. Having two or one larger TEF segments could potentially force the ΔTorque to become zero halting power production and aerodynamically braking the rotor instead of using pitch control to feather and shutdown the wind turbine. This research is not focused on using TEF as an aerodynamic brake and hence more research and experiments are needed to further strengthen this argument.

Second, M_{FW} is presented for the four cases in Figure 6.17b. Focusing on the operating range of $\alpha_F = \pm 20°$, the plot clearly shows the that relationship between α_F and M_{FW} is linear for all β angles, tip speed ratios and even when r/R is changed. When β decreased from 6° to 3°, the two M_{FW} data sets shifted upwards as expected but more importantly the slope of the data did not change. This is significant because it shows that the TEF control capability is the same when the turbine is operating under different conditions. Another important finding is that when r/R=0.82 the slope of the M_{FW} data for both β angles is steeper than r/R=0.66. The M_{FW}/α_F slope is equal to 3.6 Nm/10° when

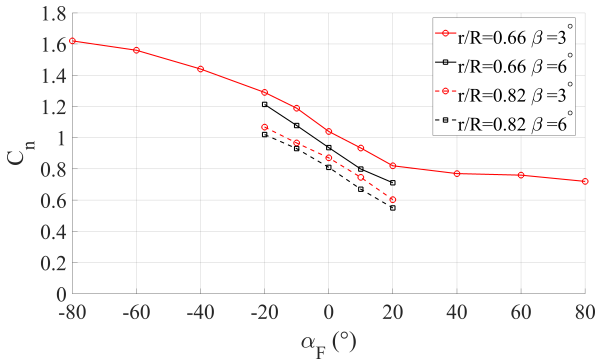
r/R=0.82 and is equal to 2.2 Nm/10° when r/R=0.66 and that is equivalent to a slope reduction of 40%. This clearly shows that when the TEF is centered at r/R=0.82, the control capability is significantly greater than when the TEF is centered at r/R=0.66. This was expected because Burton *et al.* [7] and Hau [50] both showed that the blade load per unit length in the flapwise direction increases steadily up to r/R≈0.92 where it is significantly reduced after that due to the tip loss effect discussed in Section 2.4.2. The M_{FW} magnitude is dependent on both: the blade load and the moment arm. Since both of these variables keep increasing up to r/R≈0.92 then it makes most sense to place the TEF as close to this area as possible. When the TEF is centered at r/R=0.82 (flap located between r/R=0.73 and 0.91), it controls the loading on the blade segment that contributes most to M_{FW}. On the other hand, when the TEF is centered at r/R=0.66 (flap located between r/R=0.56 and 0.75), it controls the loading on the blade segment that contributes less to M_{FW}. Beyond $\alpha_F = \pm 20°$ range, the M_{FW} trend is no longer linear and it tapers off with no significant change in M_{FW}. This non-linearity exists because C_n is no longer linear outside the operating range and is discussed in more detail after the C_n plots are discussed. Based on the evidence presented so far, the relationship between α_F and M_{FW} is linear as long as $\alpha_F = \pm 20°$.

Finally, the C_n data is presented for the four cases in Figure 6.17c. Focusing on the operating range of $\alpha_F = \pm 20°$, the results are parallel to each other indicating a similar slope. This shows that the linearity between α_F and C_n is independent of r/R location, β angle, and tip speed ratio. This was also expected because from the static results, in Section 5.1.1, it was concluded that the influence of the TEF on C_n is linear for the entire range of α and is not affected by the stall angle or other factors. Beyond $\alpha_F = \pm 20°$ range, the trend is no longer linear as seen in Figure 6.17c. It is interesting to show that C_n keeps increasing as α_F decreases even at extremely large negative flap angles where it is expected for the blade section to be stalled. At large positive α_F, C_n does not continue to decrease as α_F increases. This trend in the data is explained better by looking at the ΔC_p contour plots presented next.



(a) Rotor Torque

(b) Flapwise Moment (out of plane)



(c) C_n

Figure 6.17: Cycle-averaged turbine performance versus α_F for case 2b.R1 and 2b.R2 where $\beta = 3°$ and $6°$, $\gamma = 0°$, λ=3.5 and the flap is centered at r/R=0.82 and 0.66.

Similar to the ΔC_p contour plots presented in Figure 6.16 for case 2b.R1, Figure 6.18 presents ΔC_p contour plots for α_F = [-80°, -20°, 0°, 20°, 80°] for case 2b.R2 where λ = 3.5, $\gamma = 0°$, $\beta = 3°$ and r/R=0.66. This provides a clear insight on how the pressure distribution changes with r/R and for extreme α_F. When comparing Figures 6.18.b and d to Figure 6.16 where r/R decreased from 0.82 to 0.66, the negative region present at $\alpha_F = 20°$ is not present anymore. This could be due to a change in Re and α increasing from 8° to 11° when r/R changed (α is obtained from the OpenFast model in Figure 6.7). For $\alpha_F > -20°$, there is no indication from the contour plots, in Figure 6.18, that the blade segment is stalled since ΔC_p is concentrated at the LE. Differently, for $\alpha_F = -80°$, ΔC_p is no longer concentrated at the LE and ΔC_p is significantly increased across the entire airfoil chord and from Section 5.1, this is indicative of stall. From the 2D static results in

Section 5.1, it was found that even though the blade is stalled, C_L kept increasing similar to what is found here in the C_n data in Figure 6.17c. Another interesting case is $\alpha_F = 80°$, where the flow is expected to separate but ΔC_p is still concentrated at the LE. For this reason, the trend in C_n tapered off in Figure 6.17c for large α_F. The measurements do not provide enough information to conclude with certainty whether the flow over the blade is stalled or not. What has been found is that 3D flow effects discussed in Sections 2.4.2 and 6.2 have a significant impact on blade stall that typically leads to a less dramatic stall. More experiments and visualization are needed to study the dynamics of stall on a rotating blade.

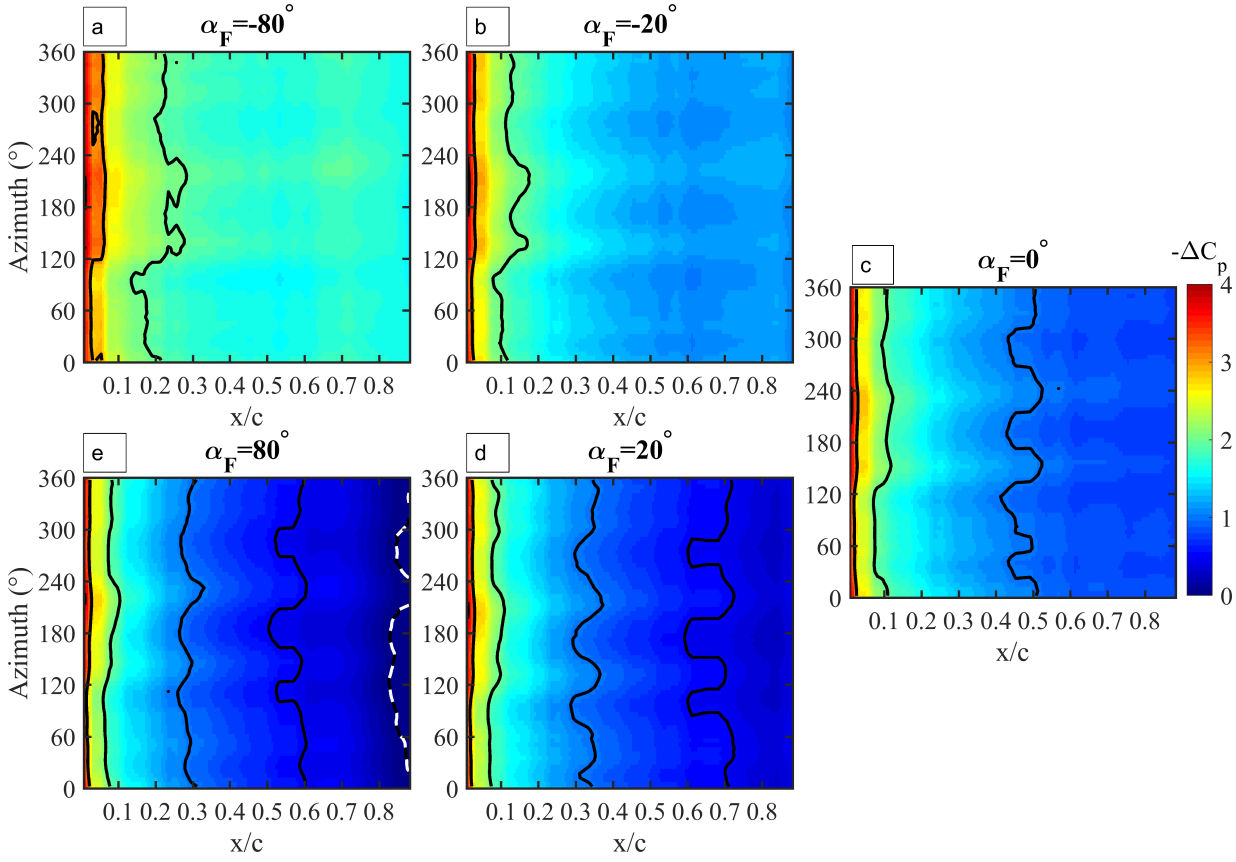
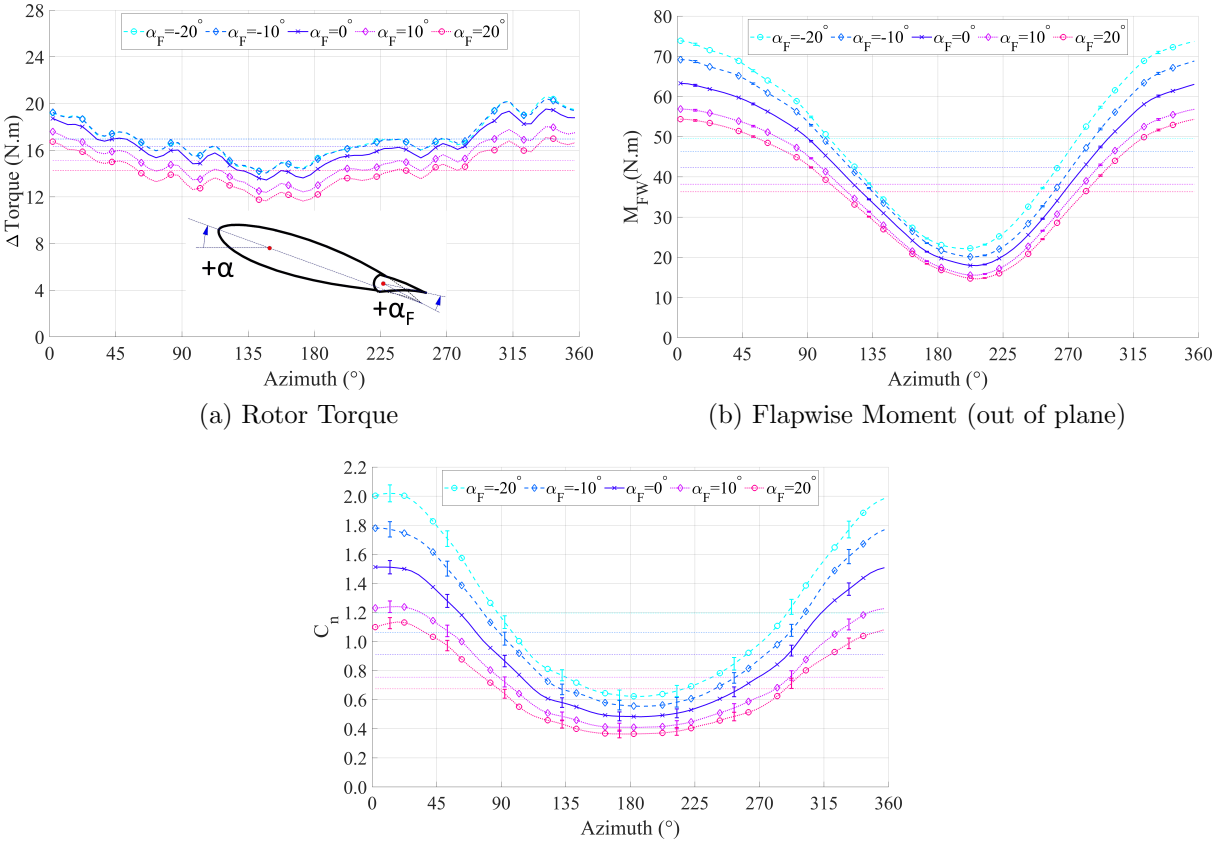


Figure 6.18: Contours of $-\Delta C_p$ versus x/c versus ψ at r/R=0.66 for a) to e) α_F = [-80°, -20°, 0°, 20°, 80°] for case 2b.R2 where $\lambda = 3.5$, $\gamma = 0°$, and $\beta = 3°$. The iso-lines on the plot represent constant $-\Delta C_p$ values=[0 0.5 1 2 3 4]. The iso-line of $\Delta C_p = 0$ is marked in white dashes.

6.3.4 Yaw=30° Flap at r/R=0.82

Similar to case 2b.R1 that was presented in Section 6.3.2, case 2c is plotted in Figure 6.19 for the same condition but when the turbine is yawed. This way the influence of α_F on yawed turbine aerodynamics is studied and compared to the non-yawed cases. Case 2c also presents the opportunity to study how the TEF controls loads on a yawed turbine operating at the onset of stall where $\beta = 3°$ and λ=3.5. The variation in all three variables with α_F is very similar to what was found for non-yawed turbine. This indicates that the TEF is capable of controlling turbine loading in yawed and non-yawed conditions equally. This is important because, as mentioned in the introduction, utility-scaled wind turbines spend the majority of their time in yawed conditions and it is essential for the TEF to attenuate structural loads in these different conditions. The data presented so far shows that the TEF is capable of equally controlling the load on the turbine for different yaw angles, blade pitch angles, and wind speeds even when the turbine is operating at the onset of stall and the load fluctuation are high.



(a) Rotor Torque

(b) Flapwise Moment (out of plane)

(c) C_n at r/R=0.82

Figure 6.19: Turbine performance for various α_F for case 2c where $\beta = 3°$, $\gamma = 30°$, and λ=3.5. Solid lines represent experimental data while dotted lines represent the cycle-average. Every 4$^{\text{th}}$ data point is marked on the solid lines for clarity.

Just like ΔC_p was plotted in Figure 6.16 for non-yawed cases, the contour plot in Figure 6.20 is used to study ΔC_p in yawed cases for the minimum and maximum α_F. When comparing Figure 6.20.a, $\alpha_F = -20°$, and 6.20.b, $\alpha_F = 20°$, there is an increase in ΔC_p across the entire chord of the airfoil, but the change in ΔC_p is more concentrated around the TE region. Similar to what was discussed in the non-yawed case 2b.R1, the negative $-\Delta C_p$ region is due to a pocket created around the flap hinge where the pressure is positive. This indicates that the flap is capable of reversing the pressure polarity close to the TE significantly modifying the moment coefficient about the quarter chord.

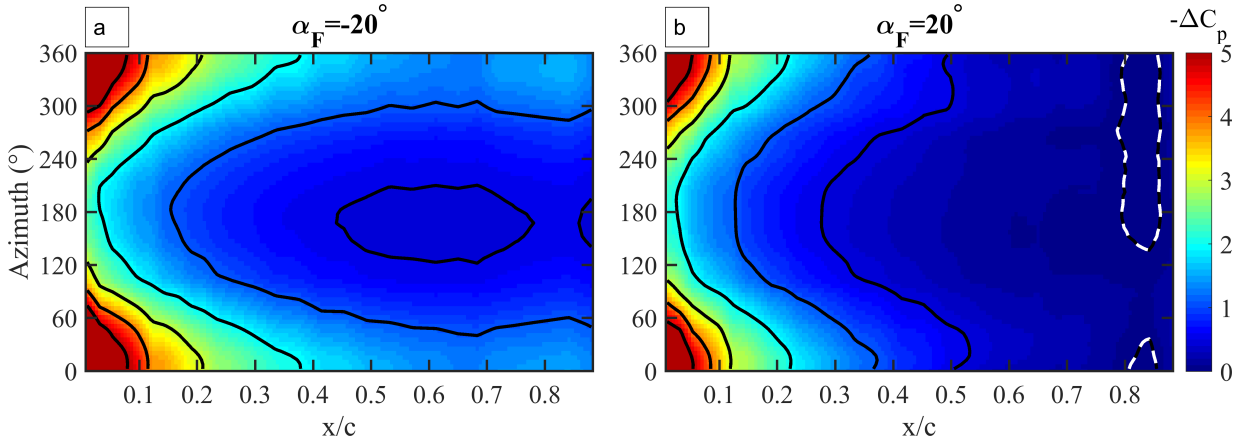


Figure 6.20: Contours of $-\Delta C_p$ versus x/c versus ψ for a) $\alpha_F = -20°$ and b) $\alpha_F = 20°$ for case 2c where $\lambda = 3.5$, $\gamma = 30°$, and $\beta = 3°$. The iso-lines on the plot represent constant $-\Delta C_p$ values=[0 0.5 1 2 3 4 5 6]. The iso-line of $\Delta C_p = 0$ is marked in white dashes.

Now that all the cases have been presented for this section where α_F was varied, the influence of pitch and flap could be compared and discussed. The cycle-averaged data for both of these cases was presented and compared in Section 6.1.3. This section focuses on the differences that were concealed by cycle-averaging the data and that is mainly when the turbine is yawed. When comparing the pitch cases in Figure 6.9 to the flap cases in Figure 6.19, it was found that decreasing β significantly increases load fluctuations in M_{FW} and C_n. On the other hand, changing α_F keeps the load fluctuations about the same but the load pattern is shifted up and down. It was also found that as β decreases, the possibility of dynamic stall increases significantly whereas changing α_F does not influence the possibility of stall. For example, it was concluded from Figure 6.11 that when β decreases from 6° to 0° the blade would start to operate in the dynamic stall region. Contrarily, it was concluded from Figure 6.19 that a change in α_F does not force the bade section to operate in dynamic stall. From the 2D dynamic stall experiments in Section 5.4 it was concluded that the TEF was not capable of controlling the formation and development of dynamic stall but rather only reduces its effect. On the other hand, the oscillating α_{mean} which is equal to the pitch angle of the blade has a larger influence on the formation and magnitude of dynamic stall. This suggests that it would be best to keep β constant and attenuate the loads using the TEF.

6.3.5 TEF Influence Summary

A complete and a comprehensive set of data was presented for different α_F angle on a steady operating wind turbine where ΔTorque, M_{FW} and C_n are plotted versus azimuth. The data showed that negative α_F angles were capable of positively augmenting ΔTorque (turbine power output) in low wind speed conditions only and that is useful because the turbine efficiency is increased when it is producing less power. Comparison between the results presented in this section and 2D wind tunnel data and other experimental work showed that positive α_F is capable of controlling turbine loading better than negative angles due to the upper limit on the lift coefficient and the tendency of stall for high positive α_F. In some cases when the flap is activated, specially for negative angles, a new vortex occurs where the flap separates from the blade, reducing the effective α on a small section of the inboard blade and reducing overall blade loading. From the ΔC_p contour plots, the TEF is capable of changing ΔC_p along the entire length of the chord.

After testing the TEF at two distinct r/R locations (0.66 and 0.82) and comparing them to each other under different wind turbine operating conditions, a few important conclusions could be made. It was found that the α_F influence over ΔTorque is not linear and the relationship is dependent on multiple external factors such as blade stall, λ, β and r/R. The TEF was not capable of controlling rotor torque as efficiently as blade pitch. As for the relationship between α_F and M_{FW}, it is linear for all the cases presented. It also shows that when the TEF is centered at r/R=0.66 the control capability is reduced by 40% when compared to r/R=0.82. The linearity between α_F and C_n is constant and independent of r/R location, β angle, and tip speed ratio. For one of the cases presented, additional α_F were tested from -80° to 80° in steps of 20°. The data presented supports the idea that the TEF could be used as an aerodynamic brake and it could then be used to assist or even replace the pitch control of utility-scaled turbines. ΔTorque is reduced by 37% when α_F is deflected to -80° when r/R=0.66 and there should be an even greater reduction when r/R increases to 0.82. Thus having two or one larger TEF segments could potentially force the ΔTorque to become zero, aerodynamically braking the rotor and replacing the pitch control system to feather or shutdown the wind turbine. Beyond $\alpha_F = \pm 20°$ range, the trend in M_{FW} and C_n is no longer linear and tapers off with no significant change at extreme flap angles. This shows that the linear range in controlling turbine loading is when $\alpha_F = \pm 20°$.

Turbine performance parameters were also studied for different α_F on a yawed turbine. It was found that the TEF is capable of equally controlling the load on the turbine for different yaw angles, blade pitch angles, and wind speeds even when the turbine is operating at the onset of stall and the load fluctuations are high. When comparing pitch load

control capability to that of flap, it was found that decreasing β significantly increases load fluctuations in M_{FW} and C_n. On the other hand, changing α_F keeps the load fluctuations about the same but the loads are increased or decreased. The possibility of dynamic stall increased when β changed but it was kept constant when α_F changed. This suggests that it would be best to keep β constant and attenuate the loads using the TEF.

Chapter 7

Wind Turbine Load Alleviation

The previous chapter presented a detailed and a comprehensive set of experiments that showed how the loading on the wind turbine varies under different conditions in steady and unsteady cases. It also showed how a TEF could manipulate turbine loading at fixed angles under the same conditions. The main aim of this chapter is to use the data and conclusions from the previous chapter to reduce or eliminate load fluctuation experienced by the rotor. This reduction is achieved by continuously actuating the flap or the pitch, thereby actively modifying the aerodynamics of the blades during rotation. To replicate unsteady behavior on wind turbines, γ was set of 30° for all the cases investigated in this chapter. Only $\lambda = 3.5$ (highest free stream velocity) was used in this set of experiments because it produced the largest load fluctuations on the turbine. If the pitch or flap system is capable of reducing the load fluctuation under the set γ and λ, it surely can do so for lower γ or higher λ.

This chapter is split into three main sections. First, the flap system is used exclusively to reduce load fluctuation on the wind turbine blades under different pitch angles and flap r/R locations. Second, the pitch system is used for the same purpose instead of the flap system. Finally, the flap and pitch systems are compared to each other to determine the most effective and efficient method in reducing load fluctuation. The first two sections are descriptive at times because the main purpose is to present all the data sets at the beginning, prior to analyzing them. The third section analyzes all the cases presented, compares the pitch and flap system with each other and compares the data presented in this study to data found in the literature. An overall conclusion about which of these two systems is most effective at reducing load fluctuations is identified.

7.1 Dynamic Flap Cases

7.1.1 Outline

The main purpose of this section is to present quantitative and qualitative sets of data about how the flap system can attenuate load fluctuation when the turbine is operating in unsteady conditions. The equation of flap motion and the different experimental cases that were tested are discussed in Section 4.2.2. Although numerous experimental cases were investigated, only the most interesting and important ones are presented in this section. A list of these, together with the variables measured and the corresponding figures are listed in Table 7.1.

Table 7.1: Test matrix for dynamic motion for pitch cases

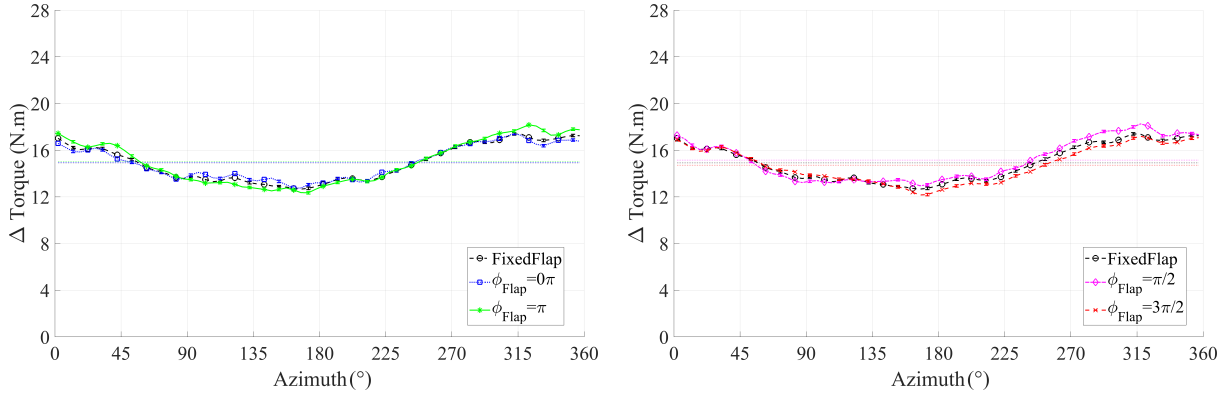
Case	$\beta(^\circ)$	$\alpha_{amp,F}(^\circ)$	TEF r/R Location	Variables	Figure
3a	3	20	0.82	ΔTorque, M_{FW}, C_n, PSD for M_{FW} and C_n	Figures 7.1 and 7.2
3b	6	20	0.82	ΔTorque, M_{FW}, C_n, $-\Delta C_p$	Figures 7.3 and 7.4
3c	3	27	0.66	ΔTorque, M_{FW}, C_n, C_M, $-\Delta C_p$	Figures 7.5 and 7.6

7.1.2 $\beta = 3^\circ$ Flap at r/R=0.82

Case 3a is presented first in Figure 7.1 where $\alpha_{amp,F} = 20^\circ$, $\beta_{mean} = 3^\circ$ and r/R=0.82. The flap motion follows a sinusoidal motion expressed in Equation (4.2). The flap phase, ϕ_{Flap}, is the phase offset between the flap motion and the blade azimuth position, ψ. The four phases together with the FixedFlap case (flap is not oscillating) are plotted into two plots, $\phi_{Flap} = 0\pi$ and π in the first plot and $\phi_{Flap} = \pi/2$ and $3\pi/2$ in the second plot. The FixedFlap case is included in both plots for reference. Before presenting the data, it is important to note that the main focus of this research concerns $\phi_{Flap} = 0\pi$ or in-phase because this setting produces the lowest load fluctuations. The other three phases are presented for the sake of completeness, when it seems appropriate.

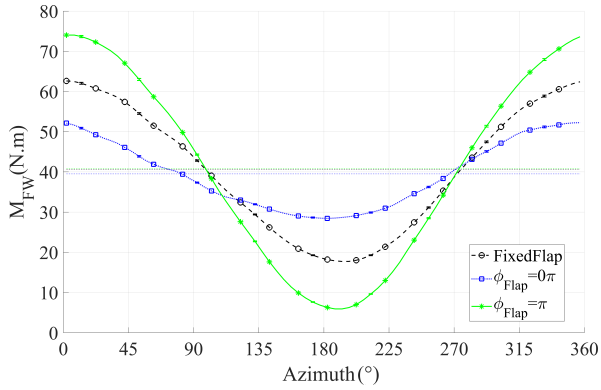
Rotor ΔTorque for the four different ϕ_{Flap} cases are presented in Figures 7.1a and 7.1b. For $\phi_{Flap} = 0\pi$ the ΔTorque did not change within uncertainty limits when compared to the FixedFlap case. The largest difference was found to be less than 2% for the other

three phases. This clearly indicates that oscillating the TEF does not influence ΔTorque significantly, and for the most important case, $\phi_{Flap} = 0\pi$, ΔTorque did not change at all. This is in alignment with what was found in Section 6.3 where the TEF did not significantly change ΔTorque with TEF actuation. The flapwise moment, M_{FW}, is plotted next in Figures 7.1c and 7.1d. This set of plots clearly show how the TEF is capable of manipulating M_{FW} that represents the entire out-of-plane blade root moment. For the $\phi_{Flap} = 0\pi$ case, the peak and trough are both reduced, thereby reducing the fluctuation in blade loading. When $\phi_{Flap} = \pi$ the complete opposite occurs, which was expected. The M_{FW} cycle average, which appears in the plot as a dotted line, is increased by 1% for the latter case and decreased by 2.6% for $\phi_{Flap} = 0\pi$. In both cases the change is minor and could be ignored. The purpose of the TEF is not to reduce the average blade loading but rather to eliminate the load fluctuation that occurs in a cycle. These plots thus prove that the TEF is fully capable of reducing the load fluctuations. When $\phi_{Flap} = \pi/2$ and $3\pi/2$, the TEF motion shifts the M_{FW} cycle left and right without changing the load fluctuation. This is expected because α_F minimum and maximum angles occur when the azimuth equals to 90° or 270°. Finally, Figures 7.1e and 7.1f display the performance parameter C_n for all four phases, and prompt the same remarks and conclusions outlined above for the M_{FW} plots. In conclusion, the TEF was capable of reducing fluctuation in M_{FW} and C_n but not in ΔTorque. The different phases show that the TEF can manipulate the turbine performance parameters at any point on the cycle, and that point is determined by the variable ϕ_{Flap}.

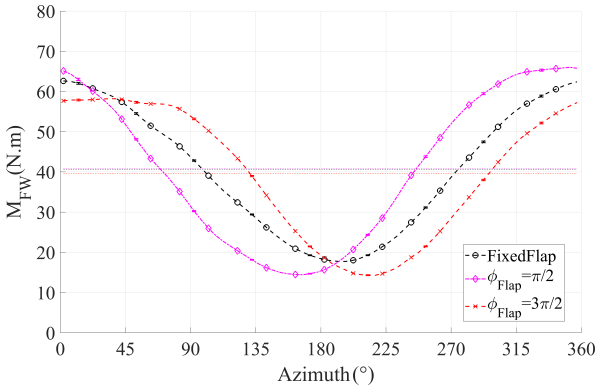


(a) Rotor Torque

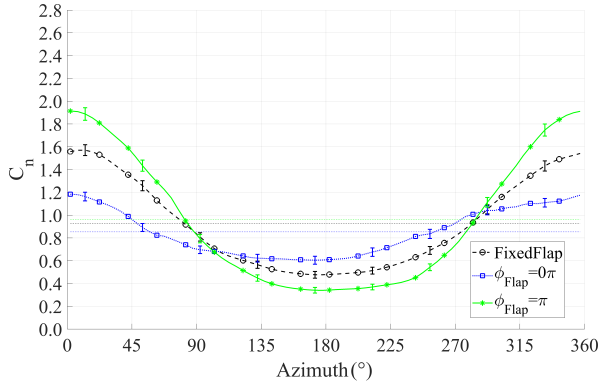
(b) Rotor Torque



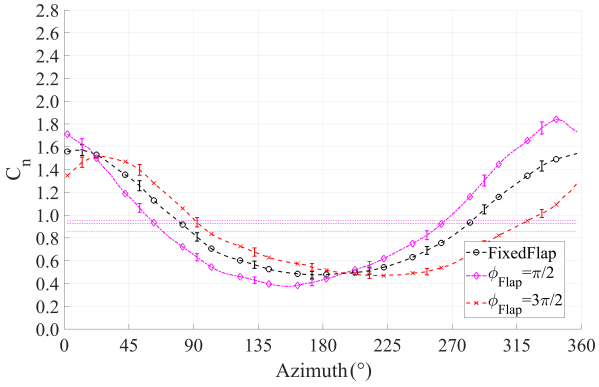
(c) Flapwise Moment (out of plane)



(d) Flapwise Moment (out of plane)



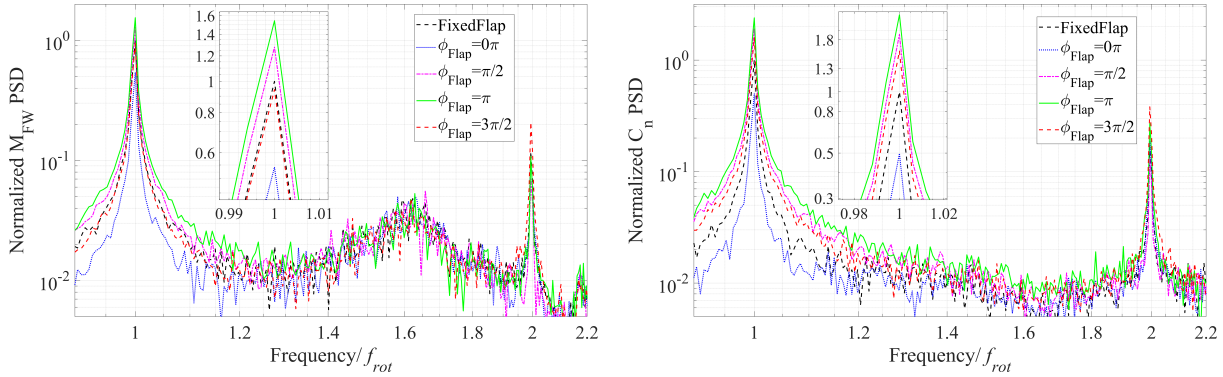
(e) C_n at r/R=0.82



(f) C_n at r/R=0.82

Figure 7.1: Turbine performance with an oscillating flap for different flap phases (ϕ_{Flap}) for case 3a where $\alpha_{amp,F} = 20°$, $\beta_{mean} = 3°$, $\gamma = 30°$, λ=3.5 and r/R=0.82. The dotted horizontal lines represent the cycle average.

The previous plots illustrated how the TEF is capable of manipulating and decreasing the blade load fluctuation in a qualitative way. However, Figure 7.1 does not provide quantitative information about the load fluctuation reduction. To do so, analysis in the frequency domain is the method of choice in the literature [96, 98, 139] as was discussed in Section 4.6.4. Power spectral density (PSD) versus frequency plots could be used to compare the various cases quantitatively, analogous to what was done in Section 5.2. The PSD plots for M_{FW} and C_n are presented in Figures 7.2a and 7.2b, respectively, for the various flap cases (ϕ_{Flap}). Both plots are normalized with the rotational frequency of f_{rot} =3.33 Hz on the x-axis and with the FixedFlap maximum peak on the y-axis. Both axes are plotted using a $\log_{10}$ scale to better show the frequency and amplitude distribution. An inset is used to magnify the results around the turbine rotational frequency, f_{rot}. In both plots two distinct peaks occur at Frequency/f_{rot}=1 and 2 corresponding to one and two events per rotor revolution or more commonly labeled as 1P and 2P. The second peak occurs due to harmonics in the system resulting from physical vibration in the turbine. The magnitude of the 2P peak is about 12% and 7% of the 1P peak for M_{FW} and C_n, respectively. This indicates that the dominant loads are occurring at 1P. For the M_{FW} parameter only in Figure 7.2a, there also exists a wider peak or a crest at Frequency/f_{rot}=1.6 corresponding to a frequency of 5.3 Hz. This increase in PSD magnitude is mainly due to the coupling between the load fluctuations and the natural frequency of the blade, which was found to be 5.1 Hz statically. Due to aerodynamic loads, the natural frequency of the blades does change as was reported by Berg *et al.* [103]. The magnitude of this peak is less than 5% of that occurring at 1P, which makes it less significant. A PSD reduction of 46% and 52% was found in M_{FW} and C_n, respectively, when $\phi_{Flap} = 0\pi$ or in-phase. This reduction is significant and meaningful as it reduces vibration not just at the peak frequency but also around its vicinity as well. Comparisons of the data gathered in this case and the corresponding data for the other cases, as well as relevant data published in the literature, may be found in Section 7.3.



(a) Spectral Desnity for M_{FW}

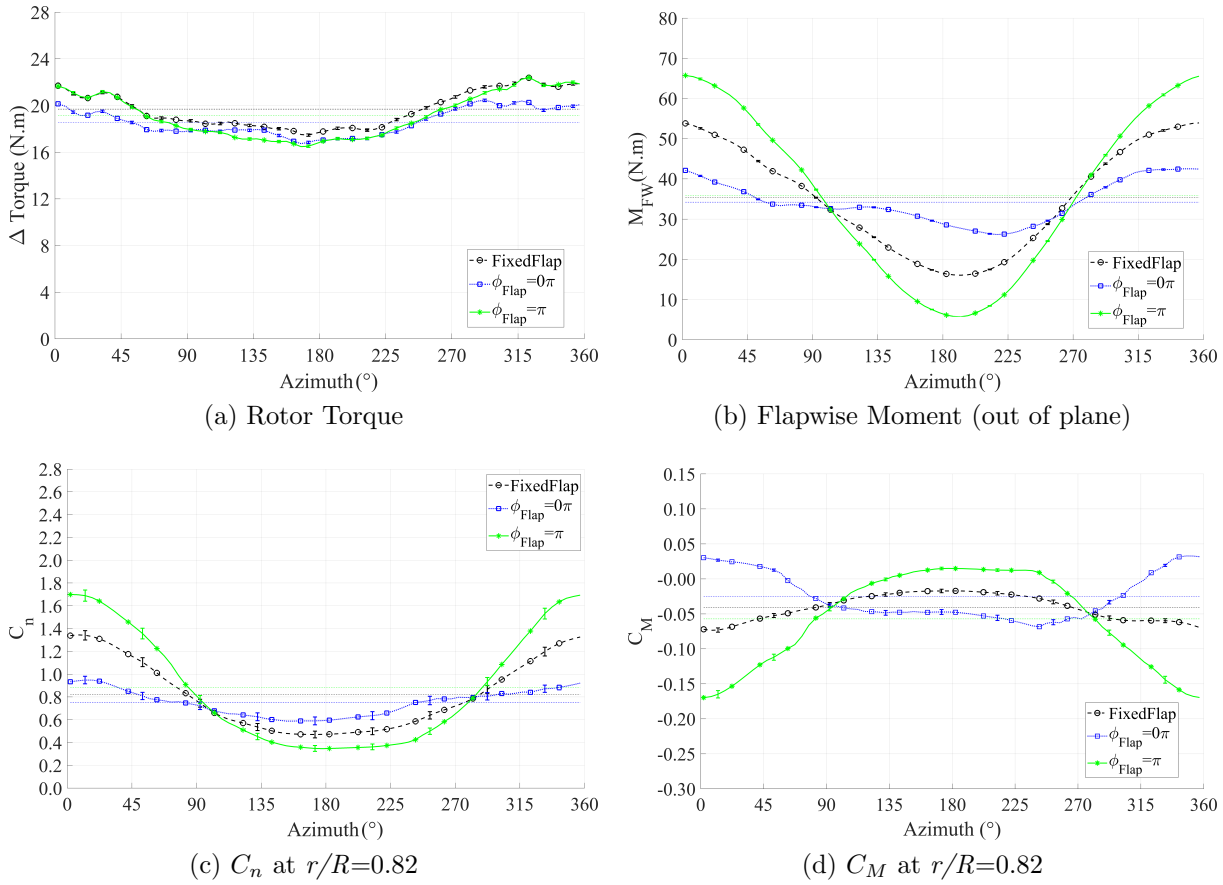
(b) Spectral Density for C_n at r/R=0.82

Figure 7.2: Normalized power spectral density distribution for a)M_{FW} and b)C_n for different flap phases (ϕ_{Flap}) for case 3a where $\alpha_{amp,F} = 20°$, $\beta_{mean} = 3°$, $\gamma = 30°$, λ=3.5 and r/R=0.82. Both axes use a $\log_{10}$ scale and an inset is shown to magnify the results around the peak frequency.

7.1.3 $\beta = 6°$ Flap at r/R=0.82

Case 3b is presented next, which differs from case 3a in that β increases from 3° to 6°. The turbine performance parameters are plotted in Figure 7.3. This time, $\phi_{Flap} = \pi/2$ and $3\pi/2$ have been omitted since no new information could be obtained and the graphs exhibit trends that are similar to those presented in Figure 7.1. It is observed in Figure 7.3a that the trend in ΔTorque changes for different ϕ_{Flap} contrary to the observation made from the previous case 3a. ΔTorque cycle average is reduced by 5% and 3% for $\phi_{Flap} = 0\pi$ and π, respectively. Not only was the average reduced but the fluctuation in the cycle was also reduced for $\phi_{Flap} = 0\pi$. A reduction of 5% in turbine power output is a small price to pay to reduce the fluctuation in rotor torque because the latter reduction exerts less stress on the blades, gearbox and motor in the nacelle. The reason there is a change in ΔTorque for case 3b and not case 3a can be traced back to Section 6.3.2, where it was deduced that the TEF influence over ΔTorque increases when β increases from 3° to 6°. This is mainly due to the fact that a larger section of the blade is stalled when $\beta = 3°$, thereby increasing the drag coefficient. Because the TEF influence over ΔTorque increased, case 3b leads to a larger change in ΔTorque than case 3a. Looking at the M_{FW} data in Figure 7.3b, the $\phi_{Flap} = 0\pi$ data appears almost flat unlike the pattern presented in case 3a. In Section 6.2.3 it was concluded that the M_{FW} fluctuations increase as β decreases. This observation shows that the load fluctuations were greater for case 3a than for case 3b, and the TEF motion was not fully capable of reducing the higher fluctuations. This load

fluctuation reduction in M_{FW} and C_n comes at a cost, however, and that is usually paid by an increase in C_M fluctuations, as seen in Figure 7.3d. Any motion in the TEF will tend to increase the fluctuations in C_M. The reason for this increase will be explained using the $-\Delta C_p$ contour plots found in Figure 7.4.



(a) Rotor Torque

(b) Flapwise Moment (out of plane)

(c) C_n at r/R=0.82

(d) C_M at r/R=0.82

Figure 7.3: Turbine performance with an oscillating flap for different flap phases (ϕ_{Flap}) for case 3b where $\alpha_{amp,F} = 20°$, $\beta_{mean} = 6°$, $\gamma = 30°$, λ=3.5 and r/R=0.82. The dotted horizontal lines represent the cycle average.

The PSD for M_{FW} and C_n are have been omitted since neither graph provides any novel data trends apart from a reduction in amplitude for the different phases which are summarized later in Section 7.3. Contours of $-\Delta C_p$ for case 3b are plotted in Figure 7.4 for the FixedFlap case and when $\phi_{Flap} = 0\pi$ and π. A descriptive account of the FixedFlap contour can be found in Section 6.2.3 and Figure 6.11. This section focuses more on how

the TEF motion affects $-\Delta C_p$ over the blade chord. First, the FixedFlap case is compared with $\phi_{Flap} = 0\pi$. The kinematics of flap motion are more clearly plotted in Figure 4.1 showing the relationship with α_F and cycle period. The contour plot could be split into two distinct regions. When $\psi = 180°$, α_F is equal to $-20°$ and $-\Delta C_p$ is increased, whereas, when $\psi = 0°$ or 360 °, α_F is equal to 20° and $-\Delta C_p$ is decreased. Although there is a $-\Delta C_p$ change across the entire chord due to the TEF motion, this change is mostly concentrated at the TE. This is in alignment with the conclusions derived from the 2D pitching airfoil experiments with a pitching flap in Section 5.2 and from the steady flap cases in Section 6.3. Based on the results displayed in Figure 7.4 and in the two sections previously mentioned, the TEF manipulates $-\Delta C_p$ at the TE to counteract the variation occurring at the LE. This phenomenon is a characteristic of the TEF and is observed in the 2D studies in Chapter 5 as well as on the rotating wind turbine blade. Second, the FixedFlap case is compared with $\phi_{Flap} = \pi$. In this scenario, the complete opposite occurs and the TEF magnifies the variation in $-\Delta C_p$ with ψ because the motion of the flap is reversed. In some regions, the TEF creates an area where $-\Delta C_p$ is negative at x/c=0.8, analogous to the behavior observed in Section 6.3.4 and Figure 6.20. This large variation in $-\Delta C_p$ at the TE caused by the flap motion leads to a significant shift in the surface pressure center along the airfoil chord. This center of pressure shift is quantified and is seen more clearly in the C_M plot that was presented earlier in Figure 7.5d. Variation in C_M causes variation in the pitching moment at the root of the blade but is not as problematic as variation in the blade root moment. The STD(ΔC_p) was also explored, but the corresponding plot has not been included since it does not show any variation with a change in ϕ_{Flap}.

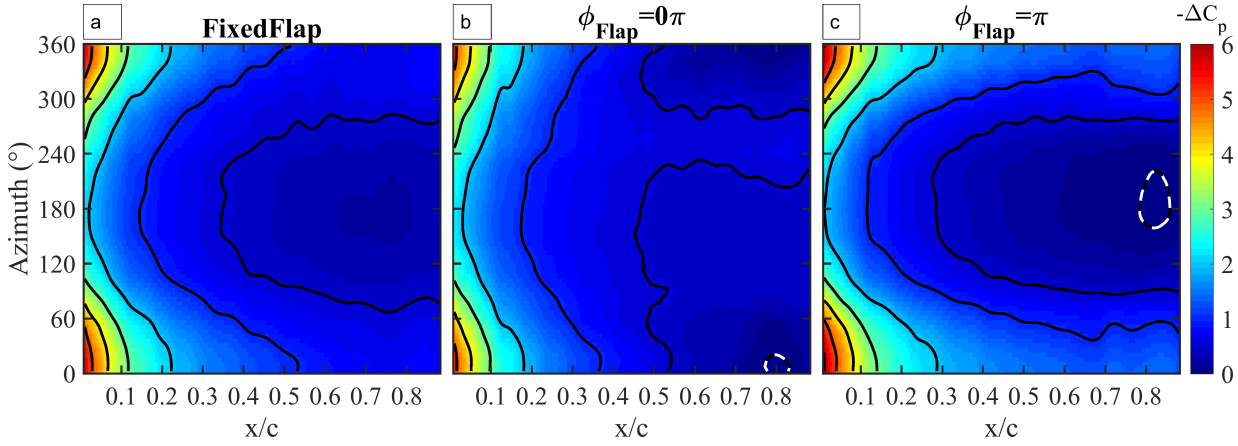
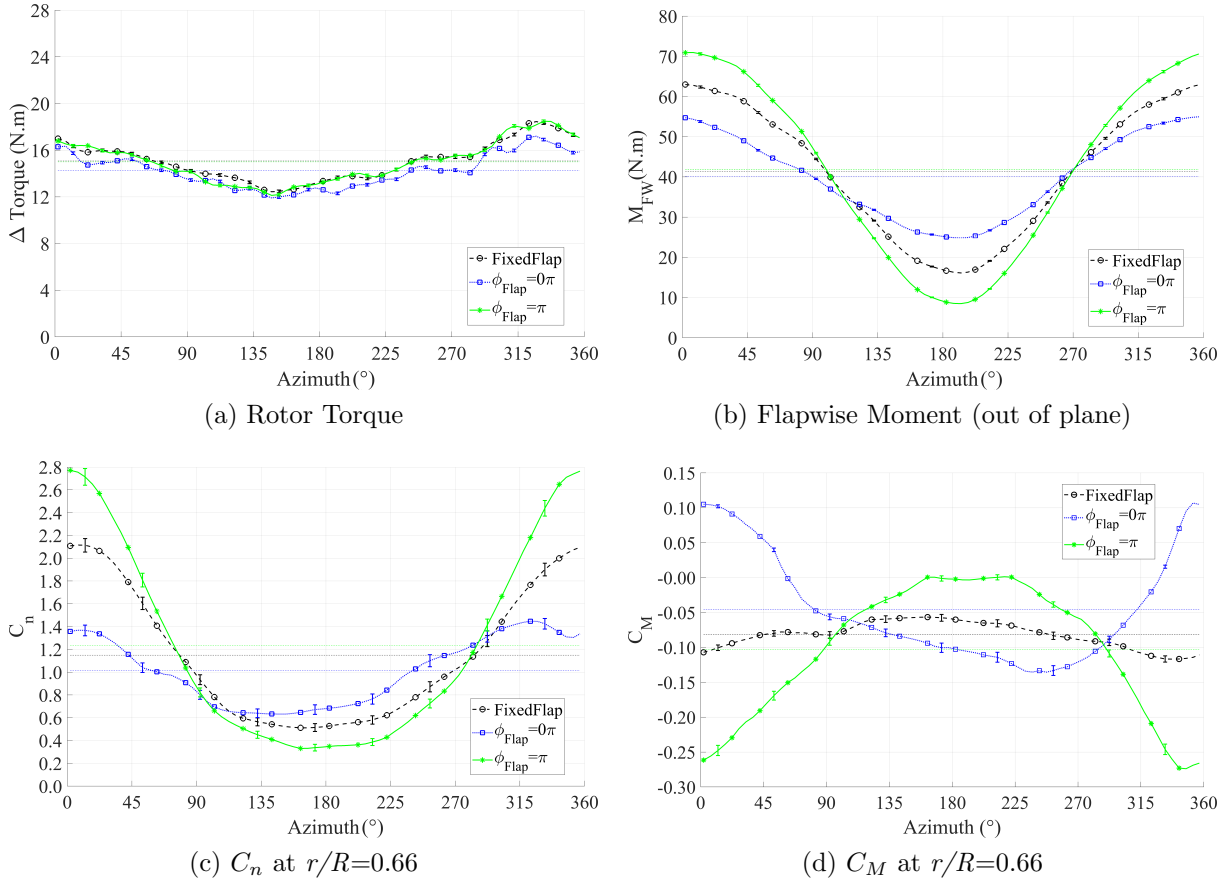


Figure 7.4: Contours of $-\Delta C_p$ versus x/c versus ψ for a) FixedFlap b) $\phi_{Flap} = 0\pi$ c) $\phi_{Flap} = \pi$ for case 3b where $\alpha_{amp,F} = 20°$, $\beta_{mean} = 6°$, $\gamma = 30°$, λ=3.5 and r/R=0.82. The iso-lines on the plot represent constant $-\Delta C_p$ values=[0 0.5 1 2 3 4 5 6]. The iso-line of $\Delta C_p = 0$ is marked with white dashes.

7.1.4 $\beta = 3°$ Flap at r/R=0.66

For the third set of plots, the TEF flap r/R location was changed from 0.82 to 0.66 as per specified for case 3c. The TEF motion amplitude, $\alpha_{amp,F}$, was also increased from 20° to the maximum allowable amplitude of 27° due to restriction by the controller. Such a large amplitude is not recommended, since the plots in Figure 6.17 provided convincing evidence that the linear range of the TEF is within ±20°. The setting in this particular case was chosen to see what happens when the TEF angle increases beyond its linear range. In Figure 7.5 the turbine performance parameters are plotted for case 3c where $\beta = 3°$. In the ΔTorque plot, there is a reduction of 5% in power output for $\phi_{Flap} = 0\pi$. which is similar to what was found in case 3b. This is because the TEF influence over ΔTorque is significant when r/R=0.66 and $\beta = 3°$, as was concluded from Figure 6.17. For the M_{FW} and C_n data, there is a reduction in fluctuation similar to what was seen in other cases. More quantitative analysis of load reduction is provided in Section 7.3. The C_M data are also plotted below to illustrate how any TEF motion significantly increases C_M fluctuation. This fluctuation is better explained using the $-\Delta C_p$ contour plots found in Figure 7.6.



(a) Rotor Torque

(b) Flapwise Moment (out of plane)

(c) C_n at r/R=0.66

(d) C_M at r/R=0.66

Figure 7.5: Turbine performance with an oscillating flap for different flap phases (ϕ_{Flap}) for case 3c where $\alpha_{amp,F} = 27°$, $\beta_{mean} = 3°$, $\gamma = 30°$, λ=3.5 and r/R=0.66. The dotted horizontal lines represent the cycle average.

The $-\Delta C_p$ contour plots for case 3c are plotted in Figure 7.6. As indicated in Section 6.2.3 in conjunction with Figure 6.11, the blade is stalled around $\psi = 180°$ because of the unsteady behavior when the wind turbine is yawed. For $\phi_{Flap} = 0\pi$, the TEF motion reduced $-\Delta C_p$ at the LE and can be seen in the iso-line shift towards the LE, particularly at $\psi = 360°$ and $0°$. The complete opposite occurs when $\phi_{Flap} = \pi$ because of the reversal of the TEF motion. Figure 7.6 shows that the TEF tends to have more influence over ΔC_p at the TE rather than at the LE, which is in alignment with the conclusions made earlier. By increasing the amplitude of the TEF motion, a more notable manipulation of $-\Delta C_p$ is seen, and is reflected in the $C_L - \psi$ plot in Figure 7.5c. The negative $-\Delta C_p$ regions, marked with white dashes, occur in both cases when α_F is at its highest angle of

+27°. Negative α_F angles, on the other hand, dramatically increased $-\Delta C_p$ at the TE, especially when $\phi_{Flap} = \pi$ indicating that the flow is still attached over the TE even with such high flap angles of -27°. This large variation in $-\Delta C_p$ at the TE caused by the TEF motion causes a major shift in the surface pressure center along the airfoil chord. This effect, in turn, changed the C_M data presented in Figure 7.5d. For example, by looking at $\phi_{Flap} = 0\pi$ and $\psi = 0°$ or 360°, $-\Delta C_p$ is high at the LE and negative at the TE. This discrepancy indicates that there is high suction at the LE and negative suction or positive pressure at the TE producing a large nose-up pitching moment as seen in the $C_M - \psi$ plot.

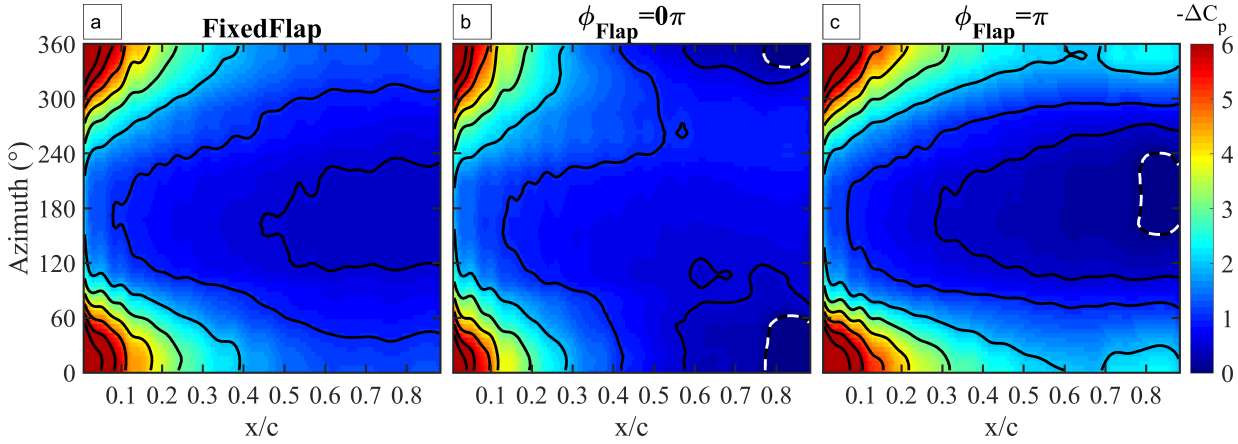


Figure 7.6: Contours of $-\Delta C_p$ versus x/c versus ψ for a) FixedFlap b) $\phi_{Flap} = 0\pi$ c) $\phi_{Flap} = \pi$ for case 3c where $\alpha_{amp,F} = 27°$, $\beta_{mean} = 3°$, $\gamma = 30°$, λ=3.5 and r/R=0.66. The iso-lines on the plot represent constant $-\Delta C_p$ values=[0 0.5 1 2 3 4 5 6]. The iso-line of $\Delta C_p = 0$ is marked with white dashes.

7.2 Dynamic Pitch Cases

7.2.1 Outline

After reducing load fluctuation using the TEF motion, the pitch system is now used in this section for the same purpose while keeping the TEF fixed to achieve a clean blade. The equation of motion and the experimental plan for the pitch system is outlined in Section 4.2.3. A combination of plots similar to those used to assess the TEF system will be employed to evaluate the pitch system. Table 7.2 lists the two distinct cases to be discussed, together with the variables used and the associated figure numbers. For both cases, β_{amp} was set to 5° and did not vary.

Table 7.2: Test matrix for dynamic motion the two pitch cases investigated

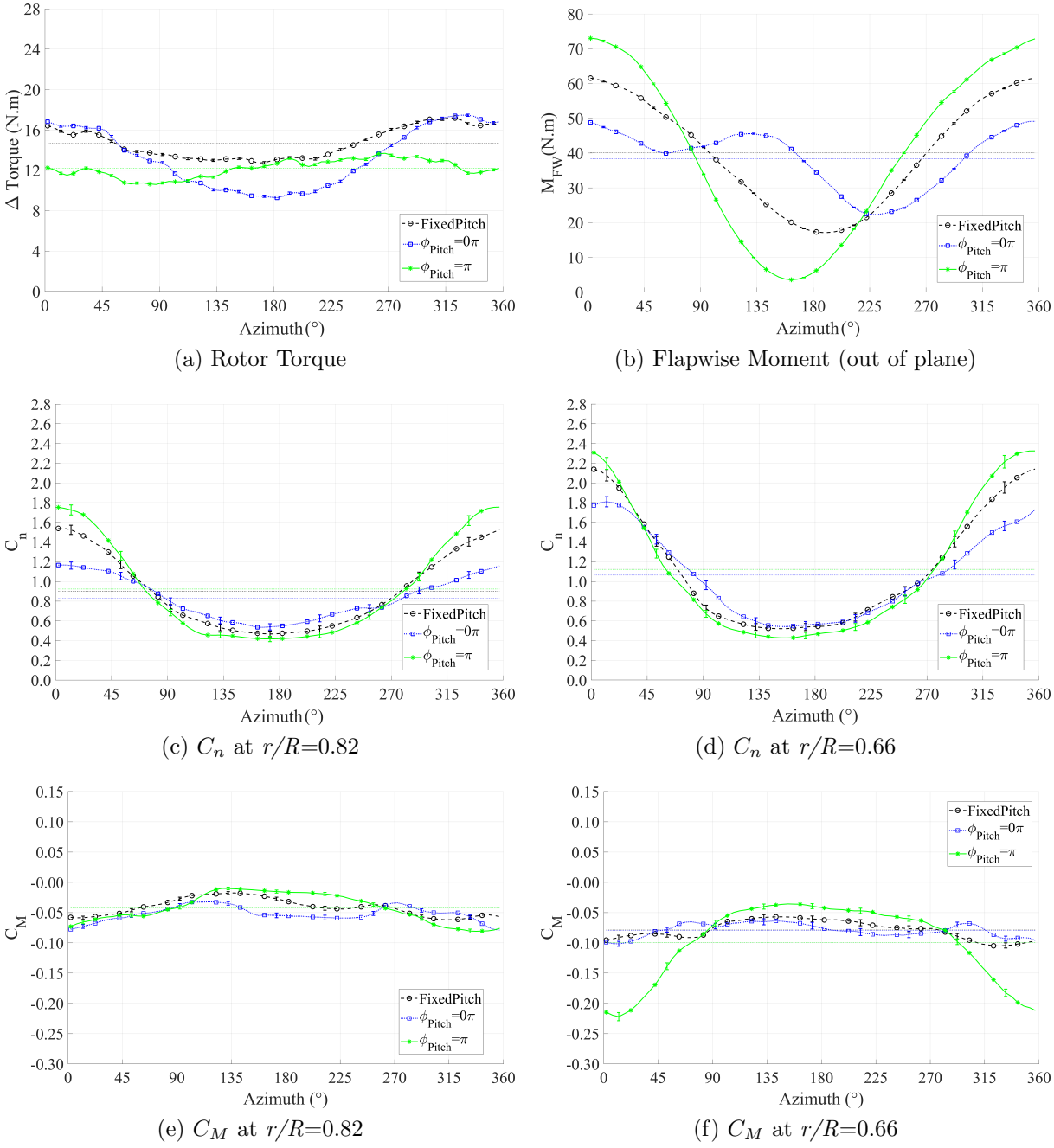
Case	$\beta_{mean}(^\circ)$	$\beta_{amp}(^\circ)$	Variables	Figure
4a	3	5	ΔTorque, M_{FW}, $\{C_n, C_M\}$ at r/R=0.82 and 0.66, PSD for M_{FW} and C_n	Figures 7.7 and 7.8
4b	6	5	ΔTorque, M_{FW}, $\{C_n, C_M, \Delta C_p\}$ at r/R=0.82 and 0.66	Figure 7.9 and 7.10

7.2.2 $\beta_{mean} = 3^\circ$

Case 4a is presented first in Figure 7.7 where $\beta_{mean} = 3^\circ$. Only two out of the four phases are shown in the plots because $\phi_{Pitch} = \pi/2$ and $3\pi/2$ are not of significant interest in this study. Due to the pitching motion, ΔTorque, presented in Figure 7.7a, was reduced by 10% and 17% for $\phi_{Pitch} = 0\pi$ and π, respectively, when compared to the FixedPitch case. On the other hand, the TEF motion did not reduce ΔTorque at all under similar conditions. A reduction in ΔTorque ultimately means a power output reduction and a less efficient turbine. In an ideal situation the power output should be kept constant. This power output reduction is a major disadvantage and a consequence of using the blade pitch to attenuate load fluctuation. The observed reduction could be attributed to the less efficient blade design where the pitch and chord are constant. In a properly designed blade with a variable pitch and chord, the flow over the total span of the blade should be attached. For $\phi_{Pitch} = 0\pi$, the variation in ΔTorque seems to have increased instead of decreasing as would have expected. With the data available, this observed aspect could not be fully explained. To the author's knowledge, such a trend in the data has never been reported or discussed in the literature, and that makes it rather difficult to understand this behavior with certainty. The trend in data could possibly be due to a phase lag between pitch actuation and torque change. Due to this phase lag, ϕ_{Pitch} being equal to 0π could prompt a constructive coupling, increasing the torque fluctuation. On the other hand, ϕ_{Pitch} being equal to 0π would create a destructive coupling, decreasing the torque fluctuations as seen in the figure. More experiments are needed to confirm and understand this phenomenon.

For the M_{FW} data presented in Figure 7.7b, the pitching motion reduced the blade moment fluctuations significantly when $\phi_{Pitch} = 0\pi$. A second peak appears in the data around $\psi \approx 130^\circ$, indicating that the ϕ_{Pitch} chosen might not have been the most ideal. From the step response experiment that was reported in Section 4.4.3, it was found that there is a blade rotation lag of 42° between actuation and a change in M_{FW} output. This

inherent lag in the pitch system could not be eliminated and is an obvious disadvantage. Future experiments would account for the lag mentioned to choose a more appropriate ϕ_{Pitch}. The C_n data are presented next in Figures 7.7c and 7.7d for r/R=0.82 and 0.66, respectively. The pitch system is capable of manipulating C_n only at $\psi = 0°$ or 360° and not around $\psi = 180°$. This limitation occurs because it was concluded from Section 6.2.3 and Figure 6.9 that changing the pitch angle does not influence C_n at $\psi = 180°$ but only at $\psi = 0°$ or 360°. This is because the blade section is stalled at $\psi = 180°$ and attached everywhere else. When a blade is stalled, the relationship between the pitch angle and C_n is not linear, as both the wind turbine experiments and the 2D static results demonstrated in Section 5.1. This clearly shows that the effectiveness of the pitch system in alleviating loads is highly dependent on the flow being attached over the blade. The TEF, on the other hand, does not have this dependency and can influence C_n whether the blade is stalled or not. Finally the C_M data are plotted in Figures 7.7e and 7.7f. The most important finding that emerges from these two plots is that the pitching motion does not increase the C_M fluctuation for $\phi_{Pitch} = 0\pi$. This is an advantage of the pitching system over the TEF system. In the previous section, it was found that any flap motion would increase the C_M fluctuation.



(a) Rotor Torque

(b) Flapwise Moment (out of plane)

(c) C_n at r/R=0.82

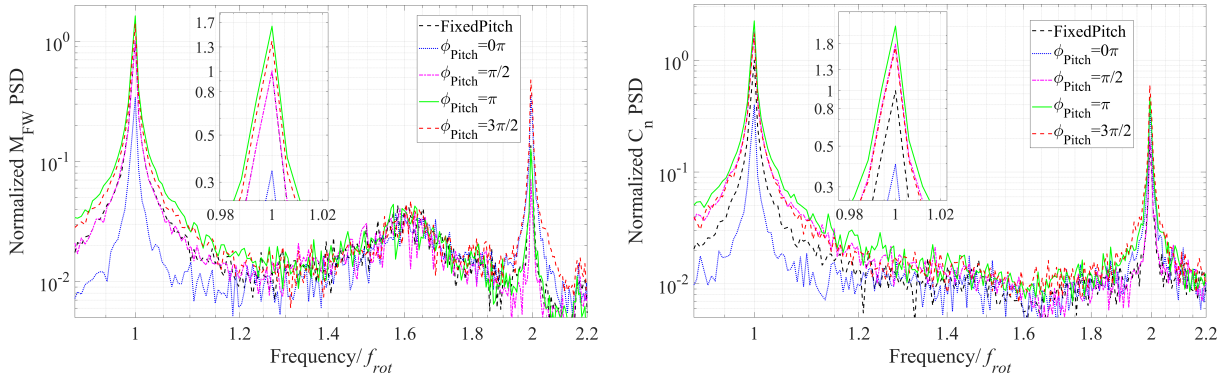
(d) C_n at r/R=0.66

(e) C_M at r/R=0.82

(f) C_M at r/R=0.66

Figure 7.7: Turbine performance with an oscillating pitch for different pitch phases (ϕ_{Pitch}) for case 4a where $\beta_{amp} = 5°$, $\beta_{mean} = 3°$, $\gamma = 30°$, λ=3.5. The dotted horizontal lines represent the cycle average.

Normalized PSD data for M_{FW} and C_n are plotted in Figure 7.8. The PSD amplitude was reduced by 66% and 60% for M_{FW} and C_n, respectively, with respect to the FixedPitch case when $\phi_{Pitch} = 0\pi$. Under the same conditions, the TEF was capable of reducing M_{FW} and C_n PSD amplitude by 46% and 52% from Figure 7.2. This is a difference of 20% and 8%, respectively, when compared to the pitch system. This difference was expected because the TEF only impacts 22% of the aerodynamic blade span, while the pitch changes the aerodynamics of the entire blade span. For a more detailed discussion and comparison of these two systems, see Section 7.3.



(a) Spectral Desnity for M_{FW}

(b) Spectral Desnity for C_n at r/R=0.82

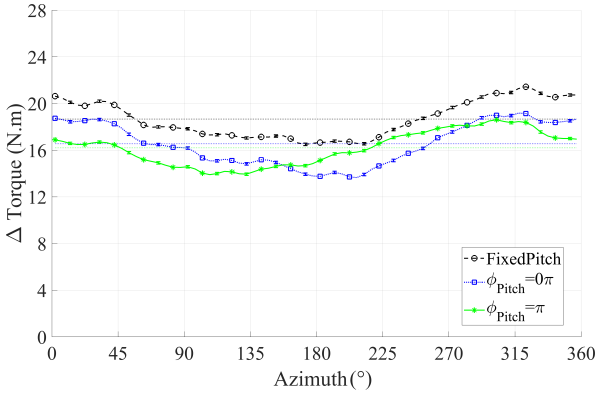
Figure 7.8: Normalized power spectral density distribution for M_{FW} and C_n at r/R=0.82 for different pitch phases (ϕ_{Pitch}) for case 4a where $\beta_{amp} = 5°$, $\beta_{mean} = 3°$, $\gamma = 30°$, λ=3.5. Both axes use a $\log_{10}$ scale and an inset is shown to magnify the results around the peak frequency.

7.2.3 $\beta_{mean} = 6°$

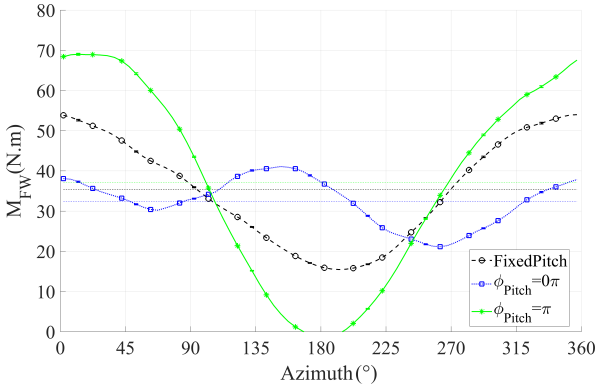
The turbine performance for case 4b is now presented in Figure 7.9 where β increased from 3° to 6°. The ΔTorque data seems to have shifted down when $\phi_{Pitch} = 0\pi$, reducing the average by 12%. Under similar conditions, the TEF system reduced the ΔTorque average by only 5% but at the same time reduced the fluctuation in ΔTorque. In the pitch system however, the reduction of the ΔTorque average was not accompanied by any reduction in fluctuation, as that variable remained the same. The fluctuation in M_{FW}, C_n at r/R=0.82 and C_n at r/R=0.66 when $\phi_{Pitch} = 0\pi$ is significantly reduced and in some cases almost totally eliminated. This reduction in fluctuation is greater than the corresponding reduction observed in case 4a where $\beta = 3°$ because as β decreases a larger section of the blade would be operating around the onset of stall or in the stall region.

In that region, the relationship between β and C_n is no longer linear thus controlling the load is no longer as effective. For this reason, when $\beta = 6°$, the blade is operating below stall in the linear range where the influence over blade loading is significant. This aspect is illustrated in greater detail in Sections 5.1 and 6.2.3. Finally, the variation in C_M did not change under the different pitch phases that were investigated. This is an advantage because for the TEF system, there was a significant increase in C_M variation. A more detailed understanding of the C_n and C_M data is obtained after presenting the ΔC_p contour plots next in Figure 7.10.

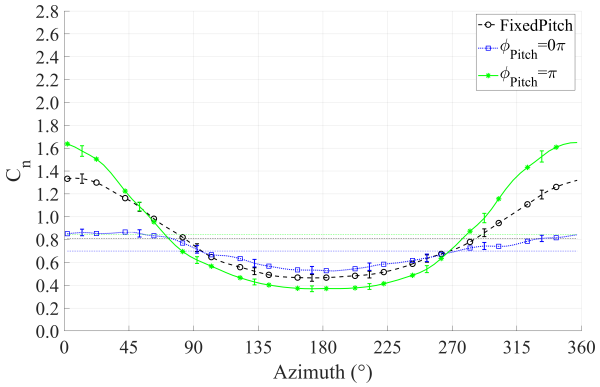
The $-\Delta C_p$ contours for different ϕ_{Pitch} are plotted at two r/R locations (0.82 and 0.66) in Figure 7.10. The contour plots for the FixedPitch cases were discussed previously in Section 6.2.3 but are reproduced again for reference purposes. Focusing on the $\phi_{Pitch} = 0\pi$ and r/R=0.82 case, the contour plots show that the pitching motion almost eliminates all the variation in $-\Delta C_p$. Unlike the TEF system, the pitching system was capable of reducing $-\Delta C_p$ at the LE while keeping the TE region unchanged. The results from TEF system that were discussed in the previous section showed that the change in $-\Delta C_p$ due to the flap motion was only concentrated at the TE with minor changes around the LE region. This is a major difference between the two systems where the TEF changes $-\Delta C_p$ at the TE while the pitch system changes $-\Delta C_p$ at the LE. This difference does not affect the final C_n or M_{FW} results; however, it does impact C_M. The pitching motion does not change the center of pressure as evident in the $C_M - \psi$ plots in Figures 7.7 and 7.9. From a root bending moment perspective, it does not matter whether the reduction in load fluctuation is occurring at the LE or the TE. However, a torsional force at the blade root would increase when the TEF system is used to attenuate load fluctuation but not when the pitch system is used, since the latter system does not change the C_M fluctuation. The reduction in $-\Delta C_p$ fluctuation when r/R decreased to 0.66 from 0.82 becomes less significant. This attenuation can be explained by studying the α variation obtained from the OpenFast model, which is plotted in Figure 6.9. At r/R=0.66, α is oscillating at a higher mean angle, forcing the blade segment to operate around the onset of stall where the relationship between blade pitch and blade load is not linear. This aspect would make the pitch system less effective at reducing load fluctuation. A better and a more detailed comparison between the pitch and the flap system is presented later in Figure 7.11. Finally when $\phi_{Pitch} = \pi$, the fluctuation in $-\Delta C_p$ is significantly increased at both r/R locations because the pitch motion is increasing the α variation with azimuth.



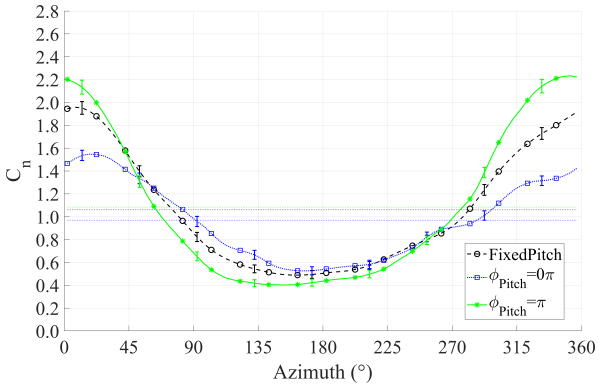
(a) Spectral Desnity for M_{FW}



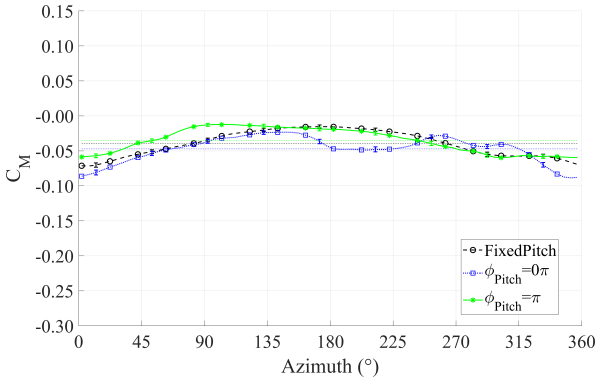
(b) Spectral Desnity for M_{FW}



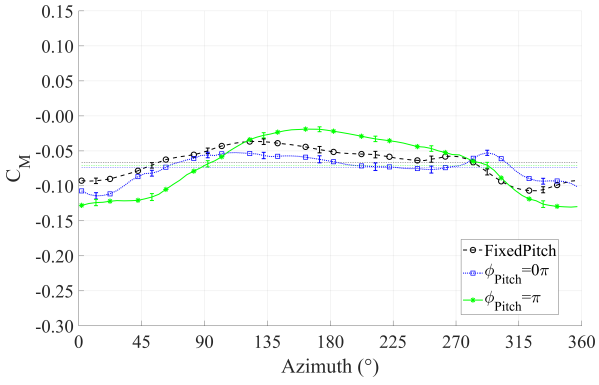
(c) Spectral Desnity for C_n



(d) C_n at r/R=0.66



(e) C_M at r/R=0.82



(f) C_M at r/R=0.66

Figure 7.9: Turbine performance with an oscillating pitch for different pitch phases (ϕ_{Pitch}) for case 4b where $\beta_{amp} = 5°$, $\beta_{mean} = 6°$, $\gamma = 30°$, λ=3.5. The dotted horizontal lines represent the cycle average.

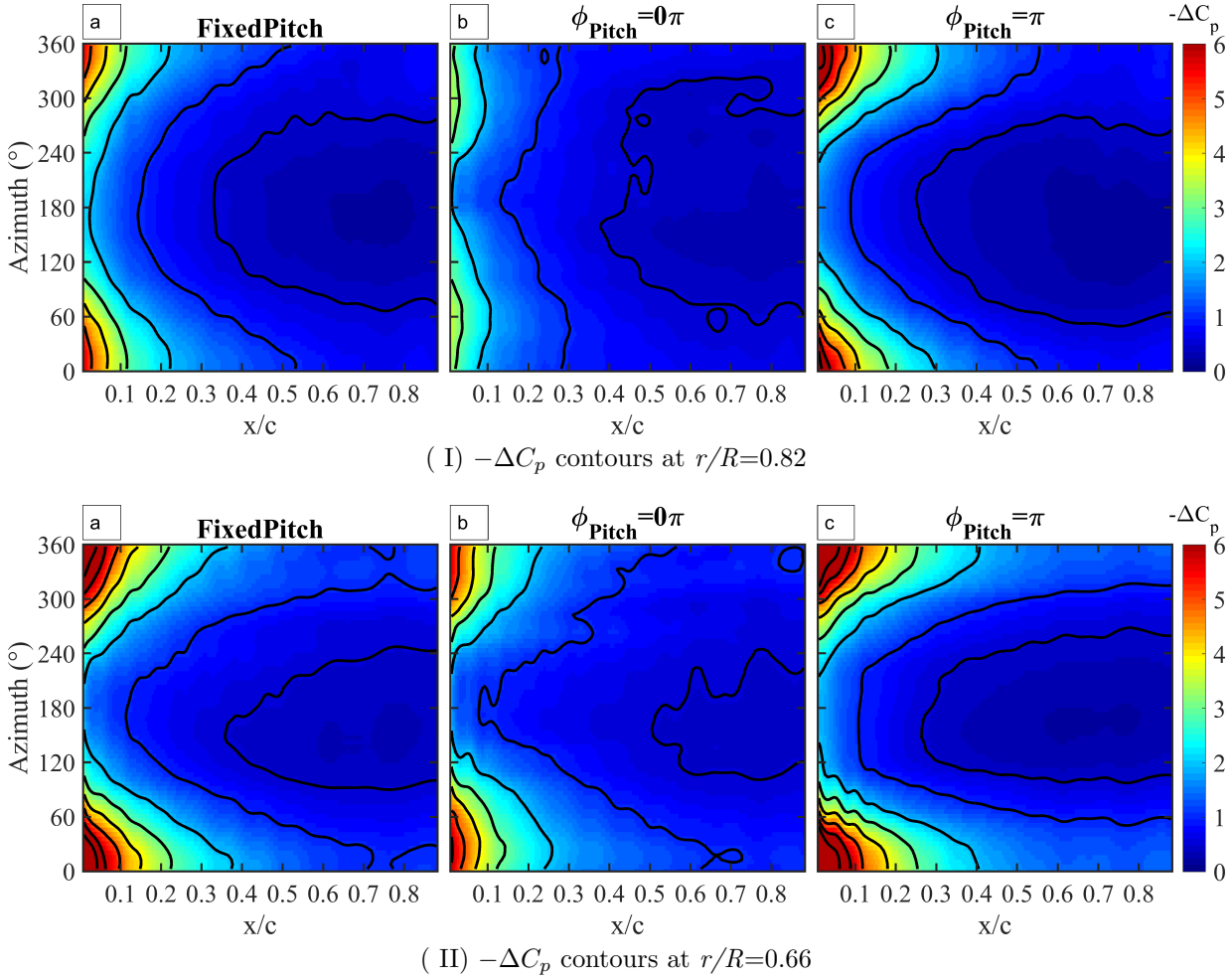


Figure 7.10: Contours of $-\Delta C_p$ versus x/c versus ψ at I) r/R=0.82 and II) r/R=0.66 for a) FixedFlap b) $\phi_{Pitch} = 0\pi$ c) $\phi_{Flap} = \pi$ for case 4b where $\beta_{amp} = 5°$, $\beta_{mean} = 6°$, $\gamma = 30°$, λ=3.5. The iso-lines on the plot represent constant $-\Delta C_p$ values=[0 0.5 1 2 3 4 5 6].

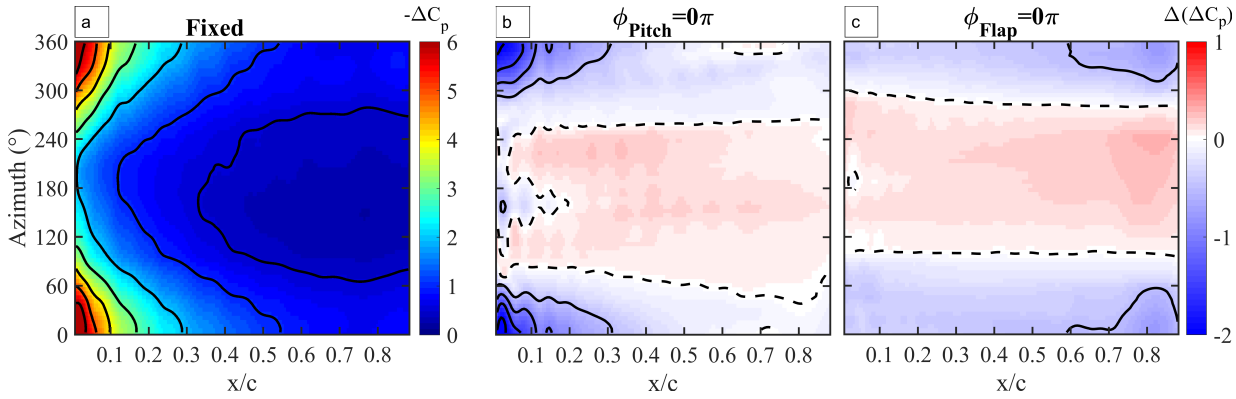
7.3 Dynamic Flap and Pitch Comparison

Now that the dynamic flap and pitch systems have been presented separately and discussed in detail, they are compared to each other and to data available in the literature. The effectiveness of each system in alleviating loads under various conditions is analyzed in detail. Most of the analysis is examined here since Sections 7.1 and 7.2 were used to present

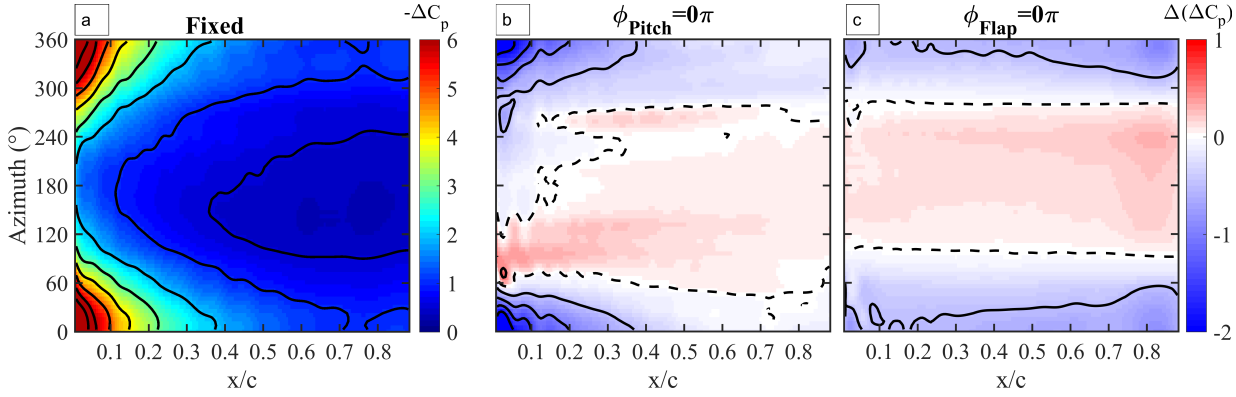
the data and provide an accompanying descriptive account. The difference between the two systems in how they manipulate surface pressure along the blade chord is analyzed first by looking at the ΔC_p contour plots. Second, a bar chart is used to compare the effectiveness of each system in reducing load fluctuations under the different conditions tested. Finally, a comparison matrix is provided to highlight the strengths and weaknesses of each system and show which system would be the best choice under various conditions.

7.3.1 ΔC_p Contour Comparison

The ΔC_p contour plots for the pitch and the flap system were analyzed in the previous two sections but to better compare them, they are plotted side by side in Figure 7.11. The Fixed case is plotted first as a benchmark for comparison, followed by $\Delta(\Delta C_p)$ for the pitch and flap systems where the value plotted is equal to the difference between the Fixed case and $\phi = 0\pi$. By choosing to plot this particular difference,, the location where each system modifies the surface pressure around the blade chord is clearly highlighted. Figure 7.11 I shows data for $\beta = 3°$ and r/R=0.82 while Figure 7.11 II shows data for $\beta = 6°$ and r/R=0.66 to cover the different cases tested. A positive and a negative change in $\Delta(\Delta C_p)$ are highlighted in red and blue, respectively, while a zero change is indicated by a white region. The contour plots clearly show that $\Delta(\Delta C_p)$ due to the pitch motion is concentrated at the LE because the iso-lines are all shifted to the LE while the white region (representing $\Delta(\Delta C_p) = 0$) is spread across the TE. On the other hand, $\Delta(\Delta C_p)$ due to the flap motion is concentrated at the TE because the iso-lines are also shifted to the TE. This interpretation aligns with the conclusions stated in the previous two sections. The main advantage of the pitch system is that it can reduce ΔC_p where it is highest and that is at the LE. On the other hand, the flap system manipulates $-\Delta C_p$ at the TE to counteract the variation occurring at the LE. This shifts the center of pressure and increases the torsional force at the blade root as seen in the $C_M - \psi$ plots in Figures 7.3d and 7.5d. Even though load reduction occurs at different x/c locations, both systems were capable of reducing M_{FW} because blade root moment measures the total force on the blade chord. Therefore, the location of load reduction only matters if the additional torsional force causes damage to the blade root. Future research should quantify the additional torsional forces and whether they are significant enough to cause blade fatigue.



(I) $\beta = 3°$ and r/R=0.82



(II) $\beta = 6°$ and r/R=0.66

Figure 7.11: Contours of $-\Delta C_p$ versus x/c versus ψ for a) Fixed case and $\Delta(\Delta C_p)$ for b) $\phi_{Pitch} = 0\pi$ c) $\phi_{Flap} = 0\pi$ where $\gamma = 30°$, λ=3.5. The constant $-\Delta C_p$ iso-lines =[0 0.5 1 2 3 4 5 6]. The $\Delta(\Delta C_p)$ iso-lines are spaced by 0.5. The iso-line of $\Delta(\Delta C_p) = 0$ is marked with white dashes.

7.3.2 PSD Reduction Comparison

Based on the results reported thus far, the best parameter that summarizes the effectiveness in load fluctuation reduction is the change in PSD amplitude at 1P. As discussed previously in Section 4.6.4, the % change in PSD have been used by the academic community to determine the effectiveness of the system. Therefor, using PSD makes it much easier to compare the data collected in this study to data available in the literature. To this end, the % change in PSD for C_n and M_{FW} are plotted in two bar charts in Figures 7.12a and 7.12b, respectively. For clarity and legibility the pitch system is marked with blue (■), the flap system with $\alpha_{amp,F} = 20°$ in red (■) and the flap system with $\alpha_{amp,F} = 27°$ in green

(■). Each plot is grouped based on its β angle of 3° or 6° and each β has two subgroups for r/R=0.66 and 0.82.

The PSD change in C_n is presented first in Figure 7.12a because it represent the local forces on the blade. Analyzing the pitch system first (■), when β decreases from 6° to 3°, the change in PSD is reduced at both r/R locations. This reduction occurs because when $\beta = 3°$, a larger section of the blade is operating in stall or at the stall onset, where the relationship between α and C_n is not linear, thereby making the pitch system less effective. At $\beta = 3°$, the load fluctuations are also inherently higher and the pitch motion in this case is not enough to attenuate the load fluctuation. When r/R decreases from 0.82 to 0.66, the change in PSD is reduced for both β angles. This reduction occurs because as r/R decreases the variation in α increases and its amplitude as well. As a result, the blade segment is forced to operate closer to stall, where the pitch motion is less effective. In addition, the variation in C_n is inherently increased when r/R decreases.

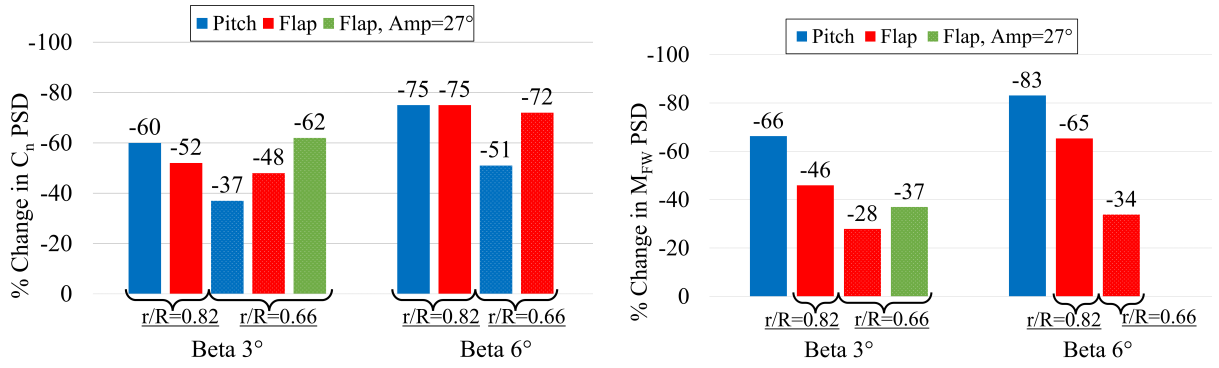
Focusing on the TEF system (■) in the same Figure 7.12a, a few important conclusions could be made. As β increased from 3° to 6° in Figure 7.12a, the effectiveness of the TEF system at reducing load fluctuation increased by about 25%. This result was expected because as was concluded from Figure 6.15 in Section 6.3.2, the control capability of the TEF over C_n does decrease when β decreases. When r/R decreases from 0.82 to 0.66, the results indicate that there is only a slight reduction in PSD % change as opposed to a larger reduction seen in the pitch system. This minor reduction occurs because the TEF control capability over C_n is only slightly reduced when the airfoil or blade is stalled unlike the pitch system as concluded in Section 6.3.4. As mentioned in Section 7.1.4, an additional case was run with $\alpha_{amp,F} = 27°$ but only for $\beta = 3°$. This additional case clearly indicates that if the flap oscillation amplitude increases, the attenuation of the load fluctuation is greater even though the TEF angle is operating beyond its linear range.

Finally, a comparison between the two systems in Figure 7.12a shows that the pitch system barely outperforms the flap system at r/R=0.82 but when r/R decreases to 0.66 the flap system outperforms the pitch system. This insight is important because it shows that when the pitch system is operating near or in stall, then its effectiveness at attenuating load fluctuation is reduced significantly. In contrast, the effectiveness of the flap system is independent whether the blade is stalled or not. Figure 7.12a clearly indicates that the pitch and flap are very comparable at reducing C_n fluctuation, which is similar to the conclusion that was drawn based on Figure 6.4 in Section 6.1.3.

Unlike the C_n parameter that measures the load on a small blade section, M_{FW} measures the load on the entire blade. Thus making the latter variable a more important parameter in determining the effectiveness of the overall system. The % change in M_{FW}

PSD is plotted in Figure 7.12b for the different cases tested. Analyzing the flap system first (■), the % change in M_{FW} PSD increases when β increases from 3° to 6° and when $\alpha_{amp,F}$ increases from 20° to 27°. This is similar to the findings reported concerning the C_n PSD and occurs for the same reasons. The most important conclusion from this data is related to the optimum location of the TEF. The bar chart clearly shows that the flap effectiveness is higher when r/R=0.82 at both β angles. This finding was expected because of the conclusions and discussions made in Figure 6.17b and Section 6.3.3 demonstrated that the flap control capability over M_{FW} was higher when r/R=0.82. This conclusion aligns with the data presented by Andersen *et al.* [91] who numerically simulated a wind turbine with a TEF to find its optimal location for reducing load fluctuation the most. They concluded that depending on whether the blades are stiff or elastic the TEF should be located at r/R=0.96 and r/R=0.73, respectively. Usually, beyond 90% the tip losses would dominate. In this case, the blade is elastic but not as elastic as a utility-scale turbine. Thus, placing the TEF between r/R of 0.73 and 0.9 would be the most ideal.

Focusing on the pitch system (■), its effectiveness at reducing M_{FW} fluctuation is reduced as β decreased similar to what was found in the C_n data. The data indicate that the pitch system was capable of outperforming the TEF system at reducing M_{FW} fluctuation. That particular result is not surprising as the TEF occupies only 22% of the aerodynamic blade span or about 4% of the blade surface area, while the pitch system controls the entire blade span. However, this remark does not mean that the pitch system is more effective. There are many other factors to take into account when determining the effectiveness of the system such as the blade span ratio, the step response time, the power and torque requirements for the actuation system, the influence over rotor power output, or even the feasibility of such a system and whether it can be built for utility-scale turbines. All these parameters are discussed in more detail in Section 7.3.3 to truly determine the most effective system at reducing load fluctuation on the wind turbine. As was suggested by Castaignet *et al.* [96], multiple TEF sections could be used on a single blade, thereby increasing the TEF effectiveness at alleviating loads and possibly exceeding the effectiveness of the pitch system. This possibility arises because Figure 7.12a showed that the TEF outperforms the pitch system at reducing C_n fluctuation at r/R=0.66, where a second TEF is most likely to be installed.



(a) PSD Amplitude Change in C_n

(b) PSD Amplitude Change in M_{FW}

Figure 7.12: A bar chart summarizing the % PSD change in a)C_n and b)M_{FW} for $\beta = 3°$ and 6° at r/R=0.82 and 0.66.

The data presented in Figure 7.12 is compared to data available in the literature to study the differences and similarities. To the author's knowledge, no C_n data on a full-scale wind turbine equipped with a TEF have been reported in the literature, which highlights the novelty, contribution and usefulness of this study. Thus the % PSD change in C_n cannot be compared to any other published study, however, the M_{FW} data can. Castaignet *et al.* [96] (which was discussed in Section 2.4.5) measured a 20% PSD reduction in the M_{FW} 1P amplitude with the use of an oscillating TEF. The current study, on the other hand, observed a reduction between 30% to 65%. The difference in % reduction is mainly due to the fact that TEF covered only 5% of the blade in their study, whereas in this investigation it covered 22% of the aerodynamic blade. Other reasons for this difference could be due to the type of controller used. They used a closed-loop controller while in this study an open-loop controller was used. Yet another reason could be due to the fact that they tested the TEF on a utility-scale turbine operating in an uncontrolled environment while this study was done on a small-scale turbine operating in a controlled environment. The relationship between the TEF length and the % PSD change is not linear as the influence of the TEF over loading changes with blade span location. Hulskamp *et al.* [99] (which was discussed in Section 2.4.5) conducted similar experiments with a TEF covering 27% of the aerodynamic blade span. They found that with the appropriate controller they could reduce the M_{FW} PSD amplitude between 34% and 58%, depending on the yaw angle they set. They concluded that a significant reduction in dynamic load was attained with the controllers they used. The data from the mentioned experiment is similar to what was observed in this study. Finally Navalkar *et al.* [94] used a free floating TEF as discussed in Section 2.4.5 covering 15% of the aerodynamic blade span. Load reduction in M_{FW} PSD

amplitude was measured to be between 40% and 85% depending on whether the rotor is operating in extreme unsteady conditions or not. The difference in results between their study and this study is because the aerodynamics of a free floating flap is different than a plain flap.

In view of the above results, it should be clear that it is difficult to formulate a meaningful comparison among all the different studies. Each wind turbine is operating in conditions. Moreover, as the experimental results reported here demonstrate, a slight change in operating conditions can significantly modify the effectiveness of the TEF at alleviating fluctuating loads. For example, when β changed from 3° to 6°, the TEF effectiveness changed by 20%. The novelty of this study lies in the fact that a comprehensive set of data was compiled where the TEF is operating under different conditions and the data could be accurately compared to each other. This study also presents data on using pitch motion on the same turbine to reduce fluctuation, thereby facilitating allowing meaningful and accurate comparison between the pitch and flap systems. Most of the papers mentioned have focused on creating an optimum controller for the TEF and less interest devoted to the aerodynamic aspect. On the other hand, this study adopted the opposite focus. The controller was run in an open-loop scenario, thereby eliminating the controls aspects of this project. Presenting the various cases discussed gave a complete and a comprehensive picture of the capability of the TEF and how it can influence rotor torque, blade bending moment and normal force coefficient. This level of detail and complexity has not previously been published. One of the major contributions of this study is that it provides a quantitative and qualitative understanding of how the TEF can manipulate blade loading and how the TEF compares to individual pitch control. In addition, this research provided surface pressure measurements on a rotating blade equipped with a TEF, a novelty that is not found in the literature.

7.3.3 Comparison Matrix

As mentioned in the earlier section, there are many factors and parameters to consider when determining whether the pitch or the flap system is more effective at reducing load fluctuation. Table 7.3 summarizes the different parameters to be taken into consideration in order of importance from high to neutral to low. The importance was determined based on the literature review and the data analyzed throughout this thesis. Following a brief discussion, conclusions are stated as to whether the pitch, flap, none or both have the advantage. In the introduction, it was stated that the control strategies such as pitch or flap systems are mainly designed for large utility-scale wind turbine. To this end, the parameters and discussions in this table are tailored for such turbines. A major hurdle for

the pitch system is its slow step response, since it is twice as long as the response of the flap system as was found in Section 4.4.3. As the wind turbine blades become larger and more elastic to increase effectiveness and reduce cost, the possibility of using individual pitch control to reduce load fluctuation becomes less likely. This is because the time delay in step response increases significantly making the pitch system ineffective. Designing a pitch actuation system that is capable of pitching the entire blade at the required rate is a challenge, especially as the blades get longer and larger. This consideration also fails to mention the additional stress on the pitch system due to excessive use.

Effectively reducing load fluctuations at the location where they are occurring along the blade span is a major advantage of the flap system and a feature the pitch system totally lacks. This becomes important for large-scale utility turbines operating in turbulent flow. The effectiveness of the pitch system at reducing load fluctuation depends on whether the flow is stalled or not while on the other hand, that is not the case for the flap system. This gives the TEF system the advantage, as it can control the loading in any operating condition. It was found that the power output was reduced between 0%-5% for the flap system and 10%-12% for the pitch system and that discrepancy makes the latter system less desirable. The flap system requires only a fraction of the power or torque used to drive the pitch system. Taking all these parameters into consideration, it could be concluded that individual pitch control is not an ideal solution for large-scale wind turbines. That makes the TEF system or similar technologies a better solution to reduce load fluctuation and that is aligned with the finding from the "Grand Vision for Wind Energy" report by Dykes *et al.* [3].

Table 7.3: A comparison matrix between the flap and pitch system

Parameter	**Importance**	**Discussion**	**Advantage**
Reduction in M_{FW} fluctuation	High	• 45%-65% for the flap system and 65%-80% for the pitch system.	Both
Step Response	High	• As the blade gets longer, the step response time of the pitch system will increase while it stays the same for the flap system.	Flap
Feasibility	High	• Pitch system disadvantages: pitching the entire blade at the required rate is extremely challenging. • Flap system disadvantages: reliability issues, maintenance cost and additional capital cost.	None
Localized Load Control	High	• The pitch system is not capable of localized load control but flap system can and that is a major advantage.	Flap
Blade span ratio	Neutral	• TEF only occupies 22% of the aerodynamic blade span or about 4% of the blade surface area while the pitch system of course controls the entire blade span.	Flap
Performance under different operating conditions	Neutral	• The effectiveness of the pitch system at reducing load fluctuation is dependent on the flow being attached while the TEF system is independent of operating conditions.	Flap
Influence over power reduction	Neutral	• Power output was reduced between 0%-5% for the flap system and 10%-12% for the pitch system.	Flap
Reduction in C_n fluctuation	Low	• 50%-75% for the flap system and 40%-75% for the pitch system depending on operating conditions.	Both
Power requirements	Low	• The flap system only requires a fraction of the power or torque used to drive the pitch system.	Flap
Blade Root Torsional force	Low	• Any motion in the TEF will tend to increase the blade root torsional force fluctuations while the pitch motion keeps it unchanged.	Pitch

7.4 Load Alleviation Summary

To conclude this chapter, a brief summary of the data discussed and the important conclusions are presented. The novelty and contribution of this study lies in the fact that a comprehensive set of data was compiled and analyzed, showing how the TEF motion is capable of reducing load fluctuation on a wind turbine using four performance parameters: ΔTorque, M_{FW}, C_n and ΔC_p. This study also presents data on using pitch motion on the same turbine to reduce load fluctuation. The combined data facilitated a meaningful and accurate comparison between the pitch and flap systems.

Throughout the data presented, the effectiveness of the pitch system in alleviating loads was determined to be highly dependent on the flow being attached over the blade. When the blade is operating around the onset of stall or in the stall region, the effectiveness of the pitch system is reduced. On the other hand, the TEF does not have this dependency and its effectiveness does not change whether the blade is stalled or not. This feature is important because if the turbine is operating in unsteady conditions the pitch system would become effective, however, the effectiveness of the flap system does not change. It was also found that the pitching motion causes a 10% to 12% reduction in ΔTorque or rotor power output. On the other hand a smaller reduction between 0% and 5% was seen due to the flap motion and that amount represents a benefit over the pitch system. This reduction is acceptable because the TEF was capable of effectively reducing stress on the blades, gearbox and motor in the nacelle, thereby increasing the lifespan of the turbine and reducing maintenance cost.

The ΔC_p contour plots demonstrated that the main advantage of the pitch system lies in its ability to reduce ΔC_p where the fluctuation is high and that is at the LE. On the other hand, even though the flap system reduces ΔC_p across the entire chord, most of the reduction is concentrated at the TE. This causes a shift in the pressure center along the airfoil surface significantly increasing C_M variation and that, in turn, increases the torsional force at the blade root. However, this effect does not modify the capability of the TEF to reduce the load fluctuations because from a load perspective, it does not matter whether the reduction is occurring at the LE or the TE.

By plotting the change in PSD amplitude at 1P for the flap and pitch systems under different conditions in the same bar chart, it was possible to compare both systems and to data found in literature. The most important parameter in determining the effectiveness of the overall systems is M_{FW} because it measures the load on the entire blade. The TEF was found to be more effective at attenuating load fluctuation when r/R=0.82 as compared to r/R=0.66 under different environmental conditions. The % change in PSD

due to the TEF and the pitch system was found to be between 45%-65% and 65%-80%, respectively. Even though the pitch system outperformed the TEF system, it does not mean that the pitch system is more effective. Instead, it shows that even with the TEF only occupying 22% of the aerodynamic blade span or about 4% of the blade surface area, it was capable of significantly reducing the fluctuation and hence it is very comparable to the pitch system. Some of the main advantages of the TEF over the pitch system are: a much quicker time response, effectively reducing load fluctuation where they are occurring along the blade span, no reduction in power output and much lower torque requirements to actuate. Furthermore, as the wind turbine blades become larger to increase effectiveness and reduce cost, the possibility of using individual pitch control to reduce load fluctuation becomes less likely. That makes the TEF system or similar technology the only solution for reducing load fluctuation.

Chapter 8

Concluding Remarks

8.1 Summary

After each major results section or chapter, a detailed conclusion was presented. This section summarizes the important and high-level conclusions from each of the three Results Chapters.

2D Experimental Campaign Conclusions

Based on static 2D measurements, it was found that the TEF is equally capable manipulating airfoil coefficients when the flow over the airfoil is attached or stalled. The static results also showed that even though the flap is capable of manipulating the coefficient of pressure over the entire chord, most of the change is concentrated at the LE. The experimental data showed that a change in flap angle resulted in a movement of the airfoil surface center of pressure, thereby changing the moment coefficient.

To study how a pitching TEF can reduce the dynamic stall effects, a cambered 2D airfoil was oscillating under different reduced frequencies (k) and mean pitch angles (α_{mean}). The novel experimental rig was able to clearly measure the multiple peaks in the airfoil coefficients indicating multiple LEV. Based on the comprehensive set of experiments, it was found that the TEF was capable of decreasing or eliminating any possibility of flutter or aeroelastic instabilities that may lead to severe vibration and mechanical failure if the structural dynamics permit. The TEF can also manipulate the airfoil coefficients and loads at any point on the cycle and that point is determined by the flap phase, ϕ. Thus the

latter parameter should be determined based on α_{mean} and k because the load peaks occur at different locations. It was found that for the appropriate ϕ, C_L amplitude is reduced by at least 26% while the root bending moment amplitude is reduced by at least 24%. The data indicate that the TEF is not capable of eliminating the LEV completely but it can reduce the impact of the LEV on the airfoil performance.

Wind Turbine Full-Scale Testing Conclusions

To study different aspects of blade loading, ΔTorque, M_{FW} and C_n are measured on a wind turbine operating in a wide array of conditions. In the non-yawed cases, the experimental data strongly indicate that 3D flow effects are present along the entire span of the blade and not only on the inboard section of the blade as originally thought. For the yawed cases, experimental data show that dynamic stall behavior on a rotating blade is very different than on a 2D airfoil segment and this is mainly due to 3D flow effects and increased turbulence. The novel sensors installed on the wind turbine were clearly able to show, with certainty, the location of dynamic stall and to determine whether the blade is stalled or not. It was found that as the r/R location decreases or moves closer to the root of the blade, the amplitude/mean of oscillation and k both increase leading to a more significant dynamic stall cycle. When possible, the experimental data collected were compared to the OpenFast model by NREL. The results highlight weaknesses in modeling tip loss, stall delay, post stall and 3D flow effects. OpenFast was capable of accurately predicting blade loading on a wind turbine operating in steady conditions but in unsteady or yawed conditions the accuracy degrades.

From the comprehensive set of experimental data presented, the TEF influence over wind turbine blade loading was accurately determined. Negative α_F angles were capable of positively augmenting ΔTorque in low wind speed conditions only and such insight is useful because the turbine efficiency can be increased when it is producing less power. It was found that the α_F influence over ΔTorque is not linear. An important conclusion is that the relationship between α_F and M_{FW} is linear for all the cases presented as long as α_F is operating within = $\pm 20^\circ$. When the TEF is centered at r/R=0.66 the control capability is reduced by 40% when compared to r/R=0.82. The linearity between α_F and C_n is constant and independent of r/R location, β angle, and tip speed ratio. After testing the TEF on a yawed turbine, it was found that the TEF is equally capable of controlling the load on the turbine for different yaw angles, blade pitch angles, and wind speeds even when the blade is stalled. It was also found that changing the flap angle keeps the possibility of dynamic stall the same, unlike when the blade pitch angle is changed.

Wind Turbine Load Alleviation Conclusions

The novelty and contribution of this study lies in the fact that a comprehensive set of data was analyzed showing how the TEF and pitch motion are capable of reducing load fluctuation on a wind turbine using four performance parameters: ΔTorque, M_{FW}, C_n and ΔC_p. Based on the results reported, it was found that when the turbine is operating in unsteady conditions the pitch system would become less effective at reducing load fluctuation but for the flap system the effectiveness does not change. This is a major advantage of the TEF system. The surface pressure measurements showed that the pitch and the flap systems are predominantly capable of manipulating ΔC_p at the LE and TE, respectively. As a consequence, any motion in the TEF will tend to increase the fluctuations in C_M. The TEF was found to be more efficient at attenuating load fluctuation when r/R=0.82 as compared to r/R=0.66 under different environmental conditions.

The reduction in load fluctuation due to the TEF and the pitch systems was found to be between 45%-65% and 65%-80%, respectively. This shows that even with the TEF occupying only 22% of the aerodynamic blade span or about 4% of the blade surface area, it was capable of significantly reducing the fluctuation and it is very comparable to the pitch system. Some of the main advantages of the TEF over the pitch system are: a much quicker time response, effectively reducing load fluctuation where it occurs along the blade span, no reduction in power output and much lower power requirements to actuate. Furthermore, as the wind turbine blades become larger to increase efficiency and reduce cost, the possibility of using individual pitch control to reduce load fluctuation becomes less likely. That makes the TEF system, or similar technology, the only solution to reduce load fluctuation.

Overall Conclusions

As stated in the introduction, the motivation for this research was to investigate an aerodynamic control strategy that is capable of reducing fatigue levels at the wind turbine blade root to increase lifespan. Another benefit to this study is to develop a new technology that can overcome the "square cubed law" so manufacturers can continue to increase the diameter of wind turbines in pursuit of higher power output. The data compiled and analyzed throughout this thesis provides a methodical and comprehensive argument to support the use of TEF on a utility-scale turbine to reduce load fluctuation and fatigue levels at the blade root. The detailed experimental data was able to shed light on the effects of dynamic stall, stall delay and 3D flow induced by the blade rotation on an operating wind turbine. The data will no doubt play an important role in improving model uncertainty and

thereby help turbine manufacturers to design blades without using greater-than-optimal safety factors to account for the various inaccuracies in the current design tools.

8.2 Project Objectives Achieved and Contribution

During the length of the PhD program the author has presented peer-reviewed contributions at 6 international conferences and published 4 high caliber peer-reviewed journal papers as illustrated in Appendix A. The author continues to work on future publications that arose from the research presented. This highlights the novelty and contribution of the presented research. This section highlights each of the five objectives achieved that were outlined in the introduction in Section 1.3. The novelty of the work completed is also discussed in each of the sections.

1. Experimental Rig

The custom-designed and -built experimental rig exceeded expectation in terms of reliability and repeatability. Surface pressure measurements on a rotating blade are very scarce and the data collected in this project will play an important role in validating and improving wind turbine models. Wireless data collection made this set of data possible without the use of slip rings that tend to increase noise levels in the data. Actively and dynamically pitching the entire blade and the TEF made the load alleviation experiments possible. The TEF was the workhorse of this experimental setup. It functioned exceptionally well even with high flap angles that exceeded design constraints.

2. 2D Airfoil with TEF

The 2D static airfoil coefficients for a cambered airfoil are unique because they are presented for a wide range of pitch (-5° to 50°) and flap angles (-40° to 60°). Previous research has focused on using a TEF for rotorcraft engineering but this current research focused on using TEF solely on wind turbines as there are some major differences between the two in terms of geometry and operating conditions. This project expands on the limited data available that examine the impact of TEF motion on wind turbine specific airfoils or cambered airfoils in general operating in deep dynamic stall. A comprehensive set of experiments was carried out to study the impact of the reduced frequency, the amplitude/mean of oscillation and TEF motion phase shift.

3. Model and Experimental Data Comparison

A comprehensive set of experimental data on a wind turbine operating in a controlled environment in a variety of conditions is uncommon in the published literature. Hence, this makes the experiments presented in this project unique. The data has also been compared to OpenFast, a widely used design code by NREL, to highlight its strengths and potential opportunities to increase its accuracy and reduce uncertainty in the predictions it provides.

4. Wind Turbine with TEF

Surface pressure measurements on a rotating blade equipped with a TEF have never previously been reported. This shed some light on how a TEF is capable of manipulating the flow field around the blade segment. The comprehensive set of data collected will be an excellent resource for modelers to develop new models to simulate TEF on a wind turbine or validate existing models. The data also determined the influence of a TEF on rotor torque, blade moment and normal force coefficient.

5. Load Alleviation

Most of the previous studies have focused on creating an optimum controller for the TEF, rather than on its aerodynamic aspects. This study on the other hand, does the opposite. Careful analysis of the various cases considered gave a complete and a comprehensive picture of the capability of the TEF and also how it can reduce fluctuation in rotor torque, blade bending moment and normal force coefficient. This level of detail has not previously been reported. The results validated a much needed new technique to alleviate load fluctuation on large utility-scale wind turbines to further decrease the levelized cost of energy (LCOE) as mentioned in the introduction. With the use of TEF, the "Grand Vision for Wind Energy" proposed by Dykes *et al.* [3] will be one step closer to completion.

8.3 Recommendations

While the experimental design and setup were successful at collecting phase-averaged data and actuating the pitch and flap system, several opportunities were identified to improve the overall usability and reliability of the experiments.

Experiment Design

- Trailing Edge Flap: Using a more powerful motor to actuate the trailing edge flap would reduce the backlash in the system to less than 0.5°. A more robust design could be used to strengthen the coupling between the motor and TEF shaft that was a source of further backlash in the system. Using a timing belt to connect the actuator to the TEF would possibly increase the flap angle accuracy. Berg *et al.* [53] summarized different TEF actuation designs that could possibly be used.
- Data Acquisition System: Although the DAQ system was capable of phase-averaging the data for this set of experiments, it was operating at its limits. It is recommended to invest in better synchronous DAQ cards with high data acquisition rate at least for the pressure transducer data.
- Modular blade: The modular blade design was both a strength and a weakness in this experimental campaign. It is a strength because it allowed testing of the TEF at different blade spanwise locations. On the other hand, it is a weakness because the constant chord and pitch blade design is inefficient, forcing some segments of the blade to operate in stall.
- Surface pressure: The pressure transducers used throughout the experiments have proven themselves to be very reliable although one transducer failed during the experiments. It is recommended to choose the transducer range with a much smaller safety factor and build two sets of pressure transducers to account for the change of r/R location.

Future Experiments and Research Possibilities

- Aerodynamic Brake: To determine whether TEF is capable of aerodynamically braking the rotor to shut down the wind turbine and replacing the pitch system, more detailed experiments are needed.
- Variable twist and chord: It is highly important to study whether the TEF control capability changes when it is installed on a blade with variable twist and chord.
- Three-bladed turbine: It is recommended to replace the two counter-weights that balanced the rotor with actual aerodynamic blades to increase the induction factor and produce positive torque measurements.
- Closed-loop controller: The controller for the TEF was run in an open-loop scenario, thereby eliminating the controls aspects of this project. For future projects it is important to include a closed-loop controller to actively monitor the loads and actuate the TEF accordingly.

- Angle of attack measurements: Angle of attack measurements on a wind turbine blade with a TEF are non-existent thus it is important to study how the TEF influences angle of attack measurements.
- Longer TEF: The TEF in this project occupied 22% of the aerodynamic blade span or about 4% of the blade surface area. It is recommended to make the TEF longer to increase its influence over blade loading and achieve a larger control authority, thereby further reducing the load fluctuation.
- Accounting for lag: From the step response experiment described Section 4.4.3, it was found that there is about 42° of blade rotation lag between TEF actuation and a change in blade moment output. Future experiments would account for this lag to achieve higher load fluctuation reduction.

References

[1] Global Wind Energy Counsil, "Global Wind Report 2018," Tech. Rep. April, 2019, www.gwec.net.

[2] Canadian Wind Energy Association, "Installed Wind Energy Capacity in Canada," 2020," https://canwea.ca/wind-energy/installed-capacity/ (Accessed: 2020-01-31).

[3] K. Dykes, P. Veers, E. Lantz, and E. al., "IEA Wind TCP: Results of IEA Wind TCP Workshop on a Grand Vision for Wind Energy Technology," National Renewable Energy Laboratory (NREL), Tech. Rep. April, 2019.

[4] P. S. Veers, T. D. Ashwill, H. J. Sutherland, and E. al., "Trends in the design, manufacture and evaluation of wind turbine blades," *Wind Energy*, vol. 6, no. 3, pp. 245–259, 2003.

[5] T. K. Barlas and G. A. M. van Kuik, "Review of state of the art in smart rotor control research for wind turbines," *Progress in Aerospace Sciences*, vol. 46, no. 1, pp. 1–27, 2010.

[6] GE Renewable Energy, "Haliade-X 12 MW offshore wind turbine platform," 2020," www.ge.com/renewableenergy/wind-energy/offshore-wind/haliade-x-offshore-turbine.

[7] T. Burton, N. Jenkins, D. Sharpe, and E. Bossanyi, *Wind Energy Handbook*, 2nd ed. Wiley, 2011.

[8] D. E. Shipley, M. S. Miller, M. C. Robinson, M. W. Luttges *et al.*, "Dynamic stall occurrence on a horizontal axis wind turbine blade," National Renewable Energy Laboratory (NREL), Golden, CO (United States), Tech. Rep. July, may 1995, http://www.osti.gov/servlets/purl/61151/.

[9] J. G. Leishman, *Principles of Helicopter Aerodynamics*, 2nd ed. Cambridge University Press, 2006.

[10] P. A. Fleming, A. Ning, P. M. O. Gebraad, and K. Dykes, "Wind plant system engineering through optimization of layout and yaw control," *Wind Energy*, vol. 19, no. 2, pp. 329–344, feb 2016.

[11] R. Damiani, S. Dana, J. Annoni, P. Fleming *et al.*, "Assessment of Wind Turbine Component Loads Under Yaw-Offset Conditions," *Wind Energy Science Discussions*, no. September, pp. 1–25, 2017.

[12] D. E. Berg, D. G. Wilson, M. F. Barone, B. R. Resor *et al.*, "The Impact of Active Aerodynamic Load Control on Fatige and Energy Capture at Low Wind Speed Sites," in *European Wind Energy Conference and Exhibition 2009, EWEC 2009 (Vol. 4, pp. 2670-2679)*, 2009.

[13] M. Hand, D. Simms, L. Fingersh, D. Jager *et al.*, "Unsteady Aerodynamics Experiment Phase VI: Wind Tunnel Test Configurations and Available Data Campaigns," *National Renewable Energy Laboratory, NREL*, vol. TP-500-299, no. Phase VI, 2001.

[14] J. G. Schepers, K. Boorsma, T. Cho, S. Gomez-iradi *et al.*, "Final report of IEA Task 29, Mexnext (Phase 1): Analysis of Mexico wind tunnel measurements," *ECN Research*, vol. Task 29, M, p. 312, 2012.

[15] J. Jonkman and M. Sprague, "OpenFast Software," 2019," https://nwtc.nrel.gov/OpenFAST.

[16] J. J. Bertin and R. M. Cummings, *Aerodynamics for Engineers*. Pearson Prentice Hall, 2009.

[17] J. D. J. Anderson, *Fundamentals of Aerodynamics*, 5th ed. McGraw-Hill Education, 2011.

[18] D. Wood, *Small Wind Turbines: Analysis, Design, and Application*. Springer, 2011.

[19] J. F. Manwell, J. G. McGowan, and A. L. Rogers, *Wind Energy Explained: Theory, Design and Application*, 2nd ed. John Wiley&Sons Ltd, UK, 2009.

[20] W. J. McCroskey, "Unsteady Airfoils," *Annual Review of Fluid Mechanics*, vol. 14:285-311, pp. 285–311, 1982.

[21] T. C. Corke and F. O. Thomas, "Dynamic Stall in Pitching Airfoils: Aerodynamic Damping and Compressibility Effects," *Annual Review of Fluid Mechanics*, vol. 47, no. 1, pp. 479–505, 2015.

[22] J. G. Leishman, "Dynamic stall experiments on the NACA 23012 aerofoil," *Experiments in Fluids*, vol. 9, no. 1-2, pp. 49–58, 1990.

[23] K. Gharali and D. A. Johnson, "Dynamic stall simulation of a pitching airfoil under unsteady freestream velocity," *Journal of Fluids and Structures*, vol. 42, pp. 228–244, 2013.

[24] K. Gharali and D. A. Johnson, "PIV-based load investigation in dynamic stall for different reduced frequencies," *Experiments in Fluids*, vol. 55, no. 8, 2014.

[25] K. Gharali and D. A. Johnson, "Effects of nonuniform incident velocity on a dynamic wind turbine airfoil," *Wind Energy*, vol. 18, no. 2, pp. 237–251, feb 2015.

[26] T. Lee and P. Gerontakos, "Investigation of flow over an oscillating airfoil," *Journal of Fluid Mechanics*, vol. 512, pp. 313–341, 2004.

[27] S. Wang, D. B. Ingham, L. Ma, M. Pourkashanian *et al.*, "Numerical investigations on dynamic stall of low Reynolds number flow around oscillating airfoils," *Computers and Fluids*, vol. 39, no. 9, pp. 1529–1541, 2010.

[28] Y. S. Baik, L. P. Bernal, K. Granlund, and M. V. Ol, "Unsteady force generation and vortex dynamics of pitching and plunging aerofoils," *Journal of Fluid Mechanics*, vol. 709, pp. 37–68, 2012.

[29] C. W. Pitt Ford and H. Babinsky, "Lift and the leading-edge vortex," *Journal of Fluid Mechanics*, vol. 720, pp. 280–313, 2013.

[30] T. Cebeci, M. Platzer, H. Chen, K.-C. Chang *et al.*, *Analysis of Low-Speed Unsteady Airfoil Flows*. Springer New York, 2005.

[31] M. Masdari, M. Seyednia, and A. Tabrizian, "An experimental loading study of a pitching wind turbine airfoil in near- and post-stall regions," *Journal of Mechanical Science and Technology*, vol. 32, no. 8, pp. 3699–3706, 2018.

[32] R. Green, E. Gillies, and Y. Wang, "Trailing edge flap flow control for dynamic stall," *Aeronautical Journal*, vol. 115, no. 1170, pp. 493–503, 2011.

[33] M. Sun and S. Sheikh, "Dynamic stall suppression on an oscillating airfoil by steady and unsteady tangential blowing," *Aerospace Science and Technology*, vol. 3, no. 6, pp. 355–366, 1999.

[34] D. Weaver, K. McAlister, and J. Tso, "Control of VR-7 Dynamic Stall by Strong Steady Blowing," *Journal of Aircraft*, vol. 41, no. 6, pp. 1404–1413, nov 2004.

[35] B. L. Smith and A. Glezer, "The formation and evolution of synthetic jets," *Physics of Fluids*, vol. 10, no. 9, pp. 2281–2297, 1998.

[36] T. C. Corke, P. O. Bowles, C. He, and E. H. Matlis, "Sensing and control of flow separation using plasma actuators," *Philosophical Transactions of the Royal Society A: Mathematical, Physical and Engineering Sciences*, vol. 369, no. 1940, pp. 1459–1475, 2011.

[37] M. L. Post and T. C. Corke, "Separation Control Using Plasma Actuators: Dynamic Stall Vortex Control on Oscillating Airfoil," *AIAA Journal*, vol. 44, no. 12, pp. 3125–3135, 2006.

[38] B. Heine, K. Mulleners, G. Joubert, and M. Raffel, "Dynamic Stall Control by Passive Disturbance Generators," *AIAA Journal*, vol. 51, no. 9, pp. 2086–2097, 2013.

[39] P. Martin, J. Wilson, J. Berry, T.-C. Wong *et al.*, "Passive Control of Compressible Dynamic Stall," in *26th AIAA Applied Aerodynamics Conference*, ser. Guidance, Navigation, and Control and Co-located Conferences. American Institute of Aeronautics and Astronautics, aug 2008.

[40] R. M. Rennie and E. J. Jumper, "Experimental measurements of dynamic control surface effectiveness," *Journal of Aircraft*, vol. 33, no. 5, pp. 880–887, sep 1996.

[41] J. S. Vipperman, R. L. Clark, M. Conner, and E. H. Dowell, "Experimental Active Control of a Typical Section Using a Trailing-Edge Flap," *Journal of Aircraft*, vol. 35, no. 2, pp. 224–229, mar 1998.

[42] K. Nguyen, "Active Control of Helicopter Blade Stall," *Journal of Aircraft*, vol. 35, no. 1, pp. 91–98, jan 1998.

[43] D. Feszty, E. A. Gillies, and M. Vezza, "Alleviation of Airfoil Dynamic Stall Moments via Trailing-Edge Flap Flow Control," *AIAA Journal*, vol. 42, no. 1, pp. 17–25, jan 2004.

[44] H. A. Madsen, P. B. Andersen, T. L. Andersen, C. Bak *et al.*, "The potentials of the controllable rubber trailing edge flap (CRTEF)," in *EWEC 2010 Proceedings online*. EWEC 2010 Proceedings online, 2010, p. 11.

[45] L. O. Bernhammer, G. A. M. van Kuik, and R. D. Breuker, "How far is smart rotor research and what steps need to be taken to build a full-scale prototype?" *Journal of Physics: Conference Series*, vol. 555, 2014.

[46] C. Bak, M. Gaunaa, P. B. Andersen, T. Buhl *et al.*, "Wind Tunnel Test on Wind Turbine Airfoil with Adaptive Trailing Edge Geometry," in *45th AIAA Aerospace Sciences Meeting and Exhibit*, no. January, 2007, pp. 1–12.

[47] J. Lee, J. Han, H. Shin, and H. Bang, "Active load control of wind turbine blade section with trailing edge flap : Wind tunnel testing," *Journal of Intelligent Material Systems and Structures*, vol. 25, no. 18, pp. 1–10, 2014.

[48] E. Houghton and P. Carpenter, *Aerodynamics for Engineering Students*, 5th ed. Butterworth Heinemann, 2002.

[49] I. H. Abbott and A. E. V. Doenhoff, *Theory of Wing Sections: Including a Summary of Airfoil Data*. Dover Publication Inc., 1959.

[50] E. Hau, *Wind turbines: Fundamentals, technologies, application, economics*, 3rd ed. Springer, 2013, vol. 9783642271.

[51] P. McKay, R. Carriveau, and D. S.-K. Ting, "Wake impacts on downstream wind turbine performance and yaw alignment," *Wind Energy*, vol. 16, no. 2, pp. 221–234, mar 2013.

[52] M. Drela and H. Youngren, "XFOIL 6.97," 2000," https://web.mit.edu/drela/Public/web/xfoil/ (Accessed: 2017-04-26).

[53] J. C. Berg, B. Resor, J. Paquette, and J. White, "SMART Wind Turbine Rotor: Design and Field Test," *Sandia National Laboratories*, no. SAND2014-0681, 2014.

[54] M. S. Selig and J. L. Tangier, "Development and Application of a Multipoint Inverse Design Method for Horizontal Axis Wind Thrbines," *Wind Engineering*, vol. 19, no. 2, 1995.

[55] UIUC Applied Aerodynamics Group, "PROPID," 2019," https://m-selig.ae.illinois.edu/propid.html.

[56] A. Abdelrahman and D. A. Johnson, "Development of a Wind Turbine Test Rig and Rotor for Trailing Edge Flap Investigation: Static Flap Angles Case," *Journal of Physics: Conference Series*, vol. 524, p. 012059, 2014.

[57] T. Gallant and D. A. Johnson, "Flow angle measurement of a yawed turbine and comparison to models," *Wind Energy Science Discussions*, vol. 2, no. January, pp. 1–17, jan 2017.

[58] C. Hansen, "AirfoilPrep: An Excel workbook for generating airfoil tables for AeroDyn and WT_Perf," 2014," https://nwtc.nrel.gov/AirFoilPrep.

[59] L. A. Viterna and D. C. Janetzke, "Theoretical and experimental power from large horizontal-axis wind turbines," *NASA*, vol. TM-82944, no. 12, p. 72, sep 1982.

[60] Z. Du and M. Selig, "A 3-D stall-delay model for horizontal axis wind turbine performance prediction," *1998 ASME Wind Energy Symposium*, pp. 9–19, jan 1998.

[61] A. Eggers, K. Chaney, and R. Digumarthi, "An Assessment of Approximate Modeling of Aerodynamic Loads on the UAE Rotor," *41st Aerospace Sciences Meeting and Exhibit*, jan 2003.

[62] G. Hayman, R. Damiani, and J. Jonkman, "Development and Validation of a New Blade Element Momentum Skewed-Wake Model within AeroDyn Preprint," *National Renewable Energy Laboratory, NREL*, no. December, 2015.

[63] R. R. Damiani, G. J. Hayman, and J. M. Jonkman, "Development and Validation of a New Unsteady Airfoil Aerodynamics Model Within AeroDyn," *AIAA Journal*, no. January, pp. 1–20, 2016.

[64] J. M. Jonkman, "Modeling of the UAE Wind Turbine for Refinement of FAST _ AD Modeling of the UAE Wind Turbine for Refinement of," *National Renewable Energy Laboratory*, vol. TP-500-347, no. December, 2003.

[65] I. H. Abbott and H. Greenberg, "Tests in the variable-density wind tunnel of the NACA 23012 airfoil with plain and split flaps," *National Advisory Committee for Aeronautics*, vol. NACA-TR-66, no. NACA-TR-661, 1939.

[66] E. N. Jacobs and R. M. Pinkerton, "Pressure Distribution Over a Symmetrical Airfoil Section with Trailing Edge Flap," *National Advisory Committee for Aeronautics*, no. Report No. 360, 1931.

[67] W. McCroskey, L. Carr, and K. McAlister, "Dynamic Stall Experiments on Oscillating Airfoils," *AIAA Journal*, vol. 14, no. 1, pp. 57–63, jan 1976.

[68] M. S. Boutilier and S. Yarusevych, "Parametric study of separation and transition characteristics over an airfoil at low Reynolds numbers," *Experiments in Fluids*, vol. 52, no. 6, pp. 1491–1506, 2012.

[69] M. Raiola, S. Discetti, A. Ianiro, F. Samara *et al.*, "Smart Rotors: Dynamic-Stall Load Control by Means of an Actuated Flap," *AIAA Journal*, vol. 56, no. 4, pp. 1–14, 2018.

[70] T. Lee and P. Gerontakos, "Dynamic Stall Flow Control via a Trailing-Edge Flap," *AIAA Journal*, vol. 44, no. 3, pp. 469–480, 2006.

[71] T. Lee and Y. Y. Su, "Unsteady airfoil with a harmonically deflected trailing-edge flap," *Journal of Fluids and Structures*, vol. 27, no. 8, pp. 1411–1424, 2011.

[72] N. Troldborg, "Computational Study of the Risø-B1-18 Airfoil with a Hinged Flap Providing Variable Trailing Edge Geometry," *Wind Engineering*, vol. 29, no. 2, pp. 89–113, mar 2005, http://journals.sagepub.com/doi/10.1260/0309524054797159.

[73] I. Shehata, M. Y. Zakaria, A. Hussein, and M. R. Hajj, "Aerodynamic analysis of flapped airfoil at high angles of attack," *AIAA Aerospace Sciences Meeting, 2018*, no. 210059, 2018.

[74] A. Zanotti and G. Gibertini, "Experimental assessment of an active L-shaped tab for dynamic stall control," *Journal of Fluids and Structures*, vol. 77, pp. 151–169, 2018.

[75] A. Zanotti, "Retreating Blade Dynamics Stall," PhD, Politecnico di Milano, 2012.

[76] A. Zanotti and G. Gibertini, "Experimental investigation of the dynamic stall phenomenon on a NACA 23012 oscillating airfoil," *Proceedings of the Institution of Mechanical Engineers, Part G: Journal of Aerospace Engineering*, vol. 227, no. 9, pp. 1375–1388, 2013.

[77] W. J. McCroskey, "The Phenomenon of Dynamic Stall," *DTIC Document NASA*, 1981.

[78] P. Gerontakos, "An Experimental Investigation of Flow Over an Oscillating Airfoil," Thesis, McGill University, 2004.

[79] S. Schreck, T. Sant, and D. Micallef, "Rotational Augmentation Disparities in the MEXICO and UAE Phase VI Experiments," *National Renewable Energy Laboratory*, vol. CP-500-477, 2010.

[80] M. O. Hansen, *Aerodynamics of Wind Turbines*, 2nd ed. Earthscan UK, 2015.

[81] R. Pereira, G. Schepers, and M. D. Pavel, "Validation of the Beddoes-Leishman dynamic stall model for horizontal axis wind turbines using MEXICO data," *Wind Energy*, vol. 16, no. 2, pp. 207–219, 2013.

[82] J. Schepers and H. Snel, "Model Experiments in Controlled Conditions," *ECN Research*, vol. ECN-E–07-, 2007.

[83] T. J. Larsen, H. A. Madsen, and K. Thomsen, "Active load reduction using individual pitch, based on local blade flow measurements," *Wind Energy*, vol. 8, no. 1, pp. 67–80, 2005.

[84] E. A. Bossanyi, "Individual blade pitch control for load reduction," *Wind Energy*, vol. 6, no. 2, pp. 119–128, 2003.

[85] T. K. Barlas and G. A. M. van Kuik, "State of the art and prospectives of smart rotor control for wind turbines," *Journal of Physics: Conference Series*, vol. 75, no. 1, p. 012080, jul 2007.

[86] S. J. Johnson, C. P. C. V. Dam, and D. E. Berg, "Active Load Control Techniques for Wind Turbines," *Sandia National Laboratories*, vol. SAND2008-4, no. August, pp. 1–132, 2008.

[87] S. J. Johnson, J. P. Baker, C. P. van Dam, and D. Berg, "An overview of active load control techniques for wind turbines with an emphasis on microtabs," *Wind Energy*, vol. 13, no. 2-3, pp. 239–253, mar 2010.

[88] M. A. Lackner and G. van Kuik, "A comparison of smart rotor control approaches using trailing edge flaps and individual pitch control," *Wind Energy*, vol. 13, no. 2-3, pp. 117–134, mar 2010.

[89] M. Lackner and G. A. M. Van Kuik, "The Performance of Wind Turbine Smart Rotor Control Approaches During Extreme Loads," *Journal of Solar Energy Engineering*, vol. 132, no. 1, pp. 011 008 1–18, 2010.

[90] J. Jonkman, S. Butterfield, W. Musial, and G. Scott, "Definition of a 5-MW reference wind turbine for offshore system development," *National Renewable Energy Laboratory*, vol. TP-500-380, no. February, pp. 1–75, 2009.

[91] P. B. Andersen, L. Henriksen, M. Gaunaa, C. Bak *et al.*, "Deformable trailing edge flaps for modern megawatt wind turbine controllers using strain gauge sensors," *Wind Energy*, vol. 13, no. 2-3, pp. 193–206, mar 2010.

[92] M. Gaunaa and P. B. Andersen, "Load reduction using pressure difference on airfoil for control of trailing edge flaps," in *EWEC 2009 Proceedings online*, 2009.

[93] L. S. Miller and G. A. Quandt, "Atmospheric Tests of Trailing-Edge Aerodynamic Devices," *National Renewable Energy Laboratory, NREL*, vol. SR-500-223, no. January, 1998.

[94] S. T. Navalkar, L. O. Bernhammer, J. Sodja, E. van Solingen *et al.*, "Wind tunnel tests with combined pitch and free-floating flap control: data-driven iterative feedforward controller tuning," *Wind Energy Science*, vol. 1, no. 2, pp. 205–220, oct 2016.

[95] D. Castaignet, J. J. Wedel-Heinen, T. Kim, T. Buhl *et al.*, "Results from the First Full Scale Wind Turbine Equipped with Trailing Edge Flap," *28th AIAA Applied Aerodynamics Conference*, vol. 2010-4407, 2010.

[96] D. Castaignet, T. Barlas, T. Buhl, N. K. Poulsen *et al.*, "Full-scale test of trailing edge flaps on a Vestas V27 wind turbine: active load reduction and system identification," *Wind Energy*, vol. 17, no. 4, pp. 549–564, apr 2014.

[97] J. W. Van Wingerden, A. W. Hulskamp, T. Barlas, B. Marrant *et al.*, "On the proof of concept of a 'smart' wind turbine rotor blade for load alleviation," *Wind Energy*, vol. 11, no. 3, pp. 265–280, 2008.

[98] A. W. Hulskamp, J. W. van Wingerden, T. Barlas, H. Champliaud *et al.*, "Design of a scaled wind turbine with a smart rotor for dynamic load control experiments," *Wind Energy*, vol. 14, no. 3, pp. 339–354, apr 2011.

[99] T. Barlas, W. van Wingerden, A. Hulskamp, G. M. van Kuik *et al.*, "Smart dynamic rotor control using active flaps on a small-scale wind turbine: aeroelastic modeling and comparison with wind tunnel measurements," *Wind Energy*, pp. n/a–n/a, oct 2012.

[100] D. Berg, J. Berg, D. Wilson, J. White *et al.*, "Design , Fabrication , Assembly and Initial Testing of a SMART Rotor," in *49th AIAA Aerospace Sciences Meeting*, Orlando, Florida, USA, 2011.

[101] J. Berg, D. Berg, and J. White, "Fabrication, Integration, and Initial Testing of a SMART Rotor," *50th AIAA meeting*, pp. 1–9, 2012.

[102] J. C. Berg, M. F. Barone, and B. R. Resor, "Field Test Results from the Sandia SMART Rotor," *51st AIAA Aerospace Sciences Meeting including the New Horizons Forum and Aerospace Exposition*, pp. 1–10, 2013.

[103] J. C. Berg, M. F. Barone, and N. Yoder, "SMART Wind Turbine Rotor: Data Analysis and Conclusions," *Sandia National Laboratories*, no. SAND2014-0712, 2014.

[104] A. Abdelrahman, "Development of a Wind Turbine Test Rig and Rotor for Trailing Edge Flap Investigation," Masters, University of Waterloo, 2014.

[105] D. M. Somers, "The S833 , S834 , and S835 Airfoils," *National Renewable Energy Laboratory, NREL*, vol. NREL/SR-50, 2005.

[106] D. Gertz and D. A. Johnson, "An evaluation testbed for wind turbine blade tip designs-baseline case," *International Journal of Energy Research*, vol. 35, no. 15, pp. 1360–1370, dec 2011.

[107] D. A. Johnson, A. Abdelrahman, and D. Gertz, "Experimental Indirect Determination of Wind Turbine Performance and Blade Element Theory Parameters in Controlled Conditions," *Wind Engineering*, vol. 36, no. 6, pp. 716–737, 2012.

[108] Stratasys, "Fortus 360mc 3D printing machine, http://proto3000.com/fortus-360mc.php{#}Fortus-360-Tabs:Product-Specifications (Accessed: 2017-04-05)."

[109] Stratasys, "ABS-M30 Material Data Sheet, http://global72.stratasys.com/{~}/media/Main/Files/Material{_}Spec{_}Sheets/MSS{_}FDM{_}ABSM30{_}0417a{_}Web.pdf{#}{_}ga=1.52969960.1941361745.1489096759 (Accessed: 2017-04-05)."

[110] Haas Automation Inc, "Haas VF-4, http://int.haascnc.com/mt{_}spec1.asp?intLanguageCode=1033{&}id=VF-4{&}webID=40{_}TAPER{_}STD{_}VMC (Accessed: 2017-03-27)."

[111] S. Tavoularis, *Measurement in Fluid Mechanics*. Cambridge University Press, 2005.

[112] J. Holman, *Experimental Methods for Engineers*, seventh ed ed. McGraw-Hill Publishing Company, 2001.

[113] All Sensors, "Pressure Sensor Databook," pp. 211–214," https://www.allsensors.com/catalog-pdf/PC-0003{_}Rev{_}F2.pdf (Accessed: 2017-03-27).

[114] Druck, "DPI 610 Portable Pressure Calibrator, http://docs-europe.electrocomponents.com/webdocs/0401/0900766b804015bc.pdf (Accessed: 2017-04-05)."

[115] Maxon Motors, "Maxon Motor Assembly, http://www.maxonmotorusa.com/medias/sys{_}master/root/8821079310366/16-95-EN.pdfhttp://www.maxonmotorusa.com/medias/sys{_}master/root/8821080948766/16-114-EN.pdfhttp://www.maxonmotorusa.com/medias/sys{_}master/root/8817914871838/15-80-EN.pdf (Accessed: 2017-04-28)."

[116] Maxon Motors, "EPOS2 24/2, http://www.maxonmotorusa.com/medias/sys{_}master/root/8822983262238/EPOS2-24-2-Hardware-Reference-En.pdf (Accessed: 2017-04-28)."

[117] Maxon Motors, "Maxon EC-X adapter micro-controller, http://www.maxonmotorusa.com/medias/sys{_}master/root/8816247963678/498157en.pdf (Accessed: 2017-04-28)."

[118] J. W. Kurelek, A. R. Lambert, and S. Yarusevych, "Coherent Structures in the Transition Process of a Laminar Separation Bubble," *AIAA Journal*, vol. 54, no. 8, pp. 2295–2309, 2016.

[119] Galil Motion Control, "DMC-31017-BOX(2PB), http://www.galilmc.com/download/manual/man{_}3x01x.pdf (Accessed: 2017-04-28)."

[120] Omega, "Precision Strain Gages Dual-Grid for Bending Strains, http://www.omega.com/pressure/pdf/SGD{_}DUAL-GRID.pdf (Accessed: 2017-04-20)."

[121] National Instruments Corporation, "NI 9191, http://www.ni.com/pdf/manuals/372780h.pdf (Accessed: 2017-03-27)."

[122] National Instruments Corporation, "NI 9237, http://www.ni.com/pdf/manuals/374186a{_}02.pdf (Accessed: 2017-03-27)."

[123] National Instruments Corporation, "NI 9205, http://www.ni.com/pdf/manuals/374188a{_}02.pdf (Accessed: 2017-03-27)."

[124] National Instruments Corporation, "NI 9263, http://www.ni.com/pdf/manuals/373781h.pdf (Accessed: 2019-03-11)."

[125] M. Mckinnon, "Comparison of Experimental Methods in the Measurement of Wind Turbine Wakes," Masters Thesis, University of Waterloo, 2018.

[126] C. B. Devaud, J. Weisinger, D. A. Johnson, and E. J. Weckman, "Experimental and numerical characterization of the flowfield in the large-scale UW live fire research facility," *International Journal for Numerical Methods in Fluids*, vol. 60, no. 5, pp. 539–564, jun 2009.

[127] B. Gaunt, "Power Generation and Blade Flow Measurements of a Full Scale Wind Turbine," Master's Thesis, University of Waterloo, 2009.

[128] C. Best, "Measurement of Fuel Regression Rate of a Pool Fire in Crosswind With and Without a Large Downwind Blocking Object," Master's Thesis, University of Waterloo, 2010.

[129] T. Gallant, "Quantitative Measurement Techniques for Wind Turbine Blade Aerodynamic Performance," Master's Thesis, University of Waterloo, 2017.

[130] J. Weisinger, "Characterization of the University of Waterloo live fire research facility wind generation system," Master's Thesis, University of Waterloo, 2004.

[131] Futek Advanced Sensor Technology Inc., "Rotary Torque Sensor – Shaft to Shaft with Encoder, https://www.futek.com/files/pdf/ProductDrawings/trs605.pdf (Accessed: 2017-04-28)."

[132] Senring, "H50119 Series Through Bore Slip Ring, https://www.senring.com/pdf/h/Senring-H50119-Series-SlipRing-Catalog.pdf (Accessed: 2019-03-11)."

[133] A. Moscardi and D. A. Johnson, "A compact in-blade five hole pressure probe for local inflow study on a horizontal axis wind turbine," *Wind Engineering*, vol. 40, no. 4, pp. 360–378, aug 2016.

[134] J. B. Barlow, W. H. Rae, and A. Pope, *Low-Speed Wind Tunnel Testing*. John Wiley & Sons Ltd, 1999.

[135] R. Ramsay, M. Hoffman, and G. Gregorek, "Effects of grit roughness and pitch oscillations on the S809 airfoil," National Renewable Energy Laboratory (NREL), Golden, CO, Tech. Rep. December, dec 1995, http://www.osti.gov/servlets/purl/205563-GvbHua/webviewable/.

[136] J. Morote, "Angle of attack distribution on wind turbines in yawed flow," *Wind Energy*, vol. 19, no. 4, pp. 681–702, apr 2016.

[137] T. Gallant and D. A. Johnson, "In-blade angle of attack measurement and comparison with models," *Journal of Physics: Conference Series*, vol. 753, p. 072007, 2016.

[138] A. Cooperman and M. Martinez, "Load monitoring for active control of wind turbines," *Renewable and Sustainable Energy Reviews*, vol. 41, pp. 189–201, 2014.

[139] S. P. Evans, D. R. Bradney, and P. D. Clausen, "Development and experimental verification of a 5 kW small wind turbine aeroelastic model," *Journal of Wind Engineering and Industrial Aerodynamics*, vol. 181, no. March, pp. 104–111, 2018.

[140] J. W. Larsen, S. R. Nielsen, and S. Krenk, "Dynamic stall model for wind turbine airfoils," *Journal of Fluids and Structures*, vol. 23, no. 7, pp. 959–982, 2007.

[141] UIUC Applied Aerodynamics Group, "PROPID for Horizontal Axis Wind Turbine Design, https://m-selig.ae.illinois.edu/propid.html."

[142] F. Samara and D. A. Johnson, "In-blade Load Sensing on 3D Printed Wind Turbine Blades Using Trailing Edge Flaps," *Journal of Physics: Conference Series*, vol. 1037, p. 052023, jun 2018.

[143] M. Churchfield and S. Lee, "SOWFA Software," 2020," https://nwtc.nrel.gov/SOWFA.

[144] R. J. Moffat, "Describing the Uncertainties in Experimental Results," *Experimental Thermal and Fluid Science*, pp. 3–17, 1988.

APPENDICES

Appendix A

Publications and Conferences

During the length of the PhD program the author has attended multiple international conferences and published a series of high caliber journal paper. The author intends to include the data presented throughout this thesis in future publications.

Conferences

This is a list of the conferences the author attended and where he presented the research in this thesis. They are ordered by the date attended:

- WindTech International Conference 2015 London, Ontario, Canada. Oral presentation title: Visualization of Boundary Layer and Flow Separation using Thermography.
- WindTech International Conference 2017 Boulder, Colorado, USA. Oral presentation title: In-blade Load Sensing and Control on 3D Printed Wind Turbine Blades Using Trailing Edge Flaps.
- TORQUE Conference 2018 Milan, Italy. Poster title: In-blade Load Sensing on 3D Printed Wind Turbine Blades Using Trailing Edge Flaps.
- CSME Congress 2019 London, Ontario, Canada. Oral presentation title: Dynamic stall on an S833 airfoil with a trailing edge flap.
- Wind Energy Science International Conference 2019, Cork, Ireland. Oral presentation title: Dynamic stall on an S833 airfoil with a trailing edge flap.

- NAWEA/WindTech International Conference 2019, Amherst, Massachusetts, USA. Oral presentation title: Influence of pitch and flap system on turbine loading.
- TORQUE 2020 International Conference 2020, Delft, Netherlands. Accepted oral presentation title: Experimental Load Measurement on a Yawed Wind Turbine and Comparison to FAST.

Publications

These are the publication that have been published or accepted:

- Raiola M., Samara F. and *et al.* 2018, Title: Smart Rotors: Dynamic-Stall Load Control by Means of an Actuated Flap. Journal: American Institute of Aeronautics and Astronautics (AIAA).
- Samara F. and Johnson D. 2018, Title: In-blade Load Sensing on 3D Printed Wind Turbine Blades Using Trailing Edge Flaps. Journal: Journal of Physics. Thesis Section: 5.1
- Samara F. and Johnson D. 2019, Title: In-Blade Measurements of Cyclic Loading on Yawed Turbines with Trailing Edge Flap. Journal: Journal of Physics. Thesis Section: 6.1
- Samara F. and Johnson D. 2020, Title: Dynamic-Stall and Cyclic-Load Measurements on a S833 Blade with a Phase-Offset TEF. Journal: AIAA. Thesis Section: 5.2.1 and 5.2.2

Publication submitted:

- Samara F. and Johnson D. 2020, Title: Deep Dynamic Stall and Load Fluctuation Measurements on a S833 Airfoil with a Pitching Trailing Edge Flap. Journal: TBD. Submission number: TBD. Thesis Section: 5.2.3 and 5.2.4

Future publications:

- Samara F. and Johnson D. 2020, Title: Experimental Load Measurement on a Yawed Wind Turbine and Comparison to FAST. Journal: Journal of Physics. Thesis Section: 6.2

- Samara F. and Johnson D. 2020, Title: Trailing Edge Flap influence of turbine loading. Journal: Wind Energy. Thesis Section: 6.3
- Samara F. and Johnson D. 2020, Title: Comparison between a TEF and pitch in load fluctuation alleviation. Journal: Wind Energy. Thesis Chapter: 7

Appendix B

Technical Experimental Setup

This section shoes the detailed drawing of the different components discussed in the experiential setup with dimensions.

B.1 Detailed Drawing

B.2 S833 Surface Pressure Tap Location

Table B.1: Tap locations for the S833 airfoil

Tap Number	1	2	3	4	5	6	7	8	9	10
x/c Location	0.010	0.032	0.054	0.077	0.099	0.122	0.144	0.167	0.189	0.212
Distance between Pressure taps (mm)	1.7	4	4	4	4	4	4	4	4	4
Tap Number	11	12	13	14	15	16	17	18	19	20
x/c Location	0.234	0.257	0.296	0.335	0.375	0.414	0.453	0.493	0.532	0.571
Distance between Pressure taps (mm)	4	4	7	7	7	7	7	7	7	7
Tap Number	21	22	23	24	25	26	27			
x/c Location	0.611	0.650	0.684	0.717	0.751	0.841	0.880			
Distance between Pressure taps (mm)	7	7	6	6	6	16	7			

B.3 Maxon Servo Motor and Controller

Table B.2: Motor/gearbox/encoder specifications [115]

Motor		**Gearbox**		**Encoder**	
Diameter (mm)	8	Diameter (mm)	8	Diameter (mm)	8
Nominal Torque (mNm)	1.26	Reduction	256:1	Counter per turn	1024
Stall Torque (mNm)	5.18	Number of Stages	4	Number of Channels	3
Nominal Voltage (V)	12	Max. continuous torque (Nm)	0.08	Supply Voltage (V)	5
Nominal Speed (rpm)	22800	Max. intermittent torque (Nm)	0.12	Mass (g)	5
Power (W)	3	Max. efficiency (%)	65	Motor Commutation Signal	
Nominal Current (Amp)	0.39	Average backlash no Load (deg)	2.5		
Stall Current (Amp)	1.4	Mass (g)	4		
Sensor	No				
Mass (g)	6				

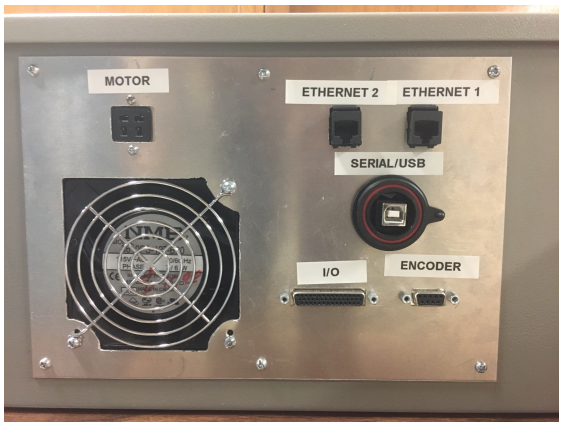
Table B.3: Maxon EPOS 24/2 controller [116]

Max. Power (W)	48
Operting Voltage Range (V)	9 to 24
Continuous Current (Amp)	2
Maximum Current Output (Amp)	4
Interface	USB
Weight (g)	28
Dimension LxWxH (mm)	55x40x18.2
Part Number	390003

B.4 Stepper Motor Controller

To operate the controller safely and provide it power an enclosure box had to be designed according to CSA standards and according to UWaterloo policy. All the components in

the enclosure were assembled and built at the university. The enclosure includes a 48 VDC 10 amp power supply, circuit breakers to protect the controller, and a fan to make sure the heat could escape the enclosure. Some pictures of the assembly are shown in Figure B.3.



(a) Front view of the Galil controller assembly enclosure



(b) Top view of the Galil controller assembly enclosure

Figure B.3: Enclosure that houses the Galil controller and power supply

B.5 OpenFast Input Files

B.5.1 Airfoil Input Files

```
! ------------ AirfoilInfo v1.01.x Input File ----------------------------------
! "S809 Airfoil, OSU data at Re=.75 Million, Clean roughness"
! Adjusted for Post Stall at r/R=.129**
! note that this file uses Marshall Buhl's new input file processing; start all comment lines with !
! ------------------------------------------------------------------------
"DEFAULT"     InterpOrd         ! Interpolation order to use for quasi-steady table lookup {1=linear; 3=cubic spline; "default"} [default=3]
1   NonDimArea        ! The non-dimensional area of the airfoil (area/chord^2) (set to 1.0 if unsure or unneeded)
0    NumCoords         ! The number of coordinates in the airfoil shape file.  Set to zero if coordinates not included.
1   NumTabs           ! Number of airfoil tables in this file.  Each table must have lines for Re and Ctrl.
! ------------------------------------------------------------------------
! data for table 1
! ------------------------------------------------------------------------
0.3   Re                ! Reynolds number in millions
0   Ctrl              ! Control setting (must be 0 for current AirfoilInfo)
true          InclUAdata        ! Is unsteady aerodynamics data included in this table? If TRUE, then include 30 UA coefficients below this line
!.....................................
-0.05   alpha0            ! 0-lift angle of attack, depends on airfoil.
14   alpha1             ! Angle of attack at f=0.7, (approximately the stall angle) for AOA>alpha0. (deg)
-14   alpha2             ! Angle of attack at f=0.7, (approximately the stall angle) for AOA<alpha0. (deg)
1   eta_e             ! Recovery factor in the range [0.85 - 0.95] used only for UAMOD=1, it is set to 1 in the code when flookup=True. (-)
6.5  C_nalpha          ! Slope of the 2D normal force coefficient curve. (1/rad)
15  T_f0              ! Initial value of the time constant associated with Df in the expression of Df and f''. [default = 3]
15   T_V0              ! Initial value of the time constant associated with the vortex lift decay process; it is used in the expression of Cvn.
```

```
1.7   T_p               ! Boundary-layer,leading edge pressure gradient time constant in the expression of Dp.
9  T_VL              ! Initial value of the time constant associated with the vortex advection process;
"Default"     b1                ! Constant in the expression of phi_alpha^c and phi_q^c.
"Default"     b2                ! Constant in the expression of phi_alpha^c and phi_q^c.
5   b5               ! Constant in the expression of K'''_q,Cm_q^nc, and k_m,q.  [from  experimental results, defaults to 5]
"Default"     A1                ! Constant in the expression of phi_alpha^c and phi_q^c.
"Default"     A2                ! Constant in the expression of phi_alpha^c and phi_q^c.
"Default"     A5                ! Constant in the expression of K'''_q,Cm_q^nc, and k_m,q. [from experimental results, defaults to 1]
18.269   S1                ! Constant in the f curve best-fit for alpha0<=AOA<=alpha1; by definition it depends on the airfoil. [ignored if UAMod<>1]
-11.324   S2                ! Constant in the f curve best-fit for         AOA> alpha1; by definition it depends on the airfoil. [ignored if UAMod<>1]
18.269   S3                ! Constant in the f curve best-fit for alpha2<=AOA< alpha0; by definition it depends on the airfoil. [ignored if UAMod<>1]
-11.324   S4                ! Constant in the f curve best-fit for         AOA< alpha2; by definition it depends on the airfoil. [ignored if UAMod<>1]
1.4   Cn1               ! Critical value of COn at leading edge separation. It should be extracted from airfoil data at a given Mach and Reynolds number.
-0.6   Cn2               ! As Cn1 for negative AOAs.
0.3     St_sh             ! Strouhal's shedding frequency constant.  [default = 0.19]
0.0016   Cd0               ! 2D drag coefficient value at 0-lift.
-0.0628   Cm0               ! 2D pitching moment coefficient about 1/4-chord location, at 0-lift, positive if nose up.
0   k0                ! Constant in the \hat(x)_cp curve best-fit; = (\hat(x)_AC-0.25).  [ignored if UAMod<>1]
0   k1                ! Constant in the \hat(x)_cp curve best-fit.  [ignored if UAMod<>1]
0   k2                ! Constant in the \hat(x)_cp curve best-fit.  [ignored if UAMod<>1]
0   k3                ! Constant in the \hat(x)_cp curve best-fit.  [ignored if UAMod<>1]
0   k1_hat            ! Constant in the expression of Cc due to leading edge vortex effects.  [ignored if UAMod<>1]
0.3     x_cp_bar          ! Constant in the expression of \hat(x)_cp^v. [ignored if UAMod<>1, default = 0.2]
"DEFAULT"     UACutout          ! Angle of attack above which unsteady aerodynamics are disabled (deg).
"DEFAULT"     filtCutOff        ! Cut-off frequency (-3 dB corner frequency) for low-pass filtering the AoA input to UA,
!.....................................
! Table of aerodynamics coefficients
78   NumAlf            ! Number of data lines in the following table
!    Alpha      Cl      Cd    Cm
!    (deg)      (-)     (-)   (-)
-180 0 0.1748 0
-170 0.23 0.2116 0.4
-160 0.46 0.3172 0.1018
-150 0.494 0.4784 0.1333
-140 0.51 0.6743 0.1727
-130 0.486 0.8799 0.2132
-120 0.415 1.0684 0.2498
-110 0.302 1.2148 0.2779
-100 0.159 1.2989 0.2933
-90 0 1.308 0.2936
-80 -0.159 1.2989 0.2933
-70 -0.302 1.2148 0.2779
-60 -0.415 1.0684 0.2498
-50 -0.486 0.8799 0.2132
-40 -0.51 0.6743 0.1727
-30 -0.494 0.4784 0.1333
-21.1 -0.56 0.3027 0.0612
-19.1 -0.67 0.3069 0.0904
-17.1 -0.79 0.1928 0.0293
-15.2 -0.84 0.0898 -0.009
-13.2 -0.7 0.0553 -0.0045
-11.1 -0.63 0.039 -0.0044
-9.2 -0.56 0.0233 -0.0051
-7.1 -0.64 0.0131 0.0018
-5 -0.392 0.013325 -0.051266486
-4 -0.331 0.012575 -0.045608313
-3 -0.256 0.011913636 -0.043964333
-2 -0.168 0.01205 -0.045854556
-1 -0.069 0.012186364 -0.050480193
0 0.043 0.011915789 -0.057367933
1 0.163 0.0116 -0.065084522
2 0.294 0.012933333 -0.074859526
3 0.404 0.014266667 -0.078213846
4 0.524 0.014485714 -0.083025112
5 0.602 0.014580952 -0.076346987
6 0.668 0.015273684 -0.069810343
7 0.735 0.016115789 -0.066028783
8 0.798 0.021 -0.063565297
9 0.844 0.026333333 -0.060192714
10 0.881 0.029509091 -0.055784464
11 0.893 0.036075 -0.047964098
12 0.900 0.048354545 -0.037015348
13 0.887 0.06202 -0.030991997
14 0.845 0.074109091 -0.023376047
15 0.790 0.08747 -0.02167331
16 0.728 0.0984375 -0.028829154
17 0.650 0.21748 -0.082875739
```

```
18 0.673 0.38306 -0.102766633
19 0.571 0.4 -0.090829764
20 0.571 0.410531343 -0.086424214
21 0.590 0.422232836 -0.088873253
22 0.609 0.433934328 -0.092523247
23 0.632 0.445635821 -0.096545564
24 0.653 0.457337313 -0.100657809
25 0.676 0.469038806 -0.105061084
26 0.695 0.484857143 -0.10927122
27 0.724 0.517142857 -0.114557191
28 0.750 0.549428571 -0.120224079
29 0.771 0.581714286 -0.12511972
30 0.791 0.614 -0.129792753
35 0.893 0.842789421 -0.155769619
40 1.008 1.574367925 -0.187472598
45 1.075 2.378 -0.219154914
50 1.127 2.403 -0.244752375
55 1.177 2.42 -0.313
60 1.1 2.455 -0.3388
70 0.971 2.472 -0.3557
80 0.385 2.476 -0.363
90 0 2.468 -0.3604
100 -0.159 1.2989 -0.36
110 -0.302 1.2148 -0.3446
120 -0.415 1.0684 -0.3166
130 -0.486 0.8799 -0.28
140 -0.51 0.6743 -0.2394
150 -0.494 0.4784 -0.2001
160 -0.46 0.3172 -0.1685
170 -0.23 0.2116 -0.5
180 0 0.1748 0
```

Appendix C

Data Calibration

C.1 Pressure Transducer Calibration

After gathering the calibration pressure data for each transducer, a linear model described in Equation C.1 is used to fit the raw data.

$$P = a \times V + b \tag{C.1}$$

Where P is the pressure in Pascals, a is the linear fit slope, V is the voltage (in V) from the transducer, and b is the Y-intercept. The slope and y-intercept are logged in Table C.1. The r-squared value is also calculated and logged in the Table C.1.

C.2 Strain Gage Calibration

The main purpose of the strain gage calibration was to relate the output of the gages to the moment on the shaft. The strain gage is directly proportional to the stress on the surface using equation C.2.

$$R_{SG} = C_{SG}\sigma_{\beta} \tag{C.2}$$

Where R_{SG} is the strain reading, C_{SG} is the strain gage constant, and σ_{β} is the surface stress on the shaft at point β. The surface stress could be related to the moment using Equation C.3.

$$\sigma_\beta = M_\beta c / I_b \tag{C.3}$$

Where M_β is the moment at point β, c is the shaft outer radius, and I_b is the area moment of inertia of the cross section. Substituting Equation C.3 in C.2 and combining all the three constants under one variable K ($K = I_b/C_{SG}c$) Equation C.4 is formed. A bias error b_k also is added to the equation to account for the offset in the strain gage reading.

$$M_\beta = KR_{SG} + b_k \tag{C.4}$$

Equation C.4 is a first degree polynomial. The slope and y-intercept could be calculated using a linear regression function built in matlab. During calibration the output of the strain gage is measured as well as the weight on the shaft which could be converted to moment. The amplitude and the strain gage offset are plotted against the shaft moment for each strain gage group in Figure C.1. After a linear regression fit the equations for both strain gage groups are in Equation C.5.

$$\begin{aligned} M_\beta &= 95.44Amp + 21.86(SG1) \\ M_\beta &= 101.11Amp + 52.61(SG2) \end{aligned} \tag{C.5}$$

C.3 Torque Sensor Calibration

The torque sensor was independently calibrated to make sure that the analog reading was accurate. While only one counterweight rod at the 3 o'clock position was installed on the parked turbine, weights were added at the tip to simulate a torque increase. After calibration, the goodness of fit was found to be exactly 1 indicating that the relationship is linear. The torque sensor was calibrated for the full range of 200 N.m. The following equation relates the torque on the shaft to the voltage obtained from the DAQ card:

$$Torque = \frac{V_{signal} - 0.282}{0.0248} \tag{C.6}$$

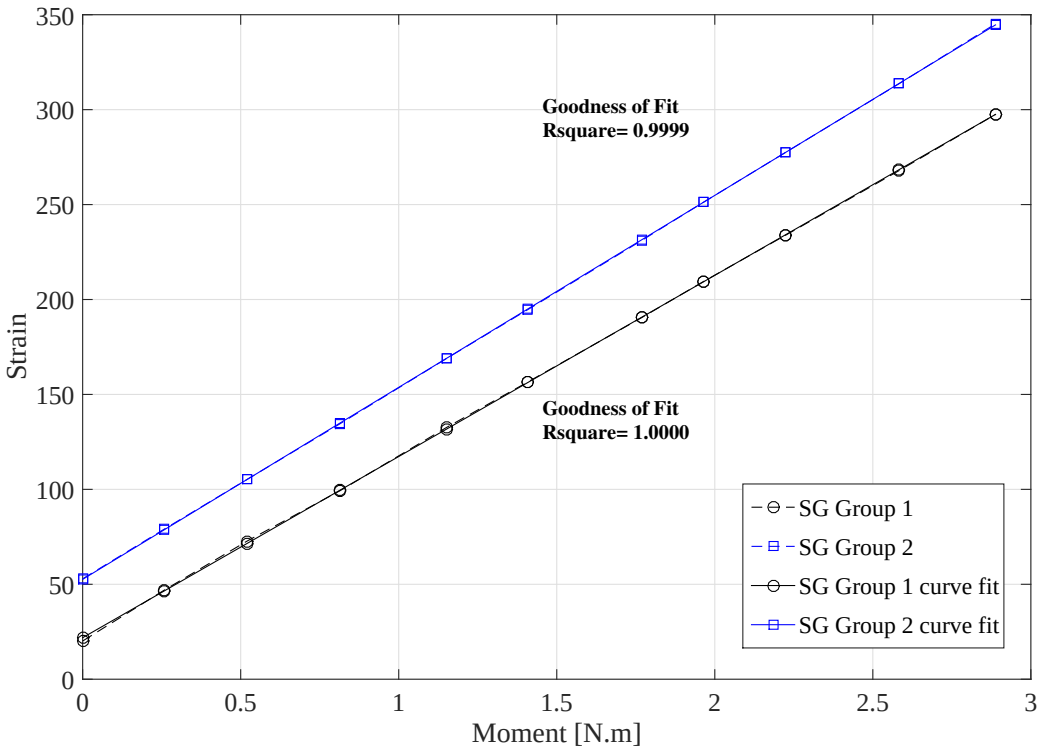


Figure C.1: Strain gage group 2 calibration for different weight. The curve fit is overlaid over the raw data

Table C.1: Pressure transducer calibration properties

Pressure Transducer ID	1	2	3	4	5	6	7	8	9	10
Linear Fit Slope	2869	2880	2882	2854	2865	2870	2876	2869	2863	2853
Y-Intercept	-730	-713	-706	-749	-742	-708	-723	-727	-740	-755
R-Square (Goodness of fit)	0.9999	0.9997	0.9995	1.0000	1.0000	0.9996	0.9998	0.9998	1.0000	1.0000
Pressure Transducer ID	11	12	13	14	15	16	17	18	19	20
Linear Fit Slope	2866	2870	2877	2858	2838	2858	2836	2846	2845	2839
Y-Intercept	-738	-738	-708	-745	-763	-702	-789	-732	-750	-784
R-Square (Goodness of fit)	0.9999	0.9999	0.9996	1.0000	1.0000	0.9994	1.0000	0.9999	1.0000	1.0000
Pressure Transducer ID	21	22	23	24	25	26	27	28		
Linear Fit Slope	2833	2838	2873	2841	2839	2840	2865	2885		
Y-Intercept	-769	-756	-716	-751	-752	-746	-737	-704		
R-Square (Goodness of fit)	1.0000	1.0000	0.9996	1.0000	1.0000	0.9999	0.9999	0.9994		

Appendix D

Uncertainty Analysis

It is not acceptable to present experimental data without understanding and calculating the uncertainties involved. It also provides confidence in the published data is accurate and reliable [144]. A brief description of experimental uncertainty will be presented along with uncertainty calculations for the different measurements devices used in this document.

D.1 Review of Experimental Uncertainty

The true value of a measurable property cannot be exactly known, and the measured value is an estimate of the true value obtained from a measurement device. Experimental uncertainty is an estimate of the difference between the true value and measured value. There are two types of uncertainties: bias uncertainty and precision uncertainty [111]. Bias uncertainty (b) is due to a constant and systematic errors present in the instrumentation. Multiple bias error could be present for a given instrument and could be combined by the root-sum-square (RSS) method. On the other hand, precision uncertainty (p) consists of random noise in the measurements. Once the two uncertainties are calculated with the same confidence level, they could be combined using the RSS method to find the total uncertainty (u_{tot}), as shown in Equation D.1.

$$u_{tot} = \sqrt{b^2 + p^2} \tag{D.1}$$

Precision uncertainty is based on statistic analysis based on the measured data. For a sample size greater than 30, Equation D.2 can be used to calculate the precision uncertainty.

$$p = \frac{2\sigma}{N_{sample}} \tag{D.2}$$

Where σ is the standard deviation and N_{smple} is the number of samples. To decrease the precision uncertainty more data samples could be taken. In some cases the desired measurement property is dependent on multiple measurements sources with each having its own uncertainty. Propagation of uncertainty could be used to calculate the uncertainty the dependent variable. If the relationship has the form of $y = f(x_1, x_2, ..., x_3)$, then Equation D.3 could be used to calculate the propagated uncertainty.

$$u_y = \sqrt{\left(\frac{\partial y}{\partial x_1}u_1\right)^2 + \left(\frac{\partial y}{\partial x_2}u_2\right)^2 + ... + \left(\frac{\partial y}{\partial x_3}u_3\right)^2} \tag{D.3}$$

D.2 Torque Sensor Uncertainty Calculations

In this section the bias uncertainty association with the torque sensor is calculated based on the uncertainty sources of the Futek rotary torque sensor [131] and are presented in Table D.1. The actual values presented in the table are based on the full scale (FS) of the torque sensor which is 200 N.m. Summing these values using the RSS method presented in equation D.3 gives a total bias uncertainty of ±0.6 N.m or ±0.3% FS, as shown in Equation D.4. The accuracy of the NI 9215 DAQ card used has a typical accuracy of 0.02% which is negligible when compared to other sources of errors.

Table D.1: Uncertainty sources for the Futek [131] Torque Sensor

Uncertainty Source	% of Full Scale	Actual Value
Hysteresis	±0.1	0.2
Non-linearity	±0.2	0.4
Non-repeatability	±0.2	0.4
Temperature Shift Span	±0.01	0.02

$$u_{b,torque} = \sqrt{0.2^2 + 0.4^2 + 0.4^2 + 0.02^2} = 0.60\ N.m\ or\ 0.3\%FS \tag{D.4}$$

D.3 Strain Gage Uncertainty Calculations

The SGD-7/1000-DY11 precision strain gages by Omega [120] was used with a tolerance of ± 0.35 %, while the NI 9237 DAQ card used to read the strain gages has an accuracy of ± 0.05% [122]. Combining both uncertainties would yield a total uncertainty of ± 0.35 % of the measured value. In this case the uncertainty in the DAQ is negligible. Additional bias uncertainty was also present due to calibration and while converting strain measurements to units of N.m. Combining all the bias uncertainties would results in a value of 0.5%. As for the precision uncertainty, it would found to be negligible due to the large number of samples taken, higher than 4000 points.

D.4 C_n Uncertainty Calculations

As discussed in section 3.1.3, the All Sensor pressure transducers was used to measure the surface pressure along the airfoil chord [113]. The output voltage ranges between 0 to 5 V corresponding to -0.1 kPa to 11.8 kPa. The offset associated with warm-up is ± 15 millivolt but that was eliminated by warming up the transducer for one hour before use. The error associated with position is ± 15 millivolt . The nominal linearity and hysteresis are both equal to ±0.05 % FS. The three sources of error that make up the bias uncertainty in the transducer are summed together in Equation D.5. To calculate the precision uncertainty, Equation D.2 was used and since the number of samples taken in higher than 4000, this makes the precision uncertainty negligible when compare to the bias uncertainty in most cases.

$$\begin{aligned} \Delta u_{T,0} &= \pm\sqrt{+\Delta u_{linearity}^2 + \Delta u_{hystersis}^2 + \Delta u_{Position}^2} \\ \Delta u_{T,0} &= \pm\sqrt{(2.5mV)^2 + (2.5mV)^2 + (15mV)^2} = 15.4mV \end{aligned} \tag{D.5}$$

Based on the calibration of the transducers, ± 15.4 mV was equivalent to ± 44 Pa. The pressure transducers are connected to the NI9205 DAQ card [123] as per Figure 3.20. The uncertainty in the DAQ card is ±3.2 mV. Using the RSS method to add the DAQ uncertainty to the total uncertainty of the pressure transducer would yield to ± 15.7 mV. This shows that the DAQ card barely contributes to the uncertainty of the pressure transducers. The DAQ does not truly measure the analog voltage simultaneously but for the purpose of this experiment and the rate of collection, it was described as simultaneous. The DAQ card could measure up to 250,000 samples/sec aggregately. The DAQ could then

measure and convert all 28 channels in 0.11 millisecond or in about 0.15 degrees of rotation based on the rotor rotational speed described here. One rotation of the blades takes about 0.3 seconds and as a result, 0.11 millisecond is a negligible time. For this reason, the data acquisition was described as simultaneous.

Now that the uncertainty in pressure is found, the next step is to calculate the uncertainty in C_p. Based on propagation of uncertainty and equation 4.4, the uncertainty in C_p is presented in Equation D.6.

$$\begin{aligned} \Delta u_{C_p} &= \pm\sqrt{(\frac{\partial Cp}{\partial P} * \Delta u_p)^2 + (\frac{\partial Cp}{\partial W} * \Delta u_W)^2} \\ \Delta u_{C_p} &= \pm\sqrt{(\frac{1}{1/2\rho W^2} * \Delta u_p)^2 + (\frac{2P}{1/2\rho W^3} * \Delta u_V)^2} \end{aligned} \tag{D.6}$$

The next and final step is using the uncertainty in C_p to calculate the uncertainty in C_n. The latter variable was calculated by averaging the upper and lower limit of C_n as seen in Equation D.7. The value of C_n is calculated based on Equation 4.5

$$\Delta u_{C_n} = \frac{\int \left(\Delta C_p(x) + u_{C_p(x)}\right) dx - \int \left(\Delta C_p(x) - u_{C_p(x)}\right) dx}{2} \tag{D.7}$$

D.5 Angular Momentum Calculations

The azimuth variation on ΔTorque measurements presented throughout chapter 6 was found to be significantly lower than the OpenFast predictions. This difference was attributed to angular moment in the rotating blades that dampens out the ΔTorque variation. In this Appendix, the angular momentum of the rotor was calculated and how it can dampen the load variation when the turbine is yawed.

To begin with, the angular momentum of the wind turbine rotor was determined by equation D.8.

$$L = I\omega = mr^2\omega \tag{D.8}$$

where L is the angular momentum, I is the moment of inertia, m is the point mass of the rotor, r is the local radius of the point mass, and ω is the angular rotation. The mass and

length of each wind turbine blade is about 5 kg and 1.77 m. Based on a rotation of 200 rpm, the angular momentum was calculated to be about 230 kgm^2/s.

From Newton's second law, the total torque acting on the wind turbine rotor could be defined as a change in angular momentum over time as expressed in Equation D.9. Therefore, to determine the relative impact of a change in torque on the angular momentum of the wind turbine rotor, the theoretical change in torque (obtained from OpenFast) could be multiplied by a length of time to determine the corresponding change in momentum.

$$\int T dt = I\omega \tag{D.9}$$

From OpenFast the maximum change in torque is approximately 30 Nm over an azimuth of 180° and that corresponds to 0.15 seconds. Based on Equation D.9, the change in angular momentum is 0.23 kgm ^{2}/s, which is significantly less than the total angular momentum of 230 kg m^2/s. Thus the torque sensor mounted to the wind turbine shaft does not see a significant change in torque despite an increased force on the blade.